Ariel Voyagers

Scuttle Mission

EMA 569: Senior Design
Engineering Mechanics: Aerospace Engineering
University of Wisconsin-Madison
May 1, 2024

Authors

Matthew Brandt

Olivia Janson

Chase Orvis

Kaden Reybrock

Supervisors

Sonny Nimityongskul

Nino Miosi

Travis Sheperd

Executive Summary

The Scuttle Mission aims to explore Uranus's moon, Ariel, to verify the existence of water under its surface. Greatly inspired by past NASA missions Dawn, Voyager, and Cassini, Scuttle looks to employ a highly optimized thruster system to complete the journey to Ariel. For this expedition, Scuttle will employ electric propulsion (EP) to end in a low-altitude orbit around Ariel, examining the feasibility of electric propulsion systems for deep-space missions. The Ariel Voyagers main objective is to determine the optimum thruster selection while creating a flight path directly to Uranus to minimize required propellant mass. The Scuttle spacecraft must travel 2.6 billion km to reach Ariel while minimizing mass and maintaining an overall mission timeline comparable to traditional propulsion methods. Scuttle must also carry a scientific payload capable of sending meaningful data back to Earth. The satellite's size is constrained only by the payload fairing dimensions of the launch vehicle, SpaceX's Falcon 9. Environment is another important consideration for the design of the spacecraft; Scuttle must be designed to survive the launch loads and address the thermal protection necessary for the scientific payload to survive in deep space.

The Scuttle Mission studies a variety of orbital paths to reach Ariel, looking to determine the most optimum profile for mass and mission duration reduction. Although employing low-thrust EP thrusters, the Ariel Voyagers compares a low-thrust mission to that of a more traditional impulsive mission. This comparison served to detail the benefits that come from utilizing an EP system, namely a mission duration outside of Earth's sphere of influence that is on par with that of impulsive methods but requires a propellant mass only 5.4% that of a traditional impulsive system.

A preliminary model, Mark I, of the Scuttle spacecraft was created to begin an analysis of the structure, done to ensure the spacecraft could survive launch loads. This structural analysis includes analytical and numerical results, utilizing ANSYS software. Additional analyses were completed to ensure all systems that make up the spacecraft operate properly and interface with each other in a reasonable way. These analyses included a structural analysis of the fuel tanks, a heat transfer analysis to ensure all parts will not be affected by the ASRGs, an analysis of the shielding needed to prevent radiation from causing instrument failure, a determination of the whipple shielding needed to keep the spacecraft safe from debris, a plumbing analysis, and a study of EP, looking into the processes that make these systems work.

Following the completion of these analyses, Scuttle Mark II was created: a complete redesign of the Mark I model. This redesign improved the practicality, eased the manufacturing, and improved the accuracy of the model to create a final product that took on the conclusions made by the analyses. With a total mass of 5,612 kg, the Scuttle Mark II spacecraft effectively uses EP to achieve its deep-space mission objectives. The Scuttle Mission is driven by discovery, and the Ariel Voyagers have taken an intrepidacious approach, pushing the boundaries of innovation in the name of exploration.

Table of Contents

1   Introduction

Beginning long before society was capable of space exploration, astronomers were curious about what surrounds humans in the solar system. As more space discoveries were made, technology advanced to a point where missions into space became viable. In 1960, the first application satellite, the Discoverer 13, was launched into Earth's orbit for weather observation [1]. Two years later, the Mariner 2 returned the first data collected from another planet, Venus [1]. Soon there were many spacecraft dedicated to taking pictures and collecting data near Earth. The Voyager 2 mission was the only early mission that had a goal of visiting every planet in deep space. It reached Uranus in 1986, nine years after its launch; the flight path took advantage of the orbital alignment of all the gas-giant planets to save time and fuel [2]. Since it often takes decades to travel out to deep space, a lot of times with no plan to return to Earth, these missions take a significant commitment and therefore are infrequent.

There is much more mystery surrounding the planets and other natural satellites beyond the asteroid belt. Similar to how past technological advancements and innovations made space exploration possible, current and future discoveries can help propel exploration into deep space. Within the scientific community, there exists an interest in exploring icy moons scattered throughout the solar system. These moons, with their icy surfaces, hold the promise of unveiling hidden oceans and distinctive geological phenomena. The fascination lies in the potential these celestial bodies have for providing insights into the conditions conducive to extraterrestrial life. One of these moons, Europa (in Jupiter's orbit), has two upcoming missions: NASA's Europa Clipper and ESA's Jupiter Icy Moons Explorer, that plan to take a closer look into the believed conditions on the surface of the moon [3]. However, the fascination with icy moons extends beyond Europa and Jupiter's other moons. Icy moons orbiting Uranus, for instance, remain largely unexplored, with no planned missions on the horizon. These specific moons may be difficult to reach, but futuristic technology may be efficient enough to unveil many of the unknowns that lay millions of miles away.

1.1   Problem Statement

The Scuttle Mission continues the tradition of advancing scientific discovery and innovation, leading to understanding the formation of the universe through a mission to Ariel, a moon of Uranus. Uranus – and specifically its major moons – have yet to be explored in an in-depth manner. Scientists recently discovered potential ocean layers beneath the icy surface of each major moon, which potentially hold evidence of current or past life forms [4]. Ariel's appeal lies in the discovery of evidence that its ocean layer has reached the surface [5]. The main goal of this deep-space mission is to scout out these areas with high-definition imaging and sensors while providing a robust system to traverse deep space.

1.2   Mission Statement

Scuttle Mission's objective is to embark on a journey from Earth to explore Uranus' moon, Ariel, shown in Figure 1.2.1). The purpose of such a satellite is to study Ariel's distinct features and potential oceanic presence. The team plans to smoothly enter a low-altitude orbit around Ariel, employing electric propulsion (EP) technology to enhance mission efficiency. The primary goal of the Ariel Voyagers is to determine the optimum thruster selection and count while creating a never before used flight path directly to Uranus in order to minimize required propellant mass. Armed with state-of-the-art scientific instruments, such as a magnetometer, near-infrared mapping spectrometer, and visible and mid-infrared cameras, the mission aims to unveil the secrets of Ariel's composition and geophysical characteristics. A crucial part of the exploration involves confirming the presence of an ocean through detailed evaluations of tidal flexing. If a presence is found, the satellite should assist a potential mission that can land on the surface of the moon by scouting the best landing location and further exploring the depths of the ocean.

Figure 1.2.1: Photograph of Uranus' Moon, Ariel [6].

2 Product Design Specifications

The Product Design Specifications (PDS) serve as a blueprint for the design team and help ensure that the Scuttle Mission spacecraft meets the intended objectives and criteria. This section highlights the most important sections in the PDS which include: the relevant standards, expected performance, the environment it is used in, size and weight, and material usage. The full PDS is shown in Appendix I (Section 11.1). Some specifications were determined by Scuttle Mission's selection of SpaceX's Falcon 9 as the mission launch vehicle to reach low Earth orbit.

2.1 Standards

The mission will be designed to NASA technical standards as given below.

1000 - Systems Engineering and Integration, Aerospace Environments, Celestial Mechanics

- NASA-HDBK-1004: NASA Digital Engineering Acquisition Framework Handbook
  This NASA handbook offers guidance on developing a digital engineering acquisition framework. It contains descriptions of data requirements and contractual language for the statement of work [7].
- NASA-HDBK-1005: NASA Space Mission Architecture Framework (SMAF) Handbook For Uncrewed Space Missions
  This NASA handbook offers guidance on developing a mission architecture for uncrewed space missions [7].
- NASA-HDBK-1009: NASA Systems Modeling Handbook For Systems Engineering
  This NASA handbook addresses systems engineering products such as the concept of operations, requirements, and verification and validation [7].

4000 - Electrical and Electronics Systems, Avionics/Control Systems, Optics

- NASA-HDBK-4001: Electrical Grounding Architecture for Unmanned Spacecraft
  This NASA handbook outlines grounding requirements for various electrical equipment including power sources like RTGs, science instruments, and attitude control. It also provides a sample ground tree for large complex spacecrafts like Scuttle [7].
- NASA-HDBK-4002: Mitigating In-Space Charging Effects-A Guideline
  This NASA handbook outlines the circumstances in which spacecraft charging may pose a concern and lists design solutions like material selection and bonding and shielding electronics with Faraday cages [7].
- NASA-HDBK-4006: Low Earth Orbit Spacecraft Charging Design Handbook
  This NASA handbook provides a summary of the plasma reactions that may occur while a high-voltage system is used in the Earth's ionosphere. This primarily applies to solar arrays so the key requirement for Scuttle Mission will be to ensure that any opening in the structure is smaller than the plasma Debye length of the orbit (5cm) to prevent plasma interactions with electronics [7].

- NASA-HDBK-4007: Spacecraft High-Voltage Paschen and Corona Design Handbook
  This NASA handbook provides a summary of the electrical design techniques that alleviate harmful effects as a result of using a high-voltage system in space. The primary goal of these practices is to isolate one conducting surface from another using electric insulation [7].
- NASA-HDBK-4008: Programmable Logic Devices (PLD) Handbook
  This NASA handbook provides a guideline and best practices for planning, designing, verifying, and maintaining programmable logic devices [7].
- NASA-HDBK-4009: Space Telecommunications Radio Systems (STRS) Architecture Standard Rationale
  This standard outlines the components necessary for a General-Purpose Processing Module (GPM), the primary control component of the radio. It also goes over the optional Radio Frequency and Signal-Processing Modules [7].

5000 - Structure/Mechanical Systems, Fluid Dynamics, Thermal, Propulsion, Aerodynamics

- NASA-HDBK-5010, VOLUME 1 AND 2: Fracture Control Implementation Handbook For Spaceflight Hardware
  These handbooks the process that should be followed to maintain fracture control. Components should be separated into three categories (Exempt, non-fracture critical, and fracture critical) and assessed appropriately. Fracture critical components must meet fracture control requirements through analysis where the component has a minimum service life factor of four and a fracture safety factor of 1.5 [7].
- NASA-STD-5001: Structural Design and Test Factors of Safety for Spaceflight Hardware
  This standard outlines NASA structural design and test factors for spaceflight hardware development and verification to ensure safe and reliable designs. For a protoflight method, the ultimate and yield design factors must meet a minimum of 1.4 and 1.25 respectively for metallic structures. It should be noted that composite structures do not follow these same design factors. All structural items subjected to significant in-plane stresses under any combination of ground loads, flight loads, or thermal loads shall be analyzed for buckling failure. Design loads for this analysis shall be ultimate loads [7].
- NASA-STD-5002: Load Analyses of Spacecraft and Payloads
  This standard outlines the methods and requirements for payload and spacecraft load analyses as well as accepted engineering practices used in NASA projects. Limit loads must be determined within a 99.87 percent probability at 50 percent confidence level [7].
- NASA-STD-5006: General Welding Requirements for Aerospace Materials
  This standard outlines the quality assurance requirements for manual, automatic, machine, and semiautomatic welding used in spaceflight applications and test equipment. The key takeaway for the Scuttle Mission is to ensure that base alloy materials follow industry specifications and, when used, weld start and runoff tabs should be the same as the alloy being joined [7].

- NASA-STD-5009: Nondestructive Evaluation Requirements for Fracture Critical Metallic Components
  This standard outlines nondestructive evaluation requirements for components where fraction control and probability of detection are required. Non-ferous materials and corrosion resistant steel and nickel-based alloys must be etched/electropolished to ensure that smeared metal does not mask cracks [7].
- NASA-STD-5012: Strength and Life Assessment Requirements for Liquid-Fueled Space Propulsion System Engines
  This standard outlines the minimum acceptable requirements for strength, fatigue, and creep for NASA liquid-fueled propulsion system engines. Factors of safety for metallic structures and components in this category are given as 1.1 and 1.4 for yield and ultimate failure respectively [7].

6000 - Materials and Processes, Parts

- NASA-STD-6012: Corrosion Protection for Space Flight Hardware
  This standard outlines the corrosion control requirements necessary to qualify materials for space flight hardware. To prevent corrosion, Scuttle Mission must round all exterior edges, utilize chemical surface treatments, and seal faying surfaces. All fasteners should also be wet installed with sealant or primer [7].
- NASA-STD-6016: Standard Materials and Processes Requirements for Spacecraft
  This document outlines the acceptable materials and processes used in the design, fabrication, and testing of all components used in spacecraft hardware. The materials used should meet the worst-case useful-life requirements outlined in the document for their particular purpose [7].

Additional documents

- MSFC-STD-3029A: Guidelines for the Selection of Metallic Materials for Stress Corrosion Cracking Resistance in Sodium Chloride Environments
  This standard outlines the guidelines for selecting metallic materials to resist stress corrosion cracking for air environments. Table I found in this standard provides the preferred materials for resisting stress corrosion cracking, broken up into categories such as aluminum alloys, copper alloys, ferrous alloys, and nickel alloys. Materials not listed in this table must be approved before use [7].
- NASA-HDBK-8715.26: Information and Best Practices Related to NASA Nuclear Flight Safety for Space Flights Involving Space Nuclear Systems
  This handbook aims to provide guidelines to create a process focused on maintaining the safety requirements for missions using nuclear systems. Nuclear-enabled missions must conduct all activities under the National Environmental Policy Agct and meet Federal nuclear launch authorization requirements [7].

2.2 Performance

The satellite's performance requirements are underscored by the need to cover approximately 2.6 billion km to reach and orbit Uranus' moon, Ariel. The Ariel Voyagers have been tasked with determining the feasibility of electric propulsion (EP) for the purpose of deep-space missions, exploring several options of thruster, power source, and propellant type. The Scuttle Mission requires an optimized thruster system for propellant mass and overall mission duration, and looks to determine how these compare with traditional impulsive thrusters. The success of the mission is dependent upon the total mass and overall duration saved by using low-thrust EP methods versus impulsive chemical methods, defined by a 5% improvement in total. This means that three possibilities can lead to a successful mission: (1) the total mass savings are in excess of 5%, allowing for a similar percentage loss in mission duration to still exceed 5%, (2) the total mass savings of the EP mission is at a deficit, but the time savings in mission duration is at minimum 5% greater than this deficit, or (3) the percentages of total mass and mission duration savings total at least 5%.

Drawing insights from the Dawn mission, which covered a distance of 6.4 billion km to reach Vesta and Ceres, dwarf planets inside the asteroid belt, the proposed satellite aims for efficiency in data collection. The Dawn mission, over its course, captured 95,000 photos and amassed a dataset exceeding 167 GBs [8]. Noteworthy was Dawn's propulsion system, comprised of ion thrusters that provided 2,000 days of thrust. This provides a baseline mission duration for comparison, as the Scuttle Mission will travel over 10 times the radial distance to reach Uranus. Accelerating with a thrust of 92 mN, these ion thrusters operated with a propellant mass flow rate of only 3.25 mg/s while carrying 425 kg of fuel [8]. This successful application of an EP systems sets a precedent that informs the optimization of propulsion and data collection strategies for the upcoming mission.

2.3 Size and Weight

The satellite's size is constrained primarily by the dimensions of the chosen launch vehicle, in this case, the Falcon 9. The maximum allowable dimensions for the satellite, as dictated by the Falcon 9, are 4.6 m in diameter and 6.6 m in length [9]. Notably, there is a tapering inclination above the main payload loading that extends for 4.8 m. These specifications define the physical boundaries within which the satellite must be designed. A diagram of the designated space is provided in Figure 2.3.1.
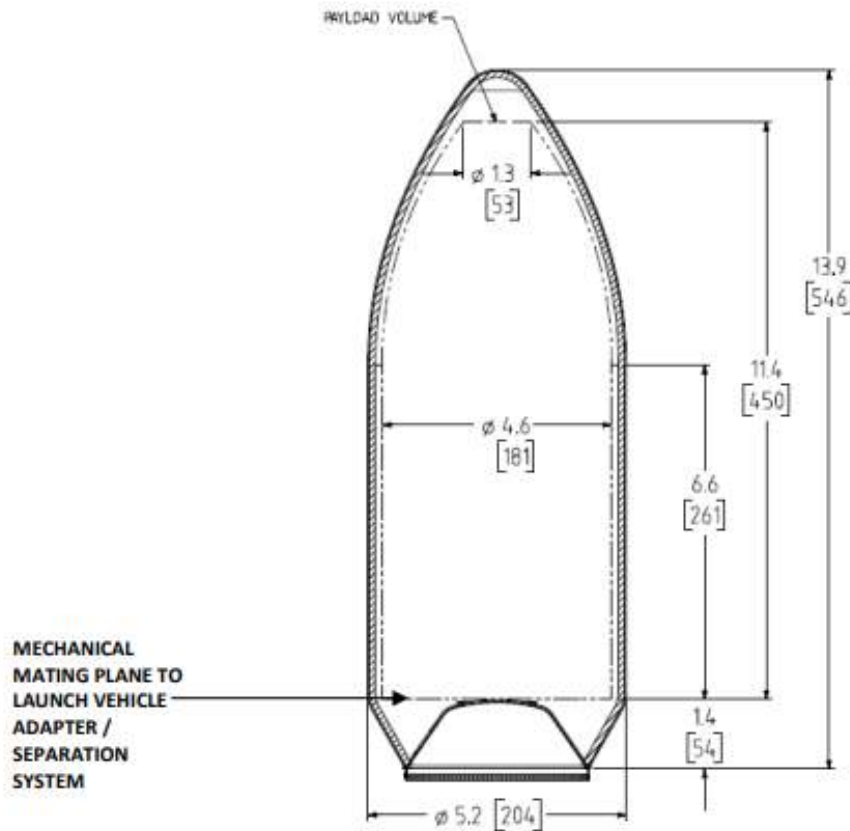
Figure 2.3.1: Provided Falcon 9 Fairing (in m) [9].

Additionally, the inclusion of various instrumentation components further influences the size of the satellite. Notable elements such as gimbals, electric propulsion/ion motor stabilization, communication equipment, radiation shielding, impact protection, and both a narrow-angle and wide-angle camera contribute to the overall spatial requirements.

The weight of the satellite is determined by factors such as the required propulsion system, the carrying capacity of the launch vehicle, and the distance the satellite will travel. Preliminary astrodynamic calculations will be instrumental in determining the optimal weight range for the satellite. The projected weight range is expected to fall between 2,500 kg and 7,500 kg, ensuring compatibility with past satellite missions. The maximum weight allowance from the Falcon 9 launch vehicle is set at 22,000 kg, providing ample margin for the satellite's payload [9].

A comparative analysis with the Dawn spacecraft indicates that the proposed satellite's weight will be slightly higher due to the increased distance it is expected to travel. Dawn, with a weight of 747.1 kg at launch and 425 kg of propellant, serves as a reference point for assessing the proposed satellite's weight parameters [8].

2.4   Environment

The satellite must endure four shock vibrations events during launch, characterized by the following frequencies and shock response spectrum peaks, seen in Figure 2.4.1:

- 100 Hz $(20\,g)$,
- 270 Hz $(240\,g)$,
- 2,000 Hz $(3,000\,g)$,
- 10,000 Hz $(3,000\,g)$,

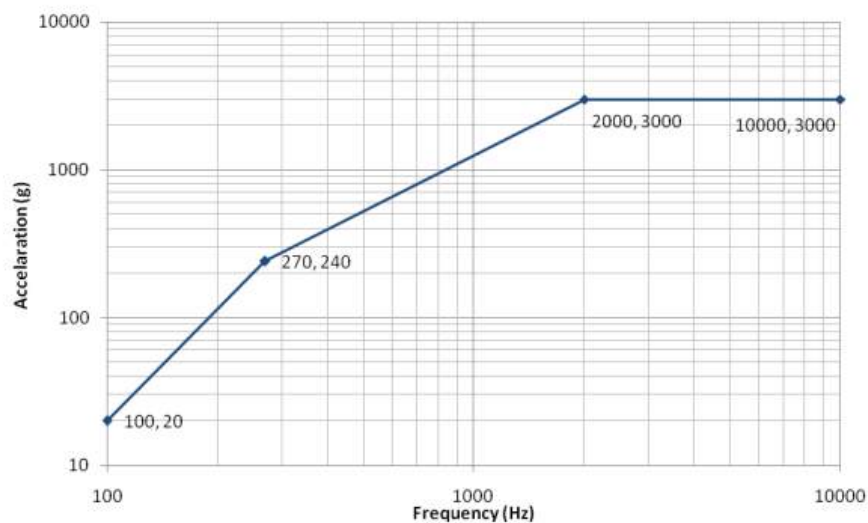where g is the gravitational acceleration on Earth [9].

Figure 2.4.1: Falcon 9 shock response at payload interface [9].

The maximum acceleration load factors experienced in the Falcon 9 cabin are $8\,g$ axially and $3\,g$ laterally [9]. Humidity levels during launch should be maintained within the range of 45% to 55% [9]. Special consideration must be given to potential corrosion from external factors, including sun exposure, solar wind, and atomic oxygen.

The satellite must operate effectively across a temperature range from -160°C to 125°C, depending on its orientation relative to the Sun. Comparable temperature ranges to those determined for the satellite are applicable, drawing parallels with the New Horizons mission that operated in similar deep space conditions. Design considerations must account for avoiding and potentially withstanding collisions with space debris, natural satellites, and micrometeorites.

2.5   Materials

In addressing space corrosion concerns arising from sun exposure, solar wind, and atomic oxygen, the satellite's main body will be constructed using a combination of titanium and

aluminum alloy materials following NASA-STD-6012 [7]. This material selection aims to mitigate the effects of corrosive elements prevalent in the space environment. The satellite's design will adhere to established and accepted materials and manufacturing practices for satellites; materials used must be present in the SpaceMAT Database [10].

The manufacturing and assembly processes will involve extensive welding to seal critical areas, necessitating rigorous testing of all welds to meet NASA's welding standards, which are mentioned in Section 2.1. Adherence to NASA-STD-6016 will guide the overall materials and manufacturing practices, ensuring compliance with recognized industry benchmarks.

Metallic material selection will specifically follow MSFC-STD-3029A standards to control stress corrosion cracking, emphasizing the importance of material durability in the harsh conditions of space. Common materials such as Kevlar, known for its lightweight and robust characteristics along with resistance to temperature changes, will be employed to protect the satellite from potential orbital debris. Aluminum alloys such as 6061-T6 and 7075-T6, chosen for their lightweight and strong properties, will also play a vital role in the construction of various satellite components.

For propulsion, the chosen propellant is xenon, selected for its nearly equivalent thruster efficiency to mercury (the highest-rated propellant). Xenon offers environmental advantages over mercury and can be stored non-cryogenically, eliminating the need for specialized cryogenic storage systems. While relatively expensive and rarer compared to other options, these factors are outweighed by its efficiency and environmental acceptability. This aligns with the successful use of xenon propellant in the Dawn mission, further supporting its NASA-approved status. The satellite's overall material and propellant selections demonstrate a commitment to reliability, efficiency, and environmental responsibility in alignment with established aerospace standards.

2.6   Impact on Society, Public Welfare, and Environment

The Scuttle mission holds significant implications for society, public welfare, and the environment. The safety considerations encompass both the spacecraft's operational aspects and its potential impact on Earth's surroundings.

2.6.1   Safety Aspects

The spacecraft design adheres to rigorous safety standards outlined by OSHA for workplace safety. User safety is a paramount concern, with a thorough assessment of potential hazards such as sharp edges, pinch points, and misuse. Public safety is diligently addressed to prevent dangers to individuals in proximity to the spacecraft's operation. As the craft will not return to Earth, the risk of off-planet contamination is nonexistent, and precautions are in place to protect society from potential unknown lifeforms. During launch, extra precautions are to be taken to ensure that a nuclear disaster could be properly contained in the case of launch failure.

2.6.2 Economic, Social, and Cultural Factors

The success of the mission holds economic, social, and cultural significance. The mission's timely execution and efficient extraction of data play a crucial role in justifying the funds expended and maintaining public trust. Symbolic gestures, such as displaying the US flag on the satellite, contribute to the mission's cultural impact.

2.6.3 Human Welfare and Exploration

The mission benefits the scientific community by providing valuable data for studying and understanding planetary systems. Additionally, by exploring oceanic environments, the mission sets the stage for future exploration and scouting potential landing spots. This, in turn, influences decisions on cost estimates and priorities for further exploration, contributing to the welfare of humanity through scientific advancement.

2.6.4 Environmental Considerations

In assessing the environmental impact of the Scuttle mission, the full product life cycle is considered. The mining of rare earth materials for the electric propulsion system and solar panels raises concerns, and precautions are taken to handle xenon propellant with care. While the spacecraft itself is not recyclable and involves one-time use, the development of technologies in power generation and space exploration may indirectly lead to innovative solutions to existing environmental problems.

In summary, the Scuttle mission encompasses a comprehensive consideration of societal, public, and environmental impacts, addressing safety concerns, economic and cultural factors, human welfare, and environmental responsibilities.

3 Mission Profile

A mission profile serves as a comprehensive outline detailing the necessary steps to plan and optimize the outcome of a mission. This encompasses the overarching mission planning and design, which provides guidance and navigation to ensure a location at a given time, and addresses resource allocation, including propellant, structural, and payload masses. The necessary steps for a successful mission are described in Table 3.0.1.

Table 3.0.1: Mission Profile Steps: Earth to Uranus

Mission Step	Description
1	Earth Parking Orbit
2	Escape Earth SOI
3	Low Thrust Spiral Insertion
4	Enter Uranus SOI
5	Orbital Insertion
6	Apply necessary ΔV to pair with Ariel

Step one, laid out in Table 3.0.1, entails the process of placing the Scuttle Mission satellite into a low Earth orbit (LEO) – defined as an altitude of 2,000 km or less – to ensure the mission vehicle is in a parking orbit. This parking orbit is the stepping stone to which the low thrust spiral ejection from Earth's sphere of influence will occur. The vehicle selected for this task is the Space Exploration Technologies Corporation (SpaceX) Falcon 9 Block 5 variant. This is a two-stage medium-lift launch vehicle, allowing for a balance between payload and cost-effectiveness due to its reusability. This rocket, in its standard form, is capable of lifting approximately 22,800 kg of payload mass into a LEO. Its first stage consists of nine rocket engines that yield 7606 kN of thrust at sea level using a mix of RP-1 fuel and liquid oxygen (LOX). The second stage utilizes a single vacuum-optimized rocket engine utilizing the same fuel and yields 981 kN of thrust [11]. This, combined with the payload nose cone size will ensure the satellite reaches its parking orbit.

Step two, escaping Earth's sphere of influence (SOI), involves reaching a distance from Earth where gravity no longer keeps an object in Earth's orbit. To escape Earth's SOI, the kinetic energy of the spacecraft must exceed the gravitational attraction of the Earth. This is equivalent to reaching what is called an escape velocity. Generally speaking, spacecrafts achieve escape at altitudes near the geostationary orbit (GEO), which is about 36,000 km above sea level. At this altitude, the escape velocity is slightly under 5 km/s. This step is essential to begin the maneuvers that will take the spacecraft into deep space.

Step three is the main challenge of the mission as low-thrust propulsion cannot use a simple Hohmann transfer to get from Earth to Uranus. This transfer sees a significantly longer impulse time due to the lower maximum force from electric propulsion engines. Finding a balance between performance and total time to complete the process will be key for a successful mission. The path of trajectory for a low thrust spiral can be seen in Figure 3.0.1. This path will be used from Earth to Uranus to limit heavy fuel consumption.
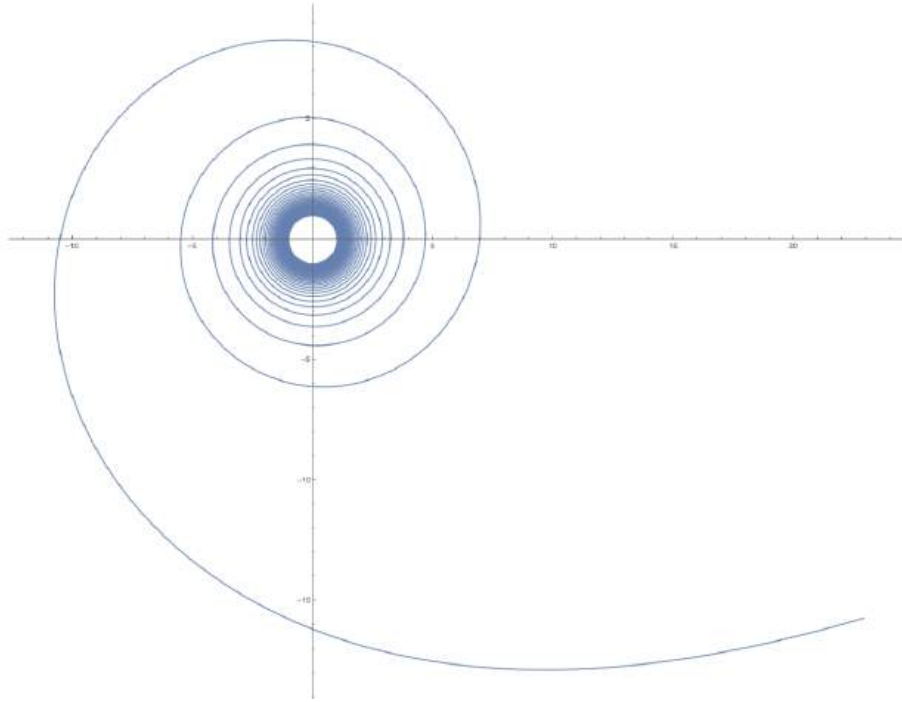
Figure 3.0.1: Low thrust spacecraft spiral trajectory.

Step four is a continuation of step three as the spiral must align with the trajectory of Uranus to allow for the satellite to be caught by the sphere of influence of Uranus, which in turn allows the satellite to orbit the planet.

Step five, orbital insertion, sees the addition of a ΔV to put the satellite into the predetermined altitude orbit around Uranus. This orbit will be as close as necessary to that of Ariel.

Step six, a ΔV application to pair the satellite with Ariel, is potentially an optional step depending on how the insertion into Uranus' orbit occurs concerning Ariel's position as the satellite may need to slow down or speed up to reach the moon. On top of that, the satellite needs to be drawn into an orbit with Ariel, which may require a ΔV to create this second orbit.

4   Additional Background

The Scuttle Mission is deeply inspired by the engineers of the past, referencing the highly technical missions and research performed by NASA and other space exploration groups around the world. The Ariel Voyagers will take the lessons gleaned from past missions and blend them with the innovation of the present, pushing the limits of engineering discovery. The task at hand relies upon an electric propulsion (EP) system, a technical advancement that has been around for decades yet has remained relatively unknown to the general public.

The following section details past missions and vehicles that contained many of the critical elements required for the success of the Scuttle Mission. In addition, a general background of EP is described, featuring a brief description of what constitutes an EP system, a summary of its inherent benefits and limitations, and a basic description of how it works.

4.1   What is Electric Propulsion?

In the vacuum of space, spacecrafts generate forward motion by exerting force in the direction opposite their intended movement. For example, if you sat on a rolling chair and threw a medicine ball forward, you would find that you would begin to move backward. The propellant is the fuel that becomes the mass or exhaust that is expelled to create this force. The greater the acceleration, the quicker a vehicle can reach high speeds, decreasing the travel time. The governing equation for all motion is Newton's Third Law of Motion, which states that force equals the product of mass and acceleration. For a spacecraft, the force created by propulsion is called thrust, and this is characterized by the mass of the exhaust material times the velocity of that same exhaust material [12]. Thus, to increase the acceleration of a rocket, at least one of the following must happen: (1) the overall vehicle mass is decreased, (2) the mass of the exhaust is increased, or (3) the speed at which the exhaust is emitted is increased.

The basic premise of EP is that electrical energy is converted into kinetic energy. This is generally done through the manipulation of ionized or charged atomic particles [12]. These particles can be accelerated to incredibly high speeds, where they are then released as exhaust to generate thrust. These ions begin as neutral noble gas propellants that are ionized during the propulsion process.

4.2   Benefits and Limitations of Electric Propulsion

Electrically propelled vehicles are fundamentally different from chemical rockets as they are limited not by energy, but by power. These systems can convert electrical energy directly to propellant kinetic energy without needing to raise the working fluid's temperature, meaning exhaust velocities can be significantly greater. This electrical energy comes from generating energy through nuclear or solar means, requiring large portions of the vehicle's total mass to do so. There exists then a balance between the desired thrust and the power required to generate that thrust, and this balance will be demonstrated and considered in greater detail in the upcoming analyses.

Chemical energy is linked to mass, and thus there is a hard upper limit of around 500 s to the specific impulse that can be obtained through chemical propulsion systems [13]. In contrast, electrical propulsion provides a way to greatly reduce propellant mass consumption because, in theory, an infinite amount of electrical energy can be added to a given amount of mass and thus there does not exist the same cap on specific impulses seen on chemical propulsion systems [13]. The caveat to all the benefits of EP lies within the minuscule thrust that these systems can apply. Due to the low thrust (less than 500 mN) provided by EP, these systems require a chemical propulsion system to get out of Earth's

atmosphere. The thrust from EP systems is so small, that it is approximately the same amount of force that it takes to lift a piece of paper [15].

4.3   Function of an Electric Propulsion System

While the process by which electric propulsion (EP) systems produce thrust varies, several generalities do exist. EP systems are characterized by the amount of power that they require to operate, falling into the following categories: low power (<1kW), moderate power (<20kW), or high power (>20kW) [16]. These systems are further categorized into the method by which they accelerate propellant: electrostatic, electrothermal, and electromagnetic thrusters. For the Scuttle Mission, only electrostatic and electromagnetic thrusters will be introduced.

In nearly all EP systems, a neutrally charged propellant is converted to a positively charged ionized state by bombarding the atom with many electrons. This is usually done with a device known as an electron-emitting cathode. This causes the neutral atom to release an outer electron to try and balance the charge around it [12].

In an electrostatic propulsion system, the positive ions are held within the chamber by a positively charged plate, and when the pressure within the chamber exceeds its threshold, it is pushed out of the chamber and accelerated by an additional plate of negative charge. This design is known as bombardment ionization, and thrusters that utilize this method are known as ion thrusters. Figure 4.3.1a provides an example of such a thruster, used on the Gravity Field and Steady-State Ocean Circulation Explorer (GOCE) in 2009.

(a) GOCE Gridded Ion Thruster.
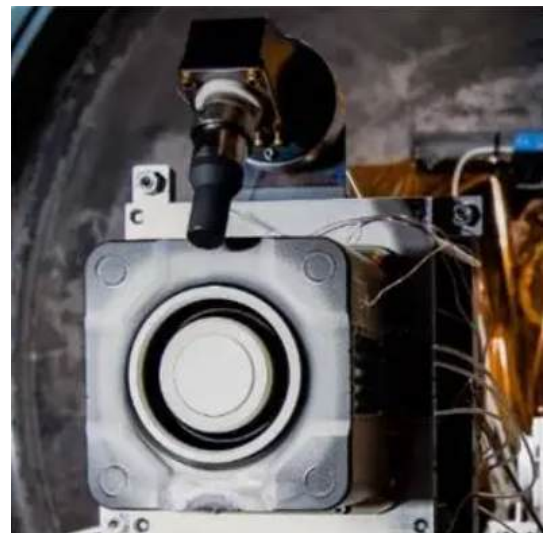
(b) Hall-Effect Thruster.

Figure 4.3.1: Electrostatic and Electromagnetic Thrusters [17].

Electromagnetic propulsion systems use an electromagnetic field to accelerate ions. The Hall Effect Thruster is the prominent electromagnetic propulsion system and accelerates

ions in a concentric ring shape. The specific Hall Effect Thruster shown in 4.3.1b is used in a NASA GRC Vacuum Test Facility. To create the ring shape, an electron-emitting cathode emits electrons that get pulled towards a central electromagnet that rotates and speeds up the electrons in a channel around itself. Then, the neutral propellant is released to these channels where they ionize on impact and are simultaneously shot out at the end of the thruster, creating thrust [17].

It should be noted that an additional electron-emitting cathode is required on the exterior of the thruster to de-ionize the propellant regardless of the type of EP system. This de-ionization is done to prevent the vehicle from acquiring a net negative charge which would attract ions back to the vehicle and eliminate thrust. Additionally, by neutralizing the propellant, erosion of the vehicle components is prevented - a factor that can severely diminish the lifetime of an EP vehicle. An example of a complete EP thruster system is shown in Figure 4.3.2, providing a detailed visual of the processes and components involved in EP.
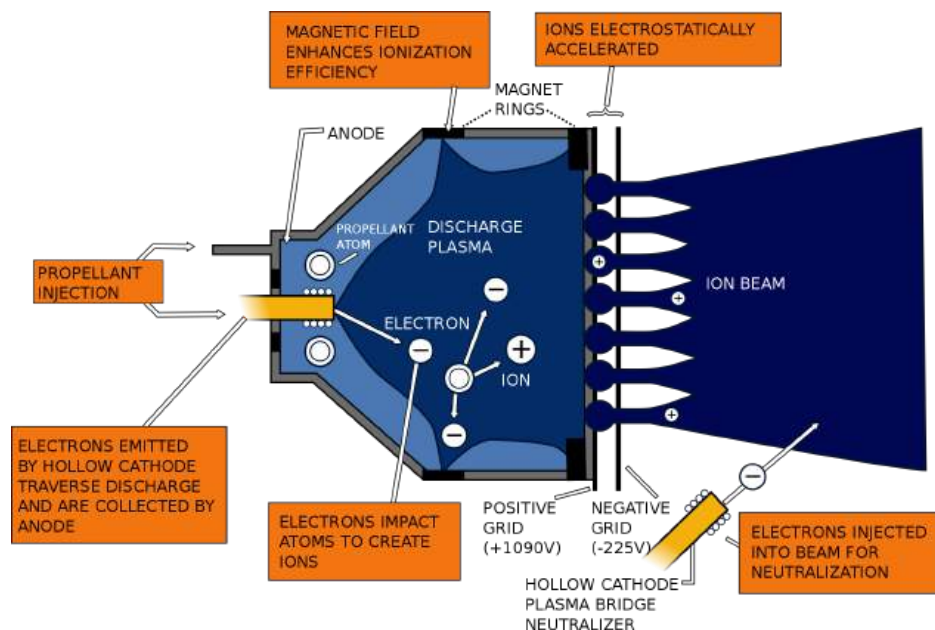

Figure 4.3.2: Illustration of Electric Propulsion System [17].

4.4   Electrical Power System

To supply power to the EP systems, a large power source must be utilized aboard the satellite. This can be done in the form of either a radioisotope thermoelectric generator or solar panels. Due to Uranus being approximately 20 astronomical units away from the sun and receiving 360 times less light than the Earth, a radioisotope thermoelectric generator will be the appropriate power source for the Scuttle Mission [18].

A radioisotope thermoelectric generator (RTG) is a system designed to provide electrical power by capturing heat loss from the natural radioactive decay of plutonium-238. RTGs use the large temperature difference between the plutonium core and space to pull the heat

through energy-generating thermocouples. This requires zero moving parts [19]. One emerging type of RTG in the world of space applications is the Advanced Stirling Radioisotope Generator (ASRG). ASRGs work by converting heat from the reactor into high-speed kinetic energy via a small magnetized piston and a companion displacer. As the piston oscillates through a coil, electric energy is generated in line with Faraday's law [20].

The Cassini mission's power supply consisted of three RTGs, which were a SIGe General Purpose Heat Source RTG (GPHS-RTG). This reactor contained 32.7 kg of plutonium dioxide, of which 28.3 kg was pure plutonium [21]. From this power source, a specific power of 5.1 We/kg (Watts of energy per kilogram) at loading time was the expected output with an efficiency rating of 6.8%. With an ASRG, approximately 6 We/kg can be collected and can operate at a system efficiency of 30% [22]. An illustration of an ASRG can be seen in Figure 4.4.3.
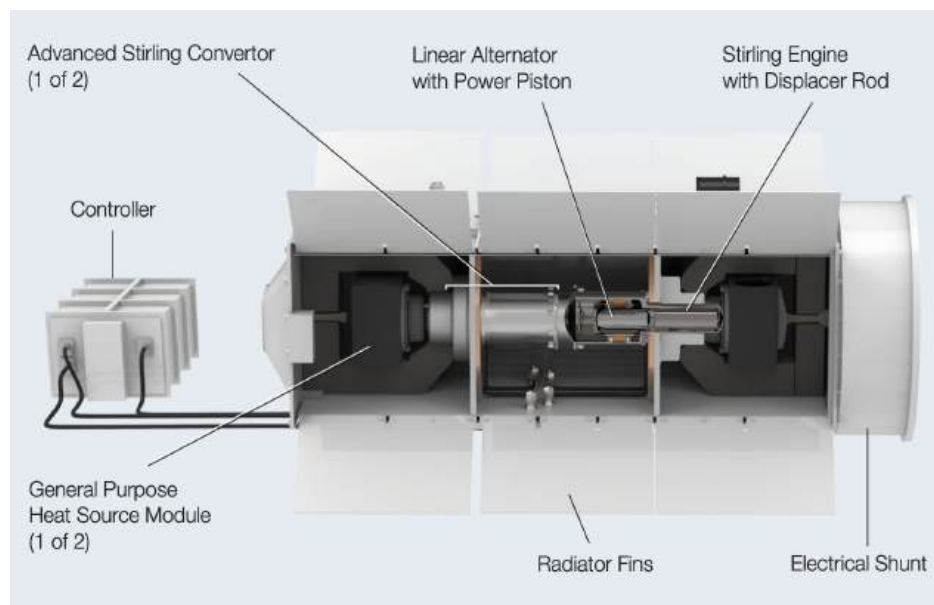

Figure 4.4.3: Illustration of SRG power system [20].

4.5   Comparable Missions and Vehicles

A major selling point of the deep-space Scuttle Mission is a highly efficient EP system. EP methods, although appearing futuristic, have been in use for nearly 60 years. Recently, a large increase has been seen in the number of spacecraft using EP, thanks in large part to the many commercially owned satellites being launched [14]. EP has primarily been used as a method of making minor adjustments to maintain or adjust orbit for satellites around the Earth; however, several deep space missions have also used the benefits of EP, including NASA's Dawn Mission, which had an ion propulsion system [15][23].

NASA's Deep Space 1 first proved the effectiveness of ion propulsion as an engineering test flight that launched in 1998 and concluded in 2001. Each of the 12 high-risk technology tests conducted during this mission were successful, one of which included ion propulsion

for deep space travel [24]. The success of this mission led to the Dawn mission, which relied upon ion propulsion to achieve its highly ambitious goals of orbiting and exploring not one but two solar system bodies. Dawn launched on September 27, 2007 and achieved Vesta orbit in July of 2011, remaining in various orbits until September of 2012. By December of the same year, Dawn had escaped Vesta orbit and left for Ceres, eventually entering orbit in March of 2015. The Dawn spacecraft remains in orbit to this day, but the thrusters ran out of propellant in 2018, ending the mission. Dawn had three ion thrusters aboard; two of which were required to provide enough thruster lifetime to complete the mission and a third as a spare. Each thruster could produce up to 92 mN of thrust, and could be throttled as needed. It uses each of the thrusters, operating them individually and providing over 2,000 days of thrust throughout the mission. The entire vehicle, thrusters, and onboard systems included, are powered by solar power, with two 8.3 m x 2.3 m solar arrays that can convert 28% of the solar energy that hits it. A nickel-hydrogen battery is also onboard to keep systems running anytime the solar arrays are directed away from the Sun [8].

The first and only spacecraft to ever visit Uranus and Neptune, NASA's Voyager 2 mission, must be noted. This mission led to the first photos ever of both Uranus and Ariel, the discovery of ten new moons and two rings surrounding Uranus, and studied all four of the gas giants up close [25]. The Voyager mission heavily utilized gravity assists about several planets to complete the flybys necessary to complete its mission and completely jettisoned its propulsion module after achieving the necessary velocity to inject the mission module onto the Jupiter trajectory. The propulsion module weighed 1,207 kg and contained a large solid-propellant rocket motor. After the jettison, hydrazine jets were used for attitude stabilization and trajectory correction maneuvers. To power the craft and its extensive scientific instrumentation, three plutonium oxide radioisotope thermoelectric generators were used to provide more than 400 W of nuclear power. To avoid interference from occurring in the instruments while the generators run, two long booms are positioned 180° from each other, with the closest instrument 4.8 m away and shielded by the bulk of the spacecraft [26].

NASA's Cassini Orbiter mission was an advanced satellite designed to study Saturn and its moons, making it the first space probe to orbit Saturn 9.5 AU from the Sun. The Cassini Mission utilized the influence of Venus, Earth and Triton to gain gravity assists [27]. To stay stable within Saturn's SOI, Cassini utilized three reaction wheel assemblies to control fine pointing, and used 16 0.5 N hydrazine thrusters for course pointing control. These were also used to alter the spacecrafts trajectory so long as the change in velocity required was less than 5 m/s. In the case that a velocity change larger than 5 m/s is required, one of two main engines can be used, where the second engine acts as a backup. In order to determine the orientation of the satellite, gyroscopes and star trackers are cross referenced to create an accurate picture of the positioning [28]. Cassini receives its power from three plutonium oxide radioisotope thermoelectric generators, each capable of providing 300 W of power for approximately 11 years. After the 11 years, the power delivery drops down to 210 W per [28]. The radiation from such a power source can have damaging effects to equipment not protected. Such an example is Cassini's DRAM which holds memory about the spacecrafts health and status. This memory is housed within 12.7 mm thick aluminum [28].

5 Concept Designs

To ensure the success of the Scuttle Mission while providing the most robust system possible for scientific discovery, many concept designs were considered. The following section details the vital concepts considered for the mission and breaks down the process by which decisions were made between ideas. Decisions were made individually for each category (listed in the following section), and were based on a number of factors specific to the category. The factors of greatest import are the performance factors listed in Section 2.2; moreover, these provide the baseline targets for the Scuttle Mission.

5.1 Preliminary Concepts

The vital concepts considered for the Scuttle Mission fall into 3 categories: (1) propulsion method, (2) type of propellant, and (3) power source method. To meet the objectives outlined in this mission, a complex propulsion system is required, deeming the decision of the preceding categorical concepts paramount to the success of the mission.

The propulsion method options consist of a pair of electric propulsion systems in Hall-Effect Thrusters (HET) and Gridded-Ion Thrusters (GIT). An impulsive chemical system is included in this report as a comparison to determine the extent to which an electrically powered system is advantageous. A fully electric propulsion system relies purely on low thrust maneuvers to reach the target destination of Ariel and also maintain attitude control. The major measurable parameters of comparison to choose the proper EP thruster include the thrust provided, total lifespan and power required for operation. HET's have been used exceedingly for small orbital changes on satellites remaining in orbit about Earth due to their ability to operate at a very high efficiency at low power, but this efficiency falls greatly when scaling these machines. GIT's, in contrast, have been tested and successfully implemented for deep-space missions with high ΔV requirements, maximizing the high specific impulse benefits of electric propulsion due to incredibly long periods of thrust with high exhaust velocities [29]. For these reasons, GIT will be the primary form of propulsion.

When using an EP system, different propellants are required than that of a typical rocket. The most common and tested such propellants include Mercury and the neutral noble gases: xenon, argon, and krypton. Different propellant types can influence the total propellant mass carried, the efficiency of the thruster, the power required to run the system, and the structural components required to hold the propellant. The notable factors that contribute to deciding the best propellant are the nature of its storage, the effectiveness and efficiency of each propellant, and the difficulty in obtaining and handling the propellant. Several propellants require cryogenic storage, specifically argon, which would require additional mass and complexity just to store the propellant and both of these would scale with the amount of propellant. The thruster to power ratio and efficiency of the propellants are as follows from greatest to least: mercury, xenon, argon, and krypton. While the most effective propellant, the use of mercury for propulsion has many environmental concerns, causing it to be unlikely to be approved in any capacity as an exhaustive propellant. Considering each of these factors, xenon is the chosen propellant for its ease of use and high effectiveness.

EP systems require large amounts of electrical energy to operate and therefore a power source capable of providing said energy. This is done in space by harnessing and converting the power of the Sun to electrical energy through solar panels or by converting nuclear power to electrical energy through an on-board reactor. Due to the deep-space nature of the Scuttle Mission and the high power requirements of an EP thruster, a nuclear reactor will be utilized. If the energy were taken from solar panels, there would be exceedingly diminishing returns as the spacecraft reaches deeper space. This requires an incredibly large solar unit, whereas nuclear reactors can consistently produce a sufficient amount of power for the entire length of the mission while taking up far less space. The specific type of nuclear reactor, its size and power specifications, are detailed in the following sections as these are highly dependent on the overall requirements of the spacecraft's operation.

6 Sizing and Orbital Mechanics

Determining the size and scale of the Scuttle Mission Satellite relies on sizing and orbital mechanics calculations. This segment outlines each component essential for achieving Scuttle Mission's objective of exploring Ariel. Initially, an overview of all devices that are needed for the scientific payload are summarized to establish a baseline. Subsequently, orbital mechanics calculations are conducted to evaluate EP against an impulsive chemical propulsion method and approximate a target wet and dry mass.

6.1 Scientific Payload

The scientific payload is the dry weight of the spacecraft with the weight of the structure holding it together subtracted. The Scuttle Mission will require equipment to collect images of various forms of Ariel's surface to determine if water exists underneath its surface. Along with the imaging equipment, the weight of the communication arrays to relay data, stabilization and navigation equipment to ensure the satellite reaches its target, and the power source are described.

6.1.1 Camera System

The Scuttle Mission spacecraft will utilize existing NASA imagery systems in the form of the Europa Imaging System (EIS). This system consists of two visible light cameras that each contain eight-megapixel sensors. This assembly, comprised of a narrow-angle and wide-angle camera, will allow the Scuttle Mission to photograph Ariel in both color imagery and stereoscopic form to give a three-dimensional appearance to the surface. Color imagery is the result of six broadband filters that can filter light in the range of 350 nm to 1050 nm. With the improved camera system, a resolution of 0.5 m per pixel at a 2 km altitude and 11 m per pixel at a 44 km altitude can be expected. This results in the ability to create a framing image of 1536 x 4032 pixels and a pushbroom image of variable x 4032 pixels. An example of the EIS system is illustrated in Figure 6.1.1 [30]. Another example showing how the pixels are manipulated is included in Figure 6.1.2 [31].
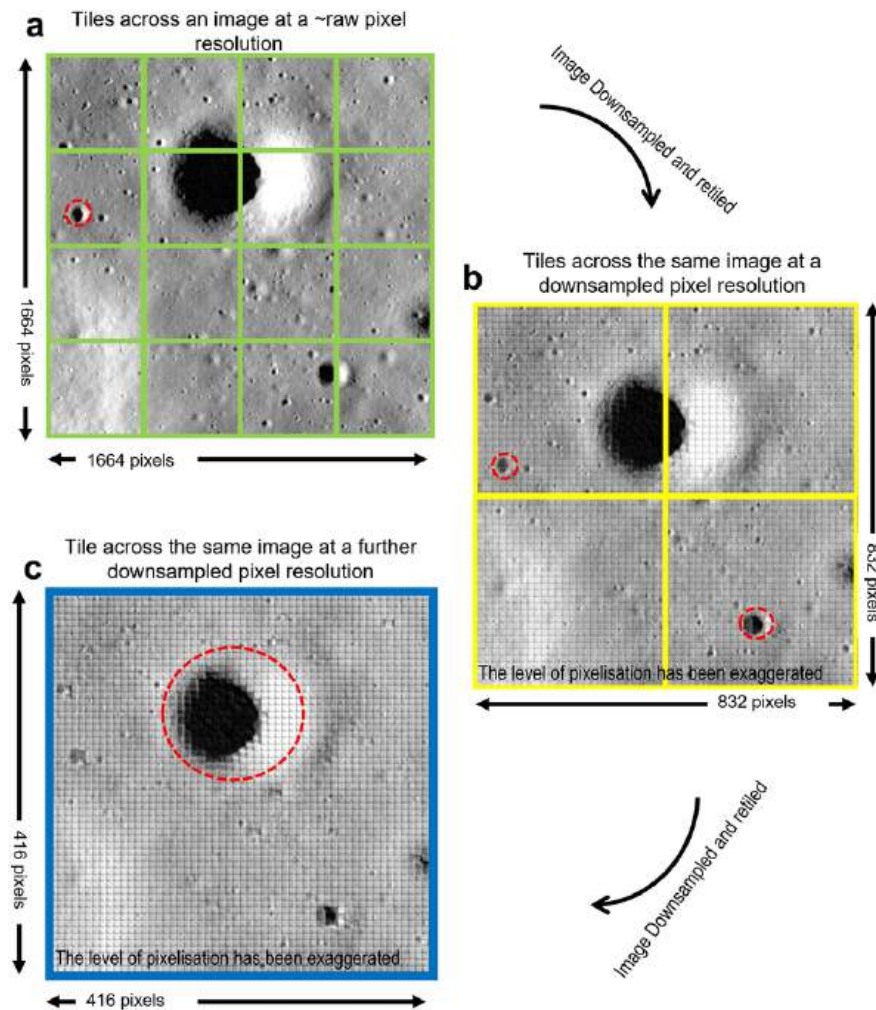
Figure 6.1.1: Europa Imaging System [31].

Figure 6.1.2: Example of downsampling from a narrow angle camera [31].

Because the EIS is still a work in progress being that Europa Clipper has yet to launch, little information has been released surrounding its size and weight. As a result, it will be estimated that it shares similar specifications as the Imagery Science Subsystem (ISS) aboard Cassini which too utilized a dual camera system. Cassini's narrow-angle camera had dimensions of 0.95 x 0.40 x 0.33 m and 0.55 x 0.35 x 0.33 m for the wide-angle camera. This resulted in a combined mass of 57.83 kg. It will also be estimated that the maximum peak operating power will be 55.90 W [32].

6.1.2 Research Equipment

Scuttle Mission will utilize four additional imagery systems to perform studies on Ariel in order to determine the composition and attempt to detect oceans underneath the surface. The first system is the Composite Infrared Spectrometer (CIRS). This system captures infrared light and splits it into its component wavelengths using one far-infrared and two mid-infrared focal planes. This allows for a temperature analysis of the body emitting these waves. Scientists can use these measurements to find heat irregularities that would hint toward water underneath the cold surface. Modeling specifications after Cassini, the CIRS has a mass of 39.24 kg, dimensions of 0.89 x 0.76 x 0.52 m, and a power draw of 26.37 W with a ramp-up to peak at 32.89 W [33].

The second piece of equipment is the Ultraviolet Spectrograph (UVS). This system collects ultraviolet lights using a telescope and separates them into their respective wavelengths using an optical grating, similar to how a prism separates light into a projection of colors. The UVS then records how bright the lights are at each wavelength which can be used to identify the makeup of substances in the view of the spacecraft. This can be used to detect liquid water that is leaking onto the surface of Ariel. The UVS can also identify what simple molecules exist on Ariel to determine whether it can support life. The Scuttle Mission will utilize the same UVS used on the Europa Clipper mission. This variation has a mass of 19.6 kg, dimensions of 0.357 x 0.362 x 0.158 m, and an operation power draw of 8.5 W [34].

Scuttle will also be equipped with a visible and infrared mapping spectrometer (VIMS). This device collects visible light and long-wavelength infrared light using a visible channel and infrared channel for two different image grating operations. This results in the waves being separated into 352 unique color component wavelengths, with 96 being visible light and 256 being infrared. VIMS was a critical part of the Cassini mission as it was instrumental in locating and analyzing hotspots on Saturn. In the case of Ariel, hotspots may hint towards moving water just below the surface. The composition can also be determined using VIMS. Scuttle Mission will use a similar device mounted to Cassini, which has a mass of 37.14 kg, dimensions of 0.78 x 0.76 x 0.55 m, and an operation power draw of 21.83 W with an occasional peak of 27.20 W [35].

Radar is the final scientific payload piece that will be added to the Scuttle Mission. This will allow scientists to map the physical terrain of Ariel regardless of visibility conditions. This is done by sending radio waves to the surface and recording how they reflect. This instrument will utilize the high-gain antenna to collect the returning radar waves. From

the surface topography, the possibility of underground water impacting the physical conditions at the surface can be analyzed. This device will be made up of three instruments: a synthetic aperture radar imager, an altimeter, and a radiometer. These components come in at a collective mass of 41.43 kg, and a power draw of 108.40 W. Other dimensions are not publicly specified but can be viewed in comparison to the high gain antenna in Figure 6.1.4 of Section 6.1.3. An example of the significance of the radar instruments is shown in Figure 6.1.3 where Cassini used them to show the existence of liquid methane oceans on Saturn's moon Titan [36].
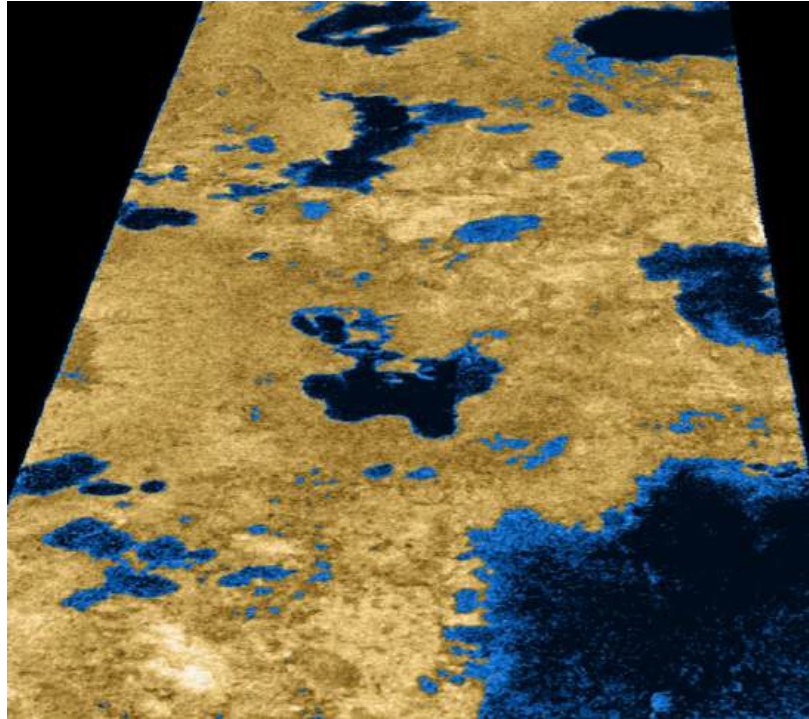

Figure 6.1.3: Radar imaging from Cassini showing the existence of liquid methane oceans on Titan [36].

CIRS, UVS, and VIMS devices all perform very similar tasks in identifying material compositions of a body and surface temperatures. Because of this, these three slightly different processes allow for data to be cross-referenced between each method to come to the most accurate conclusion surrounding Ariel. The addition of radar further paints the surface conditions of Ariel and can allow for educated theories surrounding its formation.

6.1.3 Communications

To communicate with Earth, the Scuttle Mission spacecraft will house an array of high-tech antennas operating on NASA's Deep Space Network (DSN) ground stations. A single high-gain antenna will be used as the primary form of communication. High-gain antennas excel in long-distance communication and signal strength thanks to their ability to perform precision targeting of the signals they transmit and receive regarding course

corrections and telemetry [37]. The high gain antenna also includes radar equipment that emits radio waves and captures returning waves using the dish [38]. Similar to Cassini, the dish will double as a sun shade during inner-solar system travel [38]. Cassini was equipped with a 4 m diameter high gain antenna to transmit and receive frequencies X through KU [37]. These higher frequencies are used to allow larger bandwidths, greater pointing accuracy, and minimize ionospheric effects [39]. An image of Cassini's high gain antenna during its subsystem testing can be seen in Figure 6.1.4, demonstrating the placement of the radar feeds within the high gain dish [40]. A similar 14 kg-3 m diameter antenna from L3Harris will provide acceptable performance for the Scuttle Mission with the ability to transmit X through Ku bands [40].
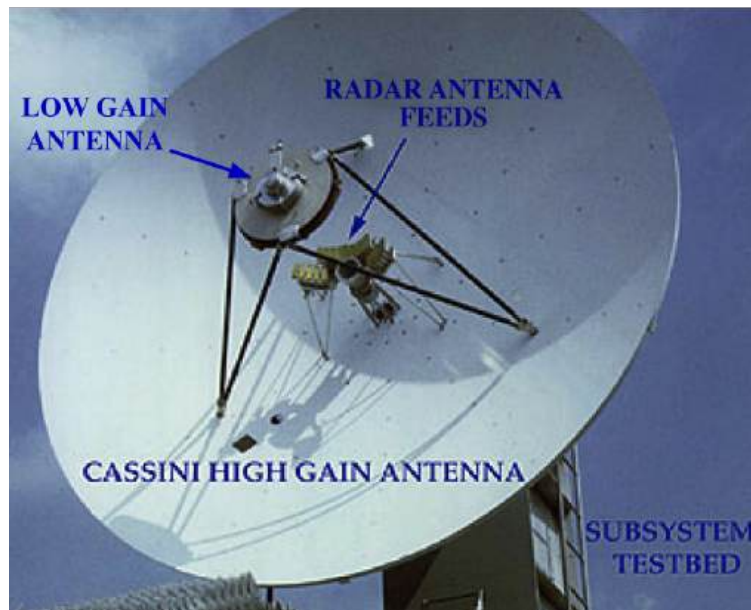

Figure 6.1.4: Cassini High Gain Antenna during testing [40].

The high-gain antenna can only be used when pointing towards the Earth. To ensure that the spacecraft can communicate with Earth at all times, two low-gain antennas with a total mass of 1 kg will be installed at each pole to provide near-perfect coverage for incoming radio signals [37]. This allows communication regardless of the orientation of the spacecraft and provides low-rate communication during emergencies and special events. The lower data rate of these antennas is attributed to their much broader focus of radio beams, meaning a weaker signal reaches Earth [41]. The DSN on Earth is still able to pick up these signals however they are not able to carry as much information as the high gain antenna. In Figure 6.1.4, Cassini's low gain antenna can be seen as the thin disk protruding the furthest from the main dish. The low gain antennas have another added benefit; scientists can troubleshoot issues with the spacecraft at any time, allowing for a level of risk mitigation [41].

The spacecraft will also require a transponder. This is a device that communicates with mission control by processing radio waves received by the antennas and transmitting a

signal back. Scuttle Mission will use the Small Deep Space Transponder (SDST) by General Dynamics shown in Figure 6.1.5 as it has been used in missions such as Cassini, Deep Space-1, and Kepler. The SDST has a mass of 3.2 kg, a size of 0.18 x 0.17 x 0.12 m, and pulls 15.8 W in its receiver and X-Band exciter configuration. This transponder, designed specifically for deep space missions, combines various communications functions. It integrates the receiver, command detector, telemetry modulator, exciters, beacon tone generator, and control functions in one box [42].

Figure 6.1.5: General Dynamics Small Deep Space Transponder [42].

The transponder will be paired with the General Dynamics X-Band Solid State Power Amplifier (SSPA) shown in Figure 6.1.6 to amplify the signals transmitted from the spacecraft. This will enhance the efficiency of long-distance communication. The variation chosen has a mass of 1.37 kg, a power draw of 63.3 W (65.5 W max), and a size of 0.18 x 0.13 x 0.05 m [42]. Two transponders and two amplifiers will be installed as a redundant system in case one fails.

Figure 6.1.6: General Dynamics X-Band Solid State Power Amplifier [42].

6.1.4   Orientation

To navigate the spacecraft through space, additional equipment will be required to orient its position in space. The Scuttle Mission will use two CT-2020 star trackers from Ball Aerospace to accomplish this, as seen in Figure 6.1.7. The second star tracker is a backup in case the first one fails. These star trackers each have a mass of 3 kg, a power draw of 8 W, and a 0.145 m diameter and 0.305 m length [43]. A star tracker works by capturing images of surrounding bright stars and constellations and comparing them to known positions of reference stars to find its three-axis orientation and position [44]. The Dawn

Mission mounted their star trackers on its top panel, in the direction of motion, pointed approximately 30 degrees apart looking horizontally away from the high gain antenna [45]. The Ariel Voyagers aim to position the Scuttle Mission star trackers in a similar configuration.

Figure 6.1.7: CT-2020 Star Tracker from Ball Aerospace [43].

Sun sensors will also be utilized to determine the orientation of the satellite concerning the Sun to perform attitude adjustments and calibrations. Similar to Dawn, Scuttle will use 16 coarse sun sensors installed on the surface of the spacecraft, eight primary sensors, and then an additional eight as backup [45]. Although the Scuttle Mission has no solar arrays to orientate, the position of the satellite relative to the sun is very important, making their presence necessary. These sensors work by allowing light to enter a small window containing photosensitive units. These units convert the protons that reach them into electrons and then electric currents that can send signals containing information. As light passes through the window, it projects an image to the base. The photosensitive units then gauge the amount of light and calculate the angle of incidence [46]. The Scuttle spacecraft will feature Bradford coarse sun sensors – shown in Figure 6.1.8 – 0.110 x 0.110 x 0.03 m in size with a mass of 0.215 kg [47].
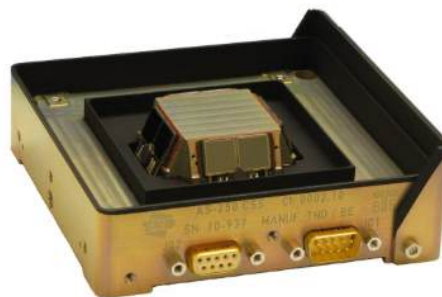

Figure 6.1.8: Bradford Space Coarse Sun Sensor [47].

Orientation is also determined through the use of gyro stabilizers. These mechanical systems help determine the attitude control and angular velocity of the spacecraft. They

can also help the spacecraft align its high-gain antenna with Earth or align its camera towards a predetermined target of interest. Scuttle Mission will be equipped with three two-axis gyroscopes, each having masses of 2 kg [45].

6.1.5 Stabilization

Scuttle Mission aims to perform its stabilization and attitude control using reaction wheels and hydrazine thrusters. Reaction wheels work by spinning in the direction opposite to that of the rotating spacecraft. Like Dawn, Scuttle Mission will utilize the same three-axis control with protection against failure [45]. The complete assembly from Bradford Space weighs approximately 20 kg with a 0.295 m diameter and 0.125 m height. Maximum gross torque is 0.265 N-m with an angular momentum storage of 25 N-m. The peak power consumption of each reaction wheel at maximum torque and speed is 168 W. At steady state operations, the reaction wheels consume 29 W each [48].

Because slowing down a reaction wheel would itself induce an unwanted torque, and relying on only reaction wheels can result in the accumulation of momentum (saturation near their maximum rotational speed) that could cause the spacecraft to lose control, low thrust hydrazine thrusters are to be used for attitude stabilization and momentum dumping of reaction wheels [49]. Hydrazine is an appropriate fuel due to its monopropellant characteristics, meaning that oxidizer is not required as thrust is created as hydrazine (N_2H_4) decomposes as it passes through a catalyst bed [50]. Cassini utilized 16 0.5 N thrusters with 132 kg of hydrazine. Due to Cassini being a comparable deep space mission, a similar setup will also be used by the Scuttle Mission. Cassini's use of reaction wheels and hydrazine thrusters is shown in Figure 6.1.9 as a reference for how they will be used on Scuttle [28]. The reaction wheels must be facing varying directions to cover a full range of movement. Cassini employs each main wheel separately on the body at equal angles apart, however additional configurations are available.
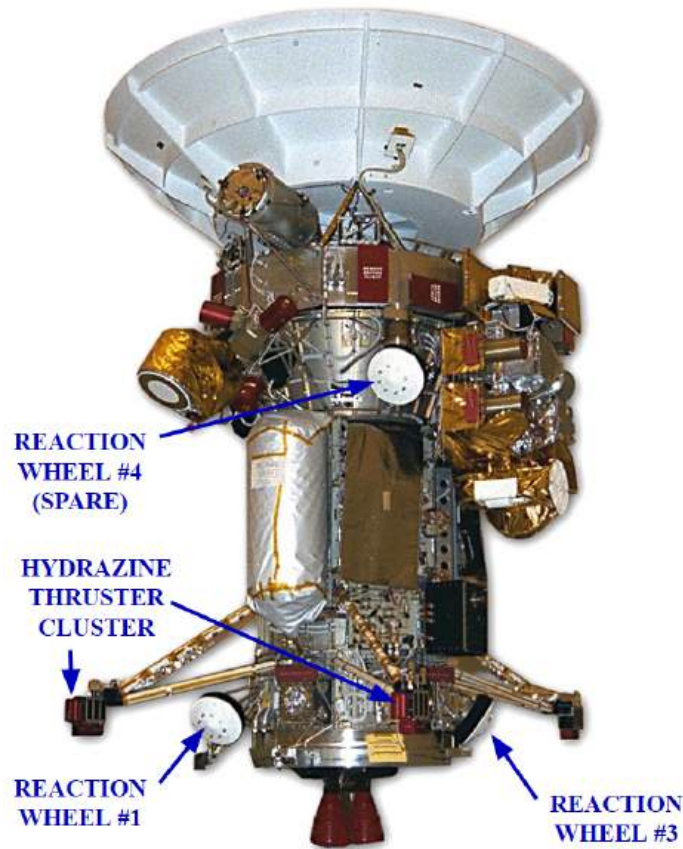
Figure 6.1.9: Diagram of Cassini's assembly of reaction wheels and thrusters [28].

6.1.6 Processing

The central computer system (CCS), is the internal brain of the spacecraft that helps coordinate the application of every part aboard the spacecraft. Little sizing information is given with regards to the size and weight of the CCSs aboard Cassini or Dawn; however, it is known that Cassini used MIL-STD-1750A processors [51] and Dawn was equipped with two redundant units comprised of a BAE RAD 6000 32-bit single board computer [45]. To communicate with mechanical devices, computers, and instruments aboard Cassini, 22,000 wire connections were used with more than 12 km of wiring used [52]. Although exact numbers are not shared for these masses, the mass of such items will be relevant.

6.1.7 Thermal Control

The Scuttle spacecraft will experience temperatures ranging from -255°C to 255°C depending on its orientation relative to the sun. To minimize the thermal sensitivity experienced by the spacecraft, it will be covered using Multi-Layer Insulation blankets. This is the same gold-colored fabric shown in Figure 6.1.10 that protected Cassini from extreme temperatures throughout its deep space mission [53]. Thermal blankets are made from layers of strong, lightweight fabrics that help to maintain safe operating temperatures as well as protect the spacecraft from micrometeoroid impacts. These layers consist of up

to 24 fabrics including aluminized Kapton, mylar, and Dacron. Thin strips of aluminum are sewn into each blanket to prevent electrical arcing as the spacecraft travels through charged particles found in space [54]. The blanket will be spaced away from the main body of the spacecraft to create an inner cavity. This will reduce the need for electrical power heaters by utilizing waste heat from the Radio-isotope Thermoelectric Generators (RTGs) to control the main body's temperature [55]. By lining the inside of the blankets with aluminum foil, they will also help protect the spacecraft from electrical charging effects as discussed in NASA-HDBK-4002 [7]. Excess heat concerns are addressed in the Heat Transfer analysis conducted in Section 8.7.

Figure 6.1.10: Thermal blanket shown being applied on Cassini spacecraft [54].

Scuttle will not be utilizing solar power so to keep instruments and hardware warm enough to operate properly, an additional source of heat may be required on various hardware. To accomplish this, Radioisotope Heater Units (RHUs) will be employed as needed. This will allow the electrical power to be allocated to operating the spacecraft's systems and instruments rather than as a heating source. RHUs provide heat through the decay of a small pellet of plutonium-238. This pellet is encased in various protective layers shown in Figure 6.1.11. The various pieces shown fit snug around the pellet. They are very lightweight and output a direct heat of 1 W [56].

Figure 6.1.11: Nested layers of protection for a plutonium-238 pellet in an RHU [56].

6.1.8　Electric Propulsion Thrusters

The Scuttle Mission utilizes an electric propulsion system, specifically using Gridded-Ion Thrusters (GIT) to travel from low Earth orbit to Ariel. While several GIT options exist, the most powerful and efficient thruster is both desired and required to achieve the goals of the Scuttle Mission. The GIT that meets this criteria is NASA's NEXT-C thruster, which provides up to 236 mN of thrust with a specific impulse of 4,155 s. This thruster draws between 0.6 - 7.4 kW of power and accelerates xenon propellant to exhaust velocities of up to 40 km/s. The NEXT-C thruster itself has a mass of approximately 13.5 kg, while its power processing unit weighs approximately 36 kg. The entire thruster system takes up the approximate volume of a cylinder with diameter of 58 cm and length 43.5 cm. Depending on the duration of thrust required for completion of the Scuttle Mission, several of these thrusters may be utilized. For reference, the NEXT-C thruster successfully completed a 5.5 year test that showed very little degradation and affirmed the full capabilities of these thrusters [57].

6.2　Power Supply

Cassini used three RTGs to produce approximately 900 W at launch, degrading to 600 W near the end of its lifespan [28]. Current ASRGs developed by Lockheed Martin Space Systems Company can capture 140-160 W of power from 1 kg of plutonium-238 (Pu-238) which is split between two general purpose heat sources (GPHS) that release 250 W at launch each. Power degrades by approximately 0.8% each year. This system weighs between 21 and 23 kg and has a specific power of 6.4 to 7.4 W/kg. The power usage data of the equipment specified in Section 6.1 is outlined in Table 6.2.1.

Table 6.2.1: Equipment mass and power usage data.

Part	Mass* [kg]	Power Input [W]	Total Power [W]
Camera (2)	57.83	55.90	55.90
CIRS	39.24	32.89	32.89
UVS	19.6	8.5	8.5
VIMS	37.14	27.20	27.20
Radar	41.43	108.40	108.40
Low Gain Antenna (2)	1	-	-
High Gain Antenna	14	-	-
Transponder (2) **	6.4	15.8	15.8
Amplifier (2) **	2.74	65.5	65.5
Star Tracker (2)	6	8	16
Sun Sensor (16)	3.44	-	-
Gyroscope (3)	6	35	105
Reaction Wheel (3)	25.5	29	87
Power Processing Unit (1)	36	7000***	-
NEXT Ion Thruster (3) **	40.5	7000	7000
TOTAL	**302.32** kg	–	**7.422** kW

* For multiple units, the stated mass is for the total
** Component not active at the same time, total power is the maximum power that is
drawn at one time *** Processes power, does not consume

6.2.1 Estimating Dry Mass

Along with the electric components that need to be present on the satellite, the payload
needs to have the necessary tanks and reactors to fuel the Scuttle Mission for its trip to
Uranus. Three main components contribute to this additional dry mass: the ASRGs to
power the satellite, the empty xenon propellant tanks, and the hydrazine and hydrazine
tank. The hydrazine, used for gyroscopes, thrusters and reaction wheels, will be considered
a part of the dry mass since it is not the primary form of propellant.

One critical component contributing to the dry mass is the Hydrazine tank system. For the
Scuttle Mission, two 58L tanks with a maximum fill capacity of 39 L will be used. The
specific tank to be used is the *58 L Hydrazine Tank - BT-01-1*, developed by ArianeGroup,
which has a mass of 8.5 kg and a volume of 39 liters [58]. Its primary purpose is to store
hydrazine, which will be utilized for the operation of RCS thrusters, gyroscopes and
reaction wheels on the satellite. With the tank full of hydrazine, the total mass of the tank
is about **95 kg**.

To meet the power requirements of the Scuttle Mission, Advanced Stirling Radioisotope
Generators (ASRGs) will be employed. The total power required for the mission is
estimated to be over 7 kW. Based on the specific power values provided for the ASRGs (6.4
to 7.4 W/kg), the mass of the ASRGs can be estimated using

$$\text{Mass of ASRGs} = \frac{\text{Total Power}}{\text{Specific Power}}. \tag{6.1}$$

Assuming a specific power of 7 W/kg (on the higher end), the mass of the ASRGs was estimated to be

$$\textbf{Mass of ASRGs} \approx \frac{\textbf{7000 W}}{\textbf{7 W/kg}} = \textbf{1000 kg}. \tag{6.2}$$

This estimation is based on the assumption that the ASRGs operate at their maximum specific power. Overall, Scuttle Mission is using 43.75 kg of Pu-238 stored within the four ASRGs.

The amount of fuel required is dependent upon the spacecraft's total mass and vice versa for a deep space mission; consequently, the Scuttle Mission xenon tanks shall be designed specifically for this mission. In addition to the amount of fuel required, this customization includes the size and tank count due to sizing constraints based on the launch vehicle. Both LEO to Earth escape and Earth escape to Uranus fuel masses shall be estimated based on values deemed appropriate in a process that works backwards from the destination to the mission start point.

6.3   Orbital Mechanics

This section will detail the path the Scuttle Mission takes to get to Ariel in three main steps: the transfer out of Earth's sphere of influence, the path to Ariel, and the orbital capture of the Scuttle Mission satellite into Ariel's SOI. Astrodynamic calculations and methods are important to determine how much fuel is needed to complete the mission.

6.3.1   Impulse Method

When making a case for electric propulsion, an analysis of high thrust impulses must be completed to determine where the losses and gains exist. To reach Uranus from Earth, Table 6.3.1 describes the necessary steps. All calculations are based on *Orbital Mechanics for Engineering Students* by H. Curtis [59].

Table 6.3.1: Impulse Mission Profile Steps: Earth to Uranus

1	Escape Earth SOI via Hyperbolic
2	Saturn SOI
3	Saturn Gravity Assist
4	Uranus Elliptical Insertion
5	Elliptical Orbit to Circular

The calculations and reasoning for each provided step will be detailed in order with the necessary constants held in Table 6.3.2.

Table 6.3.2: Constants for Space Mission

Constant	Value
Sun to Earth: R_e	1.496E8 km
Sun to Saturn: R_{sa}	1.400E9 km
Sun to Uranus: R_u	2.932E9 km
μ of Sun	1.327E11 $\frac{km^3}{s^2}$
μ_1 of Earth	3.986E5 $\frac{km^3}{s^2}$
μ_2 of Saturn	3.794E7 $\frac{km^3}{s^2}$
μ_3 of Uranus	5.794E6 $\frac{km^3}{s^2}$
r_{SOI-E} SOI of Earth	9.24E5 km

Step 1 sees the spacecraft leaving a parking orbit in LEO and entering a hyperbolic orbit to equate the excess speed the spacecraft will have as it approaches its next step. By doing a hyperbolic orbit over a Hohmann transfer, the spacecraft will be able to leave Earth's SOI. To begin the process, the velocity of the Earth around the Sun (V_{Earth}),

$$V_{Earth} = \sqrt{\frac{\mu_1}{R_e}}, \tag{6.3}$$

is 29.783 km/s, and the velocity of Saturn around the Sun V_{Saturn},

$$V_{Saturn} = \sqrt{\frac{\mu_2}{R_{sa}}}, \tag{6.4}$$

is calculated to be 9.7358 km/s. The starting point and subsequent point must be treated as an elliptical orbit around the Sun. The elliptical velocity of the Earth about the sun is treated as the perigee velocity (V_{P1}),

$$V_{P1} = \sqrt{\frac{2\mu R_{sa}}{R_e(R_{sa} + R_e)}}, \tag{6.5}$$

computed to be 40.035 km/s. The elliptical velocity of Saturn about the sun is treated as the apogee velocity V_{A1},

$$V_{A1} = \sqrt{\frac{2\mu R_e}{R_{sa}(R_{sa} + R_e)}}, \tag{6.6}$$

computed to be 4.278 km/s. To leave the SOI, the relative velocity of the spacecraft to Earth (V_{inf}) will need to be calculated, represented as

$$V_{inf} = V_{P1} - V_{Earth}, \tag{6.7}$$

with V_{inf} equivalent to 10.252 km/s. Next, the burnout velocity and velocity of the spacecraft in the parking orbit must be found. The radius of burnout, denoted by r_{bo}, will

be approximated at 6678 km, 300 km above the surface of the Earth. Parking orbit velocity (V_c) is denoted by

$$V_c = \sqrt{\frac{\mu_1}{r_{bo}}} \tag{6.8}$$

which was determined to be 7.726 km/s. Burnout velocity, V_{bo}, was calculated using

$$V_{bo} = \sqrt{V_{inf}^2 + \frac{2\mu_1}{r_{bo}} - \frac{2\mu_1}{r_{SOI-E}}} \tag{6.9}$$

and resulted in a velocity of 14.954. The required ΔV to enter the hyperbolic orbit is the difference of V_{bo} and V_c, which results in a required velocity impulse of 7.228 km/s. An illustration of the hyperbolic trajectory change can be seen in Figure 6.3.1.
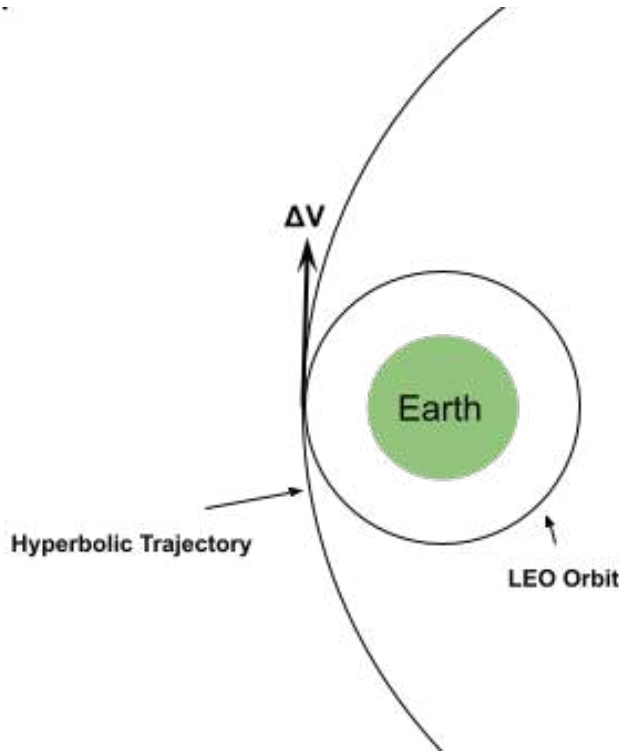
Figure 6.3.1: LEO to Hyperbolic with applied V visualizer

Step 2, approaching Saturn's SOI, is used to determine the angle change of the spacecraft's flight path. The relative velocity of the spacecraft concerning Saturn (V_{inf-S}) was found using

$$V_{inf-S} = \sqrt{\frac{\mu}{R_{sa}}} \left(1 - \sqrt{\frac{2R_e}{R_{sa} + R_e}}\right) \tag{6.10}$$

which gives V_{inf-S} equal to 5.458 km/s. This equation assumes that the spacecraft

approaches Saturn with a parallel velocity vector. To find δ, the change in angle when exiting the gravity assist, the equation,

$$\delta = 2arcsin\left(\frac{1}{1 + \frac{r_{bo-S}V_{inf-S}}{\mu_2}}\right),$$ (6.11)

returns the value of 108.065° when using a Saturn burnout radius (r_{bo-S}) of 300,000 km to avoid Saturn's rings. Using a two-body IVP solver (Appendix III), it is estimated that this portion of the voyage will take 5.78 years.

A plot of this method can be seen in Figure 6.3.2, where the red dot is Saturn, green is Earth, and yellow is the Sun.
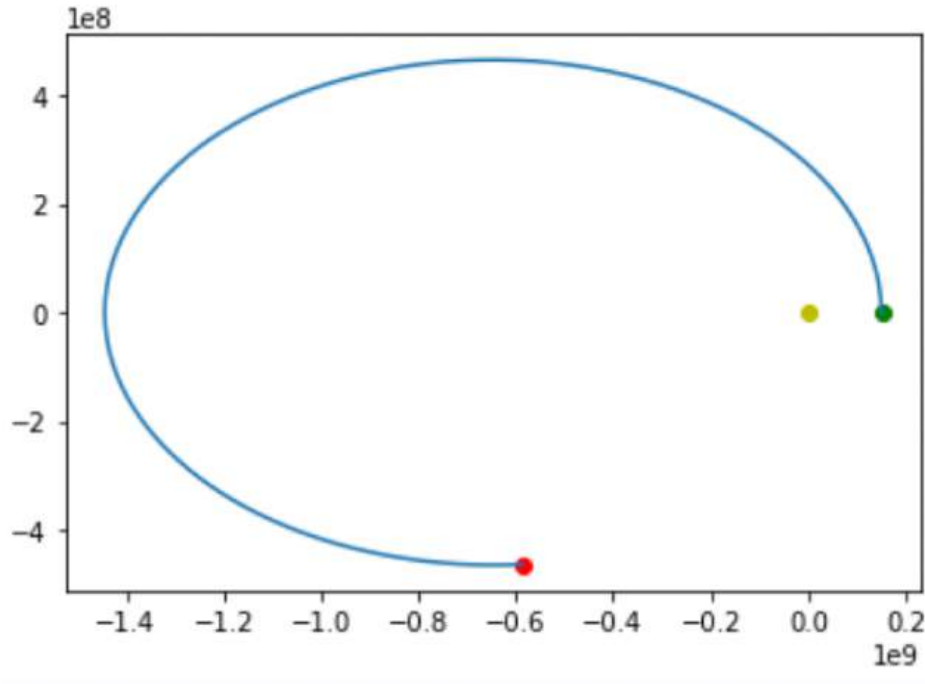
Figure 6.3.2: 2 Body approximation travel trajectory Earth to Saturn.

Step three is the Saturn flyby where a gravity assist is utilized to increase the velocity of the spacecraft leaving Saturn's SOI. The exiting velocity from Saturn, V_{s-out}, can be found using

$$V_{s-out}^2 = V_{Saturn}^2 + V_{A1} - 2V_{Saturn}V_{inf-S}\cos(\delta)$$ (6.12)

which results in a 12.551 km/s exit velocity. A depiction of this process is shown in Figure 6.3.3.

Figure 6.3.3: Saturn Gravity Assist Depiction

Because the velocity change is vectorial, the difference in velocities cannot be subtracted to determine the impulse gain (ΔV_{out}). Instead,

$$\Delta V_{out}^2 = 2V_{inf-S}\cos(\frac{\delta}{2})$$

(6.13)

is used to find the actual impulse of 8.835 km/s. Using a two-body IVP solver (Appendix III), the estimated travel time was 4965 days. It is important to recognize that velocity must be broken into its X and Y components with respect to δ for the IVP solver. An illustration of this travel can be seen in Figure 6.3.4.

Figure 6.3.4: 2 Body approximation travel trajectory Saturn to Uranus.

Step four is the insertion of the spacecraft into an elliptical orbit about Uranus. Within the sphere of influence of Uranus, there exits several rings that present a barrier to any spacecraft. The radius of Uranus' rings can be approximated as 102,280 km from the surface of Uranus [60]. With the current incoming velocity from step 3, the perigee radius would place the spacecraft within the inner rings, thus an impulse of ΔV 1 km/s is added to allow for a more appropriate insertion that will be depicted subsequently. The velocity of Uranus about the Sun (V_{Uranus}) was found using

$$V_{Uranus} = \sqrt{\frac{\mu_3}{R_u}} \qquad (6.14)$$

and had a value of 6.727 km/s. With the impulse before insertion, the velocity of the spacecraft (V_{s-out}) is now 13.551 km/s. Thus, the velocity of the spacecraft about Uranus V_{inf-U} is found to be 6.824 km/s in the direction away from Uranus using

$$V_{inf-U} = V_{s-out} - V_{Uranus}. \qquad (6.15)$$

The target moon of Ariel has an orbital period around Uranus of approximately 217,728 s (T_{period}), which will be the Scuttle Missions target period for the elliptic orbit around Uranus to limit the subsequent impulses. The semi-major axis of Ariel's orbit (a_{Ariel}) given the period is described as

$$a_{Arial} = \left(\frac{T_{period}\sqrt{\mu_3}}{2\pi} \right)^{\frac{2}{3}} \qquad (6.16)$$

and results in a value of 190,904.328 km for the semi-major axis and the approximate radius of Ariel's orbit. This approach velocity is depicted in Figure 6.3.5
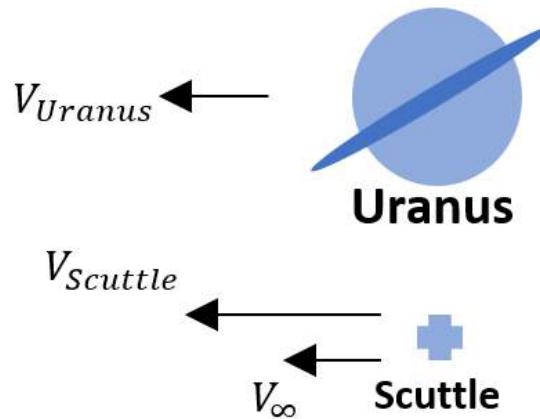
Figure 6.3.5: Velocity depiction of Uranus and Scuttle.

From this, the apogee radius (r_{a2}) can be calculated using

$$r_{a2} = \frac{2\mu_3}{(V_{inf-U})^2}, \tag{6.17}$$

and is 248,845.877 km. The current orbit is elliptical, and thus it is necessary to find the eccentricity (e_u) of this orbit, which can be found in the equation

$$e_u = -1 + \frac{r_{a2}}{a_{Ariel}}. \tag{6.18}$$

This results in an orbit with an eccentricity of 0.304. With these values known, the ΔV required to enter this orbit can be calculated with

$$\Delta V = V_{inf-U}\sqrt{\frac{1 - e_u}{2}}, \tag{6.19}$$

resulting in an impulse of 4.027 km/s. Furthermore, the perigee radius of the orbit (r_{p2}) can be calculated with

$$r_{p2} = a_{Ariel}(1 - e_u) \tag{6.20}$$

and is equal to 132,869.412 which is outside the rings of Uranus. Figure 6.3.6 serves to illustrate the target elliptical orbit with respect to Uranus and Ariel.
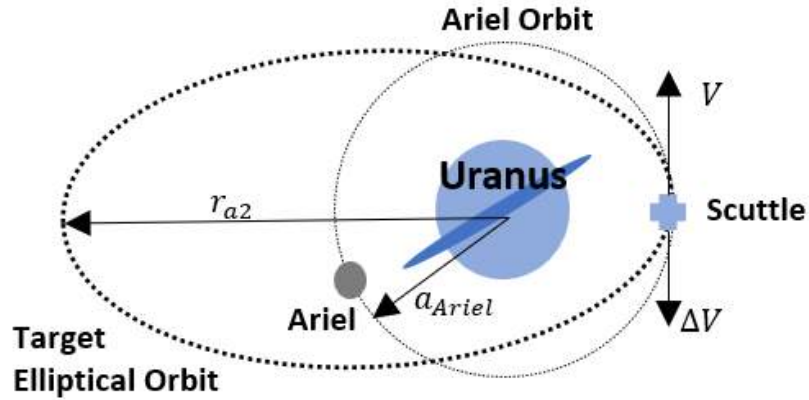
Figure 6.3.6: Target elliptical orbit.

Step five is the transformation of the elliptical orbit to a circular orbit as Ariel has an eccentricity of 0.0034 [61], which will be approximated as 0.0. Because the perigee and apogee radii are known, using

$$V_{2a-p} = \sqrt{\mu_3\left(\frac{2}{r_{p2-a2}} - \frac{1}{a_{Ariel}}\right)}, \tag{6.21}$$

the perigee velocity (V_{p2}) is 7.541 km/s, and the apogee velocity (V_{a2}) is 4.027 km/s. The velocity of a circular orbit at Ariel's radius, which is equal to the semi-major axis of the current orbit, is

$$V_{Ariel} = \sqrt{\frac{\mu_3}{a_{Ariel}}} \tag{6.22}$$

and has a velocity of 5.509 km/s. To find the required alterations to reach this circular orbit from the elliptical, a Hohmann transfer is used, and the impulse (ΔV_{F1}) at apogee that will be applied is

$$\Delta V_{F1} = \sqrt{\frac{\mu_3}{r_{a2}}} \left(\sqrt{\frac{2a_{Ariel}}{r_{a2} + a_{Ariel}}} - 1 \right), \tag{6.23}$$

where the impulse was found to be -0.329 km/s, meaning the spacecraft needs to slow down. For the 2nd step of the Hohmann process, the impulse (ΔV_{F2}) required to put it in the final circular orbit was solved using

$$\Delta V_{F2} = \sqrt{\frac{\mu_3}{a_{Ariel}}} \left(1 - \sqrt{\frac{2r_{a2}}{r_{a2} + a_{Ariel}}} \right) \tag{6.24}$$

and found to be equal to 0.352 km/s, meaning another velocity increase is required. This change in orbit is detailed in Figure 6.3.7.
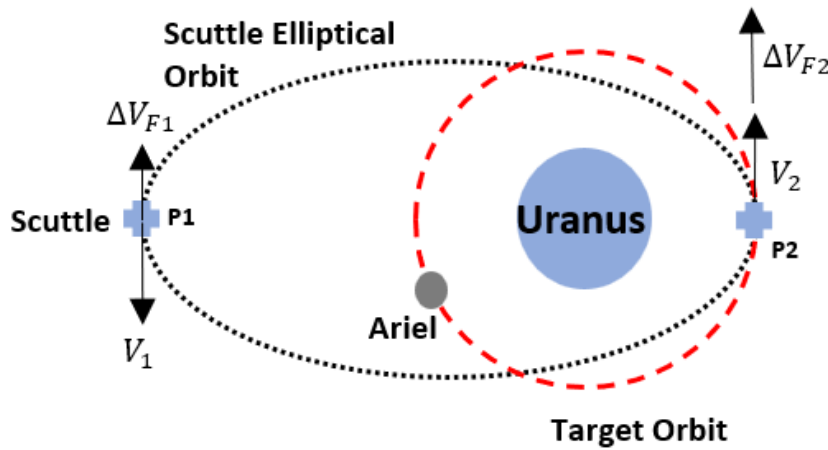
Figure 6.3.7: Target circular orbit.

To calculate the time required for this Hohmann transfer,

$$T_{tr} = \frac{\pi}{\sqrt{\mu_{sa}}} \left(\frac{r_{a2} + a_{Ariel}}{2} \right)^{\frac{3}{2}} \tag{6.25}$$

is solved to give a time of approximately 1.5 days. Compiling the duration of each of the mission maneuvers , the overall time to reach Ariel was determined to be 7,076 days; however, this assumes that the planets are in the optimum position, meaning that this mission can drastically change depending on time and planet location.

The mass of the propellant required to perform these impulses can be approximated using the Tsiolkovsky rocket equation [62],

$$\Delta V = I_{sp} g_o ln \left(\frac{m_o}{m_f} \right),$$
(6.26)

where ΔV is the accumulation of impulses, I_{sp} is the specific impulse of the rocket, g_o is Earth's gravity, and m_o and m_f are the initial and final masses respectively. Using a final mass of 3000 kg, an ISP of 450 s [63], and a total impulse due to fuel burn of 12.936 m/s. Using the Tsiolkovsky equation with the assumption that the tanks are massless and the ion thrusters and xenon tanks are removed, the resulting mass left over after all propellant has been burned would be 2790 kg. With this value, 52268.025 kg of propellant would be needed. Additionally, the mass of the tanks required to hold this fuel would balloon this number well over the approximation.

6.3.2 EP Low Earth Orbit to Earth Escape

The Scuttle Mission objective is to get to Uranus, but before the path to Uranus is plotted, there needs to be a distinction as to how the spacecraft gets from LEO to a heliocentric orbit. With the low thrust produced by EP, impulsive maneuvers cannot be utilized and thus a different approach must be taken. The most efficient low thrust maneuver involves a constant thrust applied purely circumferential to the craft's current orbit. This method is described by H.S. Tsien, an aeronautical and mechanical engineer, in the 1953 Journal of the American Rocket Society excerpt *Take-Off From Satellite Orbit* [64]. Tsien provides an approximate solution to the governing equations, allowing for simple relations to be made to determine the significant parameters for Earth's escape.

Before describing the approximate solution and the plots that follow, the equations of motion and variables involved must be defined. The basic equations that govern the motion of an object in space are described in polar form as

$$\frac{d^2 r}{dt^2} = R + r \left(\frac{d\theta}{dt} \right)^2 - g \left(\frac{r_0}{r} \right) \text{ and}$$
(6.27)

$$\frac{d}{dt} \left(r^2 \frac{d\theta}{dt} \right) = r\Theta.$$
(6.28)

where R is the radial thrust force, Θ is the circumferential thrust force, r_0 is the radius of the initial circular orbit, and g is the gravity experienced in the initial orbit.

These equations governing the motion of a spacecraft in orbit are subjected to equilibrium

initial conditions that state the spacecraft is initially in a steady circular orbit described by the gravitational pull of the celestial body. These conditions are described by

$$r_0 \left(\frac{d\theta}{dt} \right)_0^2 = g, \tag{6.29}$$

$$\left(\frac{dr}{dt} \right)_0 = 0, \text{ and} \tag{6.30}$$

$$\ddot{\theta} = 0. \tag{6.31}$$

Additionally, for the spacecraft to have enough energy to escape Earth's gravitational field at the end of a powered flight, the total energy of the system should be balanced. This instant where the kinetic energy of the spacecraft is equivalent to the potential energy of Earth's gravitational field occurs at time $t = t_1$. This energy balance can be shown as

$$\frac{1}{2} \left[\left(\frac{dr}{dt} \right)_1^2 + \left(r\frac{d\theta}{dt} \right)_1^2 \right] - g \left(\frac{r_0^2}{r_1} \right) = 0. \tag{6.32}$$

To analyze the equations of motion and develop an approximate solution, several non-dimensional variables are defined as

$$\nu = \frac{\Theta}{Mg}, \tag{6.33}$$

$$\rho = \frac{r}{r_0}, \text{ and} \tag{6.34}$$

$$\tau = t\sqrt{\frac{g}{r_0}} \tag{6.35}$$

where ν is the circumferential thrust factor, M is the total initial mass of the spacecraft, ρ is the non-dimensional radial distance, and τ is the non-dimensional time.

Using these non-dimensional variables, the equations of motion become

$$\frac{d^2\rho}{d\tau^2} = \rho \left(\frac{d\theta}{d\tau} \right)^2 - \frac{1}{\rho^2}, \text{ and} \tag{6.36}$$

$$\frac{d}{d\tau} \left(\rho^2 \frac{d\theta}{d\tau} \right) = \nu\rho \tag{6.37}$$

with the following initial conditions:

$$\left(\frac{d\theta}{d\tau}\right)_0 = 1, \tag{6.38}$$

$$\left(\frac{d\rho}{d\tau}\right)_0 = 1, \tag{6.39}$$

$$\left(\frac{d^2\rho}{d\tau^2}\right)_0 = 0 \tag{6.40}$$

at $\rho = 1$, $\tau = 0$. The governing differential equation is produced upon combining equations 6.36 and 6.37 in

$$\frac{d}{dt}\left(\rho^3\frac{d^2\rho}{d\tau^2} + \rho\right)^{\frac{1}{2}} = \nu\rho. \tag{6.41}$$

This third-order differential equation does not have a simple general solution, meaning approximations must be made to obtain a solution. For small values of ν (and therefore thrust), it is expected that the acceleration will be very small and therefore the term $\rho^3\frac{d^2\rho}{d\tau^2}$ in equation 6.41 is much less than ρ. Tsien uses this assumption to approximate equation 6.41 as

$$\frac{1}{2}\frac{d\rho}{\rho^{\frac{3}{2}}} = \nu d\tau, \tag{6.42}$$

which has a solution for the given initial conditions of

$$\rho = \frac{1}{(1 - \nu\tau)^2}. \tag{6.43}$$

Since ν is very small, the radial velocity and acceleration are not exactly zero, but very close. It is thus concluded that equation 6.43 is a good approximation of the exact solution. Using this same approximation, Tsien defines the angular velocity as

$$\frac{d\theta}{d\tau} = \frac{(1 - \nu\tau)}{\rho}. \tag{6.44}$$

The end condition of equation 6.32 can be reassembled in terms of the non-dimensional variables as

$$\frac{4\nu}{(1 - \nu\tau_1)^6} - (1 - \nu\tau_1)^2 = 0 \tag{6.45}$$

which has the solution for the non-dimensional end time, τ_1,

$$\tau_1 = \frac{1 - (2\nu)^{\frac{1}{4}}}{\nu}. \tag{6.46}$$

Appendix 11.2 details the steps taken to solve these equations for various parameters and plots the following relations. Utilizing equation 6.43, ρ can be plotted against τ for various values of ν, meaning that thrust and vehicle mass are the variable parameters. Using the dimensional relations defined previously, the radial position and corresponding time can be determined. An example plot of these variables is shown in Figure 6.3.8, using the 236 mN of thrust provided by NASA's NEXT-C thruster. Earth's sphere of influence ends at an orbital radius of 1e9, meaning that all values beyond this threshold are no longer viable with this model.
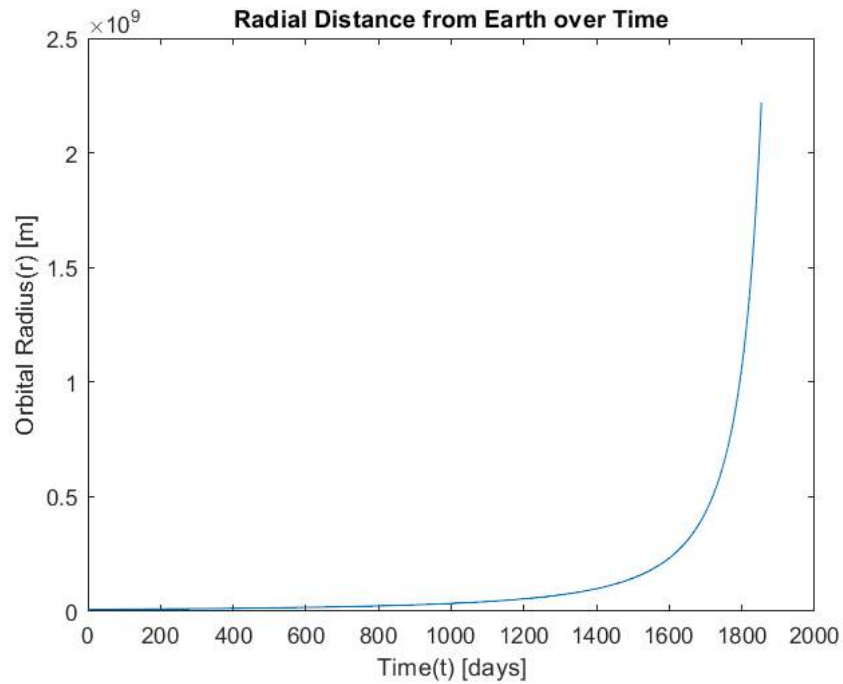
Figure 6.3.8: Orbital radius over time for $\Theta = 0.236$ N and $M = 5839$ kg.

The angular velocity through the duration of the burn can be plotted using equation 6.44 and the dimensional time relation, which results in a plot resembling Figure 6.3.9. For ease of comprehension, the angular velocity is given in deg/s.
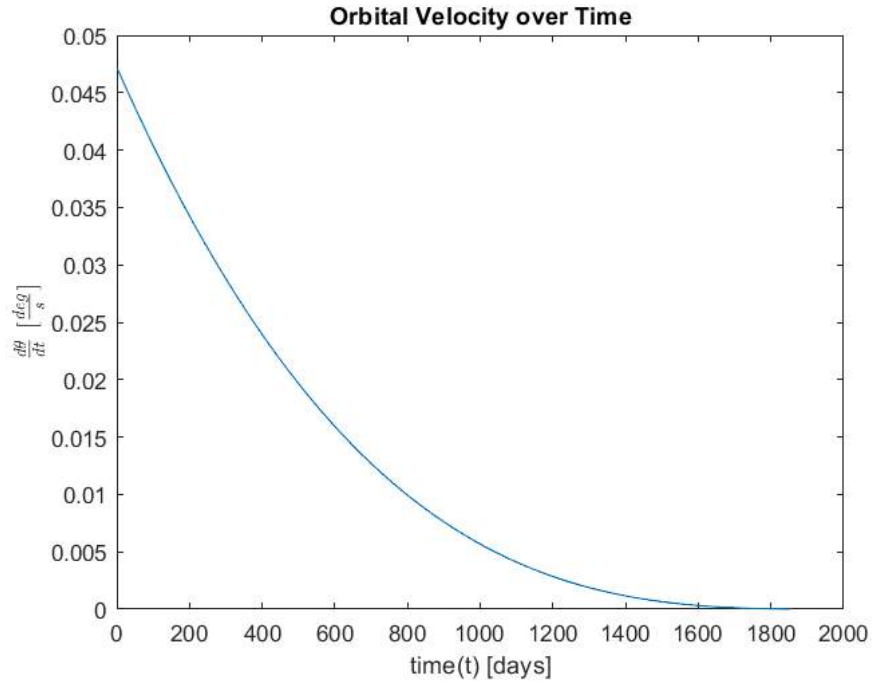
Figure 6.3.9: Angular velocity over time for $\Theta = 0.236$ N and $M = 5839$ kg.

With the initial angular position set to zero and the angular velocities known for every point in time, a simple Euler method time-stepper can be used to approximate the angular positions for each point in time. This, when combined with the already determined radial positions, can be plotted on a polar plot to visualize the spacecraft trajectory as shown in Figure 6.3.10. Earth's SOI is plotted as a reference, yet the trajectory plot continues until the end condition is satisfied even if the spacecraft no longer has the same gravitational field.
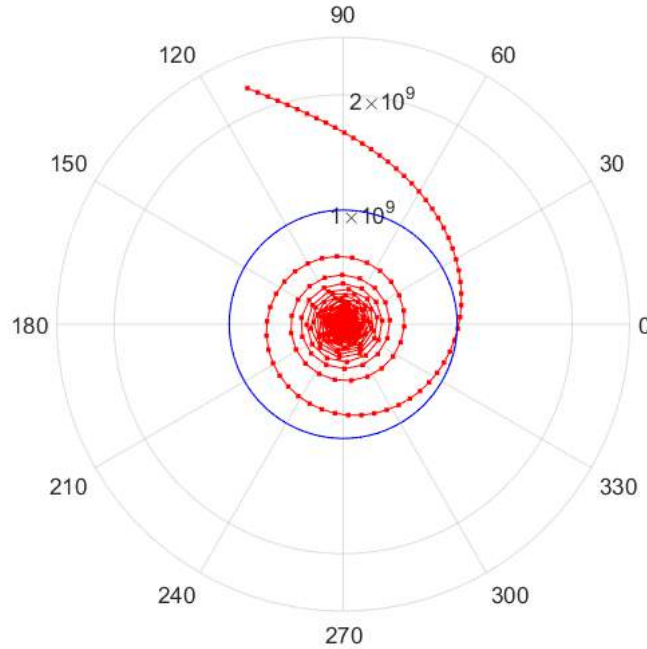
Figure 6.3.10: Spacecraft trajectory over time for $\Theta = 0.236$ N and $M = 5,839$ kg.

In post-processing this data, the number of revolutions and the duration of the thrust can be obtained. While the preceding figures are purely explanatory and proper parameters will be chosen throughout this project, the current parameters ($\Theta = 0.236$ N and $M = 5,839$ kg) yield a trajectory that has 5,603.3 revolutions over 1,853 days (approximately 5 years).

To determine the mass of xenon propellant required by the thrusters for this extended maneuver, an elementary calculation can be made by rearranging the thrust equation 6.47 to determine the mass flow rate of the exhaust and multiplying this value by the total time that it takes to escape Earth's SOI using

$$\dot{m} = \frac{\Theta}{u_e}, \text{ and} \tag{6.47}$$

$$M_p = \dot{m}t_1. \tag{6.48}$$

With this calculation utilizing the parameters previously defined, the mass of propellant needed for the maneuver is found, and added to the non-propellant mass that makes up the rest of the spacecraft. If this sum is within 5% of the total mass of the craft used in the initial conditions of the calculation, this is the proper propellant mass needed. Otherwise, the sum will replace the previously used total mass of the craft and the code must be run again until convergence is found to the 5% specification.

The mass of the vehicle was initially approximated at 5,500 kg with the fuel for this maneuver occupying 575 kg of this mass. After convergence, the total mass of the vehicle was found to be **5,839 kg with 915 kg of propellant mass** required for the Earth

escape maneuver. This value of the total mass was required for each of the preceding plots to identify the trajectory and time-varying parameters of the low thrust orbit.

6.3.3   Heliocentric Path to Uranus

Following the exit of Earth's SOI, the Scuttle Mission spacecraft will traverse Ariel's SOI using a similar approach to what was defined in the previous section. For the simulation, the orbits of Earth and Uranus are assumed to be perfectly circular at their average distance from the Sun and the 0.7° inclination change from the Earth-Sun plane is to be ignored. Figure 6.3.11 shows the two-dimensional coordinate system that is referred to for the rest of this section.
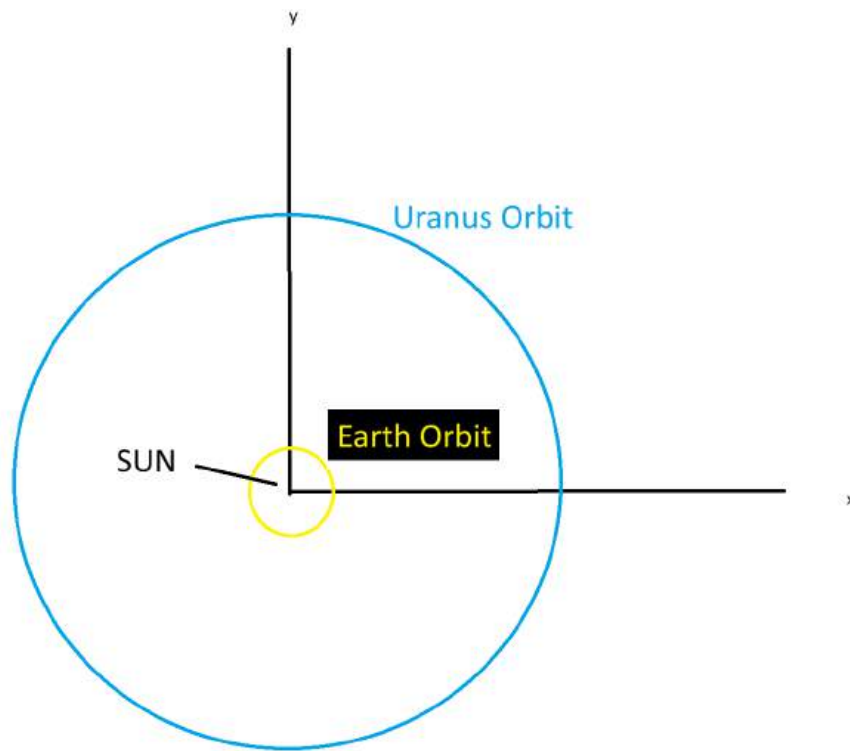
Figure 6.3.11: Coordinate system used in Section 6.3.3: Heliocentric Path to Uranus

The path to Uranus after escaping Earth's SOI is defined by the following differential equations for a continuous thrust satellite, provided by *Orbital Mechanics & Astrodynamics* by Bryan Weber [65].

The equations of motion for a spacecraft in a gravitational field with continuous thrust are given by

$$\ddot{x} = -\frac{\mu x}{r^3} + \frac{T}{m}\frac{\dot{x}}{v}, \tag{6.49}$$

$$\ddot{y} = -\frac{\mu y}{r^3} + \frac{T}{m}\frac{\dot{y}}{v}, \text{ and} \tag{6.50}$$

$$\ddot{z} = -\frac{\mu z}{r^3} + \frac{T}{m}\frac{\dot{z}}{v} \tag{6.51}$$

where μ is the heliocentric gravitational parameter, x is the x-position in the defined coordinate system, r is the distance to the origin in the defined coordinate system, T is the thrust, m is the mass of the spacecraft, and v is the magnitude of the spacecraft's speed [65].

To relate mass for these differential equations, its first-time derivative is solved with respect to thrust and specific impulse using

$$\frac{dm}{dt} = -\frac{T}{I_{sp}g_0} \tag{6.52}$$

where $\frac{dm}{dt}$ is the rate that mass is changing in the spacecraft, I_{sp} is the specific impulse, and g_0 is standard sea-level gravity.

To define initial velocity, an arbitrary initial position is defined on the x-axis, making the direction of the initial velocity in the y direction. The initial velocity is calculated using

$$\mathbf{v}_0 = \sqrt{\frac{\mu}{r_0}}\hat{\mathbf{j}} \tag{6.53}$$

where $\mathbf{v}_0$ is the initial velocity, and r_0 is the initial radius.

The initial state vector $\mathbf{Y}_0$ comprises three position coordinates (x, y, z), three velocity components $(\dot{x}, \dot{y}, \dot{z})$, and the mass (m). The initial position is chosen on the x-axis, and the initial velocity is in the y-direction which results in

$$\mathbf{Y}_0 = [r_{LEO}, 0, 0, 0, v_{LEO}, 0, m_0]. \tag{6.54}$$

The equations of motion are integrated using the SciPy library's `solve_ivp` function. The solver employs the DOP853 method, a 7th-order Runge-Kutta scheme, to solve the system of ODEs. The Python code can be seen in Appendix IV (Section 11.4).

Event functions are present to detect specific occurrences during the integration. The three occur during the following scenarios:

- **reached_destination:** Triggered when the spacecraft reaches the destination radius.
- **mass:** Terminates integration if the mass becomes zero.

- **orbit:** Records each time the y-component of the position crosses zero, helping to count the number of orbits.

Table 6.3.3 shows the parameters chosen for the calculations carried out by the code. These were chosen based on specifications from NASA's Gridded Ion Thrusters (NEXT-C). This calculation requires an input of an initial mass, which was chosen to be 6500 kg, which is an approximation solely based on a number slightly larger than that off the mass of the spacecraft in LEO detailed in Section 6.3.2.

<div align="center">Table 6.3.3: Mission Parameters to Ariel</div>

Parameter	Value
T (Thrust)	236 mN
I_{sp} (Specific Impulse)	$4,190$ s
m (Mass of satellite)	$6,500$ kg
r_E (Distance from Earth to Sun)	1.496×10^8 km
μ (Heliocentric Gravitational Parameter)	1.327×10^{11} km^3/s^2
r_U (Distance from Uranus to Sun)	2.9318×10^9 km

In the simulation, the team found that the satellite completed six orbits, utilizing 3,443 kg of propellant during a time of flight of 6,940 days, as shown in Table 6.3.4. Nearly 70% of the spacecraft mass would be fuel with much of the remaining mass likely taken up by the tanks themselves to transport the fuel. Figure 6.3.12 shows the plot of the flight path from the escape point of Earth's SOI to Ariel, where the blue line represents Earth's orbit and the dashed orange line is Uranus' orbit. These calculations are just a first iteration – a baseline conformation – and are to be improved upon when the method of Section 6.3.2 is implemented in a heliocentric manner.

<div align="center">Table 6.3.4: Simulation Results</div>

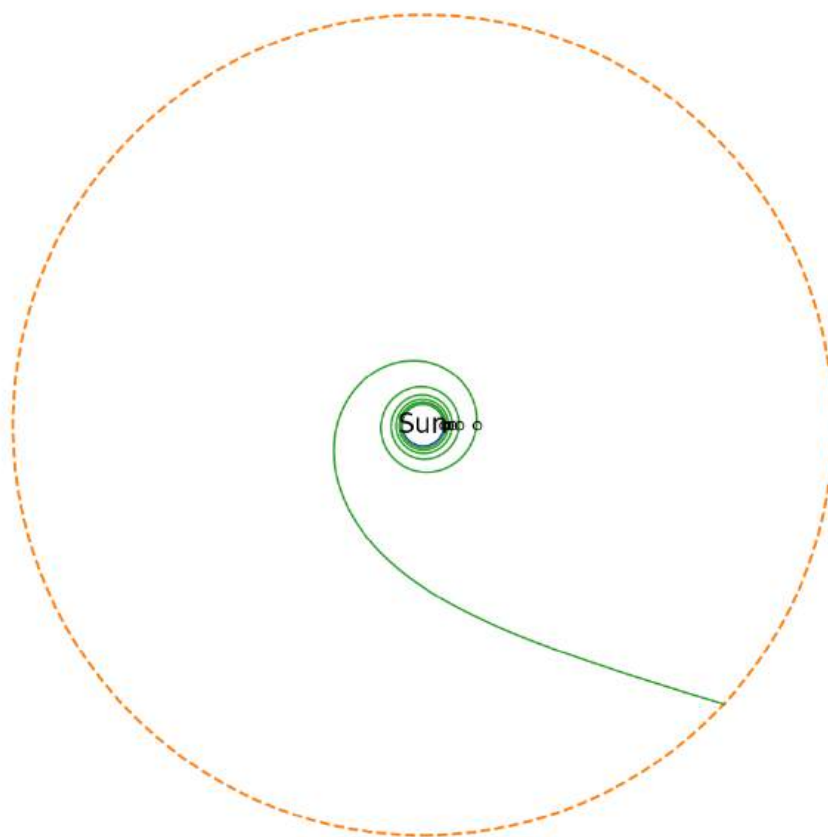| Result	Value
Number of Orbits	4
Propellant Used	3,443 kg
Time of Flight	6,940 days
Speed at Destination	19.4018 km/s

Figure 6.3.12: Flight path from escape point of Earth's SOI to Uranus.

Since the main objective of the mission is to be captured into Ariel's orbit, the final velocity is important to consider. Calculated previously in Section 6.3.1 at equation 6.22, the desired final velocity for the satellite to match the speed that Ariel is orbiting Uranus at is 5.509 km/s, assumed to be in the direction perpendicular of that of its radius of orbit. The final velocity from the parameters given in Table 6.3.3 was seen to be 19.4 km/s, which is much too fast to be able to enter and stay in Ariel's SOI. A ΔV would need to be generated to slow down the spacecraft in order to hit the desired velocity which would require impulsive thrusters and more propellant. This method is simply not feasible because of the massive amount of propellant needed to generate a large enough ΔV. Therefore, the team decided to go in another direction: shutting off the ion thrusters during the middle of the journey. The next step in the analysis must then be to determine where the thrusters should be shut off, and the corresponding time.

The first step in the process to find the ideal spot to cut off the power to the ion thrusters is to modify the simulation code to two separate simulations: one where the thrusters are providing thrust and one where the thrust is set to zero. The first code iteratively changes the distance from the sun where the engine is to cut at; the position and velocity vectors are provided to the second simulation as initial conditions where the thrust is set to zero, and the ending point is at Uranus' distance from the Sun. The two variables that change

with this iterative process are the initial mass of the satellite in simulation one, m, and the final distance for simulation one, r_F, where the thrusters are to stop firing. Table 6.3.5 summarizes the differences in parameters. r_I for simulation two is determined by the initial conditions provided by simulation one and m for simulation one is set by the amount of propellant used to get to the changing r_F value, similar to the process described during the original simulation. Simulation 2 is not the final value used and is simply an intermediate step.

Table 6.3.5: Comparison of Mission Parameters for Simulations 1 and 2

Parameter	Simulation 1	Simulation 2
T (Thrust)	236 mN	0 mN
I_{sp} (Specific Impulse)	4,190 s	0 s
m (Mass of satellite)	*Dependent Variable*	4500 kg
r_I (Initial Distance to Sun)	1.496×10^8 km	*Det. by sim 1*
μ (Heliocentric Gravitational Parameter)	1.327×10^{11} km^3/s^2	1.327×10^{11} km^3/s^2
r_F (Distance from Uranus to Sun)	*Independent Variable*	2.9318×10^9 km

After plugging in values for r_F, a convergence point was found to give a final velocity of 6.8904 km/s when the thrusters were shut off at a distance of 985,000,000 km away from the Sun. The initial mass in this convergence simulation is 4,925 kg. Table 6.3.7 shows the rest of the results for the convergence simulation.

Table 6.3.6: Position and Velocity Vectors

Result	Simulation 1	Simulation 2	Total
Number of Orbits	4	0	0
Propellant Used	1,922 kg	0 kg	1,922 kg
Time of Flight	3,876 days	3,227 days	7,103 days
Speed at Destination	15.0553 km/s	6.8904 km/s	–

In Figure 6.3.13, the flight path is shown with the thrusters being shut off at the solid pink line. The satellite's position is highlighted by the maroon circle when this occurs as well.
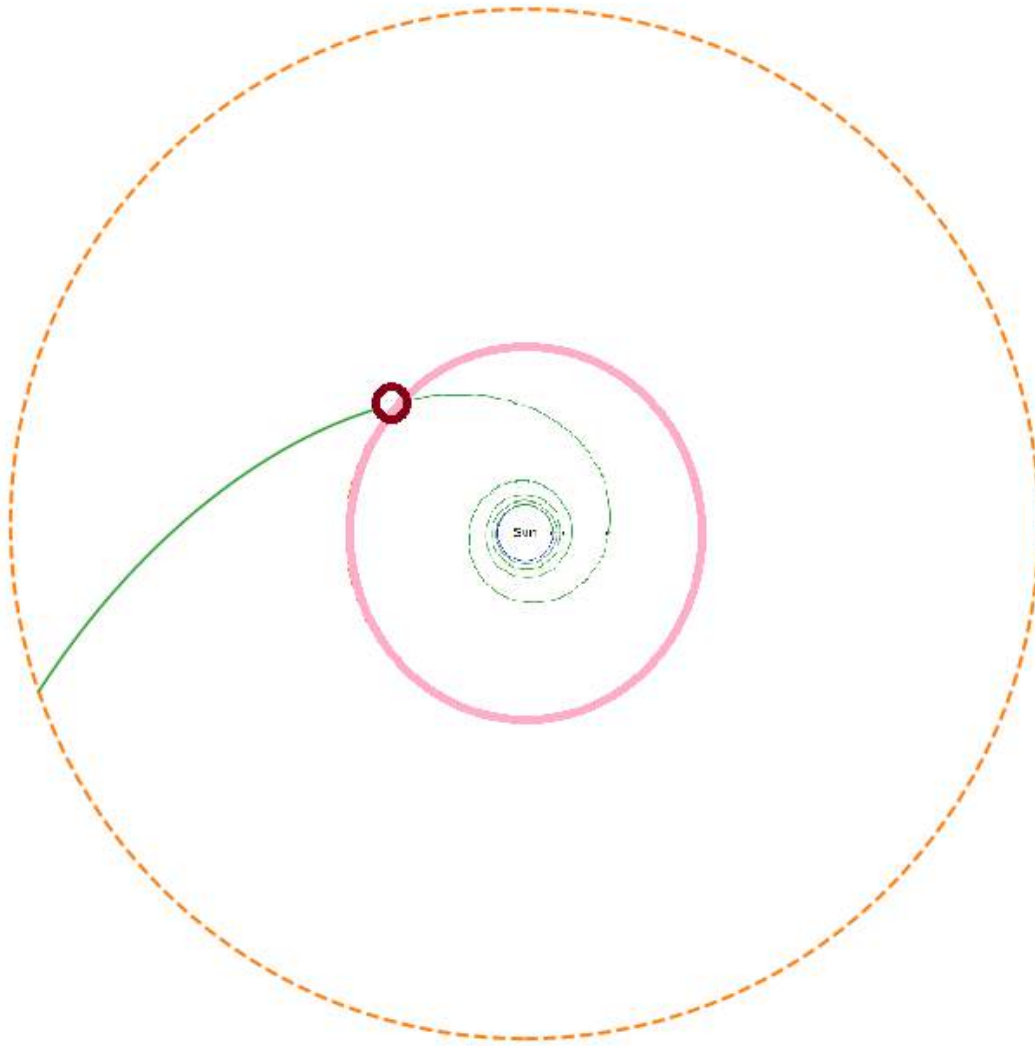
Figure 6.3.13: Combined flight path from GEO to Uranus, featuring both simulation flight paths.

At the intersection point of the spacecraft and Uranus' flight path, the position of intersect and velocity vectors in X-Y space are logged in Table 6.3.6.

Table 6.3.7: Comparison of Simulation Results for Simulations 1 and 2

Vector	X	Y
Position	-2.76e9 km	-9.50e8 km
Velocity	-3.74 km/s	-5.79 km/s

From the position vector, the spacecraft intersects Uranus' path approximately 18.935 degrees below the -X axis, represented by A. Figure 6.3.14 illustrates the correct coordinate

system directions the velocities will need to be projected upon from the X-Y coordinate system.
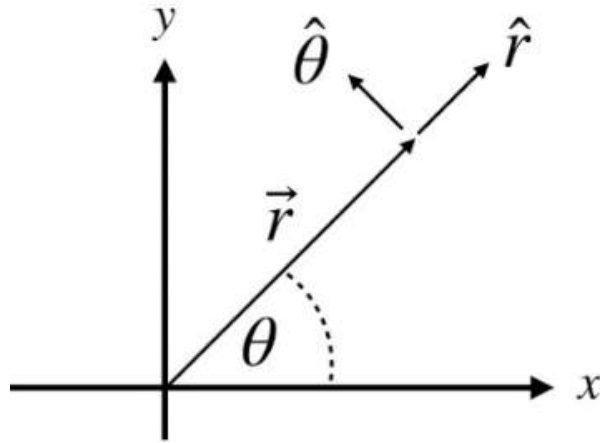
Figure 6.3.14: Direction of motion for Uranus along circular orbit

By solving

$$V_r = V_y sin(A) + V_x cos(A), \text{ and} \tag{6.55}$$

$$V_\theta = V_y cos(A) - V_x sin(A), \tag{6.56}$$

the absolute values of velocities of the spacecraft at the intersection point are 5.414 km/s in the radial direction and 4.262 km/s in the theta direction. When treating the orbit of Uranus as a circle about the Sun, its 6.727 km/s velocity makes the spacecraft appear to be moving in the opposite radial direction at 2.465 km/s. Combined with the theta direction vector, the magnitude of its velocity with respect to Uranus is 5.949 km/s, resulting in a circular orbit altitude of 163,716 km. The appearance of motion from outside of the Uranus-Spacecraft system and motion if one was positioned on Uranus is demonstrated by Figure 6.3.15.
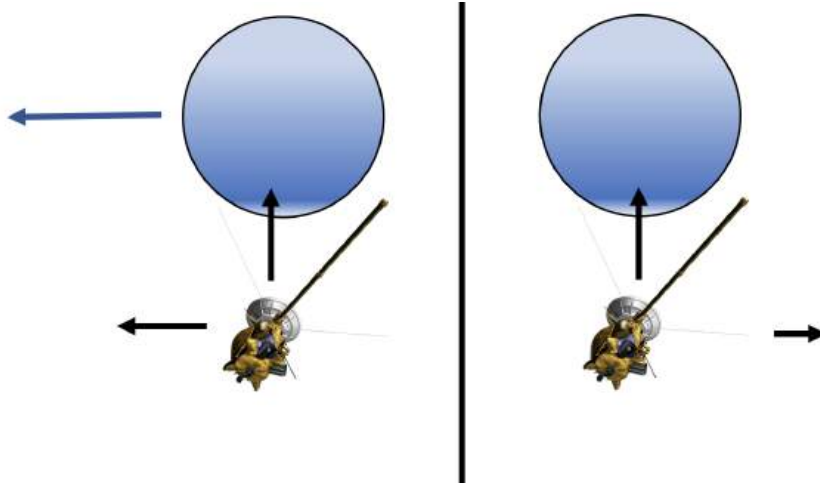
Figure 6.3.15: Motion of Uranus and spacecraft with Sun center point (Left) vs motion of spacecraft with Uranus as center point (Right)

The spacecraft would thus enter the trailing inner portion of the orbit with a positive angle above the -X axis with respect to the common X-Y plane if Uranus was positioned along the -X axis. The velocity vectors with respect to Uranus can be seen in Table 6.3.8.

Table 6.3.8: Velocity Vectors from Uranus' POV

Vector	R	θ	Magnitude
Velocity	5.414 km/s	-2.465 km/s	5.969 km/s

Overall, the process of reaching Uranus from GEO takes a little more than 19.5 years to match speeds with Uranus' moon Ariel. The EP thrusters are to be running for 3,876 days, which is a little more than half the mission time. As a result, this method effectively minimizes propellant consumption, contributing to an optimized trajectory towards Ariel.

6.4   Conclusion

This section summarizes the processes of the selection of initial mass and what that means for Scuttle Mission in terms of total mass and structural mass. Furthermore the results of the comparison between EP and impulsive chemical propulsion as well as the importance of limiting thrust time to decrease approach velocity is highlighted.

Solving for the continuous thrust astrodynamics requires mass as an input parameter, however, increasing mass to make room for more fuel itself increases the required fuel to reach the destination unless structural mass is decreased. The Ariel Voyagers deemed that an approximate mass of 3000 kg once the spacecraft reaches Ariel would be targeted. Completing each iterative step, first the LEO to escape and then escape to Uranus with the included cutoff period, an initial mass resulting in a dry mass of approximately 3000 kg was calculated. Resulting initial masses at each step is highlighted in Table 6.4.1

Table 6.4.1: Masses at each Step.

Step	Initial Mass [kg]
LEO to Earth Escape Thrusters	5839
Earth Escape to Cutoff	4925
Cutoff to Uranus	3003

In order to highlight the comparison between EP and rocket propellant methods, Table 6.4.2 contains the mission duration and propellant masses used for the different types of propulsion, and different stages of the flight in the case of EP.

Table 6.4.2: Mission duration and propellant mass comparison.

Method	Duration [days] (years)	Propellant Mass [kg]
Impulsive: Chemical Thrusters	7,076 (19.39)	52,268
EP: LEO to Earth Escape	1,853 (5.08)	915
EP: Earth Escape to Uranus	7,103 (19.46)	1,922

From this table, it is evident that using a chemical rocket would require much greater amounts of fuel. In fact, the current value of mass assumes that there is no tank mass or other supporting structure mass, therefore, the true value will be even greater. Upon lift off, the EP method would need approximately 2,837 kg of xenon. The duration of the mission for the chemical thrusters is 7,076 days, compared to 7,103 days to go from an escaped Earth orbit. This means that outside of Earth's SOI, the two methods are comparable. What favors EP is that this time does not depend on the date or position of the planets as it leaves Earth, thus the location that it reaches Uranus can be altered. The chemical method is based on perfect alignment of the planets, which is only the case at certain points in time and could delay a mission by decades. Where the EP system struggles is going from a LEO to escape as it takes 1,853 days and uses nearly one third of its propellant mass to do so. As a result, a mission that focuses on speed and efficiency would have to rely on a chemical method to escape Earth's SOI and an EP system to get to Uranus. For this EP focused mission, there is a total travel time of 8,956 days.

Notable constraints with this method of travel in regards to the astrodynamics is that any necessary course corrections would need to be realized well in advance due to the low thrust nature of the spacecraft; however, real time calculations would be calculated based on different parameters not realized in this study that help calculate any and all interference's that the spacecraft would experience through this path. For example, if the spacecraft were to be off course and deemed to miss Uranus, alterations to its flight path would have to take place in the powered portion of the spiral. If necessary, the RCS thrusts can also provide some attitude changes to help re-orientate the spacecraft to a different path to Uranus.

7 Scuttle Mission Spacecraft: Mark I

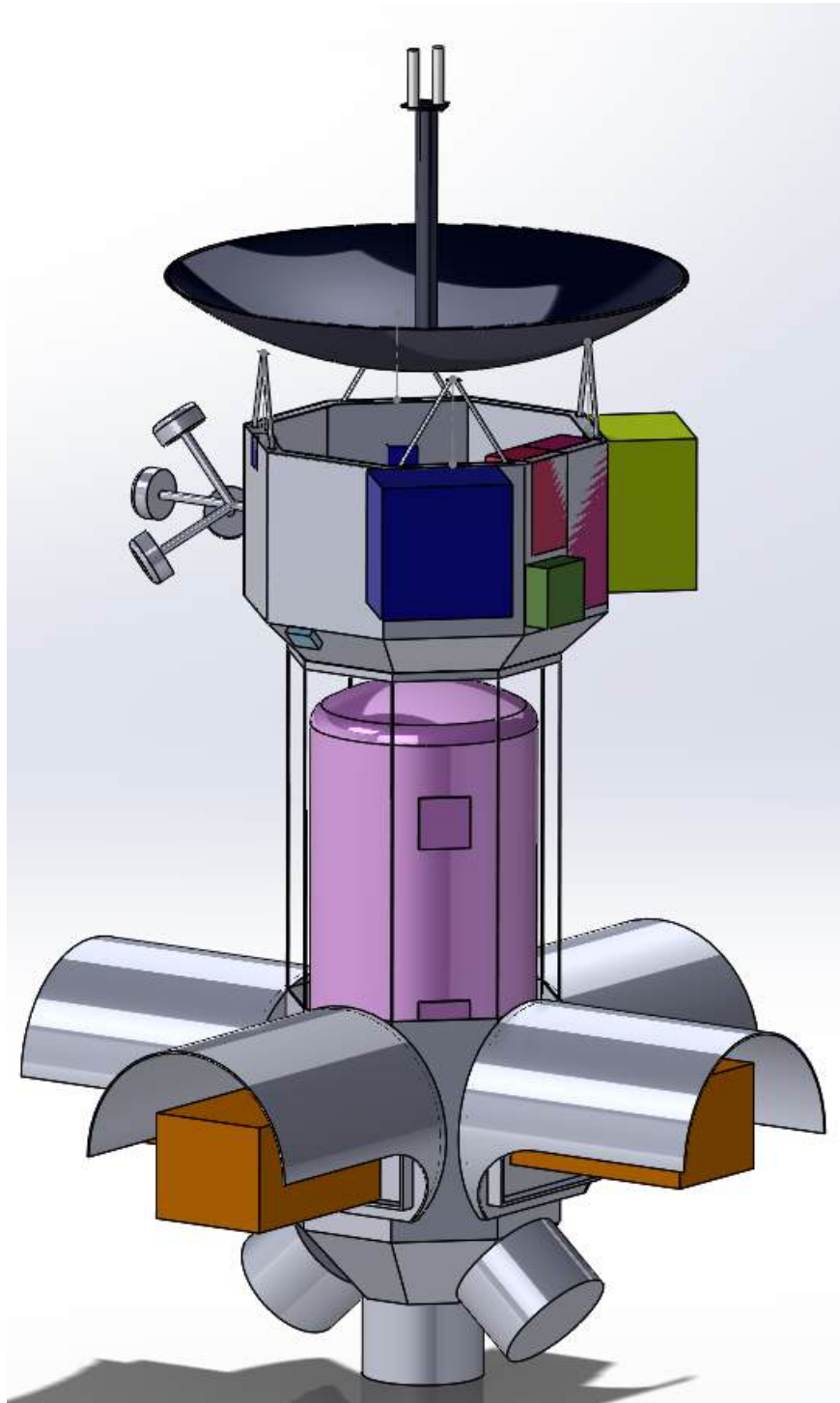The preliminary design of the Scuttle spacecraft is illustrated in Figure 7.0.1.

Figure 7.0.1: Scuttle Mission Spacecraft: Mark I

While elementary, this model was created as a baseline for analysis regarding the basic structural components that make up the spacecraft. The design provides an initial insight into the shape that the Scuttle Mission vehicle takes on, and aids in the determination of analysis areas. Noting the relative locations of the ASRGs (lower orange boxes), its shielding covers and the scientific equipment (upper colored boxes) for example, it can be seen that analysis must be done to determine how the instrumentation can be protected from being damaged by these nuclear generators.

8 Structural Design and Analysis

The Scuttle Mission spacecraft shall be designed to survive a vertical acceleration of $8\,g$ and an axial acceleration of $3\,g$ to a factor of safety of 1.5 as specified in the technical standards of Section 2.1. These peak g's result from the launch of the host vehicle carrying the spacecraft into low Earth orbit. To structurally analyze the spacecraft in its entirety, a top-down approach was taken. This was done to minimize the unknowns, filling in the gaps of the model as the required shapes and sizes were defined based upon their structural and loading requirements. Due to the unique nature of the Scuttle Mission's power source, determining effective methods and materials for heat and radiation control is imperative.

8.1 External Layout and Mounting

In order to analyze the structure of the Scuttle spacecraft, the layout of the equipment mounted onto the external panels of Scuttle must be established. The main structure will be an octagon shape, with each side of the octagon labeled in Figure 8.1.1. The high gain antenna, HGA, as well as the low gain antenna, LGA, are labelled in the center as they are intended to be mounted on the top of the spacecraft, which will denote the +Z direction.
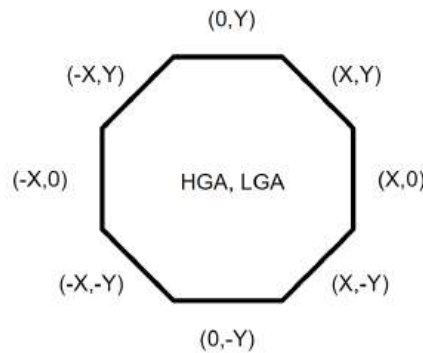

Figure 8.1.1: Scuttle Mission Structure Side Call-out

The result of this shape is that each side can have an appropriate count of equipment pieces, roughly distributing the mass of the instrumentation and ensuring adequate placement for proper operation. The scientific payload from Section 6.1 that is required to

be mounted externally was assigned a location shown in Figure 8.1.2, where ST is the label for star tracker. The positioning of equipment allows for the determination of point masses for structural calculations as the strength required to withstand the stresses caused by these masses to the required 1.5 factor of safety will be dependent on their location. Exact mass values used were pulled from Table 6.2.1 in Section 6.4.
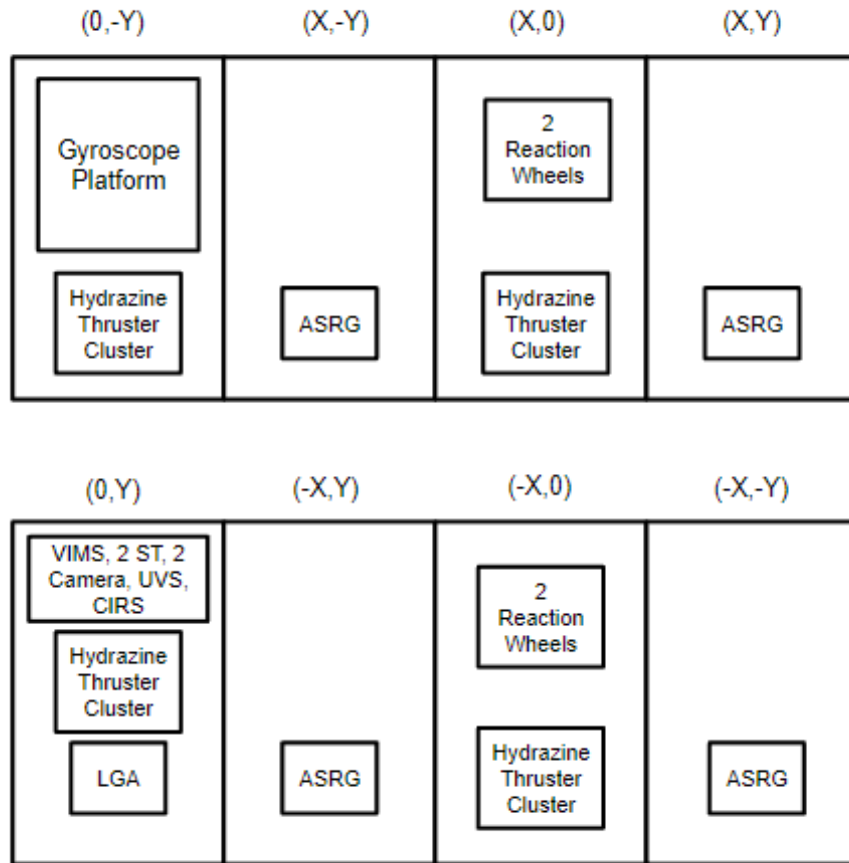

Figure 8.1.2: Scuttle Mission External Equipment Mounting Positioning

8.2 Fuel Tanks

As a crucial element to the success of the Scuttle Mission, the fuel tanks aboard the spacecraft must be designed such that their size, weight, and strength correspond to the stresses they must withstand. The fuel tanks must be capable of withstanding internal pressure loading while carrying the required amount of fuel to reach the end destination: Ariel. The following section describes the determination of the sizes used for the hydrazine and xenon tanks to meet these requirements.

8.2.1 Hydrazine Tanks

Tanks for hydrazine shall be made solely out of Titanium 6AL-4V, which has a yield stress of 880 MPa [66]. Combined with the safety factor of 1.5, the maximum allowable stress for Scuttle Mission's hydrazine tanks is 587 MPa. The design sizing of the tank will be based on the EDPM 58 Litre 01-0 hydrazine tank, which has an internal diameter of 0.240 m, and a maximum expected operating pressure of 26 bar at all instances thanks to the use of a bladder system, equivalent to 2.6 MPa [67]. Despite the name stating 58 L, the maximum propellant these tanks can actually hold is 39 L [67]. The Scuttle Mission will utilize two of these spherical tanks mounted externally. The tank that the Scuttle Mission spacecraft will use is displayed in Figure 8.2.1.

Figure 8.2.1: 58L Hydrazine Tank [67]

Using the pressure vessel equation of stress for a sphere,

$$\sigma_{sphere} = \frac{Pr}{2t},\tag{8.1}$$

where P is pressure, r is tank radius, and t is tank thickness, the required thickness of the titanium tank was determined to be 0.534 mm. This calculated value is slightly thinner than most conventional propellant tanks, but is still an acceptable value.

Due to the high pressure within the tank, the tank will experience slight budging which must be limited to avoid potentially damaging the spacecraft and mounting hardware. The change in radius and subsequent change in volume are modeled by

$$\Delta R = \frac{P(1-\nu)r^2}{2Et}, \text{ and}\tag{8.2}$$

$$\Delta V = \frac{2P\pi(1-v)r^4}{Et}, \tag{8.3}$$

where ν is Poisson's ratio and E is the Young's Modulus [68]. From these equations, the change in radius and volume experienced by the tank was calculated to be 0.000814 m and 0.000589 m^3, respectively. The conclusion drawn from the hydrazine calculations is that external mounting methods will need to allow for only minuscule tank expansion. Since the calculated wall thicknesses were so thin, the selected manufactured tank will be more than suitable for the conditions required of the hydrazine propellant. Scuttle will carry 74.33 kg of Hydrazine with this method.

8.2.2   Helium Tanks

In order for the hydrazine tanks to operate continuously, the 26 bar pressure must be continuous throughout the entire life cycle of the mission until the fuel is exhausted. For the hydrazine to be continuously squeezed by the bladder, a pressuring system is required. This will be done using Helium. It will be assumed that the hydrazine tank already contains the necessary helium to fill the remainder of the 58 L to allow for the start pressure of the hydrazine tank to be 26 bar. To calculate the required tank volume, Boyles law 8.4,

$$P_1V_1 = P_2V_2, \tag{8.4}$$

was used. Where P_1 and V_1 are the pressure and volume of the helium tank, and P_2 and V_2 are pressure and volume of the empty hydrazine tank and helium tank, which will be 26 bar to ensure the hydrazine it forced out of the tank.

To limit the size of the tank, a 200 bar pressure was chosen. With this, P_1 is 200 bar, P_2 is 26 bar, V_1 is the unknown helium tank volume and and V_2 is the unknown volume plus the volume of the hydrazine, 0.078 m^3. This results in a volume of 0.011655 m^3. However, because there will be helium lost in the connections between he two tanks, the volume will be increased by 10% to a value of 0.01282 m^3. Utilizing the Ideal Gas Law, the tank, which will be approximately 30 C, will have 100.45 moles of helium, which is approximately 0.402 kg.

A spherical tank with a volume of 0.01282 m^3 results in a diameter of .2904 m. From 8.1, still utilizing titanium Ti-6Al-4V, a tank thickness of $2.475E{-}3$ m with the 1.5 safety factor. Furthermore, Equations 8.2 and 8.3 yielded values of 0.00493 m and $0.001304m^3$ for change in radius and volume respectively. Thus, two of these thin tanks see negligible deformation and do not contribute excess unnecessary mass to the spacecraft.

8.2.3 Xenon Tanks

To maximize the amount of xenon aboard the Scuttle Mission, xenon propellant will be stored at the high pressure of 207 bar [69]. Through published studies from John-Hopkins University, the temperature of xenon at this pressure is approximately 75 °C [70]. The molecular mass of xenon is 131.293 u, which results in a density at given conditions of 934.269 $\frac{kg}{m^3}$. Using the definition of density as mass over volume and the knowledge that each tank needs to hold 1418.5 kg of xenon, the inner diameter determined using the volume of a sphere was found to be 1.426 m. From Equation 8.1, a maximum wall thickness of 0.0126 m is required to remain below the acceptable stress. Furthermore, Equations 8.2 and 8.3 yielded values of 0.002415 m and $0.015425 m^3$ for change in radius and volume respectively.

However, a perfect spherical tank of the mentioned dimensions constructed from Ti-6AL-4V weights 362.82 kg. This mass is too substantial for the Scuttle Mission spacecraft to meet its 3000 kg weight without Xenon. As a result, Scuttle Mission's xenon tanks will take inspiration from MT Aerospace AG Large Xenon Tank Assembly. These tanks house 1548 kg of Xenon with a maximum expected operating pressure of 177 bar [72]. Most noticeable, these tanks utilize an 0.8 mm thick titanium linear wrapped in a carbon fiber epoxy composite, which carries approximately 90% of the pressure load [72]. Thus, Carbon Fiber 230 GPa will be explored as the tank material. This material has modulus of 228 GPa, and maximum tensile yield stress of 4.5 GPa [71].

Due to the scale of the acceleration forces acting on the tank due to the launch, the large internal pressure, and the hard-point mounting method, a tank thickness of 23 mm of carbon fiber 230 GPa was analysed. This tank was modeled as $\frac{1}{4}$ of a spherical tank with physical constraints allowing for rest of the rank to go un-modeled. To create the shape, the internal and external boundary walls were drawing, revolved 90°. And that "solid" model was subsequently turned into a shell element using the mid-plane feature, resulting shape pictured in Figure 8.2.2.
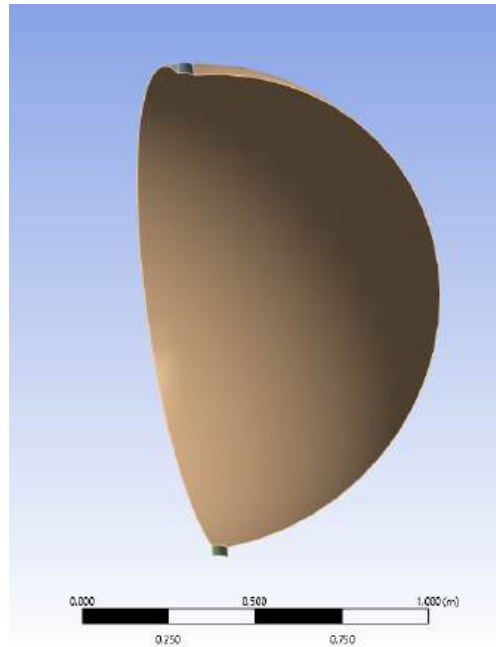
Figure 8.2.2: Quarter Spherical Mid-Plane Shape

To mesh this shape, a 1E-2 m uniform element size is used, resulting in 16583 nodes, and 16375 shell elements with 44 of the elements being TriShell3 and 16331 QuadShell4 elements. The resulting mesh is pictured in Figure 8.2.3. This is a zoomed top down down view focusing on shape of mesh.
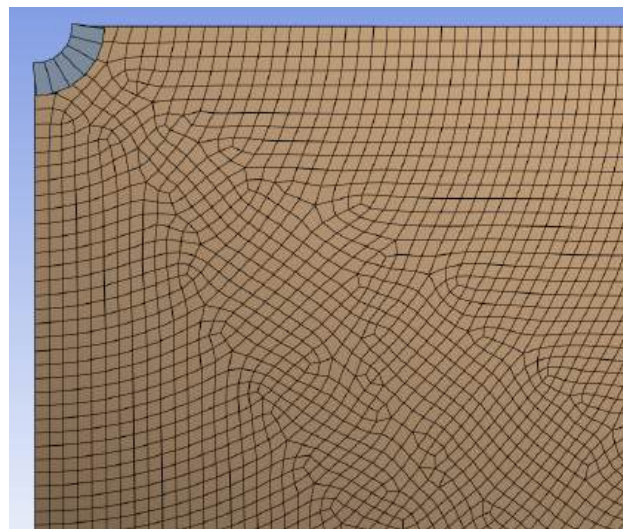

Figure 8.2.3: Antenna support definition and loading conditions.

For the first analysis with the 25 mm thick with, only a 207 MPa applied internal pressure was applied. The utilized boundary conditions can be seen in in Table (), and their exact locations within the quarter sphere color coded on Figure 8.2.4.

Table 8.2.1: Constraints and Corresponding Figure 8.2.4 Colors

Color	Displacement Constraint	Rotation Constraint
Orange	X-Displacment Fixed	X-Rotation Free
Yellow	Y-Displacement Fixed	[-]
Red	Z-Displacment Fixed	Z-Rotation Free
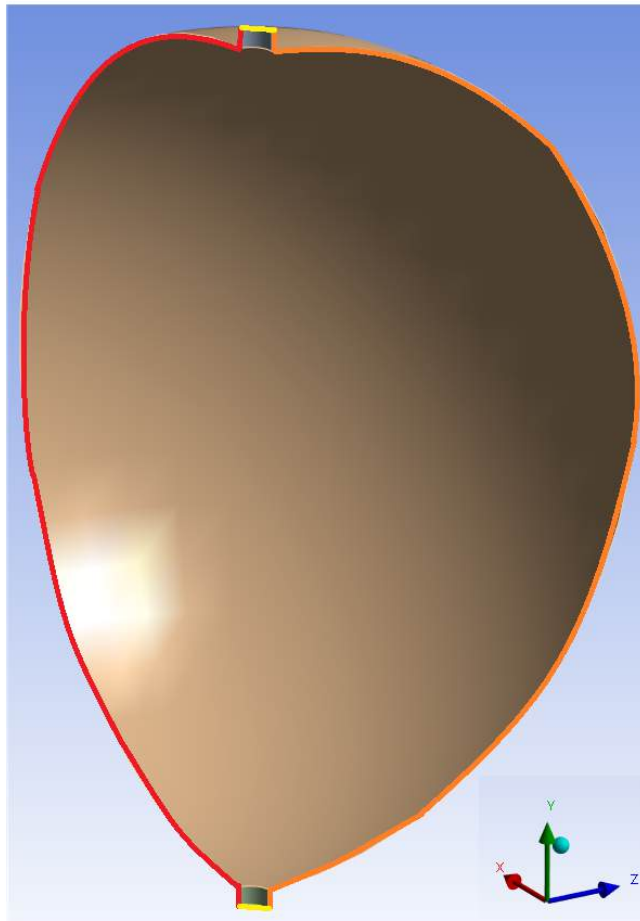
Figure 8.2.4: Boundary Conditions Color Coded.

Running a static structural model on this condition, the resulting stresses can be seen pictured in Figure 8.2.5. This image shows the tank on its side, not its usually positioning.
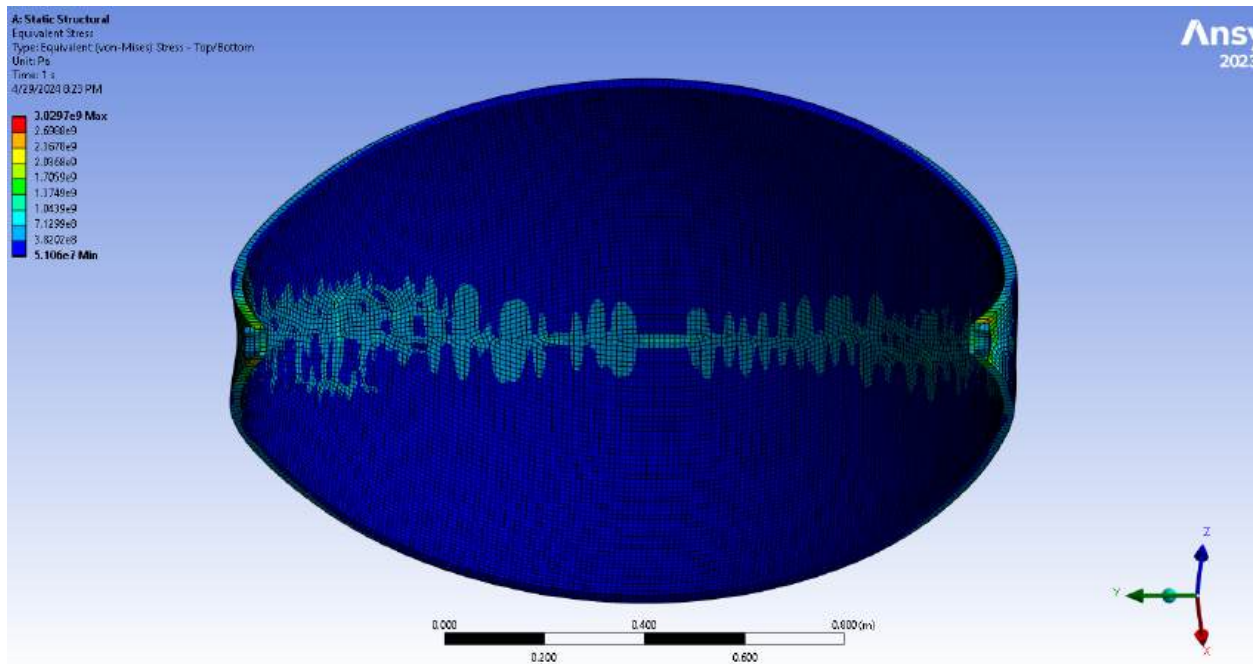
Figure 8.2.5: von Mises Stress on Spherical Vessel with due to internal pressure.

This ANSYS model will be compared with hand calculations to ensure accuracy of the entire process. One important note is that the hand calculations, which are based on Equation 8.1, assume that the tank is free to expand in all directions; however, this ANSYS model has the top and bottom lips (left and right sides in the above orientation) constrained, creating excess stress. With Equation 8.1, the stress for a internal radius of 0.713 m and a wall thickness of 0.023 m results in a hoop stress of 3.21E8. The stress in the ANSYS model peaks well above this value, but this stress is concentrated around the fixed ends. The lower stress values, between 5.106E7 and 3.82E8 fall well within an acceptable boundary that the hand calculations retrieved. Thus, the ANSYS model is appropriate to use to model this tank under additional applied conditions.

With the same mesh and boundary conditions, additional load conditions are applied. These conditions are in the form of a -Y acceleration of 78.48 $\frac{m}{s^2}$ and a +X acceleration of 29.43 $\frac{m}{s^2}$. Recalculating this model with the addition of acceleration along with the internal pressure, the new resulting stresses are shown in Figure 8.2.6.
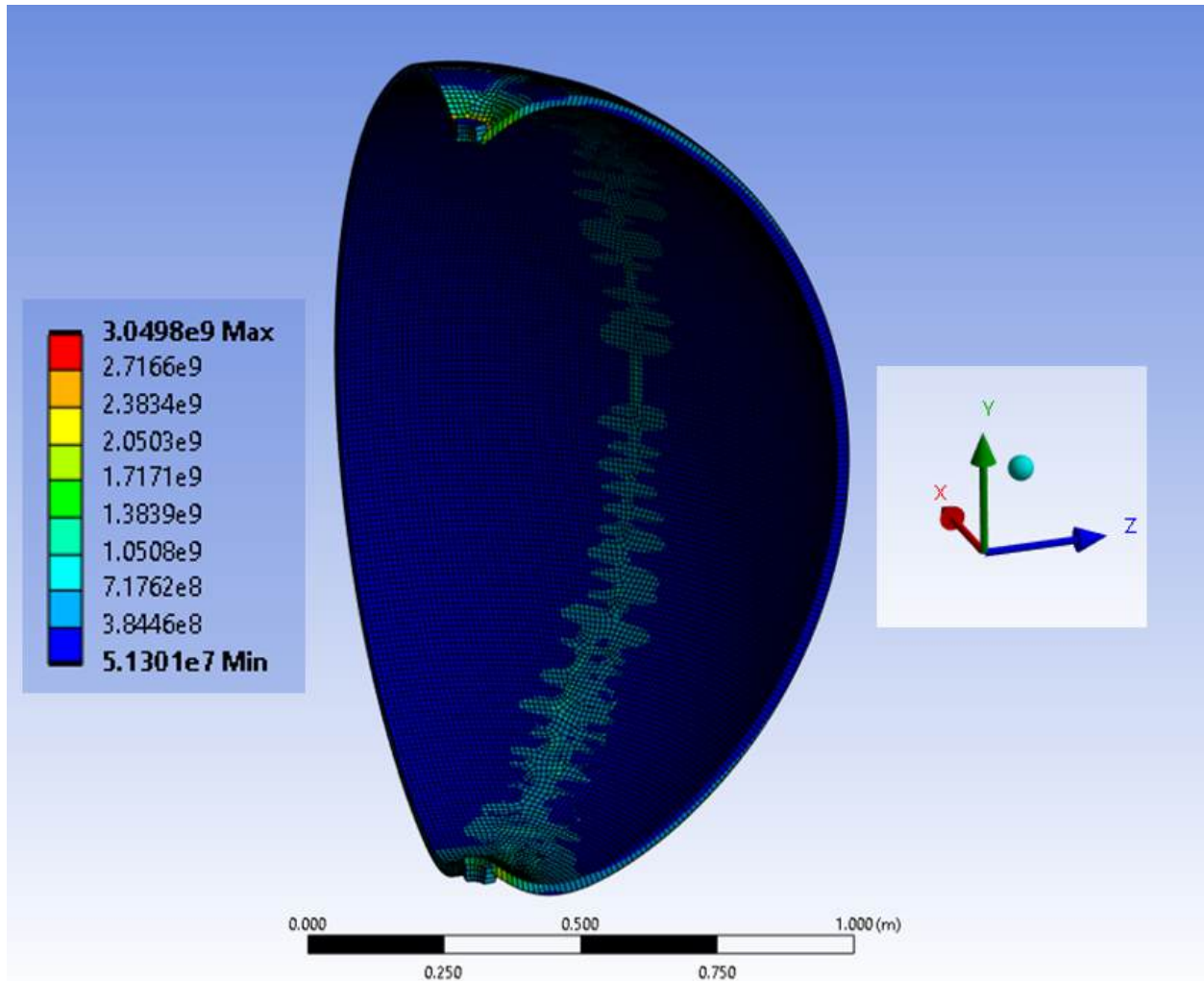
Figure 8.2.6: von Mises stress with acceleration load

From Figure8.2.6, it is seen that the maximum stress under this failure criterion method is 3.05E9 Pa, which results in a safety factor of 1.475. Concurrently, the resulting displacement plot in meters can be seen in Figure 8.2.7.
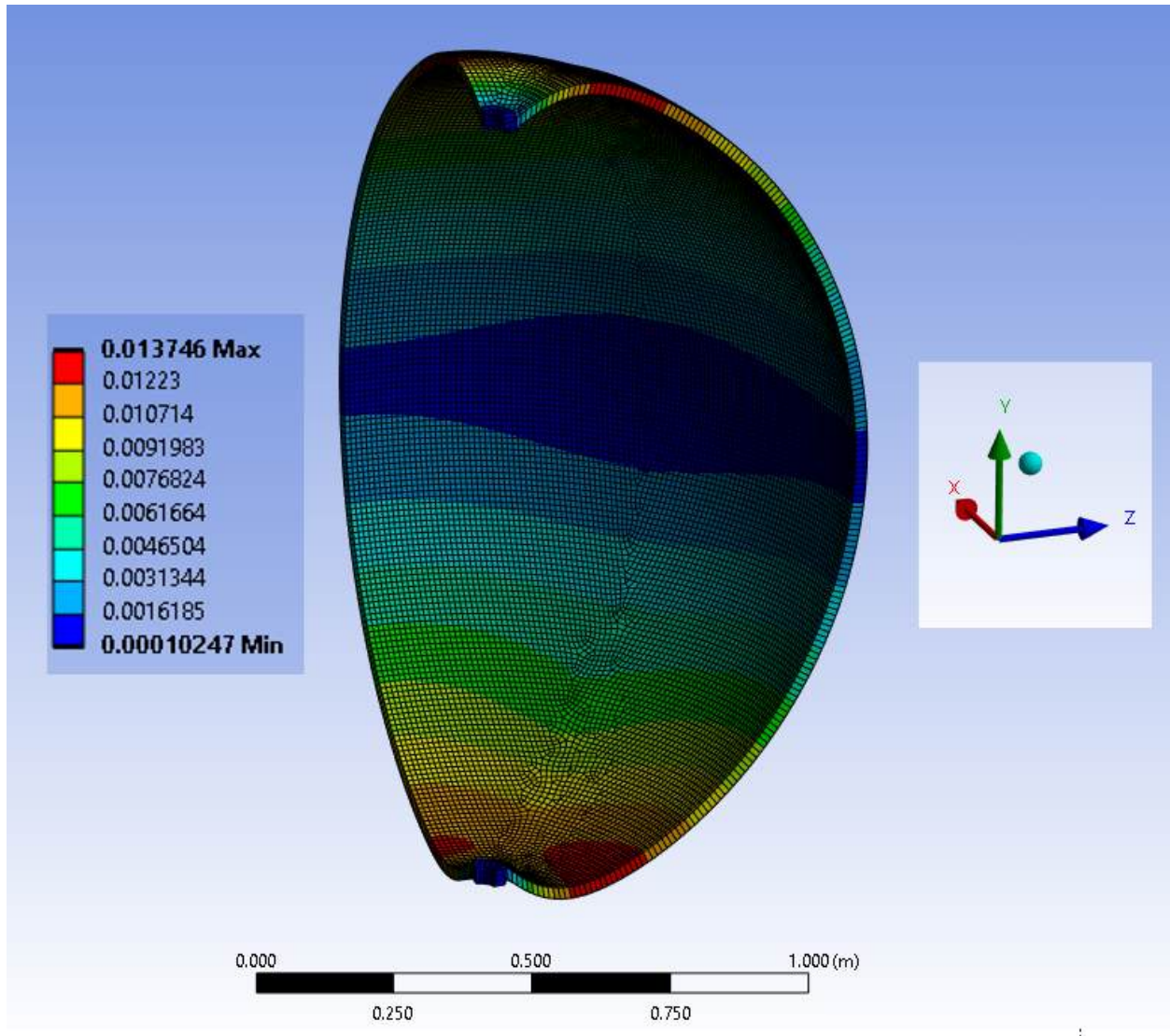
Figure 8.2.7: Absolute Displacement of tank in meters.

From this ANSYS generated figure, it can be seen that most displacement occurs near the upper top region denoted in red, with a displacement of 0.0137 m. Thus, the design needs to account for this displacement in all directions.

From this analysis, it is evident that a large tank under high pressure conditions can be made of carbon fiber and survive acceleration and pressure loads. With a new tank mass of approximately 150 kg instead of the approximately 360 kg tank when constructed from Ti-6AL-4V, the Scuttle Mission can save weight while also holding the required amount of xenon propellant. Thus, a carbon fiber tank with a radius of 0.713 m and a 0.023 m thickness will be used.

8.3 High Gain Antenna Supports

The uppermost structural members of the Scuttle Mission vehicle are the support beams that hold the high gain antenna (HGA). These supports were chosen to be in the shape of a tube with a constant inner and outer diameter. There are eight of these structural members, with pairs of two connected in a triangle as defined in Figure 8.3.1.

Figure 8.3.1: Scuttle Mark I: HGA Supports.

The height, h, was chosen to be 0.25 m to prevent the base of the dish from intersecting the upper section of the spacecraft. The material of choice for these supports is Al 6061-T6 to minimize the structural weight and provide sufficient rigidity to the HGA. The material properties of AL 6061-T6 are listed for reference in Table 8.3.1. The HGA has a mass of 14 kg as defined in Table 6.2.1, however a mass, m, of 20 kg was used for the analysis to include the additional instrumentation that is be mounted to the dish.

Table 8.3.1: Material Properties: Al 6061-T6 [73]

Property	Value	Unit
Young's Modulus (E)	68.9e3	MPa
Poisson's Ratio	0.33	-
Tensile Yield Strength	276	MPa
Shear Strength	207	MPa

Analysis of these structural members was computed purely to verify the results of the finite element model, as detailed in Section 8.5.3. Since this analysis is purely for verification purposes, only a single size and loading condition was considered for these supports. Rather than attempting to optimize the size of these supports by hand calculations, the following hand calculations were done to provide a level of confidence in the finite element model. Upon achieving an acceptable level of confidence, the size or cross section of any member within the model can be altered until the structure has been fully optimized to the 1.5 structural factor of safety, saving significant time and energy as opposed to quantifying the optimal size of each member analytically.

The tube size chosen for the supports in this analysis was taken from standard aluminum tubing sizes listed from the Continental Steel and Tube Company, and has an inner radius of 8.3 mm and an outer radius of 9.5 mm [75]. The loading condition and support definition is shown in Figure 8.3.2.
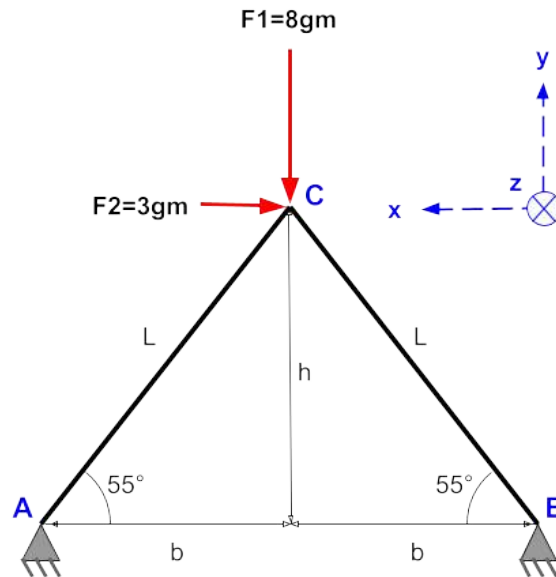

Figure 8.3.2: Antenna support definition and loading conditions.

The process by which analysis was conducted can be summarized as follows:

1. Use Newton's second law of motion and the method of joints to determine the forces within each structural member.
2. Determine the member that will carry a larger portion of the applied loads.
3. Compute the shearing force and bending moment experienced by this load-bearing member.
4. Determine the direction of the axial, bending and shear stresses, in addition to the location on the beam at which stress is maximum.
5. Calculate all stresses (axial, bending, shear) at the location of maximum stress.
6. Using the equations for Mohr's circle, determine the principal stresses.
7. Using the principal stresses, compute the von Mises stress.
8. Calculate the factor of safety using the yield and shear strengths of the material and compare it to the designated 1.5 factor of safety.

Before beginning the analysis, several parameters and equations can be defined for the system. The equations defining the stresses of the system are

$$\sigma_{axial} = \frac{F}{A}, \tag{8.5}$$

$$\sigma_{bending} = -\frac{My}{I}, \text{ and} \tag{8.6}$$

$$\tau_{shear} = \frac{VQ}{It} \text{ [74]}. \tag{8.7}$$

Torsion is neglected in this summary of the system stresses as the specified loading conditions do not create a torsional load on any of the members. Without a torsional load on the members and the absence of an external moment, the shear force due to torsion is nonexistent in this scenario. Several parameters within the preceding equations for stress can be directly computed from the chosen geometry. These parameters are calculated as

$$A = \pi(r_o^2 - r_i^2), \text{ and} \tag{8.8}$$

$$I = \frac{\pi}{4}(r_o^4 - r_i^4). \tag{8.9}$$

Recognizing that the system configuration is representative of a simple truss, the method of joints was applied. To determine the loads within each support, this method was applied at joint C as shown in Figure 8.3.3.
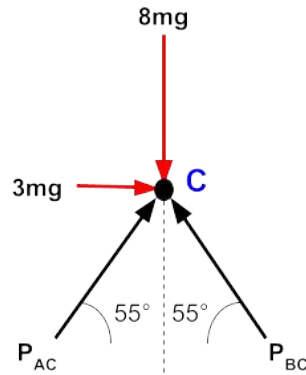
Figure 8.3.3: Force body diagram at joint C.

Utilizing Newton's second law for the static system, the sum of forces in the vertical (y) direction can be written

$$\sum F_y = 0 = -8mg + P_{AC}\sin\left(55°\right) + P_{BC}\sin\left(55°\right). \tag{8.10}$$

Doing the same for the forces in the horizontal (x) direction gives

$$\sum F_x = 0 = -3mg - P_{AC}\cos\left(55°\right) + P_{BC}\cos\left(55°\right). \tag{8.11}$$

Rearranging Equation 8.11 to solve for P_{BC} gives

$$P_{BC} = \frac{3mg + P_{AC}\cos\left(55°\right)}{\cos\left(55°\right)} = \frac{3mg}{\cos\left(55°\right)} + P_{AC}. \tag{8.12}$$

Substituting this expression back into Equation 8.10 gives the solution

$$P_{AC} = \frac{8mg - 3mg\tan\left(55°\right)}{2\sin\left(55°\right)} \text{ and therefore,} \tag{8.13}$$

$$P_{BC} = \frac{3mg\tan\left(55°\right) + 8mg}{2\sin\left(55°\right)}. \tag{8.14}$$

Comparing the values of P_{AC} and P_{BC}, it can be seen that the force within support BC is greater than that of support AC. The shear force experienced by support BC is equivalent to the component of the external loading perpendicular to the axial length of support BC. With this definition, the shear force, V, was determined to be

$$V = 3mg \sin\left(55°\right) - 8mg \cos\left(55°\right). \tag{8.15}$$

Imagining a cut within support BC, the forces acting on this beam are visualized in Figure 8.3.4 with the region at which stress was analyzed indicated by the dashed box.

Figure 8.3.4: Member BC internal force visual with analyzed stress region indicated.

Note that for the remainder of this analysis, the original coordinate system has been rotated 55° about the z-axis to define x' and y' axes in the axial and transverse directions relative to support BC to ease the stress calculation. At this location, the remainder of the parameters in Equations 8.5-8.7 can be determined. These values are

$$M = VL, \tag{8.16}$$

$$y = r_o, \tag{8.17}$$

$$Q = \frac{2}{3}(r_o^3 - r_i^3), \text{ and} \tag{8.18}$$

$$t = 2(r_o - r_i). \tag{8.19}$$

In this case, both the axial and bending stresses act in the x'-direction with the shear stress acting on the x' face in the y'-direction. Due to this, the location of maximum stress is in the upper-rightmost corner of the support as shown in Figure 8.3.4. Combining the loads gives the stresses as

$$\sigma_{x'} = \frac{F}{A} - \frac{My}{I} = \frac{P_{BC}}{\pi\left(r_o^2 - r_i^2\right)} - \frac{\left[3mg \sin\left(55°\right) - 8mg \cos\left(55°\right)\right]Lr_o}{\frac{\pi}{4}\left(r_o^4 - r_i^4\right)} = -51.28\,[MPa], \tag{8.20}$$

$$\sigma_y' = 0\,[MPa], \text{ and} \tag{8.21}$$

$$\tau_{x'y'} = \frac{VQ}{It} = \frac{\left[3mg \sin\left(55°\right) - 8mg \cos\left(55°\right)\right]\frac{2}{3}\left(r_o^3 - r_i^3\right)}{\frac{\pi}{2}\left(r_o^4 - r_i^4\right)\left(r_o - r_i\right)} = -3.11\,[MPa]. \tag{8.22}$$

Applying the equations for Mohr's circle gives the principal stresses as

$$\sigma_{1,2} = \left(\frac{\sigma_x + \sigma_y}{2}\right) \pm \sqrt{\left(\frac{\sigma_x + \sigma_y}{2}\right)^2 + \tau_{xy}^2} = 0.19\,[MPa],\ -51.47\,[MPa]\,[74], \qquad (8.23)$$

with a maximum shear stress of

$$\tau_{max} = \sqrt{\left(\frac{\sigma_x + \sigma_y}{2}\right)^2 + \tau_{xy}^2} = 25.83\,[MPa]. \qquad (8.24)$$

With the principal stresses computed, the von Mises stress can be determined. This equivalent stress was calculated to be

$$\sigma_{vM} = \sqrt{\sigma_1^2 - \sigma_1\sigma_2 + \sigma_2^2 + 3\tau_{max}^2} = 68.26\,[MPa]. \qquad (8.25)$$

The factor of safety was calculated based off the von Mises stress, resulting in

$$FS = \frac{Tensile\,Yield\,Strength}{\sigma_{vM}} = \frac{276\,[MPa]}{68.26\,[MPa]} = 4.04\,[-]. \qquad (8.26)$$

Table 8.3.2: Antenna Support Analysis Summary

$R_o[mm]$	$R_i[mm]$	$\sigma_{vM}[MPa]$	FS [-]
9.5	8.3	68.26	4.04

8.4　ASRG Supports

The Scuttle Mission spacecraft utilizes four advanced stirling radioisotope generators (ASRGs) to provide the spacecraft with the necessary power to complete the mission. Due to the large power requirements, these generators are quite large in both mass and size, requiring a strong support for mounting and rigidity during launch. These supports were chosen to be titanium tubes with a constant inner and outer diameter. Titanium was chosen to minimize the amount of material that would be required to provide structural support to the ASRGs as the length of the Scuttle Mission spacecraft already nears the maximum width of the launch vehicle payload bay with the ASRGs and vehicle body width. The material properties can be found in Table 8.4.1 for Ti-6Al-4V (Grade 5).

Property	Value	Unit
Young's Modulus (E)	113	GPa
Poisson's Ratio	0.342	-
Tensile Yield Strength	880	MPa
Shear Strength	550	MPa

There are four of these structural members, each holding a single ASRG as shown in Figure 8.4.1. The length of these supports was chosen to be 0.10 m to fit within the launch vehicle payload bay and the ASRGs have a total length of 1.2 m. The ASRGs are held in this way to provide clearance for an extending boom that surrounds this support and provides no structural support. These supports are mounted both by extending into crossing members within the body of the spacecraft and are welded to the exterior body. Each ASRG has a mass of 250 kg as defined in Table 6.2.1. This analysis was completed as a method of verification for the coming sections that utilize finite element analysis.
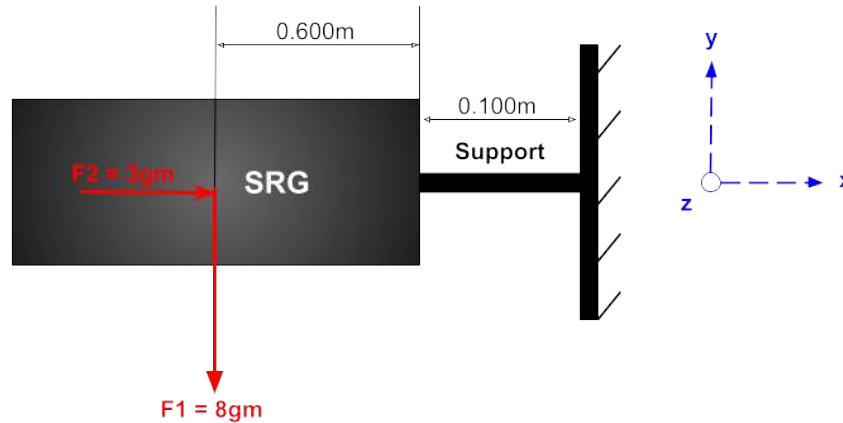
Figure 8.4.1: ASRG support definition and loading conditions.

To consider all of the possible loading conditions a single support can experience, two cases were defined as shown in Figures 8.4.2 and 8.4.4. These cases consider different orientations of the axial load defined in Section 8 and translates the forces from the ASRG to the end of its structural support. In doing this, the xyz coordinate system remains consistent. The process by which analysis was conducted can be summarized as follows:

1. Determine the forces (F_x) and (F_y) that coincide with the total force acting in the x - and y - direction respectively.
2. Determine the direction of the axial, bending and shear stresses, in addition to the location on the beam at which stress is maximum.
3. Define an inner and outer radii to run calculations.
4. Calculate all stresses (axial, bending, shear) at the location of maximum stress.

5. Using Mohr's circle, determine the principal stresses.
6. From the principal stresses, utilize the von Mises failure criterion to determine the von Mises equivalent stress.
7. Calculate the factor of safety using the von Mises equivalent stress and compare it to the designated 1.5 factor of safety.
8. Repeat from step 3 for all cases, until any case gives a factor of safety near 1.5. The calculated factor of safety must be at least 1.5 for all cases simultaneously to prevent yielding.

Case I defines the axial load in the positive x-direction, and the translated loads onto the end of the support beam for this case are shown in Figure 8.4.2.
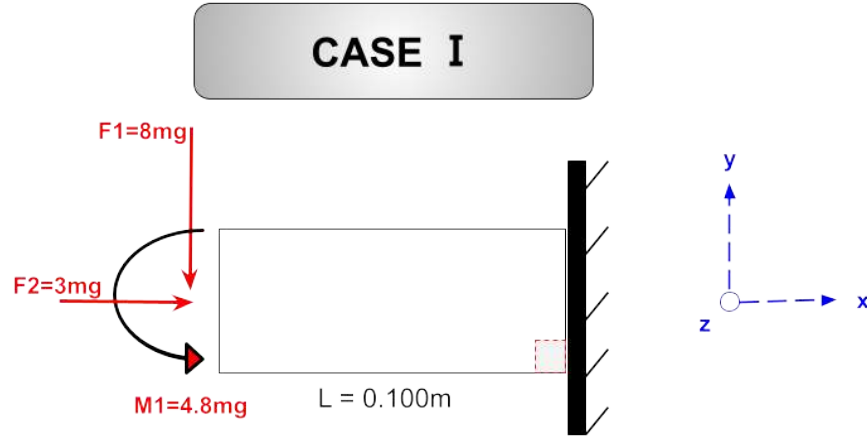
Figure 8.4.2: Loading Case 1: SRG support beam analysis

The equations and parameters defining the stresses remain consistent with Equations 8.5 - 8.9. In this first case, both the axial and bending stresses act in the x-direction with a shear stress acting on the x face in the y-direction. Due to this, the location of maximum stress is the lower-rightmost corner of the support in the orientation as indicated in Figure 8.4.2. At this location, the remainder of the parameters in Equations 8.5-8.7 can be determined. These values are

$$M = F_1 L, \tag{8.27}$$

$$y = r_o, \tag{8.28}$$

$$Q = \frac{2}{3}(r_o^3 - r_i^3), \text{ and} \tag{8.29}$$

$$t = 2(r_o - r_i). \tag{8.30}$$

The stress at this location is compressive for each of these loads, and combining the loads from Case 1 gives the stresses as

$$\sigma_x = -\frac{F_2}{A} - \frac{F_1 L y}{I} - \frac{M_1 y}{I}, \tag{8.31}$$

$$\sigma_y = 0, \text{ and} \tag{8.32}$$

$$\tau_{xy} = \frac{F_1 Q}{It}. \tag{8.33}$$

Using these stresses, the principal stresses were computed using Equation 8.23 and the maximum shear with Equation 8.24. Upon calculating these values, the von Mises failure criterion was applied with Equation 8.25, which allowed the factor of safety to be determined with Equation 8.26.

The factors of safety were computed for various tube sizes. Table 8.4.2 lists the standard titanium tube sizes considered for the purposes of this analysis, with its corresponding index.

Table 8.4.2: Standard tube sizes used for analysis [76]

Index	R_o [mm]	R_i [mm]
1	31.75	30.861
2	38.10	37.211
3	44.45	43.561
4	50.80	49.911
5	57.15	56.261
6	63.5	62.611
7	69.85	68.961
8	76.20	75.311
9	82.55	81.661
10	88.90	88.011
11	95.25	94.361
12	101.60	100.711
13	107.95	107.061
14	114.30	113.411

A plot of the factors of safety that were determined for each size (listed by index) is shown in Figure 8.4.3 summarizing the results of the Case I analysis.
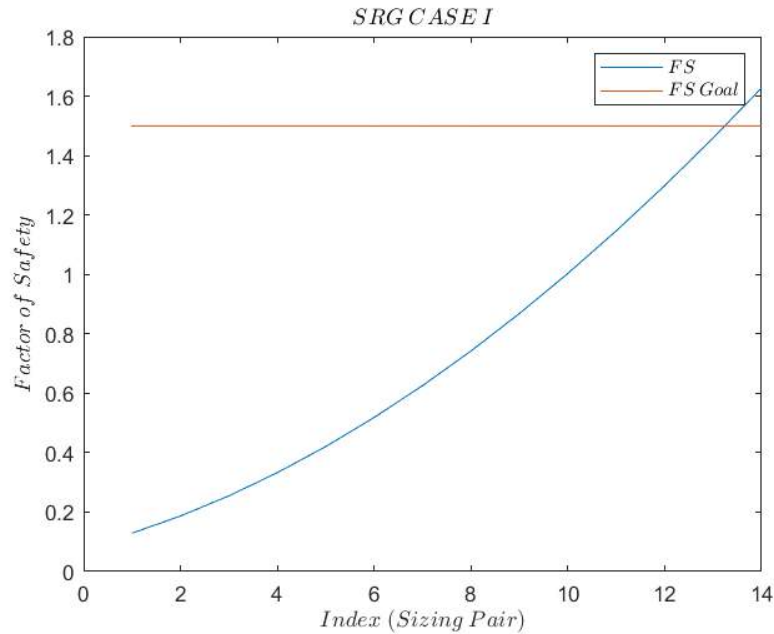
Figure 8.4.3: ASRG Loading Case 1: FS for increasing tube sizes

Case II defines the axial load in the positive z-direction, and the translated loads onto the end of the support beam for this case are shown in Figure 8.4.4.
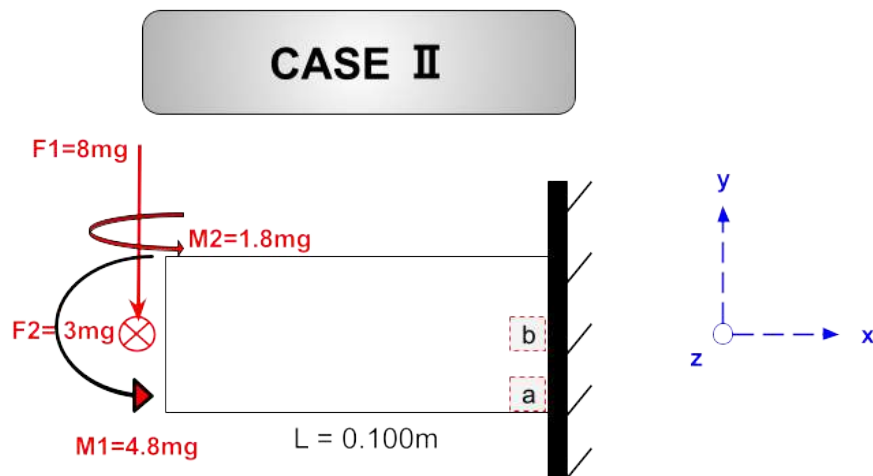

Figure 8.4.4: Loading Case 2: SRG support beam analysis

Both the axial and bending stresses act in the x-direction with shear stresses acting on the x face in both the y-direction and z-direction. Due to the loads, the location of maximum stress is at either (a) the upper-rightmost corner of the support or (b) the middle-rightmost portion of the support as indicated in Figure 8.4.2. The bending stress due to the shear force, F_1, and moment M_1 give location (a) as a region of local maximum stress, but they

do not contribute to the stress at location (b). The opposite is true for the bending stress due to the shear force, F_2, and moment, M_2. This is better visualized in Figure 8.4.5.
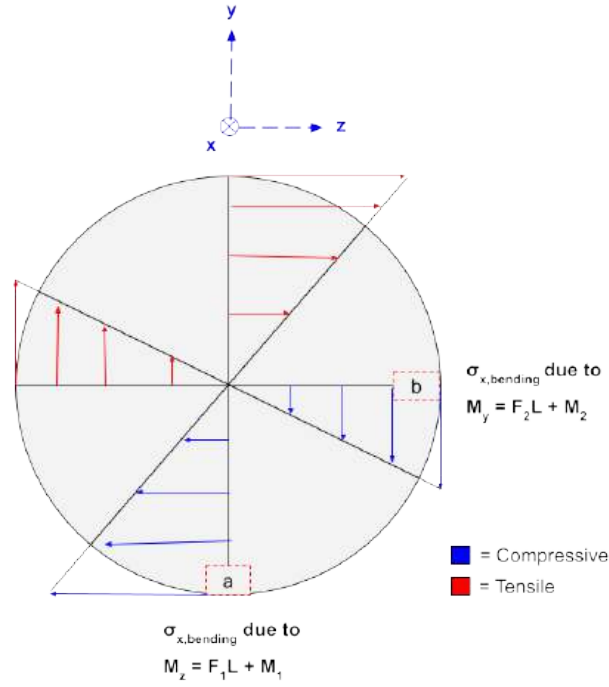
Figure 8.4.5: Case II bending stress over cross-section of ASRG support

Upon calculating the stresses at both locations (a) and (b), it was found that the region of absolute maximum stress occurs at location (a). Combining the loads from Case 2 at this region of maximum stress gives the stresses as

$$\sigma_x = -\frac{M_1 y}{I} - \frac{F_1 L y}{I}, \tag{8.34}$$

$$\sigma_y = 0, \text{ and} \tag{8.35}$$

$$\tau_{xy} = \frac{F_1 Q}{It}. \tag{8.36}$$

The analysis process previously outlined for Case I was repeated for this stress state with the factors of safety computed for the same tube sizes. A plot of these factors of safety is shown in Figure 8.4.6 summarizing the results of this analysis.
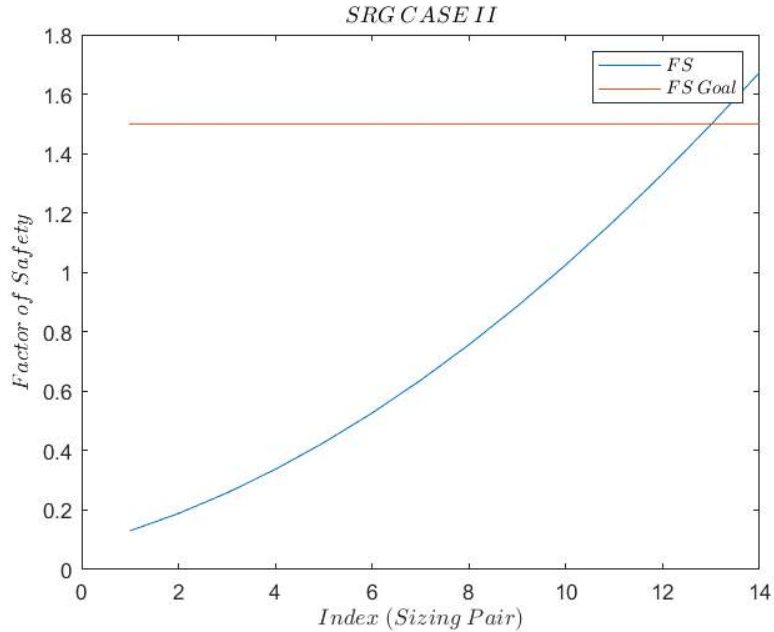
Figure 8.4.6: ASRG Loading Case 2: FS for increasing tube size

In processing the results of Case I and II, the first case contains the lowest factors of safety for each size, even though both were quite similar. The tube size chosen to support the ASRG is summarized in Table 8.4.3 with the corresponding von Mises stresses and factors of safety for each loading case. This size was chosen to adhere as closely to the required 1.5 factor of safety as possible while remaining above this value and minimizing mass.

Table 8.4.3: ASRG Support Analysis Summary

$R_o[cm]$	$R_i[cm]$	Case I FS	Case II FS	Case I σ_{vM} [MPa]	Case II σ_{vM} [MPa]
11.43	11.34	**1.628**	1.673	**540.64**	525.96

8.5   Structural Frame

The Ariel Voyagers analyzed the rest of the structural frame using a finite element model. To verify that the results from the element model were accurate, the finite element results were compared to the general magnitudes of max stresses found in the calculations carried out in the High Gain Antenna Supports (Section 8.3) and ASRG Supports (Section 8.4) sections. Once these comparisons were confirmed, then the solution to the finite element model could be trusted to compute cross-sectional area and geometry in order to satisfy the defined structural factor of safety.

The finite element model is simplified by incorporating point masses for the equipment aboard the satellite. Other simplifications made to simulate the rigid nature of the main

(xenon) tanks are also included and discussed in a more in-depth manner later in this section.

The analysis was initially ran with the general shape of the old model before it was updated to the final draft. Some of the designs thought be practical before building the final model in Solidworks were scrapped because of the infeasibility. Since the process was the same for the old finite element model and the updated one, the last section of the structural analysis (Section 8.5.5) just verifies that the old cross sections work on the newer design. The dimensions of these cross sections were not adjusted to minimize material while bringing the factor of safety close to 1.5, like the initial analysis does.

8.5.1 Geometry and Model Properties

The finite element model was built in Ansys Mechanical APDL. To start, the geometry of the model was created by extracting the points of the structure frame from a SolidWorks model of the preliminary structure. These points all shared the same coordinate system, with lengths being defined in millimeters. The lines were simply defined by listing which two keypoints the end segments were connected to. The points and lines of the model were stored in a CSV file for easy extraction and altercation for potential modifications. Figure 8.5.1 shows how the XYZ coordinate system is defined, along with all the keypoints and lines that were made to populate the structure.
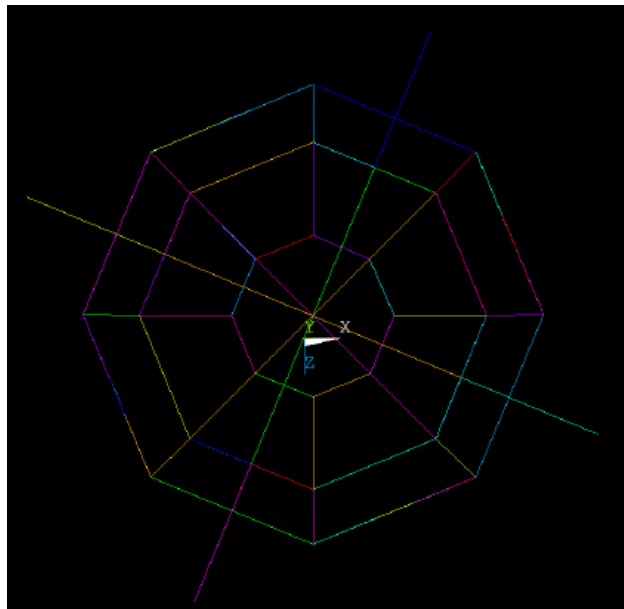
(a) XZ Plane
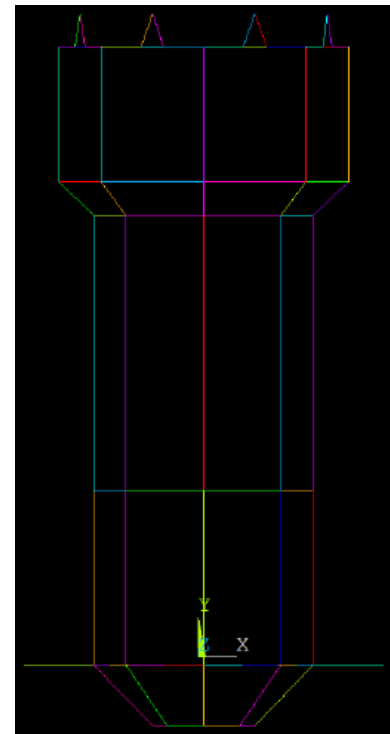
(b) XY Plane

Figure 8.5.1: Showing FEA Coordinate System and Plotted Lines.

Since millimeters was the unit of choice for distance, that determined the rest of the unit system to follow for APDL. The unit system is a FEA consistent unit system that follows a guideline so there are no errors when entering them into the model. This unit system has main units defined in Table 8.5.1.

Table 8.5.1: Units used in the FEA

Property	Unit
Mass	tonne
Length	mm
Time	s
Temperature	K
Velocity	mm/s
Acceleration	mm/s^2
Force	N (Newtons)
Moment	N*mm
Pressure	MPa
Density	tonne/mm^3

The relevant material properties of the two selected materials, Al 6061-T6 and Ti-6Al-4V are listed in Tables 8.5.2 and 8.5.3.

Table 8.5.2: Material Properties: Al 6061-T6 [73]

Property	Value	Unit
Young's Modulus	68.9e3	MPa
Density	2.7e-9	tonne/mm^3
Poisson's Ratio	0.33	-
Tensile Yield Strength	276	MPa

Table 8.5.3: Material Properties: Ti-6Al-4V (Grade 5) [66]

Property	Value	Unit
Young's Modulus	113e3	MPa
Density	4.506e-9	tonne/mm^3
Poisson's Ratio	0.342	-
Tensile Yield Strength	880	MPa

Instead of creating objects for the equipment, the Ariel Voyagers decided to utilize point masses on the model where the payloads are mounted to the structural frame. This includes both tank types, camera and sensor equipment, the high gain antenna, reactors,

and thrusters. These point masses were calculated and are sorted in Table 8.5.4. The mass values in Table 8.5.4 are the masses of the singular meshed node only, not a combined total. Some point masses were distributed along four symmetrical points where the frame is connected to the equipment, like the antenna supports and the two xenon tanks.

Table 8.5.4: Point Masses Information

Component Name	Constant #	Coordinates (mm)	Mass (tonne)	# of Points
High Gain Antenna	No. 1	(961, 4796, -494.5)	0.005	4
		(422.5, 4796, 805.5)		
		(-877.5, 4796, 267)		
		(-339, 4796, -1033)		
Gyroscope Platform	No. 2	(961, 4043.5, -494.5)	0.030	1
Cameras & Sensors	No. 3	(-877.5, 4043.5, 267)	0.200	1
Thrusters (3)	No. 4	(40, -509, -107)	0.0405	3
		(548.25, -284, 103.5)		
		(-468.25, -284, -317.25)		
Reactors (4)	No. 5	(594.8, -59, -1446.0)	0.250	4
		(-1299.7, -59, -661.8)		
		(-514.8, -59, 1232.5)		
		(1379.7, -59, 447.8)		
Xenon Tanks (2)	No. 6	(852, 1241, -107)	0.400	8
		(40, 1241, -918)		
		(-772, 1241, -107)		
		(40, 1241, 705)		
		(852, 3291, -107)		
		(40, 3291, -918)		
		(-772, 3291, -107)		
		(40, 3291, 705)		
Hydrazine Tanks (2)	No. 7	(-534, 2266, 467)	0.045	2
		(614, 2266, -681)		

To complete the geometry of the structure, Beam 189 elements were used to create the main structure; these were preferred from Beam 188 elements, because the structure experiences bending, which creates nonlinear deformations. Shell 281 elements were used with a 3 mm thickness (defined in the mid-plane) as the shielding for the satellite; these elements give an accurate representation of thin structures. Shielding was added to simulate the connection points when components were not directly connected to the outer frame structure. The model has 9,262 total elements with 24,216 total nodes.

The focus of the meshing was to fine tune the base of the structure, where the points of failure are most likely to occur. This was done with mesh sizing controls, specifically manual sizing where the length of each element was defined to be 50 mm in most areas. The top of the structure was not adjusted, because these areas are not as close to failure

considering the magnitude of loads experienced. The fully meshed model is seen in Figure 8.5.2a, the refined mesh area is shown in more detail in Figure 8.5.2b.
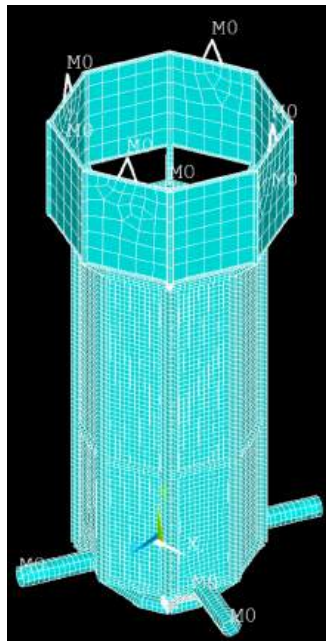

(a) Fully meshed FE model
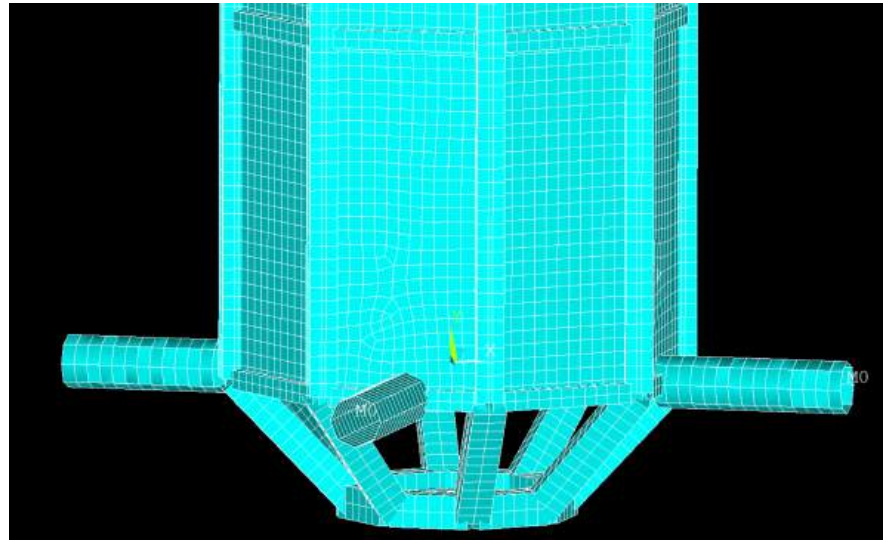
(b) Bottom view of structure, showing refined mesh

Figure 8.5.2: Meshed beam and shell elements, forming complete FE model.

Two main simplifications were made in the model. The first is how the xenon tanks were incorporated into the model. Instead of building the tanks in the model, two cross beams at the approximate two levels of where the tanks are to be supported by the frame were used to simulate the stiffness that the tanks provide to the overall structure. A separate FE model was used to estimate the stiffness of each xenon tank to determine the size of the beam cross sections. Figure 8.5.3 shows the Ansys Workbench model setup and solution, where a 1 N force was applied to the top of the xenon tank. Titanium material properties were used with a surface body geometry.
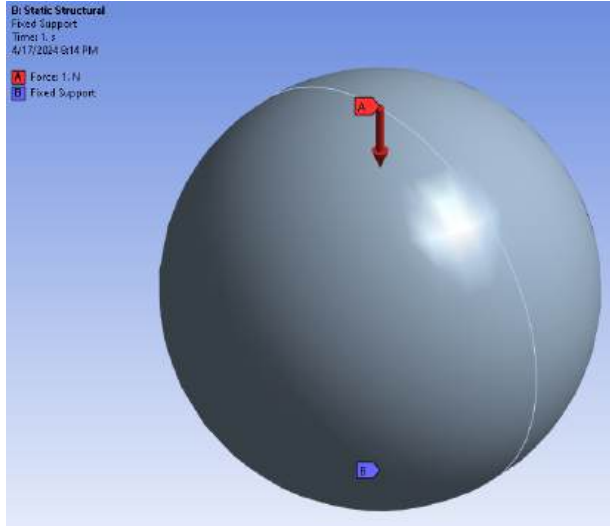
(a) Boundary conditions of FE xenon model
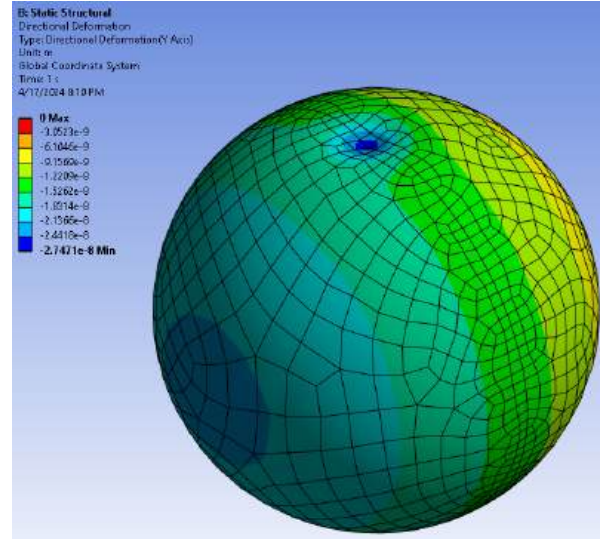
(b) Directional deflection in the vertical direction (in m)

Figure 8.5.3: FE Model of xenon tank for stiffness estimation.

From Figure 8.5.3b, the maximum deflection in the vertical direction is seen to be 2.7471e-8 m. The approximate stiffness is solved for using

$$k_{eq} = \frac{F}{x} = \frac{1[\text{N}]}{2.7471e-8[\text{m}]} = 36.4e6 \left[\frac{\text{N}}{\text{m}}\right].$$

(8.37)

The two beams that act as one xenon tank are modeled as springs in parallel. Their stiffness values are solved for assuming they are simply supported beams. The equation,

$$k_{eq} = \frac{48EI}{L^3},$$

(8.38)

where E is Young's Modulus of Al-6061, I is the moment of inertia of the beam cross section, and L is the total length of the beam, shows the relationship between stiffness and the properties of a simply supported beam. The moment of inertia of a square cross section is

$$I = \frac{l^4}{12}.$$

(8.39)

where l is the side length for the square cross section. The stiffness of both beams are added together, because they are in parallel, giving the team a relation for the side length

$$l = \left[\frac{L^3 k_{eq}}{2E}\right]^{\frac{1}{4}} = \left[\frac{1.624^3 * 36.4e6}{2 * 68.9e9}\right]^{\frac{1}{4}} = 183.4[\text{mm}],$$

(8.40)

The beams representing the tanks are shown in Figure 8.5.4; these beams were not analyzed, since they are just a placeholder for the tanks. The point masses for the tanks are applied where these beams meet the vertical support beams.

Figure 8.5.4: Xenon Tanks in FE model

The second simplification is the simplified shape of the I-beam on the vertical beams. In the CAD model, the I-beam is angled to define the corners of the structure and to be symmetric about the center. The location of the I-beams in the model can be seen in Figure 8.5.13b. The basic shape of this I-beam is shown in Figure 8.5.5. In the FE model, a regular I-beam is utilized, seen in Figure 8.5.6.
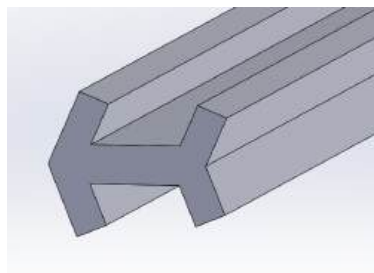
Figure 8.5.5: CAD I-beam
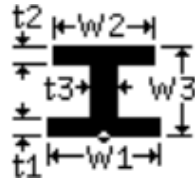
Figure 8.5.6: FE model I-beam [77]

8.5.2 Solution Approach

The solution desired for the Scuttle Mission only involves a static structural solution, where the maximum loading case is to take place on the mission: during launch. These maximum launching loads are defined at the beginning of Section 8, and are as follows: a vertical acceleration of $8\,g$ and axial acceleration of $3\,g$.

To solve in APDL, the team used a static solution where there were four distinct boundary conditions defined in coordination with the applied maximum global accelerations. The boundary conditions only fixed the displacements of the selected four nodes at the base of the structure where the middle thruster attaches to. Figure 8.5.7 shows the location on the model where these nodes are fixed. They are on the far points of the octagonal shape, where the satellite is to be mounted in the launch vehicle.
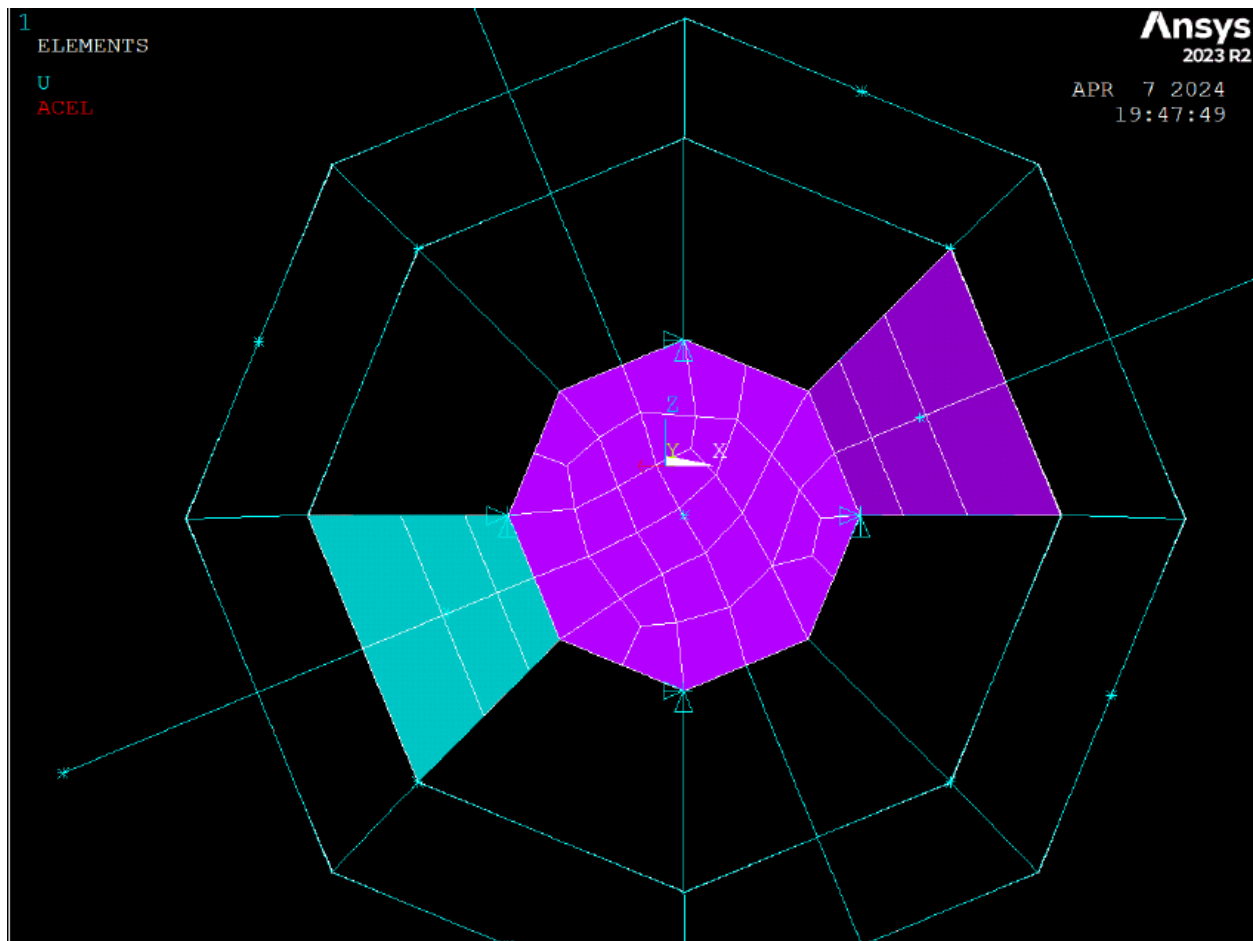
Figure 8.5.7: Bottom view of applied boundary conditions and global accelerations

The maximum accelerations were computed to be -78,480 mm/s^2 in the y-direction and 29,430 mm/s^2 in the x-direction. The signs of these accelerations were flipped and the lateral acceleration was also put on the z-axis, but the results did not change in any significant way. Therefore, this analysis does not distinguish between the different cases defined in Sections 8.3 and 8.4, meaning the direction of the lateral acceleration is always in the positive x-direction throughout the FE analysis.

The next step to verifying that the results of the analysis are correct is to verify the reaction solution in the model. Since only global accelerations were applied to the model, the total mass multiplied by the acceleration component should add up to the total reactions displayed by the model. Since the cross section geometry was changed in Section 8.5.4 (Full Analysis), the calculation shown below occurred after these changes were made.

Summing up all the point masses from Table 8.5.4 provides a value of 4.6615 tonne. The mass of the structure frame through the analysis is 0.7038 tonne. The total mass is simply the sum of these two values, which is 5.365 tonne. This means the expected reaction forces should be

$$F_{R,x} = -3 * g * m_{total} = -3 * (9810[\text{mm/s}^2]) * (5.365[\text{tonne}]) = -158e3[\text{N}], \text{ and} \quad (8.41)$$

$$F_{R,y} = 8 * g * m_{total} = 8 * (9810[\text{mm/s}^2]) * (5.365[\text{tonne}]) = 421e3[\text{N}]. \quad (8.42)$$

The sum of the reaction forces after the solution was ran gave identical values in the analytical model, seen in Figure 8.5.8.

```
PRINT F    REACTION SOLUTIONS PER NODE

***** POST1 TOTAL REACTION SOLUTION LISTING *****

LOAD STEP=      1   SUBSTEP=      1
   TIME=   1.0000        LOAD CASE=    0

THE FOLLOWING X,Y,Z SOLUTIONS ARE IN THE GLOBAL COORDINATE SYSTEM

   NODE        FX             FY             FZ
   25195   0.12989E+006  0.54889E+006  -17421.
   25208  -0.16284E+006  0.10326E+006  -25144.
   25232     38475.     -0.33402E+006  -16392.
   25256  -0.16342E+006  0.10294E+006   58958.

TOTAL VALUES
VALUE  -0.15790E+006  0.42107E+006  0.11089E-004
```

Figure 8.5.8: Sum of reactions in the FEA model

8.5.3 Comparison to Analytical Solution

This section compares results of the FE analysis to the results of the analytical solution completed in Section 8.3 and Section 8.4. The purpose of this comparison is to provide a validation of the full results of the FE model, meaning that the results not calculated analytically can be assumed to be accurate without the support of an analytical solution.

The mesh was refined at the supports for the high gain antenna and the von Mises stress solution was plotted with the supports isolated. The maximum value found through the model was 63 MPa. To compare, the factor of safety is solved for using

$$\text{FS} = \frac{\sigma_{yield}}{\sigma_{model}} = \frac{276[\text{MPa}]}{63[\text{MPa}]} = 4.38[-]. \quad (8.43)$$

Comparing this result to the value solved for in Section 8.3, the model factor of safety is about 8.5% greater than that found from hand calculated analysis. For reference, the von Mises stress calculated in the hand calculations was 68.26 MPa, which resulted in a factor of safety of 4.04. The close proximity of these calculations provides a general level of confidence in the finite element model. Figure 8.5.9 shows one of the supports that possessed the maximum stress value in the loading condition.
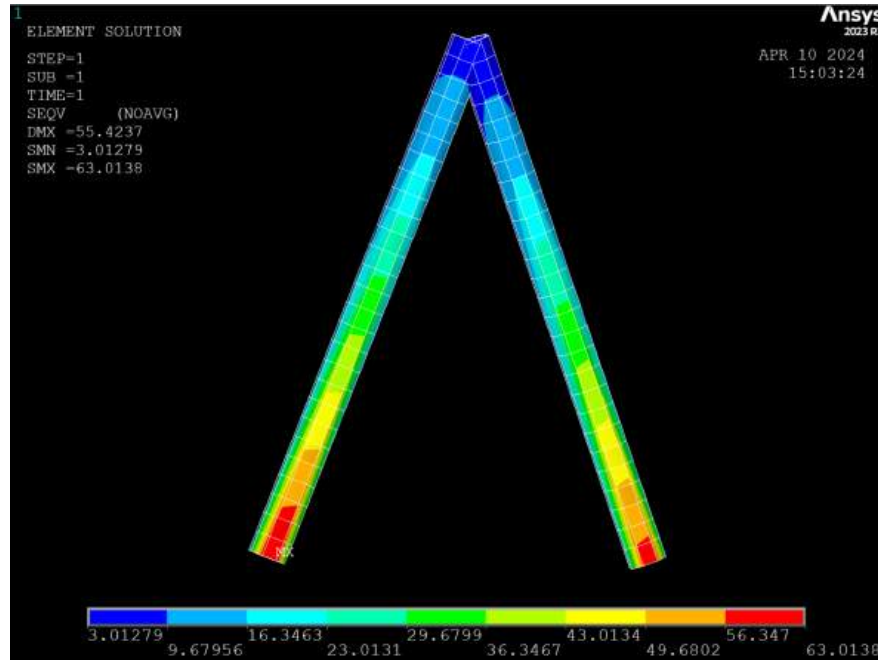
Figure 8.5.9: FE model of stresses at the antenna supports, in MPa

To raise the level of confidence in the finite element model even further, the team compared the model results to an analytical solution for the four symmetrical beams that connect the reactors to the main frame. These are 100 mm bars in the actual model but are extended out to the ASRGs center of mass in the FE model; they are seen in Figure 8.5.10. The maximum stress seen by the model is 558 MPa, which correlates closely with the analytically calculated result of 540 MPa found in Section 8.4 This percentage difference is slightly more than three percent, which further supports the FE model. The RTG supports are made of titanium so they possess a maximum stress value of 880 MPa, from Table 8.5.3. To find the factor of safety, the team uses the equation

$$\text{FS} = \frac{\sigma_{yield}}{\sigma_{model}} = \frac{880[\text{MPa}]}{558[\text{MPa}]} = 1.58[-] \tag{8.44}$$
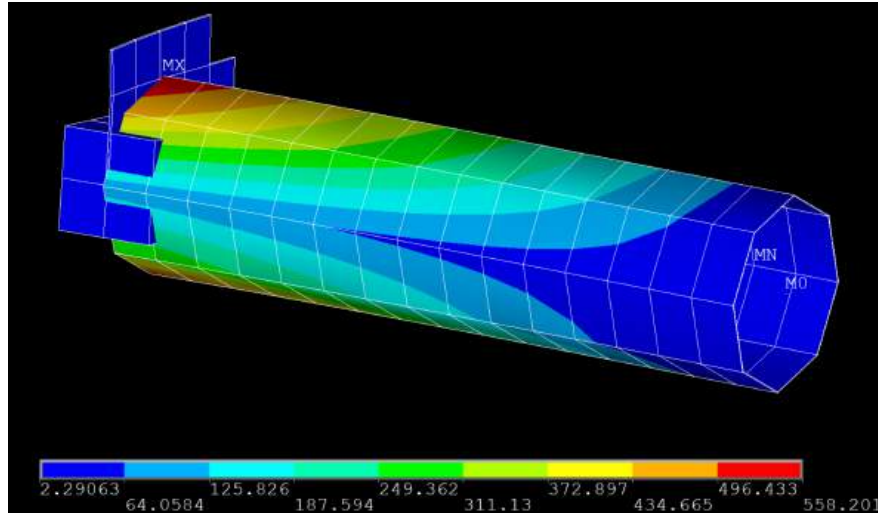
to get an answer of 1.58.

Figure 8.5.10: FE model of stresses at ASRG supports, in MPa

The conclusion made from these comparisons is that the rest of the results discussed in Section 8.5.4 are valid and can be assumed to be accurate without the support of an analytical solution.

8.5.4 Full Results

The rest of the model was analyzed in a repetitive process where the cross sections of the beams were changed to achieve the desired factor of safety, while minimizing the total mass of the structure. One example with corresponding figures is shown for the bottom of the structure, and the same process is repeated for every beam cross section that is defined. The final shapes and sizes of each cross section are summarized in Table 8.5.5.

There are seven distinct beam cross sections in the model. Figure 8.5.11 shows the FE model without any of the shell elements (shielding) to paint a clearer picture and for reference when each individual cross section is called out.
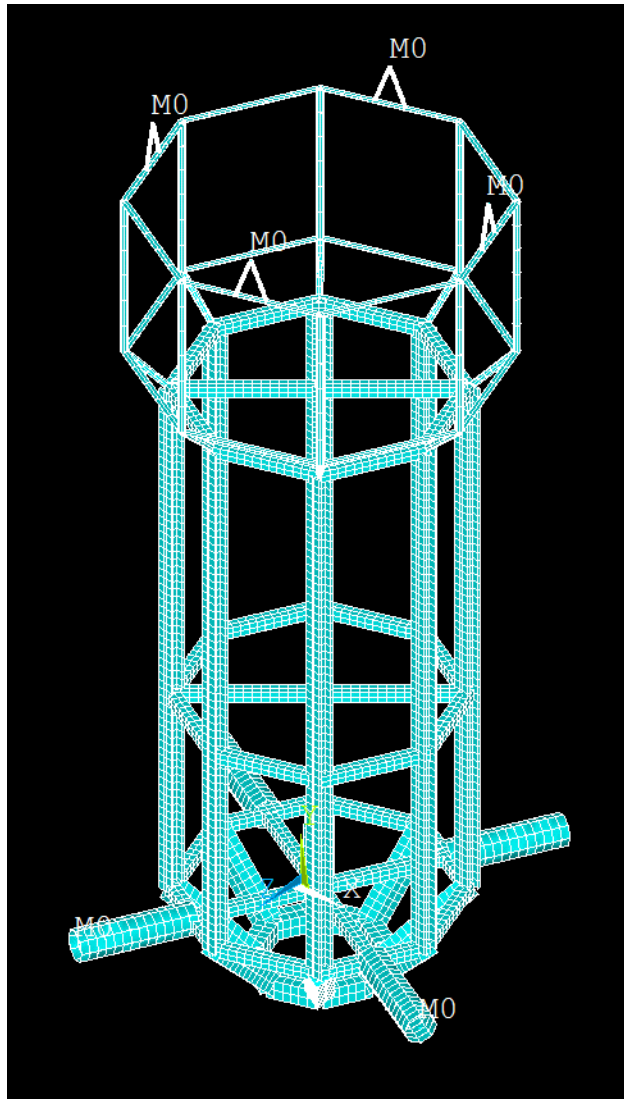
Figure 8.5.11: FE model without shielding

The first cross section to define is the bottom (cross section no. 1) of the structure. The main bottom plate is where the middle thruster is mounted to. The bottom structure includes the widening of the main frame, using the same rectangular cross sections. Figure 8.5.12 details what this cross section looks like in the modeling software. The orientation of these members do not change stress values in a significant way; therefore they were left in the default orientation.
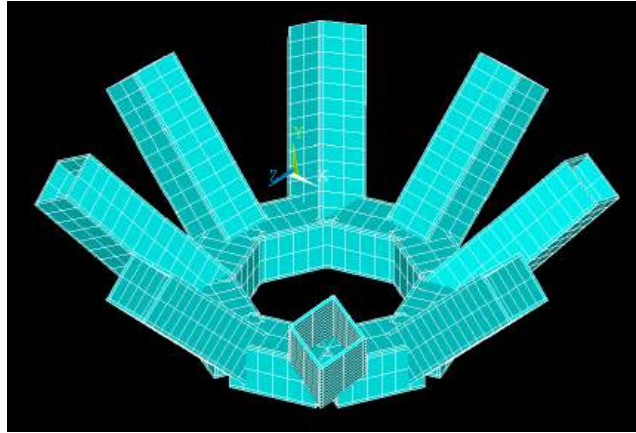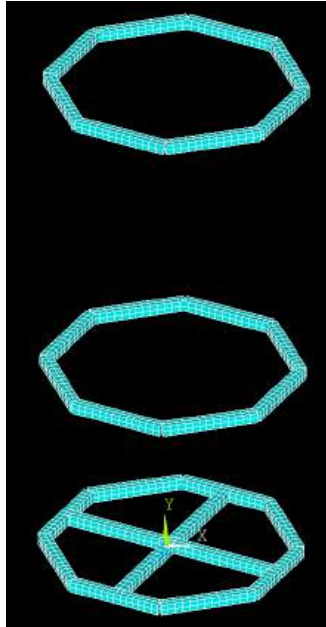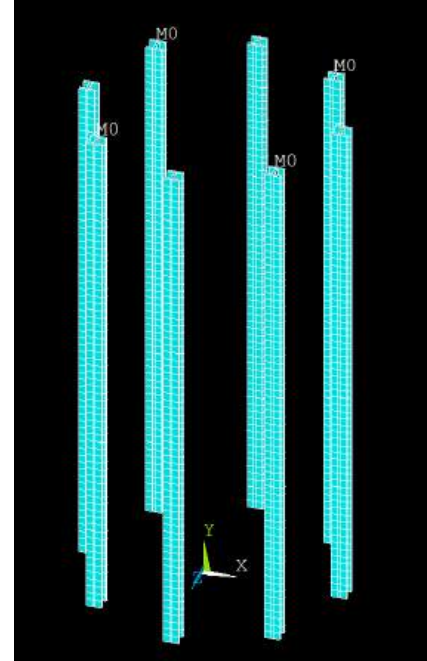
Figure 8.5.12: Bottom (no. 1) beam section

The next support to define was the base cross (no. 2), which is present at three levels of the structure. At the bottom level, there is a crossing frame to help support the ASRGs. The two other levels are the locations of the xenon tank point masses, simulating the four (eight total) locations where the tanks are mounted. The tank cross beams are also present but are not shown since they are just simulating the added stiffness the large tanks add to the structure. The vertical support that runs from the bottom level to the top level is the I-beam (no. 3) section. Figure 8.5.13 isolates the elements with these two cross-sections in the model, with the base cross in Figure 8.5.13a and the I-beam section in Figure 8.5.13b. In the CAD model, the orientation of these beams are in the radial direction. Again, similar to the bottom cross section orientations, the results did not vary in a significant way leading them to be left in their default orientation.
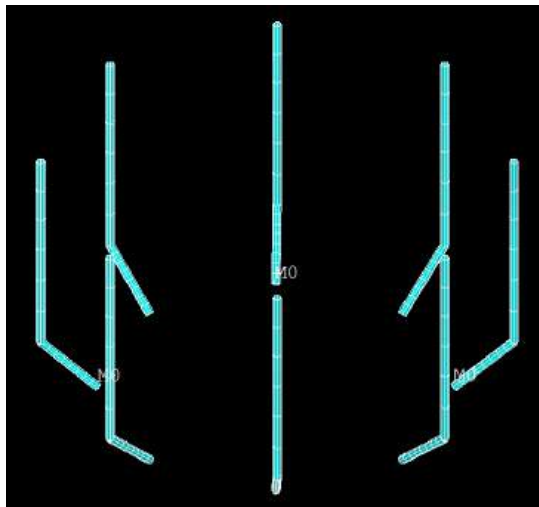
(a) Base cross (no. 2)
    beam section

(b) I-beam (no. 3) beam section

Figure 8.5.13: Base cross (no. 2) and I-beam (no. 3) beam sections.

Similar to the bottom of the frame, the top of the frame is defined by horizontal and vertical components. The top vertical (no. 4) beam section is seen in Figure 8.5.14a and the horizontal top cross (no. 5) beam section is seen in Figure 8.5.14b.


(a) Top vertical (no. 4) beam section
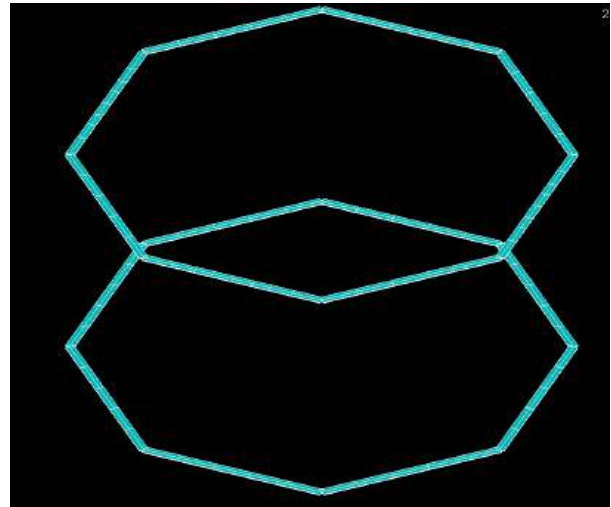

(b) Top cross (no. 5) beam section

Figure 8.5.14: Top vertical (no. 4) and top cross (no. 5) beam sections.

Finally, the high-gain antenna supports (no. 6) at the top of the structure, shown in Figure 8.5.15a, and the ASRG supports (no. 7) extending out in the four planar directions from the base of the structure, shown in Figure 8.5.15b, are defined. These were examined previously in Section 8.5.3.
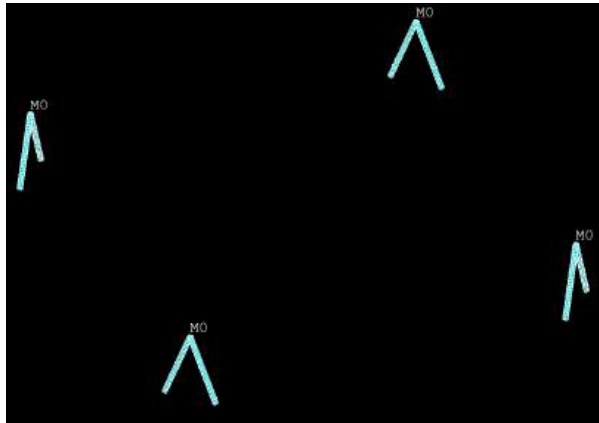
(a) HGA support (no. 6) beam section
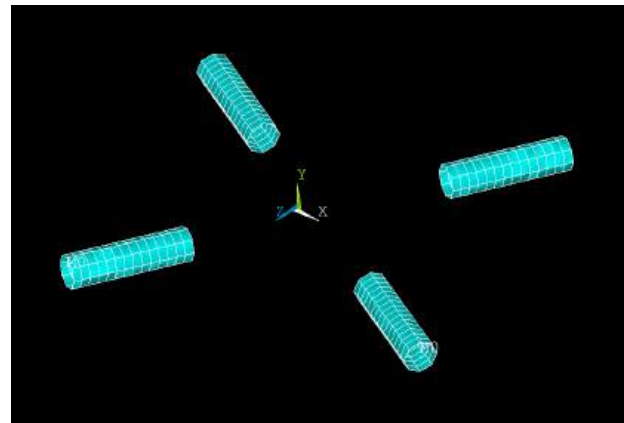
(b) ARSG support (no. 7) beam section

Figure 8.5.15: HGA support (no. 6) and ASRG support (no. 7) beam sections.

To isolate the beam supports that are to be analyzed, the elements of just that beam are selected in APDL and then the von Mises element stress is plotted on the selected elements. For the bottom support the initial beam had a hollow square cross section of 150 x 150 mm, with 10 mm thick walls. When the stress was initially plotted, the results showed that the stress concentration in the corner of the base support exceeded the value of yield deemed acceptable to the desired factor of safety, at 184 MPa. A figure of the stress is seen in Figure 8.5.16.

Figure 8.5.16: Element von Mises stresses at bottom support with 150 x 150 mm hollow cross section

The stress value with this cross section was 210 MPa, but to achieve a factor of safety of 1.5 the stress needs to be less than 184 MPa. Therefore, the team increased the size of the bottom cross section and re-ran the solution. The next solution was run with a bottom cross section of 170 x 170 mm, still with 10 mm thick walls. The results of this run are shown in Figure 8.5.17.
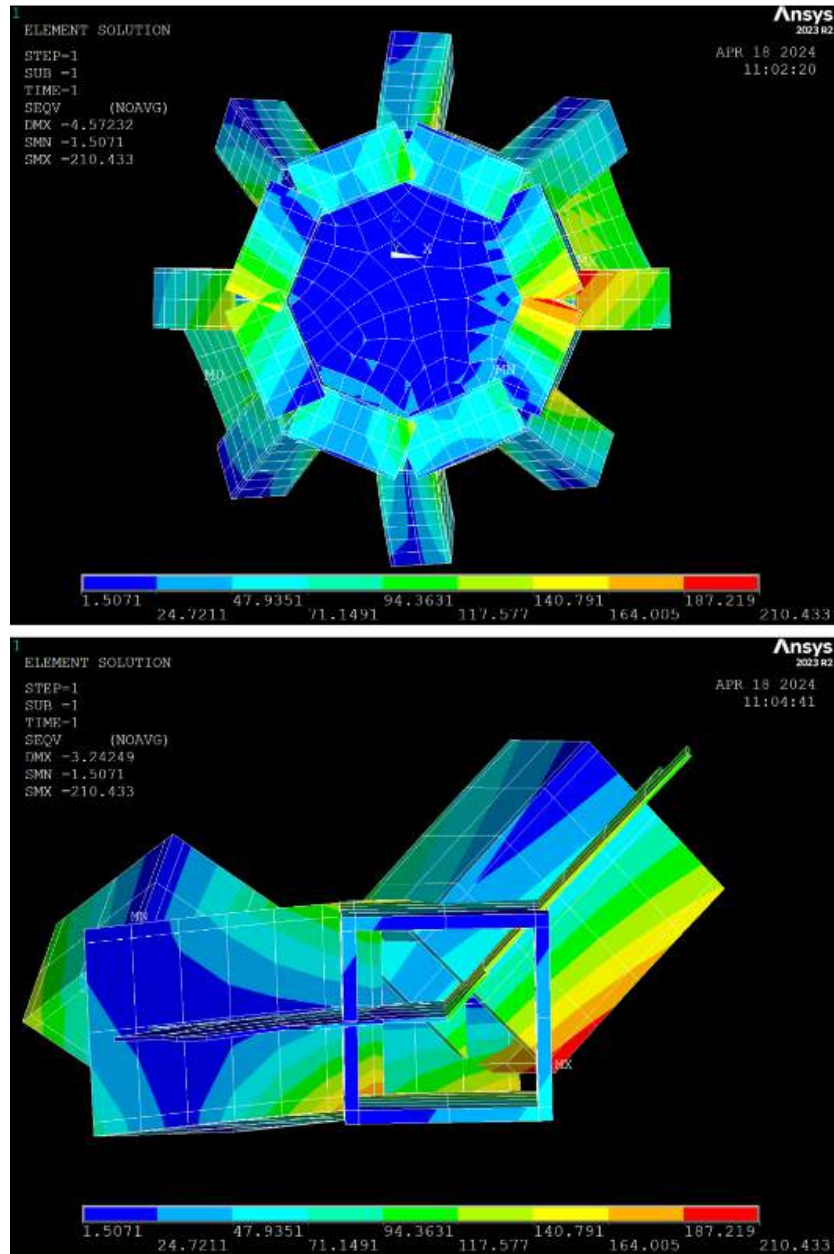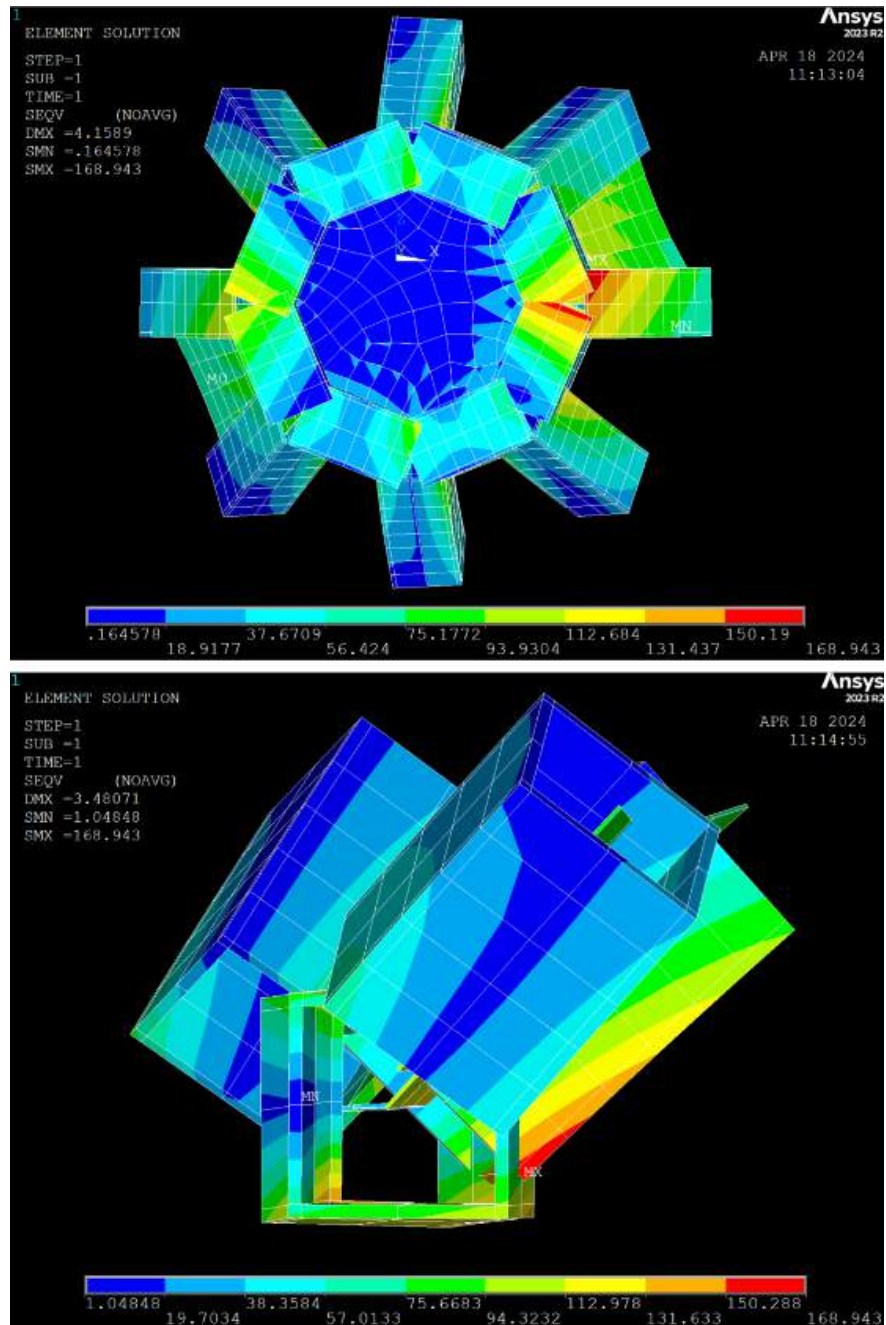
Figure 8.5.17: Element von Mises stresses at bottom support with 170 x 170 mm hollow cross section

With this updated cross section, the stress concentration shows a value of 170 MPa. Using the factor of safety and yield stress equation,

$$\text{FS} = \frac{\sigma_{yield}}{\sigma_{model}} = \frac{276[\text{MPa}]}{170[\text{MPa}]} = 1.63[-], \tag{8.45}$$

the new factor of safety is greater than the global 1.5. This value is acceptable and is bound to change slightly based off changes to the other structural cross sections when these processes are repeated. Table 8.5.5 shows the results from the rest of the geometry changes.

Table 8.5.5: Beam Section Summary Table

Name (#)	Shape	Dimensions (mm)	A (mm^2)	σ_{max} (MPa)	FS
Bottom (1)	Sq. Pipe	170 x 170; $t = 10$	6,400	170	1.63
Base Cross (2)	Sq. Pipe	75 x 75; $t = 10$	2,600	165	1.67
I-beam (3)	I-beam	100 x 100 x 18	4,752	183	1.51
Top Vertical (4)	Pipe	$r_i = 19; r_o = 20$	126	122	2.26
Top Cross (5)	Rect.	40 x 3	120	54	3.41
HGA Support (6)	Pipe	$r_i = 8.3; r_o = 9.5$	67	63	2.92
ASRG Support (7)	Pipe	$r_i = 94.4; r_o = 95.3$	536	558	1.58

For the top-cross sections, the horizontal thickness was bound by the diameter of the vertical supports so that they have the same dimension, allowing for compatibility when the shielding is added onto the structure. A view of the CAD model without the front shielding panel is seen in Figure 8.5.18. The team picked a height of 3 mm for this cross section; this did not bring the factor of safety down to a reasonable value, but the amount of material used is still very minimal.
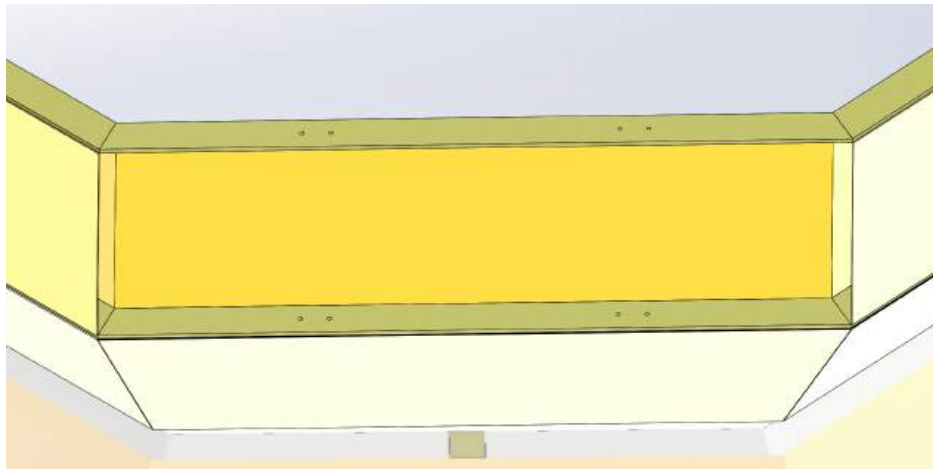

Figure 8.5.18: CAD model of top cross (no. 5) connection with Whipple shielding.

The analytical value for the antenna supports will be used even though the factor of safety is greater than the specified requirement. The amount of material used for these supports is already quite minimal, and using a smaller thickness or making the cross section smaller would not be a practical change.

8.5.5   Updated Model Results

The CAD model was updated and designed in a slightly different way to minimize problems with compatibility between the two. The main changes were two-fold: the angled base was changed to a flat base so the ion thrusters could be contained within the structure, and the main frame became about a half a meter taller, to arrange the equipment and tanks in a more effective manner. The changes and results of the model update are found in Section 9.2. The iterative nature of the design process going back and forth between creating a feasible model and making sure that model is structurally sound creates a difficult balance between both; ideally this process could have been done more times to build the most effective and efficient model as possible but the scope of the project limits this interaction.

8.6   Launch Vehicle Heat Transfer

When the spacecraft sits idle aboard the Falcon-9 rocket, approximately 23,333 W combined will be released from the ASRGs. With no action taken to remove this heat, the potential for catastrophic damage to the Scuttle spacecraft and potentially the launch vehicle is massive. However, this is a problem that has already been tackled by NASA, as previous RTG models have been equipped with an active cooling system (ACS). This system, solely designed for this problem, uses tubular passages near the base of each fin and circulates water throughout the fin channels to remove up to a maximum of 3,500 W per RTG [78]. These values are based on the GPHS-RTG with a length of 1.14 m and a diameter of 0.422 m, and covered by eight radially oriented fins and four mid span bosses [78]. Provided in Figure 8.6.1 is a graphic of the GPHS-RTG, where the fins and ACS attachment points are labeled.
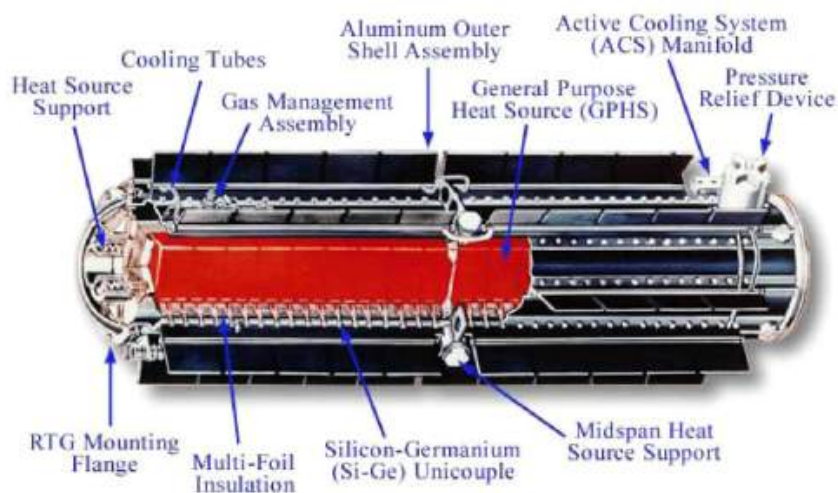

Figure 8.6.1: GPHS-RTG model detailing how the active cooling system is incorporated into the generator.

Each Scuttle Mission ASRG releases 4083 W, meaning that there is a heat draw

discrepancy; however, with the cross sectional dimensions dominating those of the GPHS-RTG, extra fins would be able to be placed on the ASRG. Fitting a larger cooling system to the launch vehicle is another possibility due to the newer launch systems supplied by SpaceX. Thus, an increase in fin count and improved cooling system efficiency would allow for the excess heat to be captured and taken away from the spacecraft.

8.7 ASRG Heat Transfer

To ensure a safe operating environment, a maximum surface temperature of the Scuttle Mission vehicle ranging between 313 K to 323 K is required, which is the maximum temperature many of the payloads can withstand. To understand the basics of how the ASRGs affect the thermal environment of the satellite, a single-node lumped mass analysis was performed for LEO following the guidance of NASA document *Spacecraft Thermal Control* [79]. This model approximates the satellite as a sphere with the same surface area as Scuttle in a circular 400 km orbit around Earth, which will be used to estimate Scuttle's temperature requirements for the five years it orbits Earth. The orbital inclination is modeled as the beta angle, β, the angle between the sun-vector and the orbit plane. This angle varies over the course of a year within a theoretical range of $\pm 90°$ and will allow the model to factor in time spent in Earth's eclipse. For a beta angle of either $\pm 90°$, the satellite will be constantly exposed to the sun. As the angle decreases, the orbit will start to intersect with the horizon of the Earth. The angle where this occurs is called the critical beta angle (β^*) and can be calculated with the radius of the Earth (R) and the altitude (h) using

$$\beta^* = \sin^{-1}\left(\frac{R}{R+h}\right).$$ (8.46)

The critical beta angle will give how much time the satellite spends in Earth's eclipse. This can be described using a piece-wise function,

$$f_E = \begin{cases} \frac{1}{180}\cos^{-1}\left(\frac{\sqrt{h^2+2Rh}}{(R+h)\cos(\beta)}\right) & \text{if } |\beta| < \beta^* \\ 0 & \text{if } |\beta| \geq \beta^* \end{cases}$$ (8.47)

The beta angle also influences the heating experienced from Earth infrared (IR) and sunlight reflected from the surface, which is referred to as Albedo. To model these heat sources, the following values will be used,

$$a = \begin{cases} 0.14 & \text{if } \beta < 30° \\ 0.19 & \text{if } \beta \geq 30° \end{cases}$$ (8.48)

$$q_{IR} = \begin{cases} 228 \ W/m^2 & \text{if } \beta < 30° \\ 218 \ W/m^2 & \text{if } \beta \geq 30° \end{cases}$$ (8.49)

where a is the unitless Albedo factor and q_{IR} is the heat flux of Earth infrared.
To accurately represent temperature during orbit, heating rates must be changed when the

satellite enters Earth's eclipse. During this time, solar radiation and Albedo must be removed. This can be parameterized using the orbit period (τ) and the eclipse function (f_E) so that the heat transfer model ignores solar radiation during the eclipse stage.

$$s(t) = \begin{cases} 0 & \text{if } \frac{\tau}{2}\left(1 - f_E\right) < t < \frac{\tau}{2}\left(1 + f_E\right) \\ 1 & \text{else} \end{cases} \tag{8.50}$$

Figure 8.7.1 provides a visual representation of the parameter s(t): a dimensionless function that is used as an input to remove solar heat while the satellite is in Earth's eclipse. An average period of 28,512 s was used in the analysis for τ and t varied from 0 to 8*τ to simulate eight orbits and determine a steady state value.
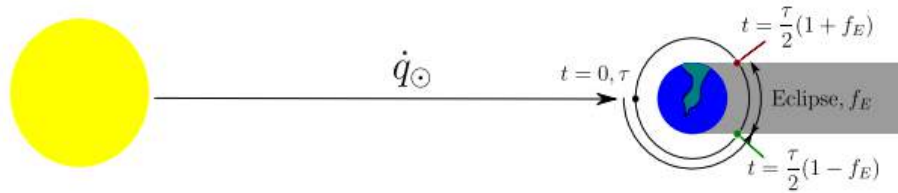

Figure 8.7.1: Model's eclipse parameters [79].

Using the parameters defined above, a heat transfer energy balance can be set up. Note that because this is a lumped mass model, internal temperature gradients are ignored for simplicity. Thus, the incident heat can be described by the sum of solar radiation, IR, Albedo, and internal heat generation using

$$Q_{in} = Q_{IR} + Q_{sol} + Q_{albedo} + Q_{gen} = q_{IR}A_{IR} + (1+a)q_{sol}A_{sol}s(t)\alpha + Q_{gen}, \tag{8.51}$$

where Q terms denote the heat (in W) coming from its respective subscript and the q terms denote the respective heat flux (in W/m^2). The area terms in this equation refer to the area that is exposed to each heat source. For this spherical model, all areas are equal to the disk profile. To obtain a surface area close to Scuttle's, a diameter of 13 m was used. For the internal heat generation, Q_{gen}, a value of 16333 W was used as it is the output heat of the ASRGs that is unusable by the spacecraft due to the system efficiency of 30%. Because the radiation leaving the satellite can be estimated using the Stefan-Boltzmann law, the total heat rate is given by

$$Q = Q_{in} - Q_{rad} = q_{IR}A_{IR} + (1+a)q_{sol}A_{sol}s(t)\alpha + Q_{gen} - A_s\sigma\epsilon T^4 \tag{8.52}$$

where Q_{in} is the sum of the heat entering the spacecraft, Q_{rad} is the heat radiating off of the spacecraft, and A_s is the area of the spacecraft that is radiating out into space. For this simulation, A_s is taken to be equal to all other areas. This equation is dependent on the absorptivity (α) and emissivity (ϵ) properties of the outer surface of the satellite. This

model was calculated under the assumption that the satellite is covered in aluminized Kapton with $\alpha = 0.15$ and $\epsilon = 0.85$. The heat sources are shown visually in Figure 8.7.2.
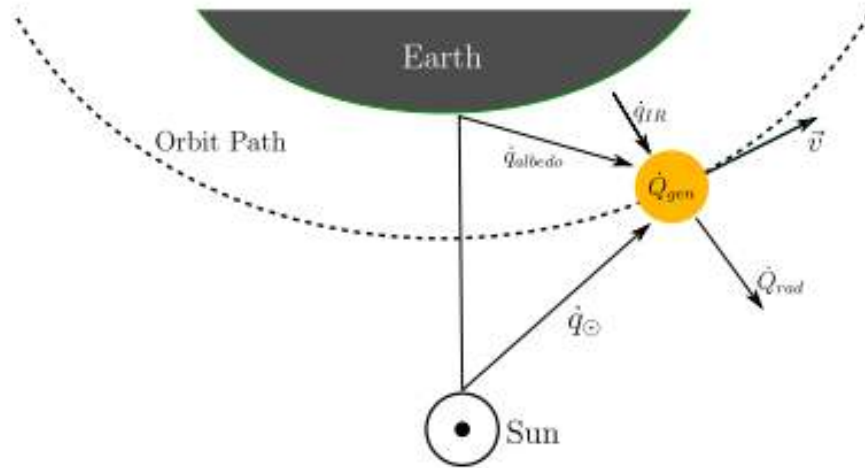

Figure 8.7.2: Heat sources used in single-node analysis model [79].

The energy balance from Equation 8.52 can be solved for temperature using the specific heat formula,

$$Q = c_p m \frac{\Delta T}{\Delta t}.$$ (8.53)

The primary material of the structure is Al 6061-T6 which has a specific heat, c_p, of 897 W/kg-K. The mass, m, is given to be equal to Scuttle's at 5,839 kg. Solving this equation for temperature results in the total heat rate as a function of time where the initial temperature at $t = 0$ is given as 293.15 K. The temperature of the spacecraft can thus be approximated over time as

$$T_{i+1} = T_i + \frac{\Delta t}{c_p m} Q_i.$$ (8.54)

The results of the model are shown in Figure 8.7.3. This graph shows that the temperature of the satellite rises over time and plateaus just over 400 K. This is 77 K higher than the maximum surface temperature required to ensure the scientific payload remains operable. The beta angle, however, appears to have very little effect on the temperature at steady state. During eclipse, the temperature only drops by 6 K at the lowest beta angle and even less at higher beta angles.
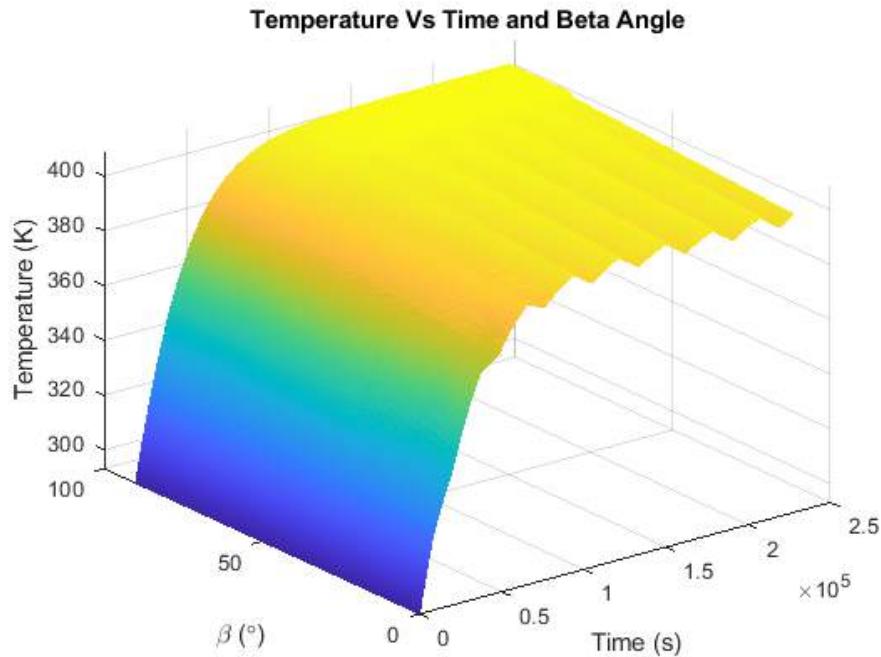
Figure 8.7.3: Single node analysis results over eight orbits.

Normally, it would be expected that the temperature increases more drastically as the beta angle increases and the satellite spends less and less time in Earth's eclipse. This relationship is shown over eight orbits in Figure 8.7.4, which details the temperature of the spacecraft due to only solar, Earth infrared, and Albedo and does not consider internal heat generation from the ASRGs. The temperature rises and falls during the orbit depending on its proximity to the sun and fluctuates at a steady state temperature range. This shows that the high temperatures experienced by the spacecraft are a direct correlation to the heat generation from the ASRGs. It is so high that the satellite cannot properly cool off during eclipse stages. Without the ASRG waste heat, the satellite would be able to operate within the required steady state range at any beta angle. The high temperature that the satellite experiences is concerning for the survival of the scientific payload. This result indicates that Scuttle may need to employ further cooling features to counteract this. This model also operates under the assumption that the spacecraft feels the entirety of the effect of the ASRG waste heat. The location of the ASRGs may play a factor that could potentially lower the overall temperature through further analysis if they are placed on a boom.
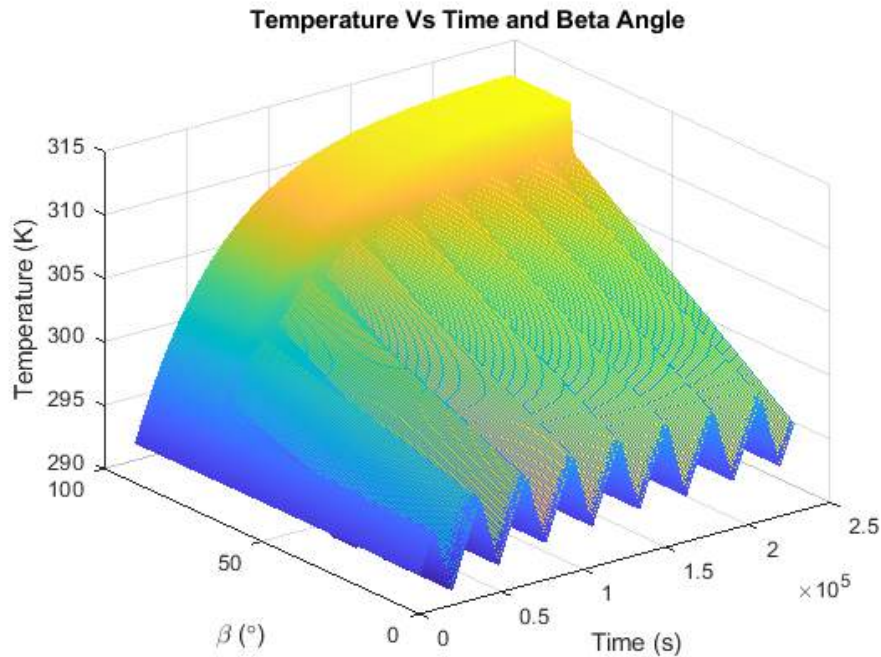
Figure 8.7.4: Single node analysis results over eight orbits without consideration of internal heat generation due to ASRGs.

Extending booms will be deployed for each ASRG to decrease the spacecraft's surface temperature. The booms will be attached in the launch vehicle such that the loading is held by fixed supports, but the ASRGs will detach from these supports once in space and extend from the booms. The maximum temperature the spacecraft experiences in Figure 8.7.4 is approximately 307 K without the effect of the ASRG waste heat. To solve for the boom temperature distribution, a steady numerical analysis was used. A depiction of the geometry to be analyzed is illustrated in Figure 8.7.5.

Figure 8.7.5: Simplistic drawing of extending boom.

In Figure 8.7.5, the red arrows denote the heat entering the system and the blue arrow represents the heat exiting the system through radiation. Simplifying the geometry into a rectangular prism, Figure 8.7.6 represents the energy balance on the left edge of the boom where the ASRG would connect.

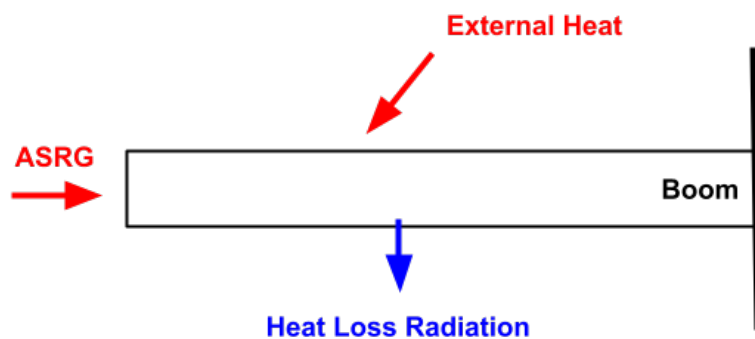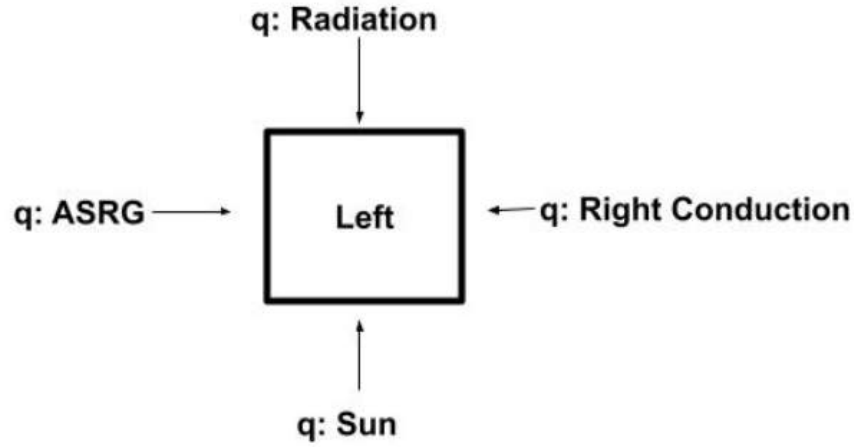Figure 8.7.6: Left control volume, energy balance, and energy balance with constants.

This energy balance figure can be described in equations using

$$0 = q_{ASRG} + q_{RightConduction} + q_{Radiation} + q_{Sun}, \text{ and} \tag{8.55}$$

$$0 = q_{ASRG} + \frac{kh^2(T_2 - T_1)}{\Delta x} + \epsilon\omega(4\Delta xh + A_F)(T_{surr}^4 - T_1^4) + q_{sun}. \tag{8.56}$$

where q_{ASRG} is the heat flux of an ASRG, q_{sun} is the heat flux of the Sun, k is the thermal conductivity of the material, h is the length of a side that makes up the square cross section, $T[i]$ is the temperature at a given node, where 1 denotes the first node on the left, M is the last node on the right and Δx is the step size that is determined by node count. blueFor just this energy balance, a A_F term is present, which represents the surface area of the fins on the ASRG, and are treated as if attached to the first node. For the radiation terms, ϵ is the emissivity of the boom material, σ is the Stefan-Boltzmann constant, and T_{surr} is the outside temperature, which is approximated at 2.7 K. These equations are formulated based on the *Introduction to Engineering Heat Transfer* textbook [80].

Figure 8.7.7 represents the energy balance that will be used to iterate through the boom in between the left and right edge. In this study, where there will be 200 total nodes, there will be 198 internal nodes that utilize this energy balance.
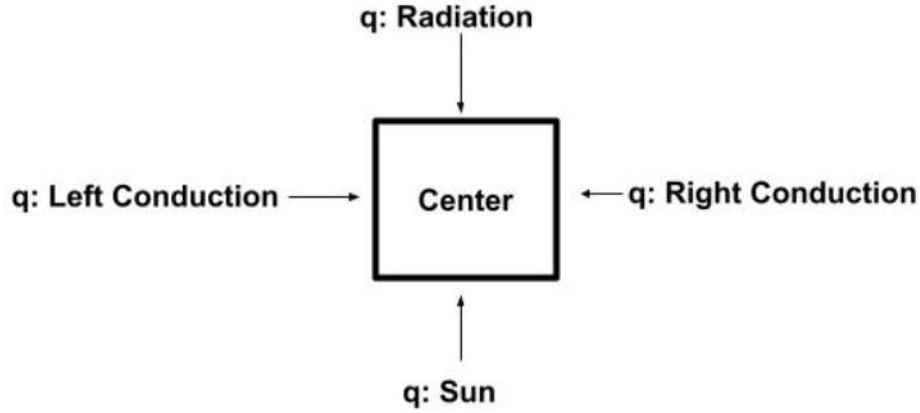
Figure 8.7.7: Middle control volume, energy balance, and energy balance with constants.

This figure results in energy balance equations for the middle control volume as

$$0 = q_{LeftConduction} + q_{RightConduction} + q_{Radiation} + q_{sun}, \text{ and} \qquad (8.57)$$

$$0 = \frac{kh^2(T_{i-1} - T_i)}{\Delta x} + \frac{kh^2(T_{i+1} - T_i)}{\Delta x} + \epsilon\omega 4\Delta xh(T_{surr}^4 - T_i^4) + q_{sun}. \qquad (8.58)$$

Lastly, Figure 8.7.8 shows the energy balance for the right edge where the boom meets the superstructure, it is assumed that the right most edge is insulated.
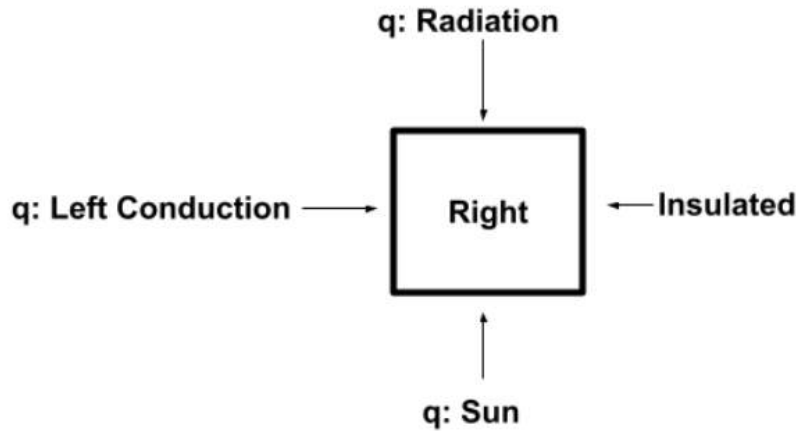

Figure 8.7.8: Right control volume, energy balance, and energy balance with constants.

Similar to the previous figures, this figure provides the energy balance equations for the right control volume with

$$0 = q_{LeftConduction} + q_{Radiation} + q_{Sun}, \text{ and} \tag{8.59}$$

$$0 = \frac{kh^2(T_{M-1} - T_M)}{\Delta x} + \epsilon\omega 4\Delta x h(T_{surr}^4 - T_M^4) + q_{sun}. \tag{8.60}$$

The next step is to determine the boom geometry required to limit the heat affecting the satellite. This was estimated to be 2.0 m long and with a cross-section of 0.015 m x 0.015 m as a starting point to limit the scale of the boom. It must be noted that the actual boom would have this material, cross-sectional area, and surface area but not necessarily the same cross-sectional shape. The material used is Al 6061-T6, with an emissivity of 0.60 and a head conduction coefficient of 237 W/m²-K [81]. The heat from a singular ASRG is 4083 W, which is the total excess heat of 16333 W divided by 4. The code in Appendix 11.6 was used to determine the heat from just the Sun, where generation and radiation were set to 0. This energy value was determined to be 37.04 W over the entire body. Thus, when solving for applied heat within each nodal control volume, the sun energy value felt on the boom shall be divided by the number of nodes. blueThe solution, calculated in Appendix 11.7, resulted in an ASRG temperature of 530.7 K, and a temperature at the end of the structure of 312.8 K, within the acceptable bounds. A plot of temperature along the boom can be seen in Figure 8.7.9.
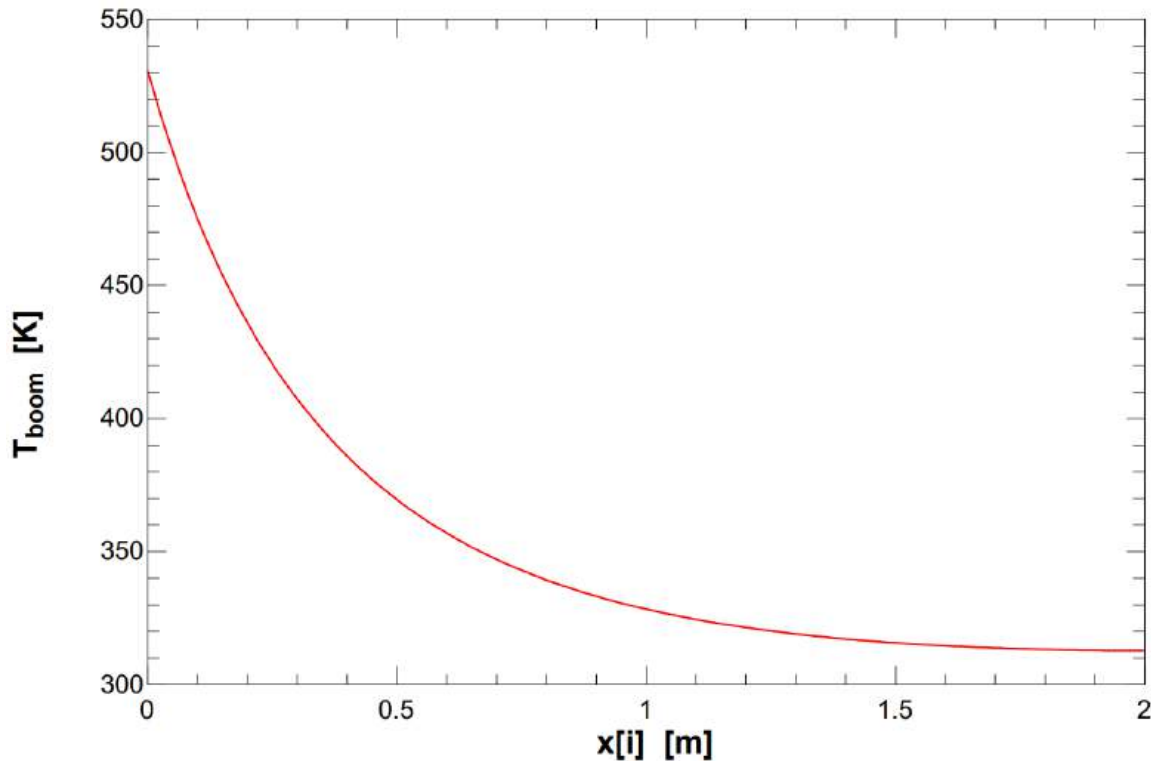

Figure 8.7.9: Temperature vs Position Plot of the Boom.

From this study, it is clear that a boom of 2 m with the determined cross-sectional area

and surface area, /textblueand the required fin surface area will result in enough heat dissipation that the ASRGs are safe to use on the Scuttle Mission spacecraft. This is verified by Figure 8.7.4, which shows that the external radiation due to the sun and other sources results in a body temperature on the main superstructure below the maximum allowed temperature.

8.8   ASRG Hold Down and Release Mechanisms

For a boom to work for the Scuttle Mission, there needs to be a mechanism that releases the ASRG from its connecting point and allows for the extension of the ASRG away from the main structure. To do this, Scuttle Mission will use electrically initiated, one-shot release mechanisms from Ensign-Bickford Aerospace and Defense Company [82]. These are also known as hold down and release mechanisms (HDRM). These work by utilizing a release rod held in place by two spools that are held tightly together by restraining wire, which itself is held by electrical fuse wires. When activated, an electrical current forces the restraining wire to unwind and separate the two pieces. This method is well-established due to its high tensile strength. Figure 8.8.1 shows how this system would work for Scuttle.
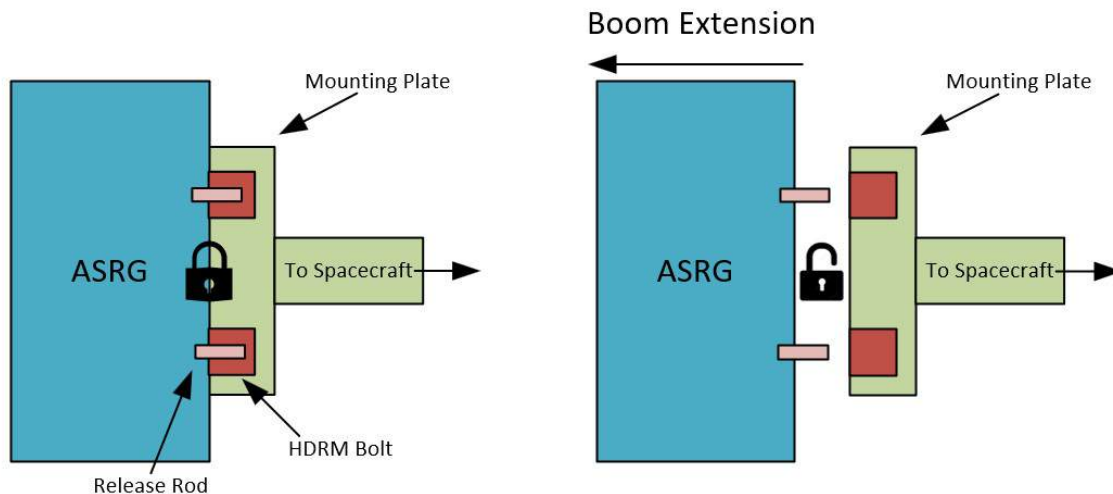
Figure 8.8.1: ASRG locked to support (Left) and unlocked and extended from main support via boom (Right)

When looking at model selection, tensile and shear loads stall be considered as each model has different load ratings. Because the male and female ends of the device will be flush, tensile stresses due to bending will not be present. Each HDRM comes with a release load, which is the load required to overcome the locking mechanism. The tensile force applied and shear force applied will be calculated as mass and launch loads. The calculations will also utilize three HDMRs per ASRG to distribute the loads. The tensile force,

$$TF = \frac{gH_a m_{ASRG}}{3}, \tag{8.61}$$

where TF is tensile force in N, g is earth gravity, H_a is horizontal launch acceleration, m_{ASRG} is the mass of a single ASRG, and SF is the safety factor of 1.5, is calculated to be 3678.75 N on each of the three HDMRs. Due to vertical acceleration being larger than horizontal and tensile strength being greater than that of shear for Ti-6Al-4V, a diameter solved with relation to stress will not be calculated. Instead tensile force will be compared to the HDMR release load data sheet. Thus, the selected HDMR shall withstand a minimum of 3679 N. Shear force on each attachment can be calculated using

$$V = \frac{gV_a m_{ASRG}}{3}, \tag{8.62}$$

where V is shear force, g is gravity on Earth, V_a is vertical acceleration due to launch, and m_{ASRG} is the mass of the ASRG. This value is calculated to be 6540 N. Subsequently, the shear stress for a solid circular cross section can be calculated using

$$\tau = \frac{4VSF}{3A}, \tag{8.63}$$

where τ is shear stress in Pa, V is shear force, SF is safety factor, and A is cross sectional area. Rewritten to solve for diameter results in Equation 8.64

$$Diameter = \sqrt{\frac{16VSF}{3\pi\tau}}. \tag{8.64}$$

With Al6061 having a shear stress of 550 mPa, the resulting diameter is approximately 5.5 mm. This results in the NEA Model 9100 HDMR being selected with a release force of 6000 N and a holding rod diameter of 6.48 mm [83]. This results in an additional mass the the Scuttle Spacecraft of 0.21 kg. An image of the HDMR can be seen in Figure 8.8.2.

Figure 8.8.2: NEA Model 9100 HDMR [83]

8.9 Radiation Shielding

To ensure that all instruments will not be affected by the ASRGs, analysis must be completed. Due to the radioactive activity present within this power source, alpha and electromagnetic radiation will exist, presenting a possible source of failure in the scientific instrumentation onboard the Scuttle Mission spacecraft. This section details the analysis done to determine whether these radiations will have adverse effects, and if so determine a method of mitigating this interference.

8.9.1 Alpha Radiation

ASRGs create power utilizing Pu-238, which is the byproduct of the irradiation of Np-237 and yields a high heat density compared to half life, optimizing strength and longevity [84]. The vast majority of radiation emitted by Pu-238, 99.9% [85], is alpha particle radiation due to alpha decay, which is the process of disintegration due to unstable nuclei dissipating energy [86]. Alpha particles lose their energy quickly over a short distance, and are often said to be easily stopped by the piece of paper, and it is well known that such particles cannot penetrate the dead layer of skin [87]. Due to its weakness over distance and lack of penetration power, these alpha particles are of no concern to the Scuttle Mission spacecraft.

8.9.2 Electromagnetic Radiation

Electromagnetic Radiation in the study of radiation surrounding Pu-238 will focus solely on gamma and beta particles. Beta radiation is an intermediate ionising process with average penetration capabilities. Gamma radiation is a lower ionising wave like radiation with high penetration characteristics [88]. It is well established that beta particles can often be stopped by thin sheets of metal or plastic [89], thus, the shielding required to limit the impacts of gamma radiation would essentially block the radiation due to beta particles.

To analyze the radiation that can pass through the ASRG outer shell, the primary photon dose rate will be calculated based on the properties of Pu-238 and a titanium shield. Dose rate is solved using

$$D_r = \frac{kSPE\frac{\mu_{en}}{\rho}e^{-T\mu}}{4r^2\pi},$$

(8.65)

where D_r is the dose rate in Gray per hour (Gy/hr), k is a constant used to convert energy fluence rate and has a value of 5.67E-7 when converting final units to Gy/hr. E is photon energy in MeV, S is the activity of the radiation source, which will need to be altered based on gamma saturation. P is the abundance of gamma rays in the form of gamma rays per disintegration. $\frac{\mu en}{\rho}$ is the mass energy absorption coefficient for the shielding material in units of $\frac{cm^{-2}}{g}$, μ is a measurement given in $\frac{1}{cm}$ and represents the photon mean free paths, and T is the shield thickness in cm. The denominator contains r, which represents the distance from a point Curie (Ci) emitting source and the outside edge of the material used for shielding [90].

To create an approximation of an ASRG, 10.9375 kg of Pu238 will be modeled as a point source with a "spherical" titanium shield surrounding the point source at a distance of 0.31 m, as that is the smallest external dimension for the ASRG and the r value for the dose rate equation. To limit potential radiation side effects, the amount of radiation the spacecraft can absorb in one year will be based off the highest absorption of radiation hardened certification values: 1 Mrad in a lifetime. [91]. With 4 generators over a 60 year life period, converting from rad/yr timescale to Gy/hr, each ASRGs external dose rate should be no larger than 0.00475 Gy/hr. However, this maximum radiation value is what the electronics are exposed to, not the dose rate just exterior to the ASRG. To find the radiation dose rate exterior of the ASRG casing, the inverse square law

$$I_1 D_1^2 = I_2 D_2^2,$$

(8.66)

is utilized where I_1 and D_1 are dose intensity and distance from source respectively, and I_2 and D_2 are the same measurements except at the second point of interest [92]. With D_1 equaling .31 m, and D_2 equaling 2 m as this is from the edge of the ASRG closest to the spacecraft to the spacecraft considering the boom length. With the intensity at point two being 0.00475 Gy/hr, the inverse square law finds that a dose rate of 0.1977 Gy/hr is acceptable just outside the ASRG. This will be the dose rate moving forward to solve for

the activity of the radiation source. The first step requires the equation

$$Sa = \frac{ln(2)N}{T_{1/2}M},$$ (8.67)

where Sa is the specific activity normalized by mass, N is the Avogadro's number (6.022E23 mol^{-1}), $T_{1/2}$ is the half life of Pu-238 in hours, and M is the molar mass of Pu-238 [93]. The half life of Pu-238 in seconds is approximately 2.7687E9, and the Molar Mass in g/mol is 238.05. The result of the specific activity is 229.49E9 Bq/sec. The value for activity was solved utilizing

$$S = mSa,$$ (8.68)

where m is the mass of the radiation source and Sa is the specific activity [93]. For the single ASRG, this value is 2.51 Bq.

The photon energy is collected from published data. The predominant gamma rays emitted from from the alpha decay of Pu-238 are 0.0436, 0.0996, and 0.152 Mev [94]. These rays have an abundance level per disintegration of 3.8E-2%, 8E-3%, and 1.1E-3%, respectively [94]. There are gamma rays associated with higher values up to 0.8 Mev; however, their abundance is negligible. The energy level for the ASRG would be the summation of the gamma ray energy levels, 0.2952 Mev, with an abundance (P) of 4.71E-2%.

To solve for $\frac{\mu_{en}}{\rho}$ and μ with titanium as the shielding, published data must be referenced. The results of published data are shown in Figure 8.9.1 [95].
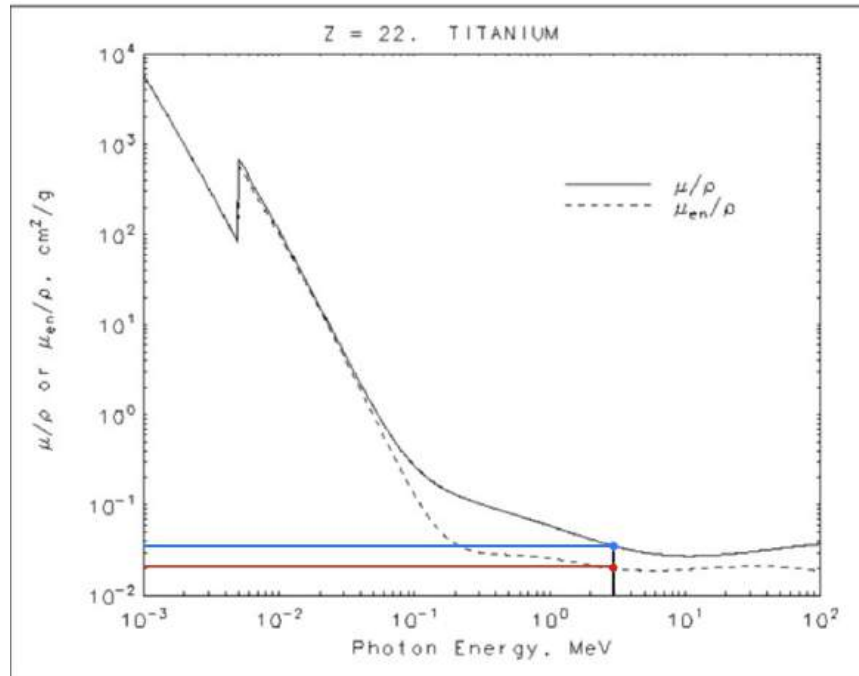
Figure 8.9.1: $\frac{\mu_{en}}{\rho}$ and $\frac{\mu}{\rho}$ [95]

The $\frac{\mu_{en}}{\rho}$ value is represented by the red dot and the blue dot represents the $\frac{\mu}{\rho}$ value. Paired with the tabulated published table data, $\frac{\mu_{en}}{\rho}$ has a value of 3.007E-2 and $\frac{\mu}{\rho}$ has a value of 1.043E-1 [95]. Multiplying $\frac{\mu}{\rho}$ by the density of Titanium to find a μ value of 0.469 cm^{-1}.

Substituting values into their respective constant locations, the thickness of titanium required is 0.00198 m. Because this value is under 2 cm, it is appropriate for the ASRG shielding to be built into the ASRG housing itself and not require extra external shielding for the equipment to be safe.

The result of this study is that both alpha and beta particles are negligible with regards to danger towards the Scuttle Mission spacecraft. Gamma particles, which pose a threat to the spacecraft, can be contained using appropriate shielding thickness build into the shell of the ASRG and due to the loss of intensity over distance. This calculation can also be described as an overestimation due the assumption that all gamma radiation is in the direction of the spacecraft.

8.10   Whipple Shielding

Over the course of any spacecraft's mission, it will likely encounter some form of debris in its path, whether it be micrometeorites or space junk. The standard method of providing protection to the vital systems of a spacecraft against impacts with this orbital debris is Whipple shielding. Whipple shielding has many forms and sizes, but can generally be summarized in three sections. The outermost shield is a thin layer of metal (usually aluminum) called the bumper, which protects mainly against low velocity debris impacts and shatters debris impacting with high velocity. The middle section is made up of mostly

empty space, but generally contains an intermediate layer of meshed and Kevlar material, slowing the shattered debris and dispersing its energy throughout its material. The innermost shield is the final layer of defense, known as the rear wall. This wall is generally thicker than the bumper, and failure of Whipple shielding is based off whether this layer is ruptured during impact [96].

To determine the optimum Whipple shielding for the Scuttle Mission spacecraft, the critical diameter of a projectile was determined for a range of velocities common for space debris. The critical diameter is the diameter at which a projectile striking the Whipple shielding will cause failure by penetrating the rear wall of the shielding for a given projectile velocity [96].

Projectiles will behave differently upon impact based upon the velocity at which they impact, and thus the equations governing the critical diameter of a projectile differ for regions of low velocity, intermediate velocity, and hypervelocity. The low velocity region varies for different projectile sizes as it is defined as the region at which the projectile will not shatter upon impact with the bumper layer, and the upper limit of this region is defined as

$$V_{LV} = \begin{cases} 1.436 \left(\frac{t_b}{d_p} \right)^{\frac{-1}{3}} & , \frac{t_b}{d_p} < 0.16 \\ 2.60 & , \frac{t_b}{d_p} \geq 0.16 \end{cases} \tag{8.69}$$

where t_b is the thickness of the bumper layer and d_p is the projectile diameter [96]. The critical diameter of a projectile in this low velocity region is calculated as

$$d_c = \left(\frac{t_w \left(\frac{\sigma}{40} \right)^{\frac{1}{2}} + t_b}{0.6 \left(cos\theta \right)^{\frac{5}{3}} \rho_p^{\frac{1}{2}} V^{\frac{2}{3}}} \right)^{\frac{18}{19}} \tag{8.70}$$

where t_w is the thickness of the rear wall, σ is the yield strength of the wall material, θ is the impact angle, ρ_p is the density of the projectile, and V is the velocity of the projectile when impact occurs.

The intermediate velocity region is the least-well defined due to the nature of fragmentation and the debris clouds that it creates. To deal with this unknown, it is common practice to use a linear interpolation between the low velocity and hypervelocity regions for the determination of critical diameter [97]. Due to this convention, this same practice will be done in this analysis.

The hypervelocity region is any projectile that exceeds an impact velocity of 7 m/s. In this region, the rear wall failure mechanism changes from cratering to impulsive, similar to that of a gaseous blast wave. The critical diameter is a more complex function in the hypervelocity region being calculated as

$$d_c = 3.918 F_2^* \left(\frac{t_w^{\frac{2}{3}} S^{\frac{1}{3}} \left(\frac{\sigma}{70}\right)^{\frac{1}{3}}}{\rho_p^{\frac{1}{3}} \rho_b^{\frac{1}{9}} (V cos\theta)^{\frac{2}{3}}} \right) \tag{8.71}$$

where S is the shield spacing, ρ_b is the density of the bumber material, and F_2^* is a scaling factor being

$$F_2^* = \begin{cases} 1 & \text{for } \frac{t_b}{d_p} \geq \left(\frac{t_b}{d_p}\right)_{crit} \\ r_{S/D} - 2\frac{\left(\frac{t_b}{d_p}\right)}{\left(\frac{t_b}{d_p}\right)_{crit}} (r_{S/D} - 1) + \left[\frac{\left(\frac{t_b}{d_p}\right)}{\left(\frac{t_b}{d_p}\right)_{crit}}\right]^2 (r_{S/D} - 1) & \text{for } \frac{t_b}{d_p} < \left(\frac{t_b}{d_p}\right)_{crit} \end{cases}, \text{ with} \tag{8.72}$$

$$\left(\frac{t_b}{d_p}\right)_{crit} = \begin{cases} 0.2 \left(\frac{\rho_p}{\rho_b}\right) & \text{for } \frac{S}{d_p} \geq 30 \\ 0.25 \left(\frac{\rho_p}{\rho_b}\right) & \text{for } \frac{S}{d_p} < 30 \end{cases} \text{ and} \tag{8.73}$$

$$r_{S/D} = \left[\frac{\left(0.6 d_p^{\frac{19}{18}} (cos\theta)^{\frac{5}{3}} \rho_p^{\frac{1}{2}} V^{\frac{2}{3}} - t_b\right) / \left(\frac{\sigma}{40}\right)^{\frac{1}{2}}}{\left(d_p / 3.918 \rho_p^{\frac{-1}{3}} \rho_b^{\frac{-1}{9}} (V cos\theta)^{\frac{-2}{3}} S^{\frac{1}{3}} \left(\frac{\sigma}{70}\right)^{\frac{1}{3}}\right)^{\frac{3}{2}}}\right] \text{ [96].} \tag{8.74}$$

The goal of this analysis was to determine a Whipple shielding configuration that protects the vitals of the Scuttle Mission spacecraft from debris less than 1 cm in diameter. Taking the bumper and rear walls to be Al 6061-T6, shield spacing, bumper thickness, and rear wall thickness were varied until the critical diameter for failure was greater than 1 cm for each of the velocity regions. The result of this analysis is shown in Figure 8.10.1 where critical diameter is plotted against impact velocity. The parameters defining the Whipple shielding are listed, characterizing a possible configuration that could be used to protect a spacecraft from debris smaller than 1 cm in diameter.
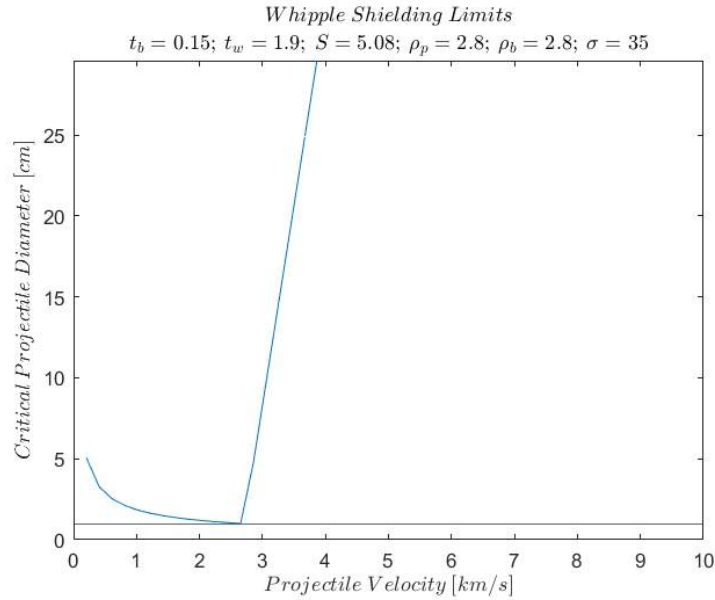
Figure 8.10.1: Whipple Shielding Limits: Critical projectile target of 1 cm (t, S in cm).

The plot in Figure 8.10.1 describes a configuration of Whipple shielding far larger than is generally used. This was done to satisfy the 1 cm required critical diameter for projectiles of the maximum density practically seen in space. Decreasing the density of the projectile to that of nylon (1.14 g/cm^3), another common space debris material, and lowering the required critical diameter to 0.5 cm allows a Whipple shielding configuration that produces Figure 8.10.2.
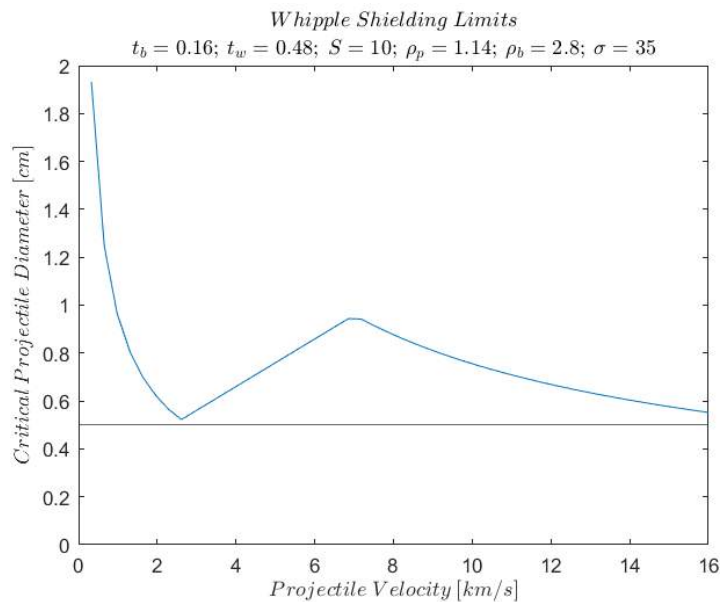
Figure 8.10.2: Whipple Shielding Limits: Critical projectile target of 0.5 cm (t, S in cm).

There are several published results from experimental testing of Whipple shielding, and these results appear to agree much more with the results of the configuration shown in Figure 8.10.2. The published results for the Whipple shielding configuration most similar to the determined values are shown in Figure 8.10.3. The All-Aluminum line represents a model more similar to the analyses detailed above [98].

Figure 5. *Stuffed Whipple (MOD-5) and All-Aluminum (Al-1) Ballistic Limits for Near Normal Impacts (0° and 15°).*

Figure 8.10.3: Results from published Whipple shielding analyses [98].

As referenced in Figure 8.10.4, the Whipple shielding configuration notably includes an intermediate layer of Kevlar, Nextel, and Mesh: each of which were not a parameter of the simple analysis conducted previously.

Table 1. Stuffed Whipple and All-Aluminum Shield Configurations

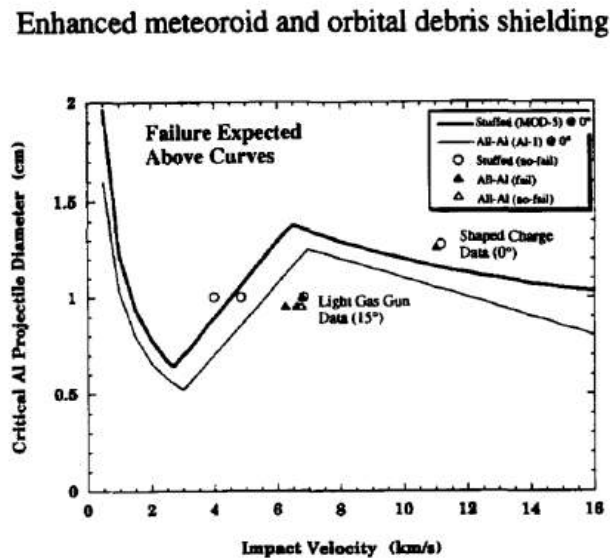| Shield Type	Size Scale Factor	Bumper	Intermediate Layer*	Rearwall	Areal Density Inter. (g/cm^2)	Total (g/cm^2)	Shield Spacing (cm)
Stuffed Whipple Shields							
B2	100%	0.127cm Al6061T6	Mesh/3 Nextel/4 Kevlar	0.32cm Al2219T87	0.458	1.71	11.4
B2-GE	100%	0.127cm Al6061T6	Mesh/3 Nextel/8-GE	0.32cm Al2219T87	0.484	1.73	11.4
MOD-1	100%	0.127cm Al6061T6	Mesh/6 Nextel/6 Kevlar	0.32cm Al2219T87	0.822	2.07	11.4
MOD-1	80%	0.10cm Al6061T6	Mesh/5 Nextel/4 Kevlar	0.25cm Al2024T3	0.658	1.64	9.1
MOD-2	100%	0.19cm Al6061T6	6 Nextel/6 Kevlar	0.48cm Al2219T87	0.792	2.67	11.4
MOD-2	67%	0.127cm Al6061T6	4 Nextel/4 Kevlar	0.32cm Al2219T87	0.528	1.78	7.6
MOD-2/GE	67%	0.127cm Al6061T6	4 Nextel/4 Kevlar/5-GE	0.32cm Al2219T87	0.628	1.88	7.6
MOD-3	100%	0.16cm Al6061T6	3 Nextel/11 Kevlar	0.48cm Al2219T87	0.652	2.45	11.4
MOD-3	67%	0.10cm Al6061T6	2 Nextel/7 Kevlar	0.32cm Al2219T87	0.424	1.60	7.6
MOD-4	100%	0.127cm Al6061T6	Mesh/10 Nextel & 1AF40	0.32cm Al2219T87	1.12	2.37	11.4
MOD-4	75%	0.10cm Al6061T6	Mesh/8 Nextel	0.23cm Al2024T3	0.83	1.74	8.6
MOD-4	67%	0.08cm Al6061T6	Mesh/6 Nextel & 1AF40	0.20cm Al2024T3	0.72	1.50	7.3
MOD-5	100%	0.16cm Al6061T6	Mesh/6 Nextel/6 Kevlar	0.48cm Al2219T87	0.822	2.16	11.4
MOD-5	67%	0.10cm Al6061T6	Mesh/4 Nextel/4 Kevlar	0.32cm Al2219T87	0.566	1.75	7.6
MOD-5	50%	0.08cm Al6061T6	3 Nextel/3 Kevlar	0.25cm Al2219T87	0.396	1.04	5.7
MOD-5	33%	0.05cm Al6061T6	2 Nextel/2 Kevlar	0.16cm Al2024T3	0.268	0.86	3.8
MOD-6	100%	0.16cm Al6061T6	26 Kevlar	0.48cm Al2219T87	0.832	2.65	11.4
All-Aluminum Shields							
Al-1	100%	0.16cm Al6061T6	0.32cm Al6061T6	0.48cm Al2219T87	0.861	2.66	11.4
Al-1	67%	0.10cm Al6061T6	0.20cm Al6061T6	0.32cm Al2219T87	0.551	1.73	7.6
Al-2	100%	0.19cm Al6061T6	0.32cm Al2219T87	0.48cm Al2219T87	0.905	2.78	11.4
Al-2	67%	0.127cm Al6061T6	0.20cm Al2024T3	0.32cm Al2219T87	0.568	1.82	7.6

Figure 8.10.4: List of several commonly used Whipple shielding configurations with the chosen configuration highlighted.

Upon comparing the conducted analyses to published results and seeing clear agreement, the Ariel Voyagers have elected to utilize MOD-5 Whipple shielding to protect the Scuttle Mission spacecraft from orbital debris that could damage vital systems [98]. The specific configuration of this MOD-5 shielding is highlighted in Figure 8.10.4.

8.11   Plumbing

This section details the main plumbing systems on board the Scuttle Mission satellite and analyses the required pressure drops from the main tanks to the thrusters.

8.11.1   Hydrazine Plumbing

Scuttle Mission will utilize a complex plumbing system to allow the hydrazine mono propellant to reach the hydrazine thrusters. This diagram is portrayed in Figure 8.11.1.
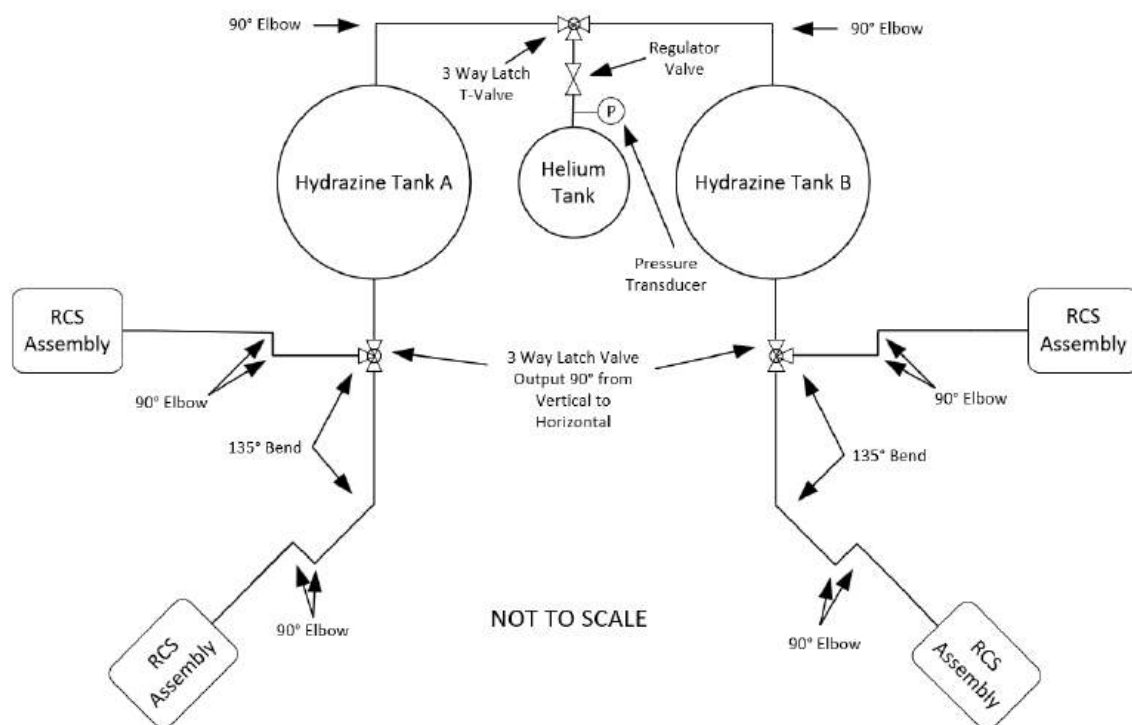
Figure 8.11.1: Helium Tank to Hydrazine Tank to Hydrazine thrusters plumbing diagram.

In this diagram, it can be seen that the single helium tank feeds both of the hydrazine tanks, and each hydrazine tank fuels two of the four RCS thruster assemblies. From the helium tank, a regulator valve controlled by a pressure transducer, which allows the central computing system to determine how much helium needs to be released based on its density to fill up the volume of hydrazine that left. From the helium tank, a 90°occurs to make the bend into the hydrazine tank, more descriptively shown in Figure 8.11.2.
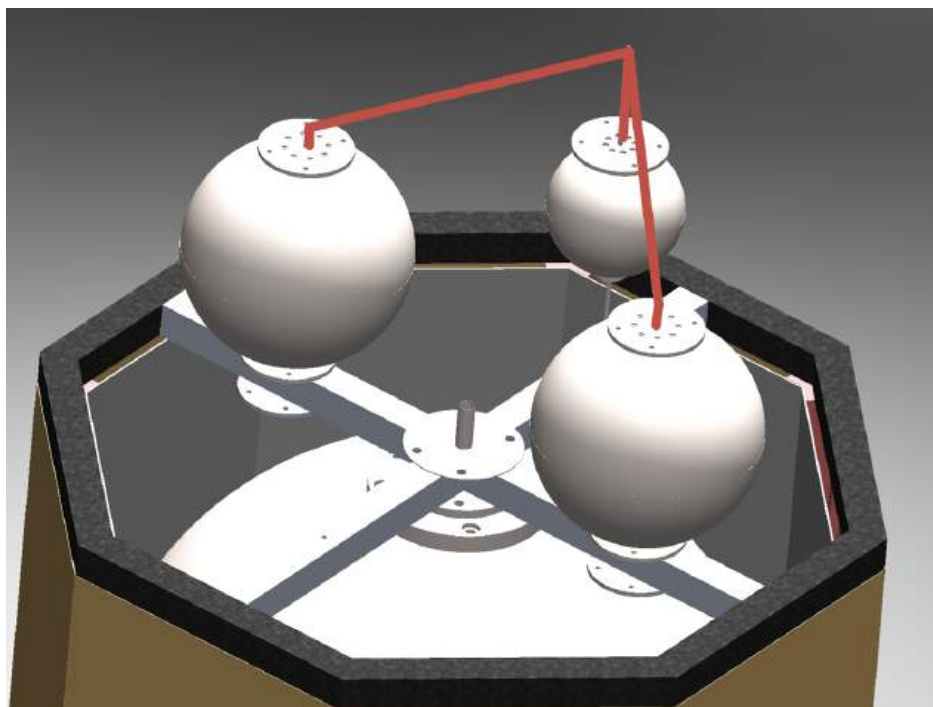
Figure 8.11.2: Red path denoting trajectory traversed by piping from Helium to Hydrazine tank

From the hydrazine tanks, the hydrazine leaves the bottom and turns 90°to either the closest hydrazine thruster, or diverges 135°horizontally to meet up below the cross beam where it again turns 135°and travels outwards. This is demonstrated more accurately in Figure 8.11.3, where the arrows denote the direction of the flow, and the image used is taken top down; however, the pipes are located below the tanks and horizontal cross frame. In Figure 8.11.1, this represents the distance from the 3 way latch valve to the first 90°elbow.
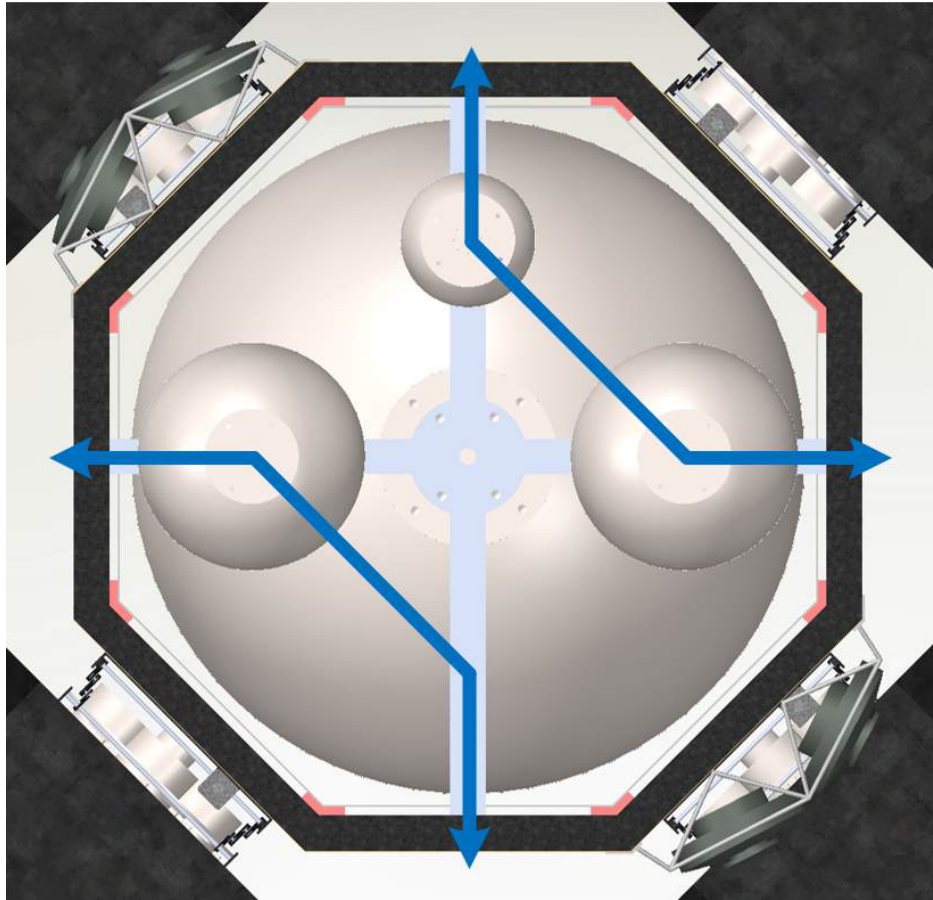
Figure 8.11.3: Horizontal Portion of Hydrazine to RCS flow layout

The next portion consists of rerouting the hydrazine upwards and then outwards to reach the RCS thruster. This is illustrated in Figure 8.11.4, where only one of the RCS thrusters is shown due to this portion being the same for all four. The blue portion denotes the section in Figure 8.11.3, and the green is the new piping portion which is the start of the first 90° bend past the 3 way latch valve below the hydrazine thruster to the RCS assembly.
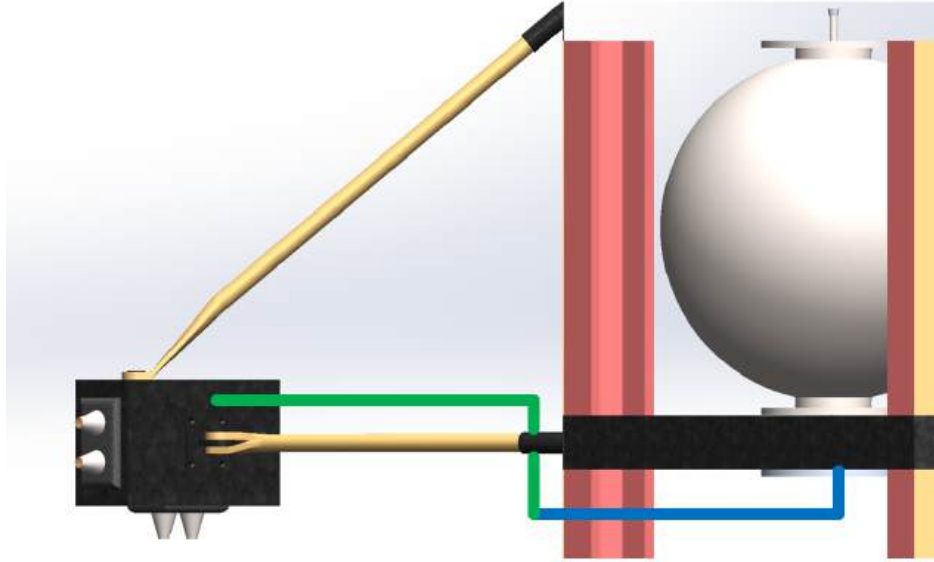
Figure 8.11.4: Exterior portion of RCS plumbing

Subsequently, the Hydrazine to RCS thruster assembly is susceptible to frictional losses which can cause the pressure of the hydrazine to change between the tank and the RCS assembly. To determine if this is an issue for the Scuttle spacecraft, the path with the most resistance, specifically the path that is not only the longest but contains the most disruptive turns (lower RCS assembly in Figure 8.11.1), will be analysed. This pressure at RCS assembly will be calculated using Bernoulli's Equation 8.75,

$$\Delta P = \frac{\rho V_2^2}{2} + \frac{nK_1 V_2^2}{2g} + \frac{mK_2 V_2^2}{2g} + \frac{fLV_2^2}{2Dg} \tag{8.75}$$

where ΔP is the difference in P_1 and P_2, the tank pressure and RCS pressure in Pa respectively, ρ is the density of hydrazine, V_2^2 is the velocity of the hydrazine flow and n is the number of 90°turns. K_1 is the 90°elbow fitting resistance, g is Earth gravity, m is the number of 135°, K_2 is the 135°elbow fitting resistance, L is the pipe length, D is the pipe diameter, and f is the Darcy friction factor for round pipe, which is calculated using

$$f = 64/Re_D. \tag{8.76}$$

Thus friction factor is dependent on the Reynolds number of a pipe with the diameter as the critical length.

A 0.5 N hydrazine thruster has a mass flow rate of 0.000212 $\frac{kg}{s}$ [99] ; however, Scuttle's RCS pods have 4 thrusters each. Therefore, both cases where only 1 thruster and all 4 are fired at the same time will be analyzed. The pipe of choice that will be used to move the fluid is the Rafael $\frac{1}{4}$" manifold piping [100]. With this dimension, 0.00635 m diameter after

conversion, the velocity of the hydrazine flow can be found using the mass flow rate definition,

$$\dot{m} = \rho A_c V, \tag{8.77}$$

where ρ is density, A_c is cross sectional area, and V is volume. With hydrazines density at 1021 $\frac{kg}{m^3}$ and dynamic viscosity 0.974E-6, the velocity of the flow for a stream that supplies just one thruster is 6.56E-3 $\frac{m}{s}$, where as a supply to all 4 thrusters results in a velocity of 2.62E-2 $\frac{m}{s}$. Solving for Equation 8.76, the friction factor for a straight round pipe with a Re_D of 43666 (turbulent flow) is 1.47E-3. An accurate table with both the straight pipe segment and angled elbow friction factors as well as count is displayed in Table 8.11.1. In this table the 135°bend is equivalent to a 45°elbow [101].

Table 8.11.1: Friction Factor for Elbows and Straights [101]

Pipe Type	Friction Factor	Count
Straight	1.47E-3	Summation of segments
90°Bend	0.86	3
135°Bend	0.46	1

Solving Equation 8.75 with a $\dot{m}$ of 2.12E-4 $\frac{kg}{s}$, ΔP is equal to 2.23E-3 Pa. Subsequently a $\dot{m}$ of 8.48E-4 $\frac{kg}{s}$ results in a ΔP of 0.356 Pa. In relation to the continuous 26 bar exit pressure of the hydrazine tank, neither of these values are significant to warrant a design change.

8.11.2   Xenon Plumbing

In order for the EP thrusters to work, the Xenon entering the propellant chamber, discharge cathode, and neutralizer cathode must be at a near vacuum level of pressure, usually 0.001 Pa. To achieve this goal, the plumbing system between the 2 Xenon tanks and 3 thrusters utilizes a two stage propellant management system that consists of a high pressure assemble (HPA) and low pressure assembly (LPA) pressure control loops [102]. Scuttle's EP plumbing diagram can be seen in Figure 8.11.5.
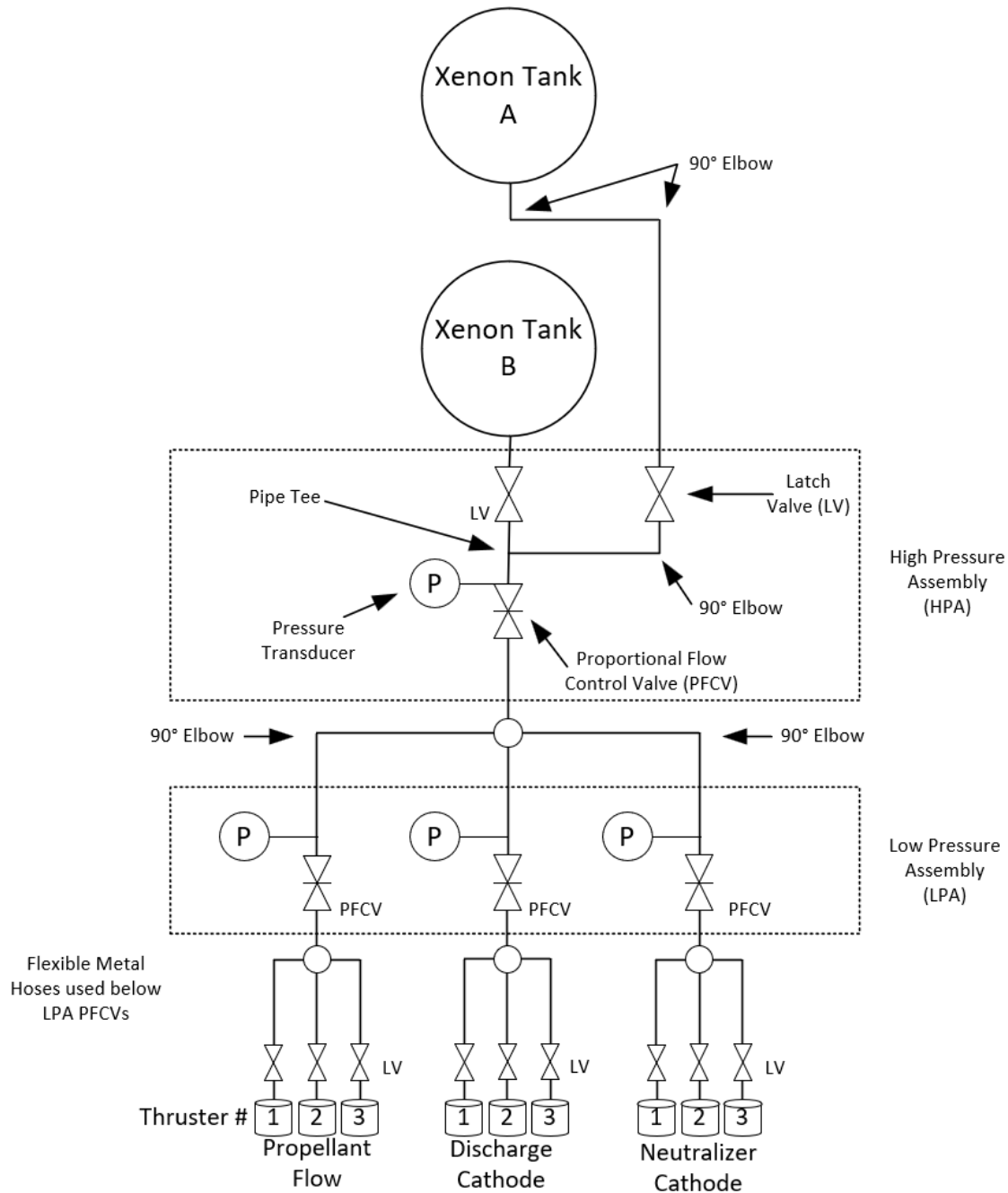
Figure 8.11.5: Xenon to EP plumbing diagram

In the HPA, pressure from the xenon tank, which is initally at 2.07E7 Pa, is regulated
down to 2.41E5 until the inlet pressure is 35psi or below. Once this critical pressure is
reached, the flow is left uninterrupted through the HPA. This is achieved through the use
of a proportional flow control valve (PFCV) in combination with a pressure transducer to
measure the valves inlet pressure [102]. From the HPA, the exiting Xenon takes three

different paths in order to regulate the pressure for the propellant flow, discharge cathode, and neutralizer cathode [102]. A PFCV is used in each of the three branches, making up the LPA [102]. Each branch regulates the pressure leaving the HPA to 1E-3 Pa [102]. Because the Scuttle spacecraft has three EP thrusters, and only utilizes one at a time, each of the 3 branches of the LPA diverges again into 3 branches in order for each LPA branch to send its regulated xenon to the correct thruster and correct location in the thruster. For the NEXT-C, its mass flow rate is 5.79E-6 $\frac{kg}{s}$ as solved in 8.12.1. An actual image of these assemblies can be seen in Figure 8.11.6.

Figure 8.11.6: HPA (Top) and LPA (Bottom) [102]

With the systems ability to fluctuate the pressures throughout the system and assemblies, pipe friction will have negligible impact on the system.

8.12   Electric Propulsion Study

The Scuttle Mission takes advantage of the benefits of electric propulsion (EP) in several ways. This section seeks to delve into the processes that make EP possible to gain a deeper understanding of the critical processes that determine the performance of EP thrusters. The Scuttle Mission utilizes the highest performing gridded ion thrusters currently in existence, the NEXT-C thrusters created by NASA and Aerojet Rocketdyne shown in Figure 8.12.1, and this section aims to "look under the hood" of these thrusters.
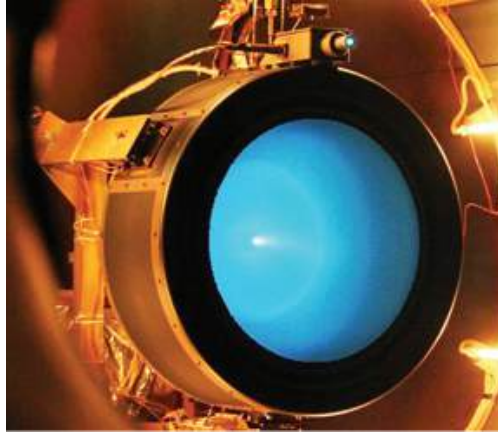
Figure 8.12.1: NEXT-C gridded ion thruster mounted for testing [103].

The known parameters of the NEXT-C thrusters are listed in Table 8.12.1. These values, while normally the final results of an analysis, will be used to reverse engineer the processes that govern function of these ion thrusters.

Table 8.12.1: NEXT-C Reported Data via Aerojet Rocketdyne [103]

Parameter	Value	Unit
Input Voltage	80 - 160	V
Total Impulse	> 24	MNs
Efficiency (System)	> 0.69	-
Mass (System)	< 50	kg
Life Capacity	> 15	yrs
Mass (Thruster)	< 14	kg
Envelope	700 x 480	mm
Max Thrust	236	mN
Max Specific Impulse	4155	s
Operating Power	7.33	kW
Beam Diameter	400	mm
Power Processing Efficiency	0.935	-

As the thrusters aboard the Scuttle Mission spacecraft utilize xenon as its propellant, Table 8.12.2 lists several useful properties of xenon and other particles.

Table 8.12.2: Xenon and Additional Useful Properties [13]

Property	Value	Unit
Molecular Mass	131.29	g/mol
Avogadro's Number	6.022e23	particles/mol
Mass of Electron	9.109e-31	kg
Mass of Xe ion	2.180e-25	kg
Charge of Xe ion	1.602e-19	C
1st Ionization Potential (Xe)	12.13	eV
2nd Ionization Potential (Xe)	21.21	eV

The analyses to follow will be separated into four sections in order to distinguish the different types of processes required to analyze the entire EP system. These sections will be an overall analysis of the thruster, an analysis of the physics that govern the motion of the particles and ions within the thruster, a brief description of the makeup of hollow cathodes, and an analysis to determine the spacing between the gridded plates that accelerate the ions to create thrust and give gridded ion thrusters their name. A basic diagram outlining the components that make up a gridded ion thruster is shown in Figure 8.12.2 for reference.
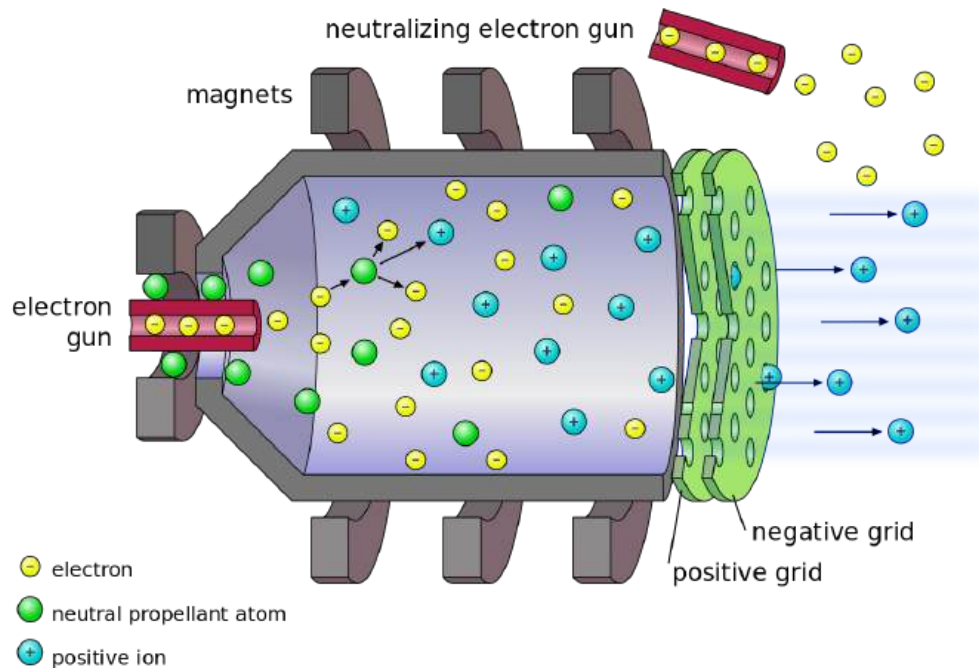

Figure 8.12.2: Gridded ion thruster diagram [104].

8.12.1 Overall Thruster Performance

Several characteristic parameters of the electric propulsion system can be determined based on the known values of the NEXT-C system listed in Table 8.12.1. By the definition of

thrust and specific impulse, the propellant mass flow rate can be determined by

$$\dot{m} = \frac{\mathcal{T}}{g_e I_{sp}} = 5.79 E^{-6} \, [kg/s], \tag{8.78}$$

and the exhaust velocity by

$$u_e = \frac{\mathcal{T}}{\dot{m}} = 40.76 \, [km/s]. \tag{8.79}$$

In an gridded-ion propulsion system, the exhaust kinetic energy of the propellant is created purely by a potential difference between the gridded plates [13]. Using the conservation of energy, the required potential difference for these thrusters can be determined as

$$\frac{mu_e^2}{2} = qV_a \; --> \; V_a = 1130 \, [V]. \tag{8.80}$$

The power, efficiency and effectiveness of EP systems are highly impacted by the characteristics of the beam it produces. These ion beam characteristics are the beam current, power and diameter. The total beam current for the NEXT-C can be computed as

$$I = \left(\frac{q}{m}\right)\dot{m} = 4.255 \, [A], \tag{8.81}$$

and beam power can be computed as

$$P_b = IV_a = \frac{\dot{m}u_e^2}{2} = 4809.818 \, [W][13]. \tag{8.82}$$

The power consumed by an electrostatic propulsion system is always greater than this beam power, because power must additionally be supplied to form ions from the neutrally charged propellant [13]. The energy required to ionize the propellant is called the ionization potential. The power efficiency describes the amount of supplied power that goes to the beam power, defined as

$$\eta_T = \frac{Beam Power}{Total Electrical Power} \approx \frac{Exhaust \; K.E.}{Exhaust \; K.E. + Charging Energy}.$$

This can be computed using

$$\eta_T \approx \frac{\frac{1}{2}mu_e^2}{\frac{1}{2}mu_e^2 + e_i + e_l} \tag{8.83}$$

where m is the ion mass, e_i is the ionization energy of the propellant and e_l is the energy loss per ion. In general, the ionization energy of the propellant is much less than the energy

loss per ion and thus this term is sometimes neglected and the energy loss per ion taken to be approximately 100 eV [13]. Since the ionization energy is known for xenon and the power efficiency is reported for the NEXT-C, the energy loss per ion will be determined to gain an understanding of the optimizations made to improve the EP system. Taking $e_l = 100eV$, the power efficiency was calculated to be 91.88%. Using Equation 8.83 and the given system efficiency value of 69%, the energy loss per ion was calculated to be approximately 509 eV. This decreased efficiency, and the increased value of e_l shows that several trade-offs must have been made within the NEXT-C propulsion system to obtain the reported thrust and specific impulse magnitudes, which are significantly larger than typical ion thrusters. For reference, the top of the line DAWN Mission ion thrusters had a maximum thrust of 91 mN and I_{sp} of 3100s [8].

To determine the amount of power supplied to the thruster, the thruster system efficiency, reported as upwards of 69%, can be rearranged as a function of this power, thrust, and I_{sp} from

$$\frac{\mathcal{T}}{2\mathcal{P}_{supplied}} = \frac{\eta_T}{g_e I_{sp}}. \tag{8.84}$$

Solving for $\mathcal{P}_{supplied}$ gives approximately 6.97 kW as being supplied to the thruster. Power processing efficiency can be approximated as

$$\eta_{PP} \approx \frac{\mathcal{P}_{input}}{\mathcal{P}_{supplied}}. \tag{8.85}$$

As a check, the reported input operating power can be multiplied by the reported power processing efficiency to determine the approximate power that goes directly to the thruster. This approximate calculation gives a value of 6.83 kW, which is a fair comparison to the computed value of 6.97 kW for the power supplied to the thruster.

8.12.2 Particle Physics within Thruster

Following the definition of the overall thruster characteristics and performance, the physics that govern ion thrusters were studied. In conducting this study, the goal was to gain a better understanding of the processes that occur within ion thrusters and to see what changes can made to improve the thruster performance.

Within the main body of an ion thruster there are a ring of permanent magnets surrounding the ionization chamber. Additionally, electrons are emitted from a device called a hollow cathode to promote ionization of the propellant. These electrons travel from the cathode to the anode, which in this case is the thruster's cylindrical inner body that constitutes the ionization chamber.

To see how a magnetic field (B-field) promotes ionization, a simple case can be considered where the magnetic field strength, B, and the electrostatic potential gradient, $\frac{dV}{dr}$ are uniform throughout the chamber. The cathode is assumed to be a long cylinder of radius

r_c and is located co-axially within the inner body cylinder of radius r_a which acts as the anode [13].

Using the basic equations of electrostatics and magnetostatics, the forces on an electron in a defined region are:

$$F_r = m_e \left(\ddot{r} - r\dot{\theta}^2 \right) = e\frac{dV}{dr} \pm er\dot{\theta}B \text{ and} \tag{8.86}$$

$$F_\theta = m_e \left(2\dot{r}\dot{\theta} + r\ddot{\theta} \right) = \pm e\dot{r}B, \text{ or}$$

$$rF_\theta = m_e \frac{d}{dt} \left(r^2\dot{\theta} \right) = \pm r \left(e\dot{r}B \right), \tag{8.87}$$

where m_e is the mass of an electron, e is the charge of an electron, B is the magnetic flux intensity, and $\pm$ depends on the direction of the axial B-field.

The electrostatic potential gradient, $\frac{dV}{dr}$, in Equation 8.86 is difficult to determine, so this equation can be integrated to make it easier to work with. Doing so allows the required field strength to be obtained in terms of the total potential drop and regardless of the shape of the potential distribution [13]. Equation 8.87 can be rewritten as

$$m_e \frac{d}{dt} \left(r^2\dot{\theta} \right) = \pm eB\frac{d}{dt} \left(\frac{r^2}{2} \right), \tag{8.88}$$

where it can be integrated to give

$$m_e r^2\dot{\theta} = \pm \frac{eB}{2}r^2 + const. \tag{8.89}$$

At the cathode, r=r_c and $\dot{\theta} \approx 0$ which gives the integration constant as $\pm \left(\frac{eB}{2} \right) r_c^2$ and the solution may be written

$$\dot{\theta} = \pm \frac{eB}{2m_e} \left(1 - \frac{r_c^2}{r^2} \right). \tag{8.90}$$

At the anode, if the electron velocity is approximately tangential, then since the sum of the kinetic energy and electrostatic potential kinetic energies of the electron remain constant,

$$m_e \frac{u_e^2}{2} = e\Delta V_a,$$

$$u_a = \sqrt{\frac{2e\Delta V_a}{m_e}} \text{ and therefore,}$$

$$\dot{\theta} = \frac{u_a}{r_a} = \frac{1}{r_a}\sqrt{\frac{2e}{m_e}\Delta V_a}, \tag{8.91}$$

where r_a is the anode radius and ΔV_a is the anode potential relative to the cathode. Substituting Equation 8.91 into 8.90 gives the characteristic equation

$$B = \frac{\left(8\left(\frac{m_e}{e}\right)\Delta V_a\right)^{1/2}}{r_a\left[1-\left(\frac{r_c^2}{r_a^2}\right)\right]}. \tag{8.92}$$

This derivation is limited only to the case of a radially uniform B-field; however, Equation 8.92 provides a means of determining the field strength needed to produce nearly tangential motion at the anode for a given ΔV_a [13]. The ideal B-field for EP would create this tangential motion for electrons at the anode, as this improves the primary electron uniformity in the ionization chamber and results in a lower discharge loss and a more uniform beam profile [105]. From Equation 8.92, the required magnet size and strength can be determined purely based upon the size and relative potential of the cathode and anode.

Now that an expression has been developed for the required magnetic field strength, the required electrostatic field strength within the chamber should be determined. Specifically, a methodology should be developed to determine how large ΔV_a should be for a given thruster. This potential difference is determined by the energy that electrons need to conduct ionizing collisions with the propellant, and this will be utilized to develop the characteristic expression for ΔV_a. The energy of an electron within an electrostatic field prior to collision is affected only by its position, and the B-field strongly affects the path that an electron will take. This demonstrates the great intertwining between the electrostatics and magnetostatics that define the functional processes of ion thrusters [13].

If an electron current is conducted through a gas, electron-atom collisions will occur. If these electrons are of a high enough energy, some of these collisions will result in ionization. As the electron energy is increase above the ionization potential of the propellant, it has been experimentally observed that the ion rate of formation increases to a maximum sharply at an electron energy about 3-5x the ionization energy of the propellant before it falls off slowly for additional increases.

If a flux of $\dot{N}_e$ electrons/(m²-s) enters a region of length dx where the atom density is n_a (assuming atoms are stationary), the rate of ion formation in ions/(m³-s) is

$$\frac{dn_i}{dt} = Q_i\dot{N}_e n_a. \tag{8.93}$$

Q_i is essentially the "cross-section" for ionization and is sometimes known as the proportionality constant. This value is the effective target area each neutral atom presents to the oncoming electron flux. If an electron strikes any part of this target area, an ionization occurs [13].

The determination of Q_i is related closely to the choice of ΔV_a, and experimental data of this relation can be seen in [106] with a summary plot of their results shown in Figure 8.12.3.
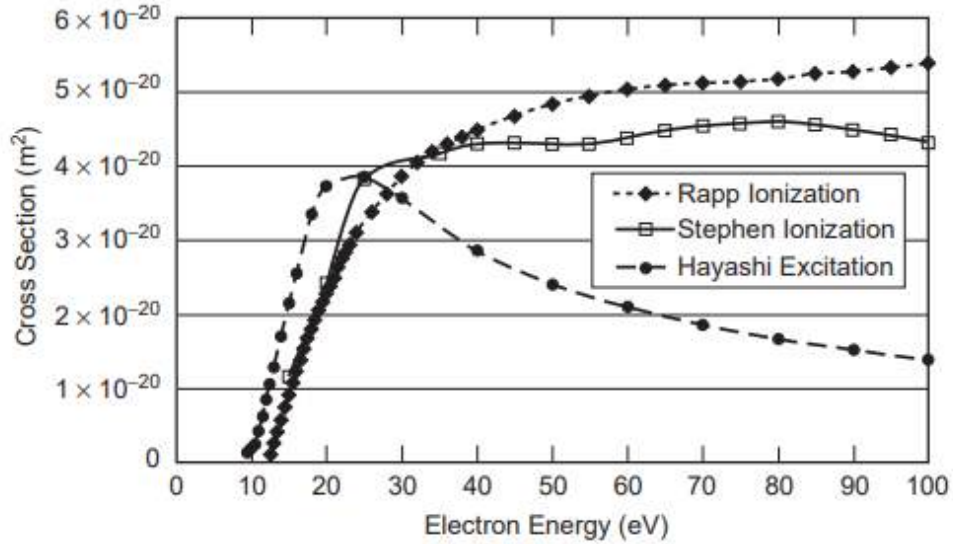

Figure 8.12.3: Ionization and excitation cross sections for xenon [106].

The choice of ΔV_a depends on the ionization potentials of the propellant, which means that for xenon, ΔV_a should be greater than the first ionization potential, 12.13 eV, and can be raised to at least the second ionization potential, 21.21 eV. The reason for wanting almost exclusively singly charged ions comes from the process that occurs outside the thruster chamber in EP. After the ionized propellant exits the thruster, it is recombined into neutral atoms by an external hollow cathode. If this recombination does not occur, the ions will be attracted back towards the thrusters and the body of the spacecraft, greatly reducing the thrust produced. Additionally, as these ions interact with the exterior structure of the thrusters and spacecraft body, the metallic structure begins to degrade. This degradation is a significant cause of failure during most lifetime assessments for ion thrusters and these thrusters are carefully designed to prevent this from happening. In practice, the potential difference can be raised even higher than the second ionization potential, because (1) the cross section for single ionization continues to rise rapidly whereas that for double ionization doesn't rise as fast and (2) the electron energy is less than ΔV_a everywhere since the potential is increasing in the radial direction [13].

Referencing Figures 8.12.3 and 8.12.4, Q_i was determined to be 3.85x10^{-20} m^2 which corresponds to a ΔV_a of 25 eV. This potential difference is just slightly above the second ionization potential of xenon and produces less than one percent of doubly charged ions according to Figure 8.12.4.
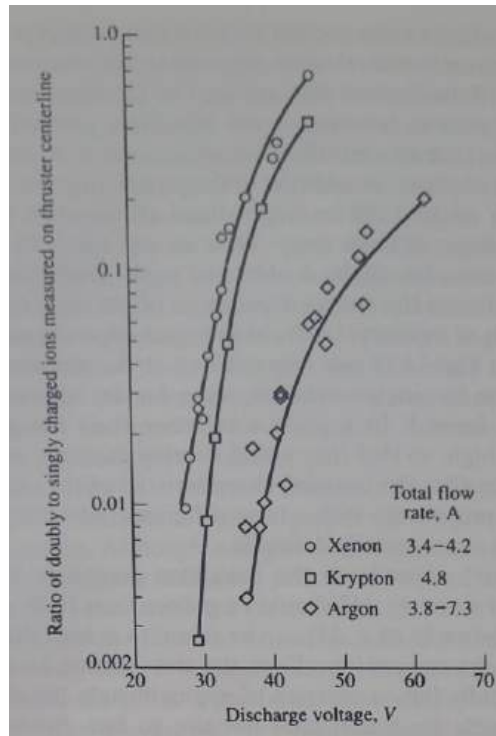
Figure 8.12.4: Ratio of doubly to singly charged ions on thruster centerline [13].

Implementing Equation 8.93, the rate of ion formation can be determined for an ion thruster with a given propellant flow rate and containing a hollow cathode that discharges at a given electron flux. This rate of ion formation is an area of optimization for ion thrusters, as the greater the ion formation rate, the faster ions can be released.

8.12.3   Hollow Cathode Basics

At this point, the physics of an ion thruster can be determined based purely upon knowledge of the discharging hollow cathode's size and properties. The optimal parameters and configuration of hollow cathodes are additional areas of study, however, only a basic outline of the components and their purpose will be laid out in this report.

Hollow cathodes, in their most basic definition, can be thought of as electron guns. Their purpose is to release electrons from an orifice so that the electrons can be manipulated to cause ionization or recombination to occur. To get these electrons, two segments are needed: a cathode insert that emits electrons and a special region of plasma in the area that these electrons are emitted. Plasma must be created for hollow cathodes to operate because it is in plasma that electrons and positively charged ions can stably exist without combining to a lower energy state neutral atom. For the purpose of these analyses, the plasma region can be thought of as a region of extreme energy, and thus extreme temperatures [107].

Coiled heaters are generally used around this plasma region to maintain proper operation and to raise the insert temperature to emissive temperatures to start the discharge.

Additionally, a heat shield is commonly used to prevent radiation losses of the cathode at operating temperatures. An orifice at the end of the hollow cathode is used to control the size and shape of the plume, and varies greatly between different ion thrusters. In general, however, ion thruster neutralizer cathodes (outside the thruster) are designed with very small diameter orifices ($\leq$ 0.3 mm), whereas ion thruster discharge cathodes are designed with orifices of less than 1 mm diameter to over 3 mm in diameter. High-current hollow cathodes for large ion thrusters can have even larger orifices, sometimes being designed without an orifice, where the insert inside diameter forms a tube exposed to the discharge plasma [107].

A basic visual that shows the location and orientation of all these components is shown in Figure 8.12.5.

(a) Basic hollow cathode configuration

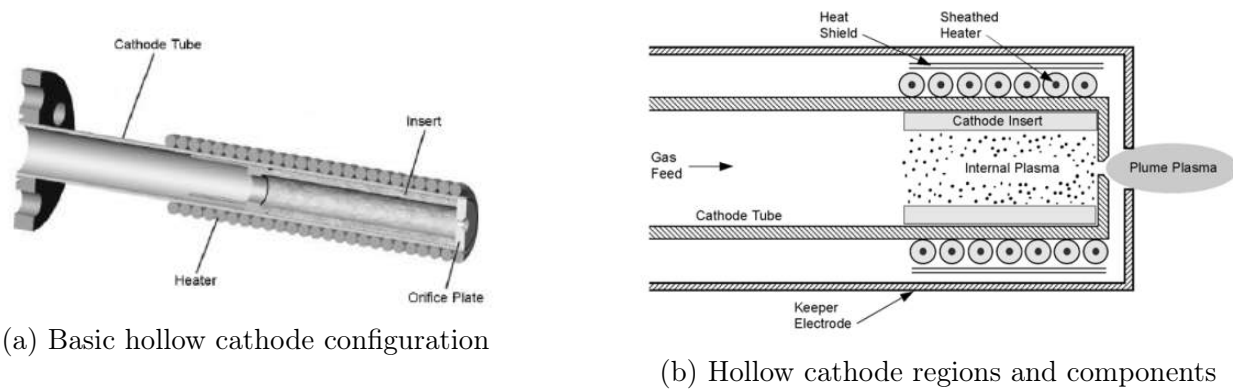(b) Hollow cathode regions and components

Figure 8.12.5: Components of a hollow cathode and their general configuration.

There is minimal information on the specific hollow cathodes used on the NEXT-C thrusters, therefore the size and shapes used to model these devices are approximated based off the preceding information and additional discussion in [107]. The shapes and sizes of the hollow cathodes used in the thruster model are summarized in Table 8.12.3.

Table 8.12.3: Hollow Cathode Model Sizing Summary

Component	Neutralizer Size	Discharge Size	Unit
Orifice Entrance Diameter	0.3	4	mm
Orifice Exit Diameter	2	4.5	mm
Insert thickness	0.65	2	mm
Cathode Tube Length	77	77	mm
Keeper Electrode Diameter	10	15.7	mm

8.12.4 Gridded Plate Spacing

The final components of gridded ion thrusters are the plates that give it their name. The relative properties of these gridded plates define the exhaust velocity that propellant can

achieve, and thus are of great import to achieving maximum thrust for a given EP system. Gridded ion thrusters typically have two plates, and the upstream plate is denoted as the screen, whereas the downstream plate is denoted as the accelerator grid.

Between the screen and accelerator grids, there exists an intense electrostatic field where the voltage gradient in the axial (flow) direction is much greater than that of the transverse direction. The ion acceleration process can be modeled by simplifying the grids as plane diodes. These plane diodes are defined as a pair of planes that offer no resistance to ion flow, but having fixed, uniform voltage on its surface. The electrostatic field between the grids will then be affected by the voltage difference across the diode and the distribution of charged ions instantaneously located between them [13].

In the following analysis, the "current" that is associated with ion flow is denoted by j and carries units of A/m^2, while the charge density is denoted by ρ_i which has units of C/m^3. Note that for these analyses, all the ions are assumed to be single charged, which is a reasonable assumption following the reasoning detailed in 8.12.2.

Looking at the potential distributions between two planar electrodes, where $\Delta V = V_a$, Hill and Peterson note in *Mechanics and Thermodynamics of Propulsion* that if no current exists between these planes, the inter-electrode potential distribution is linear. Additionally, if positive particles are made available at the higher potential electrode, the potential gradient at the surface of this electrode "extracts" particles and accelerates them to the opposite electrode. This moving charges are in essence a current between the electrodes, and incidentally, the cumulation of charges within the gap increases the potential in that region. As the charge density increases, the extraction gradient at the charge emitting surface decreases. If there were an unlimited amount of charged particles available, the current would increase until the extraction gradient falls to zero. This current is known as the space-charge-limited (SCL) current for $\Delta V = V_a$ and planar spacing $x = L$ [13]. The space-charge limitation is crucial to the design of EP systems, because it is the reason that EP has such large power requirements. The reason electric propulsion is attractive is that any amount of electrical energy can be added to a given amount of mass; however, the space-charge limitation creates an upper bound on the amount of ion current obtainable from each grid aperture [105].

The effect that charge distribution has on the potential distribution for this situation can be determined from Poisson's equation to be

$$\frac{d^2V}{dx^2} = -\frac{\rho_i}{\epsilon_0}, \tag{8.94}$$

where x is the local distance from the screen and ϵ_0 is the permittivity of free space, 8.85e-12 C^2/Nm^2. The current and charge density are related by

$$j = \rho_i u, \tag{8.95}$$

where u is the charge velocity, and the charge velocity is related to voltage by the

conservation of energy equation,

$$qV + \frac{mu^2}{2} = qV_a. \tag{8.96}$$

The kinetic energy leaving the positively charged electrode (screen) is assumed to be negligable, as the accelerated ion velocities will be magnitudes greater. The distribution of the potential and charge velocity, in addition to the current density between the electrodes can then be determined with Equations 8.94-8.96 by applying the appropriate boundary conditions.

For the purpose of this analysis, the solution for maximum charge density, ρ_i, will be found. Equations 8.95 and 8.96 can be combined and solved for the charge density, giving

$$\rho_i = \frac{j}{\sqrt{\frac{2q}{m}(V_a - V)}}. \tag{8.97}$$

Subbing this expression into Equation 8.94 gives

$$\frac{d^2V}{dx^2} = -\frac{j}{\epsilon_0 \sqrt{\frac{2q}{m}(V_a - V)}}. \tag{8.98}$$

For simplicity and ease of algebraic manipulation, let $V_a - V = V^*$ and $\epsilon_0\sqrt{\frac{2q}{m}} = \alpha$. Equation 8.98 then becomes

$$\frac{d^2V^*}{dx^2} = \alpha \left(V^*\right)^{-1/2}. \tag{8.99}$$

Multiplying both sides of this equation by $2\left(\frac{dV^*}{dx}\right)$ and rearranging gives

$$d\left[\left(\frac{dV^*}{dx}\right)^2\right] = 2\alpha \left(V^*\right)^{-1/2} dV^*. \tag{8.100}$$

This can then be integrated, resulting in

$$\left(\frac{dV^*}{dx}\right)^2 = 4\alpha \left(V^*\right)^{1/2} + C_1. \tag{8.101}$$

If current is maximized, $\frac{dV^*}{dx} = 0 = V^*$ at x=0, which sets the integration constant $C_1 = 0$. Rearranging and integrating again with the same boundary conditions gives

$$\frac{4}{3}\left(V^*\right)^{3/4} = 2\sqrt{\alpha}x, \tag{8.102}$$

and upon replacing variables, the potential distribution for a space-charge-limited current is found as

$$V = V_a - \left(\frac{9}{4}\frac{j}{\epsilon\sqrt{\frac{2q}{m}}}\right)^{2/3} x^{4/3}. \tag{8.103}$$

For electrodes with spacing L and potential difference V_a, the maximum current is then

$$j = \frac{9}{4}\epsilon\sqrt{\frac{2q}{m}}\frac{V_a^{3/2}}{L^2}. \tag{8.104}$$

All the analysis conducted at the beginning of this EP study in Section 8.12.1 can now be re-assessed and analyzed in terms of how it corresponds to the gridded plate configuration. If a beam could pass through the negative electrode (accelerator grid) without slowing down, the maximum thrust per unit area of beam is given by

$$\frac{\mathcal{T}}{A} = \frac{\dot{m}u_e}{A}, \tag{8.105}$$

where u_e is the velocity of the particle at the accelerator grid, $x = L$. The mass flow rate per unit area can be rewritten as

$$\frac{\dot{m}}{A} = \frac{\rho_e u_e}{q/m} = \frac{j}{q/m}, \tag{8.106}$$

and the exit velocity as

$$u_e = \sqrt{2\left(q/m\right)V_a}. \tag{8.107}$$

The maximum thrust per unit area then becomes

$$\frac{\mathcal{T}}{A} = \sqrt{\frac{2}{q/m}}jV_a^{1/2}, \tag{8.108}$$

or using Equation 8.104,

$$\frac{\mathcal{T}}{A} = \frac{8}{9}\epsilon_0\left(\frac{V_a}{L}\right)^2. \tag{8.109}$$

It can be seen from these results that the maximum thrust per unit area only depends on the average electrostatic field intensity, which is limited by the voltage-breakdown characteristics of the acceleration gap. Going back to the definition of I_{sp} for an ion propulsion system

$$I_{sp} = \frac{1}{g_e}\sqrt{2\frac{q}{m}V_a},$$ (8.110)

the maximum thrust per unit area can be written

$$\frac{\mathcal{T}}{A} = \frac{2}{9}\frac{\epsilon_0}{L^2}\frac{(g_e I_{sp})^4}{(q/m)^2}.$$ (8.111)

For any finite beam of diameter, D, the thrust is essentially one-dimensional, meaning thrust can be determined by

$$\mathcal{T} = \frac{2\pi}{9}\epsilon_0 V_a^2 R^2,$$ (8.112)

where R is the beam aspect ratio, D/L.

Equation 8.111 shows a strong dependence of thrust on the specific impulse. For a given propellant, the I_sp determines the acceleration potential, V_a, that limits the current density for any given spacing of the electrodes given that the source is capable of providing this current density. This means that it is advantageous to reduce the electrode (grid) spacing as much as possible.

Now that the equations have been derived, the spacing and potential difference of the gridded plates for the NEXT-C can be determined. Equation 8.111 was solved for the grid spacing, L, and given the reported properties of the NEXT-C the grid spacing was approximated to be **2.316 mm**. One study of grid separation reported successful operation with separations as small as 0.7 mm, so this result appears reasonable [108]. To determine the potential difference, V_a, of the gridded plates, Equation 8.109 was solved using this newly determined grid spacing. The potential difference between the two grid plates for the NEXT-C was thus determined to be **1131.76 V**. Comparing this value to that determined in Section 8.12.1 in Equation 8.80 shows strong agreement.

This analysis of the gridded plates assumes only two electrodes, however, it has been shown that current density can be greatly increased for a given specific impulse by using three electrodes. This three-plate system uses an "acceleration-deceleration" system that allows for operation at the maximum potential gradient. This removes the limitation on current density by specific impulse. The NEXT-C may implement this method to achieve its extreme efficiency and performance, however the basic analysis covered in this report does not include this possibility.

9 Scuttle Mission Spacecraft: Mark II

Following analysis of the structural makeup of the Scuttle Mission spacecraft, the model was correspondingly updated to match the determined size and shape requirements. At this same point, several design changes were implemented and the entire model was remade. This section contains the updated model, details the alterations and improvements made to the model, and includes a verification that this improved model continues to meet the requirements set forth at the onset of this mission.

9.1 Changes and Explanation

The changes made from the MKI spacecraft to MKII can be described as 6 overhauls. These alterations were made with practicality, ease of manufacturing, and accuracy of model in mind. The following sections detail these overhauls.

9.1.1 External Mounting and Equipment Placement

Scientific equipment, originally arbitrarily placed around and within the upper structure, moved to a single assembly on the (0,Y) face in order for all lenses to face the same direction. RCS hydrazine thruster clusters and reaction wheels were also moved to their respective faces. All of these placements are in compliance with Figure 8.1.2, used for the structural analysis. The placement of these parts are pictured with the full MKII spacecraft in Figure 9.1.1.
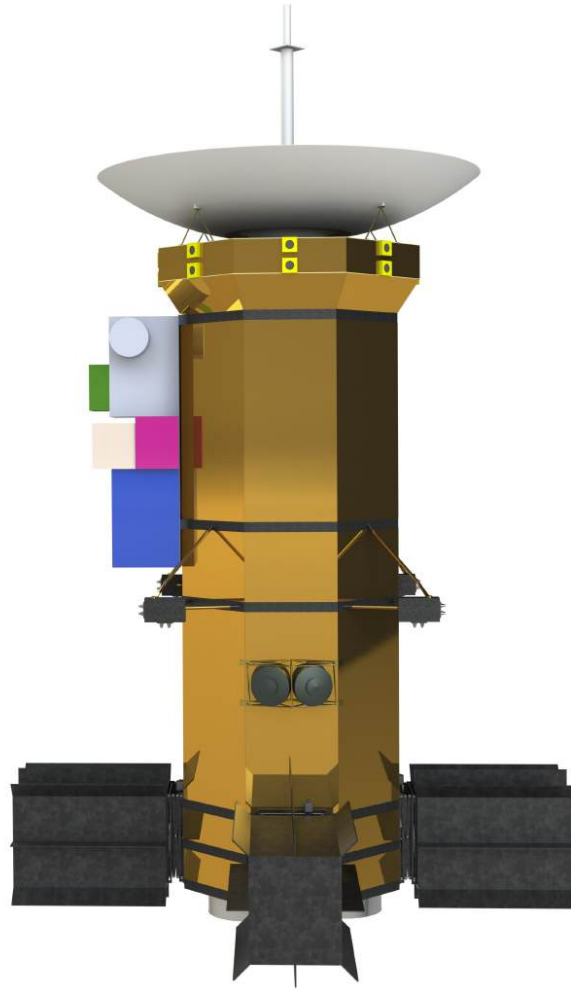
Figure 9.1.1: Scuttle MK2: Visible RCS, reaction wheels and equipment assembly .

9.1.2 Top Assembly

The top assembly contains the angled portion of the hull above the equipment to the top of the HGA. This section was decreased in height due to the equipment moving to the middle body. This helped to decrease the overall height of the spacecraft and the structural mass. Furthermore, the HGA was attached to its supports closer to the top assembly. A close-up view of this top assembly is detailed in Figure 9.1.2.
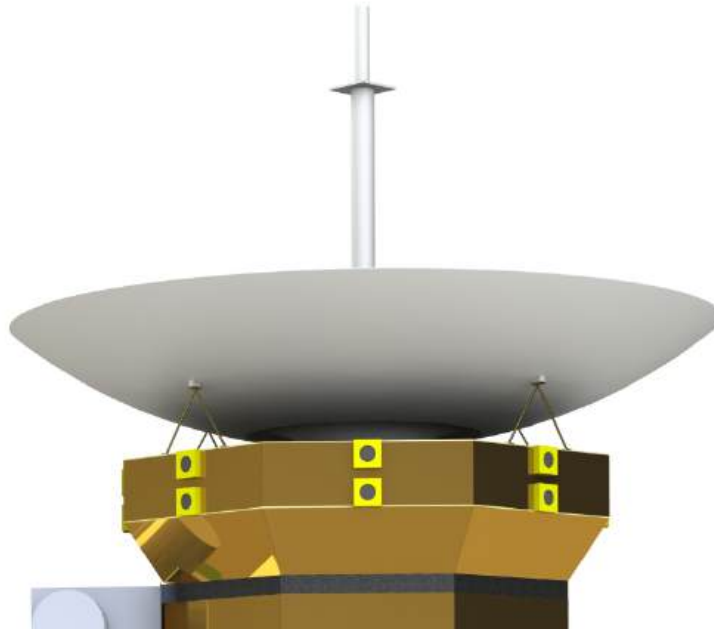
Figure 9.1.2: Scuttle MK2: Enhanced view of top assembly and HGA .

9.1.3 ASRG Mounting

Unlike Scuttle MKI, which hard mounted the ASRGs to the hull of the spacecraft, MKII deploys HDMRs to release the ASRGs from their launch supports and extend them out with a scissor boom with the assistance of a non-capture linear actuator. A collapsed view of the new ASRG boom assembly is illustrated in Figure 9.1.3, and Figure 9.1.4 details the extended position.
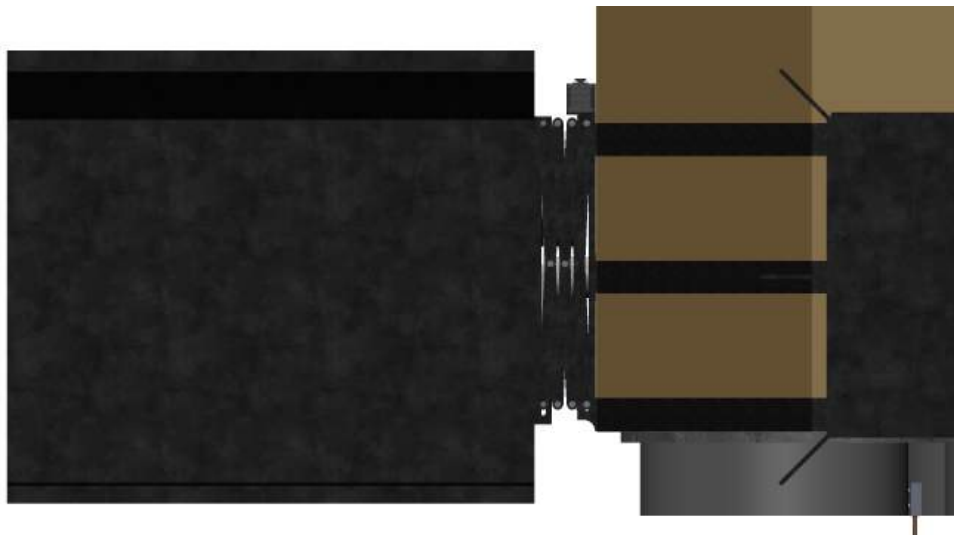
Figure 9.1.3: Scuttle MK2: Side view of collapsed ASRG boom in launch position.
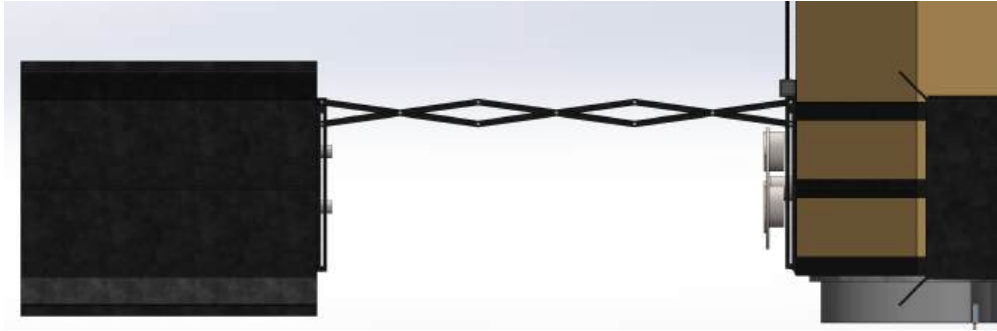
Figure 9.1.4: Scuttle MK2: Side view of extended ASRG boom in orbit and space travel position.

Figure 9.1.5 reveals the ASRG support that holds the ASRG under launch loads and the supporting plate with female HDMRs that allow it to detach from the support to be pushed out by the boom.

Figure 9.1.5: Scuttle MK2: ASRG launch mounting plate and HDMR female ends.

Subsequently, Figure 9.1.6 shows the non-captive linear actuator along with HDMR male ends.

Figure 9.1.6: Scuttle MK2: View of ASRG from mount plate detailing linear actuator rod path and male HDMR pins.

An enhanced look at the linear actuator partially extended is shown in Figure 9.1.7.

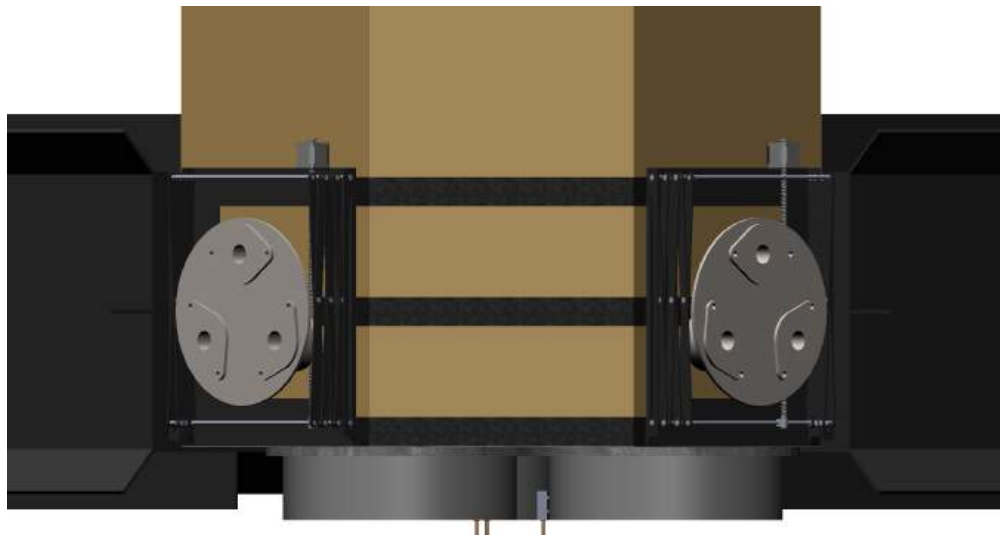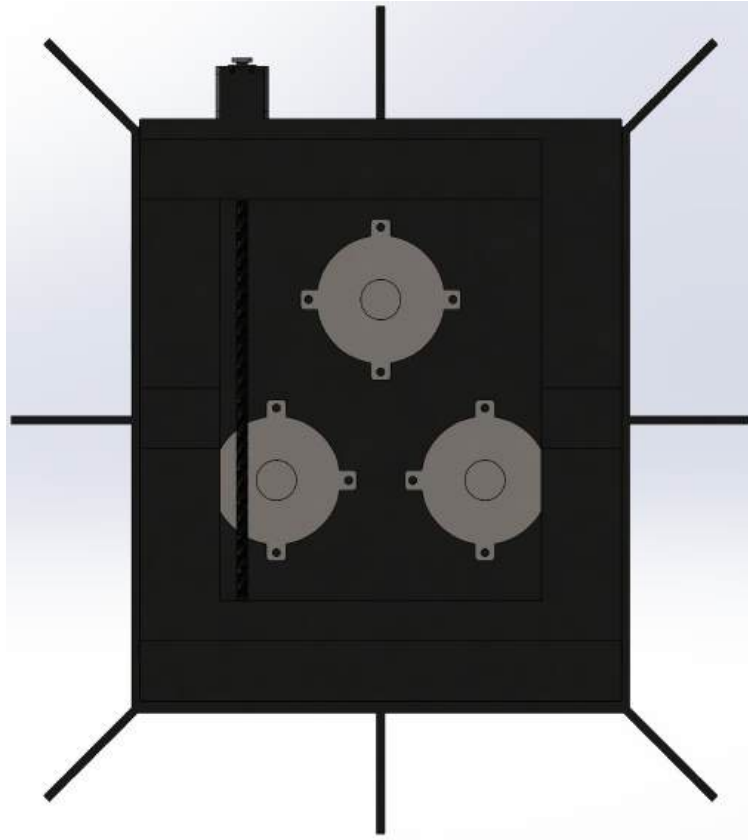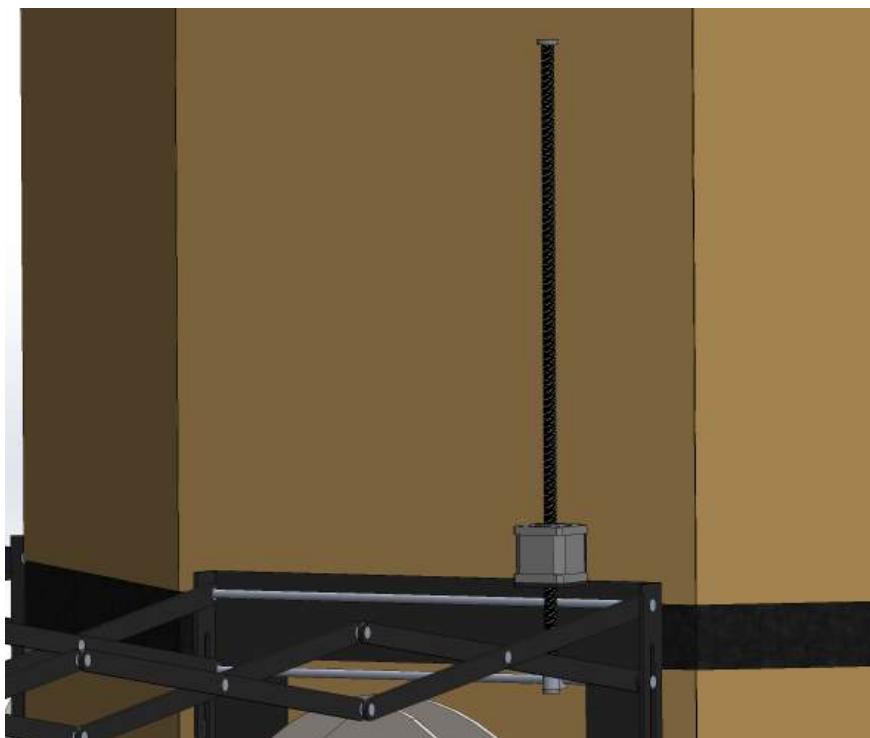Figure 9.1.7: Scuttle MK2: Detailed view of non-capture linear actuator extended with boom extension.

9.1.4 Bottom Module and EP Positioning

Scuttle MK1 saw the lower assembly have a lofted section where the upper octagon went to a smaller circular shape that could only support 1 EP thruster, The other 2 thrusters were mounted at an angle, creating a three pronged shape. Scuttle MKII holds the octagon frame shape uniform to the very bottom where all three EP thrusters are mounted in a triangle pattern pointing the same direction. The thrusters are also partially recessed into the hull. Keeping all 3 thrusters in the same direction was the main reason for this change, although the angled bottom piece was also spatially inefficient as it resulted in dead space that tanks and other equipment could not sit in, inflating the overall height. Figure 9.1.8 shows the geometric layout of the EP thrusters and Figure 9.1.9 shows the protrusion from the hull. Figure 9.1.10 shows a complete rear angled view of the Scuttle spacecraft to give a semblence of scale to the EP exit ports.
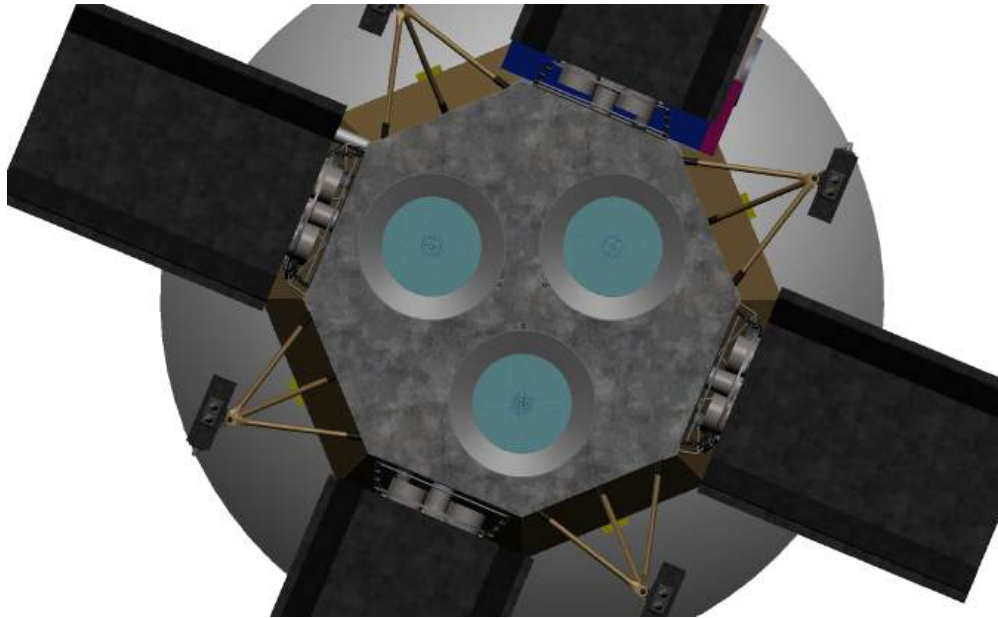
Figure 9.1.8: Scuttle MK2: Bottom view of EP thrusters.
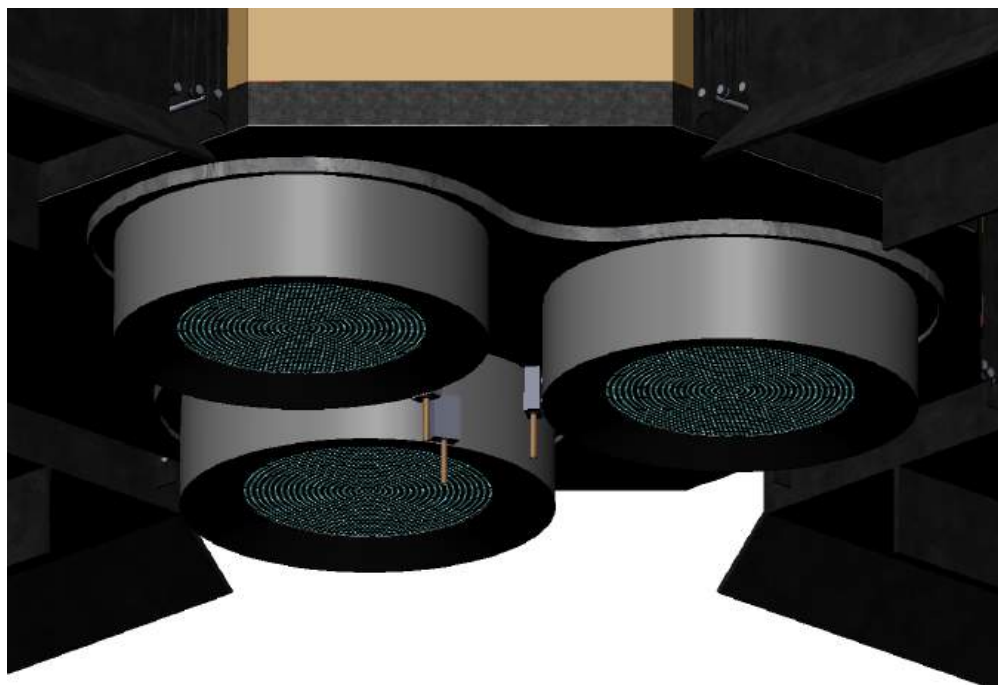
Figure 9.1.9: Scuttle MK2: Side view with EP protrusion.
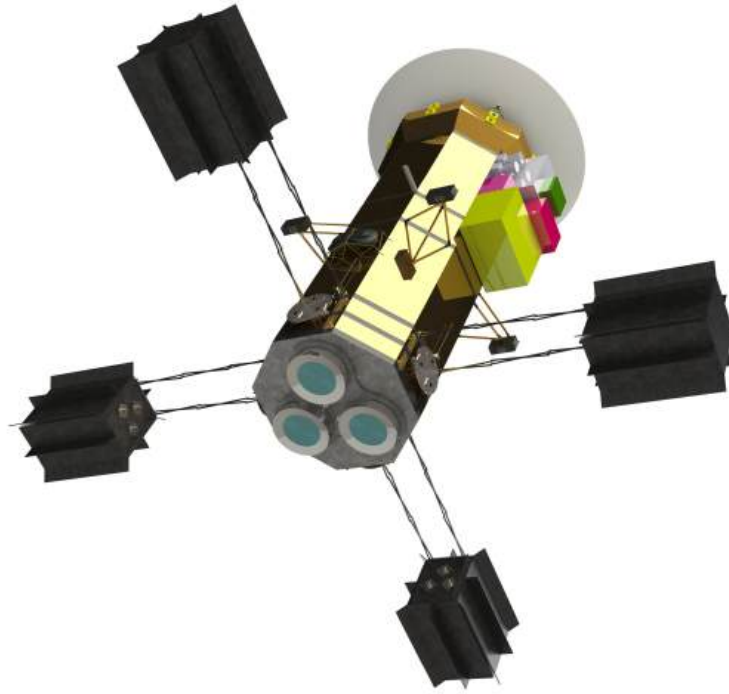
Figure 9.1.10: Rear angled view of Scuttle MKII with EP thrusters in full view.

9.1.5 Internals

As more systems were added to the Scuttle spacecraft, it became evident that the overall size and mountings were obsolete. More room was required for dual Xenon tanks and the hydrazine and helium tanks would not fit within the shielding of Scuttle MKI. The result was a longer spacecraft, and a spacecraft that takes advantage of modules. Most notably, each xenon tank received its own structural module, and these two structures were separated by a module of the exact same dimensions, apart from a height that was chosen to create the correct amount of space to mount the helium and dual hydrazine tanks. Scuttle MKII's bottom section that mounts the ASRGs and holds the EP system also utilizes the same modularity style. Figure 9.1.12 shows a full view of these modules with the black octagon sides denoting the boundaries of each modulus. Figure 9.1.11 shows a detailed perspective of the tanks in the hull.
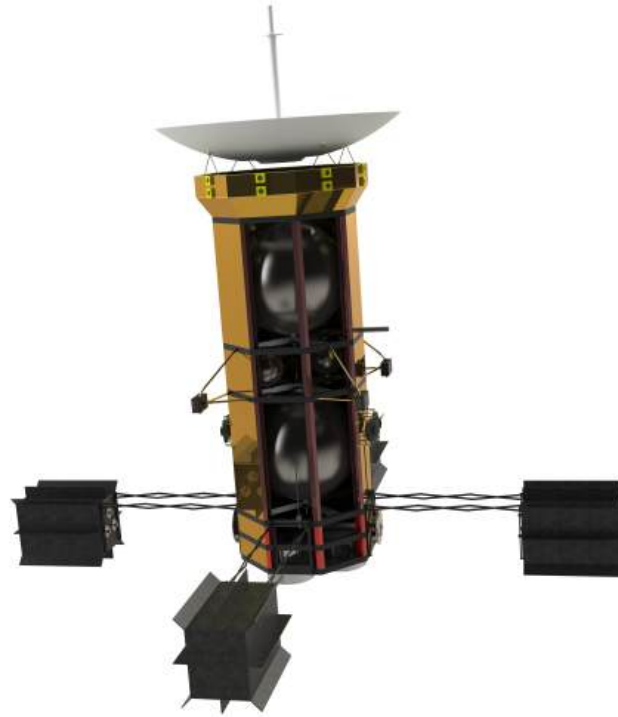
Figure 9.1.11: Scuttle cut out.

Figure 9.1.12: Scuttle cut out.

With this improved design, the updated masses of Scuttle MKII can be seen in Table 9.1.1

Table 9.1.1: Scuttle MKII mass values

Item	Mass (Kg)
Dry Weight as Modeled	2700.35
Xenon Propellant	2837
Hydrazine Fuel	74.33
Pressuring Helium	0.402

With the addition of electrical wiring and plumbing systems to this model, the total mass will increase; however, the Scuttle missions weight without xenon would be within an acceptable range of the 3000 kg originally targeted.

9.2   Analysis to Confirm Integrity of Changes

To begin the new finite element model, the same general principles from Section 8.5 are used with a model with altered geometry. Any pertinent information not found in this section is listed in Section 8.5, since the model was so similar to the original. A new coordinate system was created that was based off of the original one to make the necessary changes. Figure 9.2.1 shows how the model has changed, without the shielding. Some of the point masses were relocated due to the change in location on the CAD model. The bottom (no. 1) cross section does not exist with this model; those members were removed and the regular base cross (no. 2) cross section were used on the bottom supports.
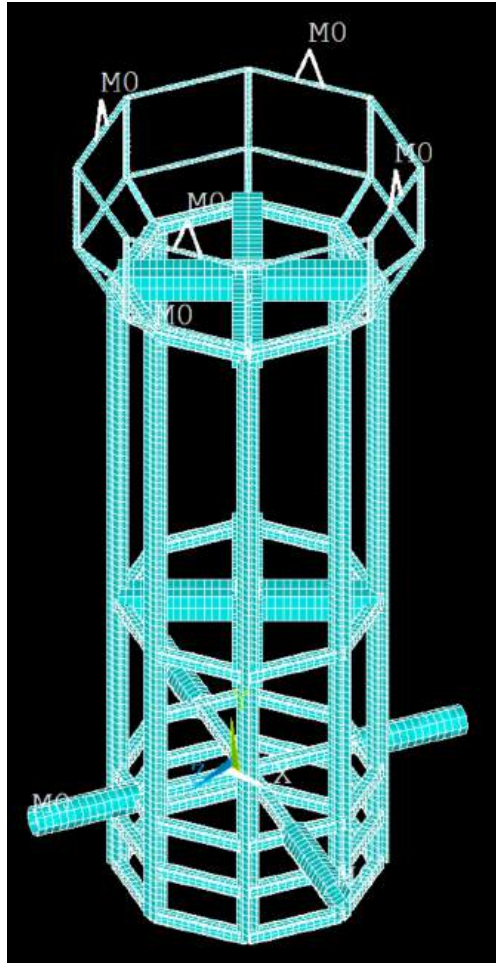
Figure 9.2.1: Updated FE model without shielding

The new model is also exclusively made out of shells (SHELL281), beams (BEAM189), and point masses (MASS21). It possesses 36,229 total nodes and 13,705 total elements. The boundary conditions were adjusted to match the payload environment closer. The lowest octagonal shape had the lines defining the beams fixed in all displacements and rotations. This fixed all the nodes on the base of the structure, which sit slightly higher than the ion thrusters would in the payload. Figure 9.2.2 shows exactly where these boundary conditions were applied.
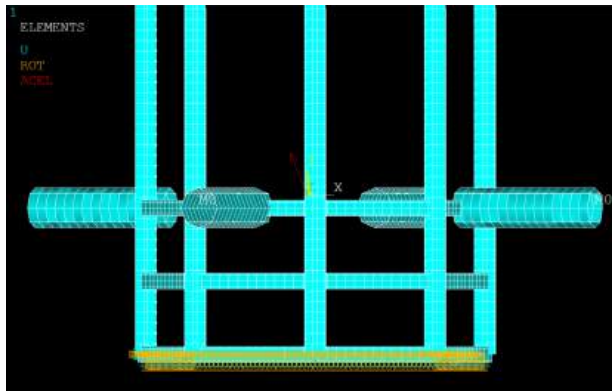
(a) Side view of fixed boundary conditions
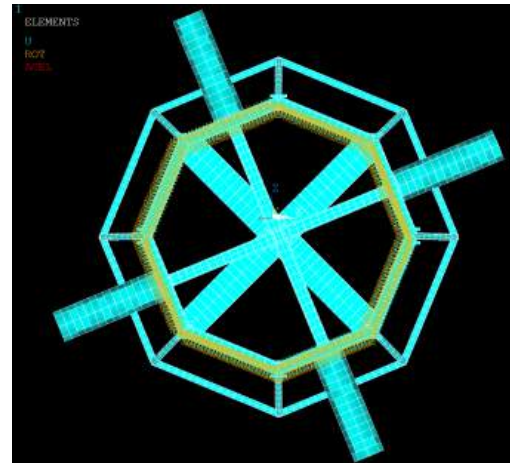
(b) Bottom view of fixed boundary conditions

Figure 9.2.2: New fixed boundary conditions applied to bottom octagonal structure.

The rest of the model stayed similar to the original one, so a solution was obtained to ensure that the new design would not fail. After inspection, the new model shows that the design is effective since no stress value exceeds the overall structural factor of safety stress value. The next set of figures explore some of the main cross sections that were defined in Section 8.5.4. Figure 9.2.3 shows the bottom cross beams in the fully loaded state. The cross section was altered to have wall thickness of 7 mm instead of 10 mm to come closer to the desired factor of safety of 1.5.
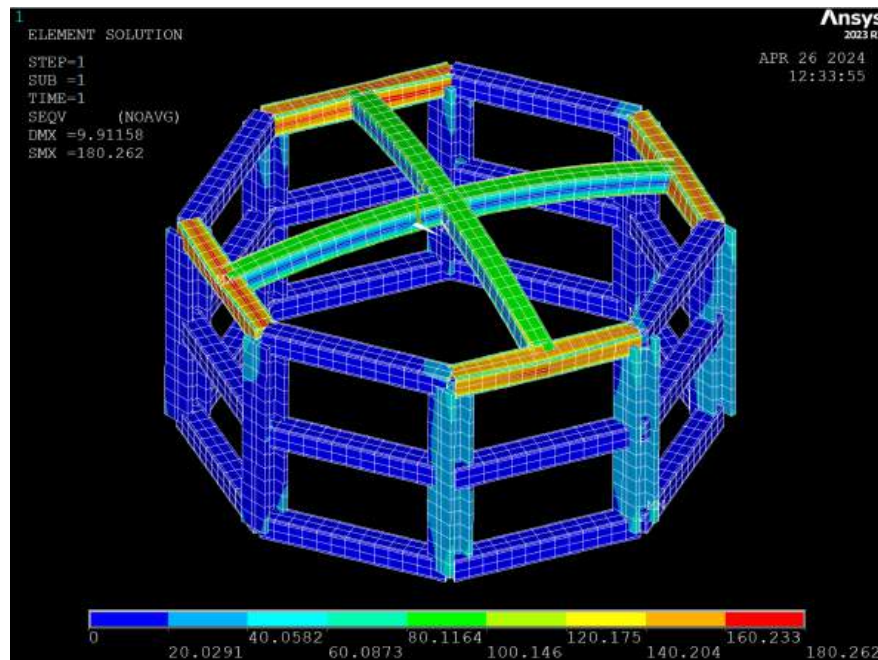
Figure 9.2.3: Bottom cross (no. 2) von Mises stress in MPa

The maximum seen in Figure 9.2.3 is 180 MPa, which is under the aluminum maximum with a 1.5 factor of safety at 184 MPa. Next, the I-beam is inspected closer in Figure 9.2.4. The section shown Figure 9.2.4 is the I-beam sections below where the RTGs are mounted; the stresses in the higher up sections are much lower.
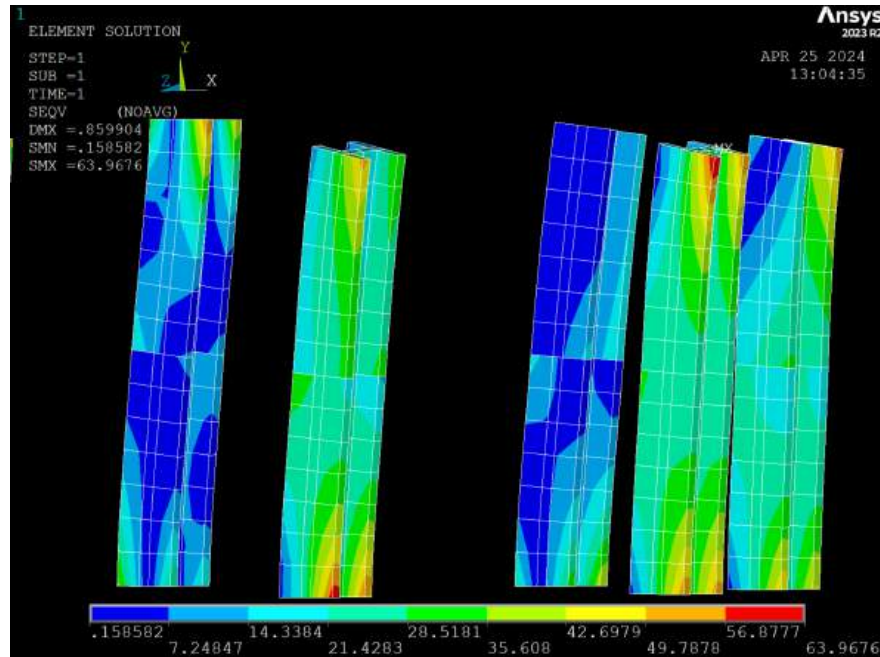
Figure 9.2.4: I-beam (no. 3) von Mises stress in MPa

Lastly, the team checked the maximum lateral displacement of the model to ensure that there would be no contact with the outer walls of the launch vehicle payload fairing. To do this, the x-displacement was plotted, which is the same direction as the lateral acceleration applied to the model. Figure 9.2.5 shows where the maximum displacement occurs, which is at a high gain antenna support.
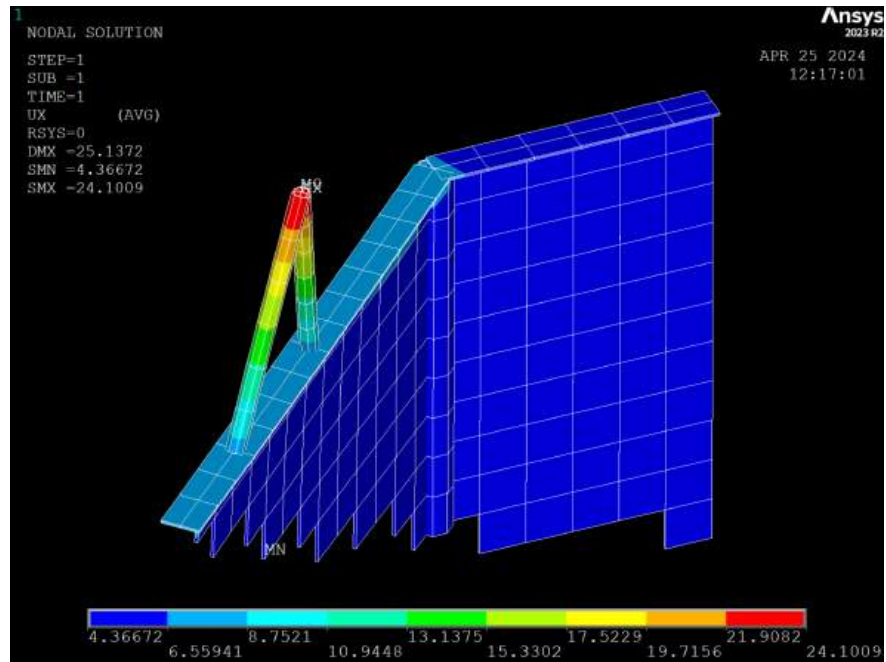
Figure 9.2.5: Maximum x-direction displacement within FE model, in mm

The maximum displacement in the x-direction is only about 3 cm, which is well less than a value that would make contact with the side of the fairing a concern. The dish has a diameter of 3 m and the diameter of the launch vehicle fairing is 4.6 m (see Figure 2.3.1). This concludes that the satellite is able to survive launch from the static loading cases it experiences.

10   Conclusion

The Scuttle Mission aims to study Uranus' moon, Ariel, to learn more about its icy surface and shed light on the creation of the universe. To complete the deep space mission to Ariel, a 2.6 billion kilometer journey, the Scuttle spacecraft will utilize continuous, low thrust, highly efficient ion thrusters to drastically reduce the mass of propellant required. To generate the necessary electric power to operate these thrusters and the on-board instruments, four experimental Advanced Stirling Radio isotopic Generators will be equipped with a combined output of 23.33 kW. At 30% efficiency, this output is enough to power one of the three ion thrusters. Thus, the thrusters will be used intermittently as needed.

In its current configuration, the Scuttle MKII has a total modeled weight of 5,612 kg when fully fueled. With the help of a SpaceX Falcon 9 rocket, Scuttle will take 24.54 years to reach Uranus via a spiral orbit about the Sun; 19.46 of those years are the trajectory to Uranus itself, comparable to the 19.39 years for a conventional rocket that utilizes a gravity assist around Saturn. Therefore the process of traveling from an escape orbit to Uranus using electric propulsion has no downside; however, the 5.08 years required to go from LEO to escape due to the large mass of the spacecraft leaves much to be desired, and would make that portion of the journey unrealistic if target time is crucial.

Due to its efficiency and spiral orbit, Scuttle's ion thrusters allow its departing date to be less defined than conventional impulsive methods. Problems arise when considering the process of continuous thrust to a point and then shutting off the engine to glide into Uranus' sphere of influence. While this is necessary to decrease velocity, any path corrections would need to occur well within its powered flight time and immediate urgent corrections would most likely be ineffective. This also leaves the Scuttle spacecraft vulnerable to potential large debris in its path.

The Scuttle mission's largest hurdle was the lack of available information surrounding complete ion thruster specifications in addition to the limited data surrounding key attributes of the ASRGs. From this, many calculations had to be approached based on comparisons to smaller test variants and potentially outdated studies. With resumed and further development of large scale ASRGs, the emitted heat from the 43.75 kg of Pu238 can be more accurately modeled and boom sizes and fin surface areas can be altered to compensate for changes. More public data on electric propulsion would give a clearer value on how their complex pressure regulation systems work and the hardware that supports the thrusters themselves. The Scuttle Mission's biggest potential change would be considering use of a chemical propellant when escaping Earth's sphere of influence rather than electric propulsion or utilizing a longer range rocket to put the spacecraft in a near escape orbit. This would drastically decrease the amount of time it takes the spacecraft to escape Earth's sphere of influence and allow the total mission time to be competitive with conventional methods of propulsion.

Scuttle Mission effectively uses ion propulsion to achieve its deep space mission of reaching Ariel. Although more data and testing would be required to completely develop this

spacecraft, Scuttle shows that electric propulsion, in combination with ASRG power systems, can deliver specialized spacecrafts to their target and relay inspiring data back to Earth. The Scuttle Mission is driven by discovery, and the Ariel Voyagers have taken an intrepidacious approach, aiming to push the boundaries of innovation in the name of exploration.
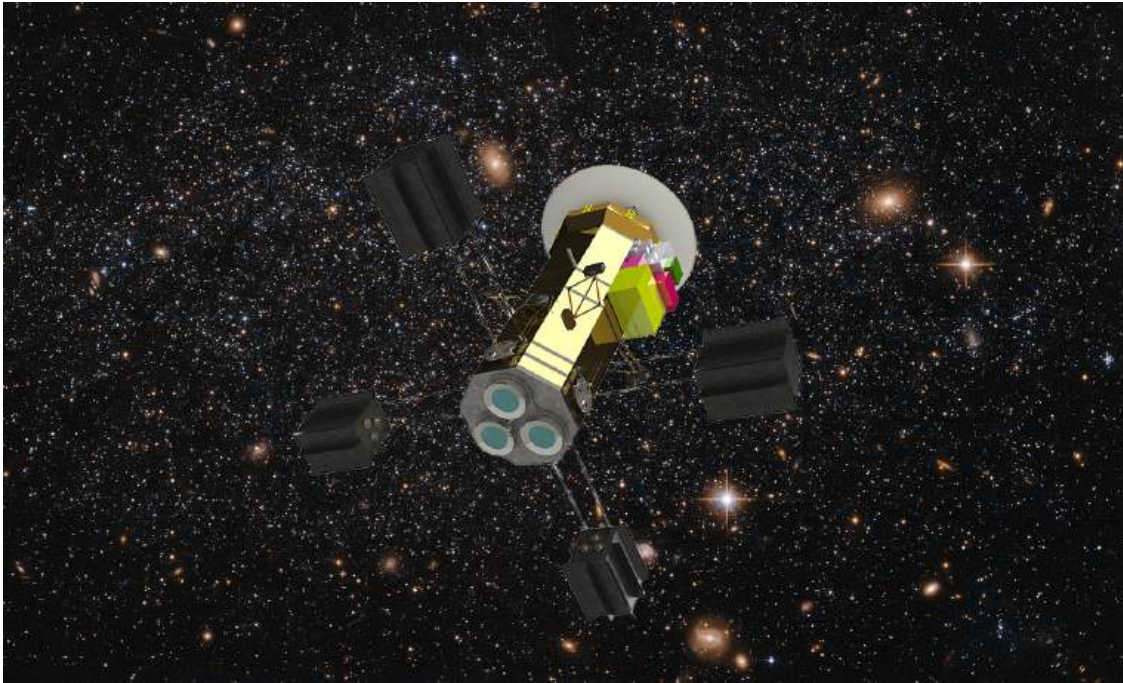
Figure 10.0.6: Scuttle satellite shown in deep space.

11 Appendix

This section contains all relevant appendices for this report.

11.1 Appendix I: Product Design Specifications

The following document shows all Product Design Specifications.

<u>**EMA 569**</u>

<u>**Product Design Specification**</u>

Product → **Scuttle Mission**

Date → **1/29/2023**

Revision → -

Group Members → **Olivia Janson, Matthew Brandt, Kaden Reybrock, Chase Orvis**

Guidelines	Specification Element	Team Design	Competition
The performance demanded or likely to be demanded should be **fully defined**. Is the performance demanded attainable in an economic manner? A common failure in specifying performance is to ask for the ultimate, rather than that which is obtainable.	**Performance**	Approximately 2.6 billion [km] Travel Distance to Uranus' Moon Ariel. Electric propulsion system (Gridded Ion or Hall Effect Thrusters) utilizing Xe, powered by solar panels. Reduce the amount of other propulsion methods as much as possible. Maintain similar time duration while decreasing mass vs chemical-based rocket.	Dawn: Traveled 6.4 billion [km]. Took 95,000 photos, 167+ GB of data collected. 3 dual-axis ion thrusters that provided 2,000 days of thrust. 0-100 [kph] in 4 days. Propellant mass flow rate of 3.25 [mg/s] while
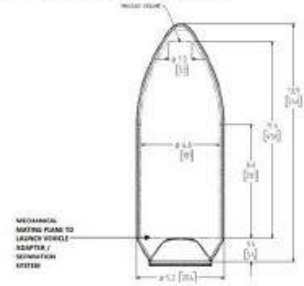
			carrying 425 kg of fuel.
All aspects of the product's likely environment should be considered and investigated: • Temperature range. • Pressure range (altitude). • Humidity. • Shock loading (gravity forces). • Dirty or dusty? How dirty? • Corrosion from fluids. • Noise levels. • Insects. • Vibration.	**Environment**	G forces vs. vibration in launch vehicle (Falcon 9): 4 shock events: 100 Hz @ 20 g 270 Hz @ 240 g 2000 Hz @ 3000 g 10000 Hz @ 3000 g Humidity during launch: 45 - 55 percent Corrosion from sun, solar wind, atomic oxygen, etc. Temperatures ranging from -255° F to 255° F depending on the orientation relative to the Sun. Avoid space debris, natural satellites, micrometeorites (Uranus rings are much closer to planet than Ariel's orbit).	Similar temperature ranges to our determined range. New horizon mission, same deep space conditions.
Is regular maintenance available or desirable? Will designing a maintenance-free product be too expensive to buy in the first place? Does the company, or indeed the market into which the product will ultimately go, have a definitive maintenance policy? Is the market used to maintaining equipment once it is purchased?	**Maintenance**	Regular maintenance will not be required and will not likely be possible after the mission begins. Redundancies will be designed wherever possible to reduce the risk of failure to the mission from a single component failure. Although not necessarily a component of this course, many	Regular maintenance not required and not likely possible. Dawn has since been retired.

• Specify ease of access to the parts that are likely to require maintenance. It is no good calling for regular maintenance if it takes 10 days to reach the part. • What is the maintenance and spares philosophy of the company and market? • What is the likely need and desirability of special tools for maintenance?		simulations, flight-tests, and instrumentation tests would be conducted on the components and the assembly of this satellite before its launch.	
Are there any restrictions on the size of the product? Size constraints should be specified initially. Does the product size and shape make it difficult to handle?	**Size**	Size and weight would be limited by required equipment, propulsion system size/weight, and carrying capacity in both size and weight of the launch vehicle that will take the satellite out of Earth's sphere of influence. Camera imaging is desired to be sent back to Earth; communication system size will influence the overall size of the satellite. Instrumentation allowing for visualization: -Gimbals -Electric propulsion/Ion motor stabilization -Communication equipment	Dawn: 1.64 meters long, 1.27 meters wide and 1.77 meters high. High-gain antenna is 1.52 meters in diameter. Solar array is 20 meters long, tip to tip.

		-Radiation shielding -Potential impact protection - Italian Camera (visible and mid infrared) -Magnetometer -Near infrared mapping spectrometer Max dimensions set by launch vehicle, Falcon 9: 4.6 (diameter) by 6.6 meters; there is inclination above main payload loading that is 4.8 meters tall decreasing in total diameter. See below for details. 	
What is the desirable weight? Should the design be modular to assist in the size/weight area? Should lifting points be provided and how many people are required to move it?	**Weight**	Comparable, but slightly more than Dawn due to the additional distance to be traveled and thus additional propellant required. No modularity is required for this vehicle and all lifting required will be done by a crane and thus areas for the crane to attach to	Dawn: 747.1 [kg]. Propellant at launch: 425 [kg].

		will be designed for transport and insertion into the launch vehicle. Weight to be determined by initial astrodynamics calculations, should not be a different size of magnitude compared to past satellites: 500 [kg] to 2500 [kg] Max weight from launch vehicle (Falcon 9): 22,000 [kg]	
Think about materials that are used in similar applications or by competitor's products. What manufacturing methods will be used (welding, forming, molding)? Does your product operate in a corrosive environment? Specific materials should be specified by quoting the appropriate standard.	**Materials**	Space corrosion from sun, solar wind, atomic oxygen, etc. addressed with using titanium and aluminum alloy materials on the main body. Will follow already accepted materials and manufacturing practices for satellites. Manufacturing/assembly practices will include large amounts of welding to seal areas, and thus all welds must be rigorously tested to NASA's welding standards. Materials and manufacturing processes following NASA-STD-6016	Dawn: Xenon propellant. NASA approved materials.

		Metallic material selection following MSFC-STD-3029A to control stress corrosion cracking Common materials: - Kevlar: lightweight and strong, resistant to temperature changes, ideal for protecting satellites from orbital debris - Aluminum alloys: lightweight and strong Propellant: Xenon - Nearly as high a thruster efficiency as mercury [Hg] (highest) - More environmentally acceptable than Hg - Relatively expensive and rarer than other options, but can be stored noncryogenically (Other EP fuels such as Argon require cryogenic storage)	
Some indication of the life of a product as a marketable entity should be sought. Is it likely to remain in production for two years or 20 years? The answer is crucial as it can affect the design approach and interacts with the	**Product Life Span**	At least 50 years, it will be a one-time use satellite. No longer than 100 years to destination. No return to Earth, will orbit Ariel until product death.	Dawn: 14 months in Vesta's orbit then to perpetual orbit around Ceres.

market and competition, tooling policy, manufacturing facility and the like.			
Is the product to be designed to current international and/or US standards? If so, then these should be specified and copies obtained. Cross-correlation of such standards should be carried out prior to commencement of the design. It is difficult, costly, time consuming and inefficient to attempt retrospective matching of designs already finalized to such standards.	**Standards and Specifications**	Designed to NASA technical standards: 1000-Systems Engineering and Integration, Aerospace Environments, Celestial Mechanics - NASA-HDBK-1004 - NASA-HDBK-1005 - NASA-HDBK-1009 4000-Electrical and Electronics Systems, Avionics/Control Systems, Optics - NASA-HDBK-4001 - NASA-HDBK-4002 - NASA-HDBK-4006 - NASA-HDBK-4007 - NASA-HDBK-4008 - NASA-HDBK-4009 5000-Structure/Mechanical Systems, Fluid Dynamics, Thermal, Propulsion, Aerodynamics - NASA-HDBK-5010 (Vol. 1 and 2) - NASA-STD-5001 - NASA-STD-5002 - NASA-STD-5006 - NASA-STD-5012	Dawn: Completed to NASA technical standards.

		6000-Materials and Processes - NASA-STD-6016 - MSFC-STD-3029A		
All products have to some degree a man-machine interface. What height, reach, forces and operating torques are acceptable to the user? Consult with potential users of the product.	**Ergonomics and Human Factors**	Mostly non-applicable once satellite is in space. Can potentially adjust imaging software if communication returns undesirable pictures. Should relay information smoothly to operator. Orientation systems will be required to ensure communication of avionic systems and testing instruments.		
Who is buying / using your product? How many units can you sell in a year? It is essential to obtain first-hand information on customer likes, dislikes, preferences and prejudices.	**Customer / Market**	Single product made for space agency use. Designed for agency's specific use/mission, including required equipment.	NASA is required to justify projects to the white house/congress to receive government funding. Most applications of electric propulsion maneuver in Earth's sphere of influence (ex.	

			SpaceX's Starlink satellites).
Most products require some form of testing after manufacture, either in the factory, on site or both. Do we sample test one in ten, one in a hundred, or what? Do we need a new test facility? How can we be sure that the product is designed to have rapid engagement with and detachment from the test rig? Data collection and product history are needed to answer these questions. An initial test specification should be written at this stage.	**Testing**	Test the electric propulsion system and solar extending array. These tests will be done to ensure the systems work both individually and in conjunction with the other on-board systems. A number of these tests will require use of Glenn Research Center's EPPL to test the electric propulsion system, as the large amount of expelled gas requires a large testing chamber to maintain a vacuum. Test scientific equipment will already be tried and true items. Many simulations, flight-tests, and instrumentation tests would be conducted on the components and the assembly of this satellite before its launch. These tests will ensure the systems will continue to operate as designed after subjected to the launch loads. Rocket to perform large impulses to get outside of Earth's SOI, is made by other source (Atlas V).	Dawn: Tested ion propulsion engine with five throttle levels.

The safety aspects of the proposed design and its place in the market must be considered. • OSHA standards for workplace safety • User safety: sharp edges, pinch points, potential misuse. • Public safety: are there potential dangers to those in or around the area the product is being used? • Human Welfare: Does your product benefit those in need?	**Safety, Public Health, and Human Welfare**	Benefits the scientific community by providing data to study and learn about planetary systems and their compositions. All communication systems will be such that they will not interfere with other Earth broadcasting satellites and communication devices. Shielding will be put in place to prevent inadvertent signal scattering. 3000-Human Factors and Health https://standards.nasa.gov/NASA-Technical-Standards Human welfare/ public safety: Protect society from unknown lifeforms if they were to be discovered. Since the craft will not return to Earth, there is not a concern of contamination.	Dawn, Starlink: FAA approval required to ensure launch is not a danger to public safety.
Economic, Social and cultural factors affecting business/products include belief systems and practices, customs, traditions and behaviors of all people in given country, and market activities influencing actions and decisions.	**Economic, Cultural, Social Factors**	Success of the mission, getting there on time and extracting the data to share with the public, with respect to funds expended in the eyes of the taxpayers. Displaying the US flag on satellite.	Dawn: First to orbit a main-belt asteroid. First to reach dwarf planet.

Consider the following in assessing your product • social classes & influence on the society • disposable income level and wealth of your customers • economic inequalities • level and access to education • level and access to health-care • health consciousness in society • buying habits and consumer preferences • conflicts within society		Success of mission with respect to future missions where the ocean can be explored (scouting landing spots, cost estimates, priority to explore). In designing an electrically powered spacecraft, several new inventions and discoveries may be made that could be used for different applications. This is seen often following innovation in the aerospace industry. One such example could be through the power plant that runs the EP system. A highly efficient plant could spark innovation in the ways to improve the power and efficiency of solar panels, making it more beneficial for everyday people and potentially more available.	Explored the two largest planetesimals. Won award at Space Symposium in 2019.
Discuss environmental cost/benefit of your product. Think about the full product life cycle including manufacturing, transportation, use, and disposal. • Product end-of-life. Is it recyclable? • Does it contain hazardous chemicals? • Is there an environmental impact from the mining of raw materials used on your product?	**Environment**	Mining rare earth materials (Electric propulsion system and solar panels). Xenon propellant to be handled with all necessary precautions. Product will not directly help environment, but through its development solar power may experience technological improvements which could	Dawn: One time use. Rocket thrust pollution. Combustion of NASA's fuel in the solid booster rocket contributes to

• Does your product help the environment? Clean energy, carbon-free transportation, clean pollution • Impact on global warming / carbon footprint • Eco-friendly materials • See these tips: https://business.vic.gov.au/business-information/sustainability/design-sustainable-products		indirectly benefit the environment. Rocket thrust pollution, increased carbon dioxide emissions. One time use, will not be recuperated.	global warming.

11.2 Appendix II: Matlab Orbital Calculations

```matlab
%% Senior Design Low Thrust Spiral Approximation
% Earth Orbit Escape
% Kaden Reybrock
% 2/19/2024

clear;close all;clc

% Knowns & Parameters
r_e = 6.371E6; % Earth's mean radius [m]
earth_soi = 994000000+zeros(1,360); % Earth's sphere of influence [m]
r_0 = 2000000+r_e; % Initial circular orbit radius (m)
g = 9.81.*(r_e./(r_e + 2000000)).^2; % gravitational accel in initial Earth orbit [m/s^2
G = 6.670E-11; % Gravitational Constant [N-m^2/kg^2]
M = 5839; % Mass of spacecraft [kg]
M_prime = 5.972E24; % Mass of Earth [kg]
Theta = .236; % Thrust [N]
c = 40000; % [m/s]

% Assume purely angular burn (in polar coord's)
nu = Theta./(M.*g); % Circumferential Thrust Factor

tau_1 = (1-(2.*nu).^(0.25))./nu; % End condition

tau = linspace(0,tau_1,1000); % Non-dimensional time
rho = zeros(1,length(tau));

for i=1:length(tau)
    rho(i) = 1./((1-nu.*tau(i)).^2); % Approximate solution for the defining EOM
end

figure(1)
plot(tau,rho)
xlabel('\tau [-]')
ylabel('\rho [-]')
title('Non-Dimensional Radial Distance from Earth over Time')

% Non-dimensional Variables
%~~~~~~~~~~~~~~~~~~~~~~~~~~~~~~~~~~~~~~~~~~~~~~~~~~~~~~~~~~~~~~~~~~~~~~~~~~~
%
%rho = r./r_0; % non-dimensional radial distance
r = rho.*r_0; % radial distance from earth

%tau = sqrt((G*M_prime)/(r_0.^3)) .* t; % non-dimensional time
t = tau./(sqrt((G*M_prime)/(r_0.^3))); % time
```

```matlab
t_1 = tau_1./(sqrt((G*M_prime)/(r_0.^3))); % Escape time
t_days = t./86400;
t_1_days = t_1/86400;


figure(2)
plot(t_days,r)
xlabel('Time(t) [days]')
ylabel('Orbital Radius(r) [m]')
title('Radial Distance from Earth over Time')

% Velocities / Rates
%~~~~~~~~~~~~~~~~~~~~~~~~~~~~~~~~~~~~~~~~~~~~~~~~~~~~~~~~~~~~~~~~
dtheta_dtau = (1-nu.*tau)./rho; % Non-dimensional angular velocity
dtheta_dt = dtheta_dtau .* sqrt(g/r_0); % Angular velocity [rad/s]
drho_dtau = (2.*nu)./((1-nu.*tau).^3); % Non-dimensional radial velocity
dr_dt = drho_dtau .* sqrt(g/r_0) .* r_0; % Radial velocity [m/s]
dtheta_dt_deg = dtheta_dt .* 180 ./ pi; % Angular velocity [deg]

total_velo = sqrt(dr_dt.^2 + dtheta_dt.^2);
escape_velo = sqrt((2.*G.*M_prime)./(r));

% Velocity Plots
%~~~~~~~~~~~~~~~~~~~~~~~~~~~~~~~~~~~~~~~~~~~~~~~~~~~~~~~~~~~~~~~~~~~~~
figure(3)
plot(t_days,dtheta_dt)
xlabel('time(t) [days]')
ylabel('$\frac{d\theta}{dt}$ [$\frac{rad}{s}$]','Interpreter','latex')
title('Orbital Position over Time')

figure(4)
plot(t_days,dtheta_dt_deg)
xlabel('time(t) [days]')
ylabel('$\frac{d\theta}{dt}$ [$\frac{deg}{s}$]','Interpreter','latex')
title('Orbital Velocity over Time')

figure(5)
plot(t_days,dr_dt)
xlabel('time(t) [days]')
ylabel('$\frac{dr}{dt}$ [$\frac{m}{s}$]','Interpreter','latex')
title('Radial Velocity over Time')

% Energy to escape Earth's SOI
%~~~~~~~~~~~~~~~~~~~~~~~~~~~~~~~~~~~~~~~~~~~~~~~~~~~~~~~~~~~~~~~~~~~~~~~~~~
%
```

```
Radial = 0.5.*(dr_dt).^2;
Centrifugal = 0.5*(r.*dtheta_dt).^2;
Energy = 0.5.*((dr_dt).^2 + (r.*dtheta_dt).^2) - g.*(r_0.^2)./r;
Gravity = (G.*M_prime.*M)./r;

figure(6)
plot(t_days,total_velo)
hold on;
plot(t_days,escape_velo)
xlabel('Time [days]')
ylabel('Velocity [m/s]')

% Polar Plots: Trajectory
%~~~~~~~~~~~~~~~~~~~~~~~~~~~~~~~~~~~~~~~~~~~~~~~~~~~~~~~~~~~~~~~~~~~~~~~~~~~~~~
theta = zeros(1,length(t));
for j=1:length(t)
    if j==1
        theta(j) = 0;
    else
        theta(j) = theta(j-1) + dtheta_dt(j-1).*(t(j)-t(j-1));
    end
end

revolutions = theta(length(t))./(2*pi);
figure(7)
polarplot(theta,r,'r.-')
hold on;
polarplot(earth_soi,'b-')
```

11.3   Appendix III: Python Impulse Calculations

```python
#!/usr/bin/env python3
# -*- coding: utf-8 -*-
"""
Created on Sun Feb 25 12:26:59 2024

@author: chaseorvis
"""

import math
import numpy as np
import scipy.integrate as int
import matplotlib.pyplot as plt

J = 1.327E11

def ODE_func(z,t):

    global G
    global m
    global J

    #position and velocity vector
    r = np.zeros(3)
    v = np.zeros(3)

    #Setting derivatives
    r[0] = z[0]
    r[1] = z[1]
    r[2] = z[2]
    v[0] = z[3]
    v[1] = z[4]
    v[2] = z[5]

    #array to hold derivatives
    drdt = np.zeros(len(z))

    #IVP application
    drdt[0] = v[0]
    drdt[1] = v[1]
    drdt[2] = v[2]
    drdt[3] = -(J*r[0]) / ((r[0]**2+r[1]**2+r[2]**2)**(3/2))
    drdt[4] = -(J*r[1]) / ((r[0]**2+r[1]**2+r[2]**2)**(3/2))
    drdt[5] = -(J*r[2]) / ((r[0]**2+r[1]**2+r[2]**2)**(3/2))
```

```
    return drdt
t0 = 0.
tEnd = 3600.*24.*4000
t = np.linspace(t0,tEnd,1000)
initial = np.array([1.5E8,0,0,0,40.035,0.])
soln = int.odeint(ODE_func,initial,t)
value = 0
time = np.zeros(1)
C_a = np.zeros(len(soln))
for i in range(len(soln)):
    C = (soln[i][0]**2+soln[i][1]**2)**(1/2)
    C_a[i] = C
    if 1.44e9 - C < 0:
        value = C
        time[0] = t[i]
        break

plt.plot(soln[:,0],soln[:,1])
print(1.44e9-value)

print(time/(60*60*24))
```

11.4 Appendix IV: Python Orbital Calculations

```python
import numpy as np
from scipy.integrate import solve_ivp
import matplotlib.pyplot as plt
from matplotlib.patches import Circle


R_E = 1.496E8  # km
mu = 1.327E11  # km**3/s**2


r_LEO = R_E + 42164  # km
v_LEO = np.sqrt(mu / r_LEO)  # km/s


r_2 = 2.9318E9  # km, GEO


r_0 = np.array((r_LEO, 0, 0))  # km
v_0 = np.array((0, v_LEO, 0))  # km/s
m_0 = np.array((6500))  # kg
Y_0 = np.hstack((r_0, v_0, m_0))


T = 0.000236  # kN
I_sp = 4190  # s
g_0 = 9.807E-3  # km/s**2

def nonimpulsive_maneuver(t, Y, mu, T, I_sp, g_0, r_2):
    r = np.sqrt(np.dot(Y[0:3], Y[0:3]))
    v = np.sqrt(np.dot(Y[3:6], Y[3:6]))
    m = Y[-1]
    dY_dt = np.zeros(len(Y))
    dY_dt[0:3] = Y[3:6]
    dY_dt[3:6] = -mu * Y[0:3] / r**3 + T * Y[3:6] / (m * v)
    dY_dt[-1] = - T / (I_sp * g_0)
    return dY_dt

def reached_destination(t, Y, mu, T, I_sp, g_0, r_2):
    r_vec = Y[0:3]
    r = np.sqrt(np.dot(r_vec, r_vec))
    return r - r_2


reached_destination.terminal = True


def mass(t, Y, mu, T, I_sp, g_0, r_2):
    return Y[-1]


mass.terminal = True
```

```python
def orbit(t, Y, mu, T, I_sp, g_0, r_2):
    return Y[1]


orbit.direction = 1


t_end = 8.73e+8  # s
t_eval = np.linspace(0, t_end, int(1E3))


sol = solve_ivp(
    nonimpulsive_maneuver,
    t_span=(0, t_end),
    y0=Y_0,
    t_eval=t_eval,
    events=(reached_destination, mass, orbit),
    rtol=1E-12,
    atol=1E-15,
    method="DOP853",
    args=(mu, T, I_sp, g_0, r_2)
)


print(sol.status)


print(sol.t_events[:2])


r_vec = sol.y[0:3].T
r = np.sqrt(r_vec[:, 0]**2 + r_vec[:, 1]**2 + r_vec[:, 2]**2)
v_vec = sol.y[3:6].T
v = np.sqrt(v_vec[:, 0]**2 + v_vec[:, 1]**2 + v_vec[:, 2]**2)
m = sol.y[-1]


plt.rc("font", size=20)
fig, ax = plt.subplots(figsize=(12, 12))
ax.set_aspect("equal")
ax.axis("off")
ax.add_patch(Circle((0, 0), R_E, ec="blue", fc="none"))
ax.annotate("Sun", xy=(0, 0), ha="center", va="center")
ax.add_patch(Circle((0, 0), r_2, ec="C1", fc="none", lw=2, ls="--"))
ax.plot(r_vec[:, 0], r_vec[:, 1], color="C2")
orbit_crossings = sol.y_events[2][:, 0]
ax.plot(orbit_crossings, np.zeros(orbit_crossings.shape), 'ko', fillstyle='none')

print(f"The number of orbits is: {sol.t_events[2].shape[0]}")
print(f"The flight used: {m_0 - m[-1]:.4F} kg of propellant")
print(f"Time of flight: {sol.t_events[0][0] / (3600 * 24):.4F} days")
```

11.5   Appendix V: Matlab Structural Calculations and Plots

```matlab
%% EMA 569 Senior Design

% Kaden Reybrock
% 4/3/2024

clear; close all; clc

% Dish support structural analysis
% CASE I

h=0.25; % Parameter (vertical height from base to dish) [m]
r_o = .0005.*[4.7625 6.35 6.35 6.35 7.9375 7.9375 7.9375 9.525 9.525 9.525 11.1125 12.7
r_i = .0005.*[2.9972 4.572 3.8608 3.4036 6.1722 5.461 5.0038 7.0358 6.5786 6.223 7.8232

% Aluminum 6061-T6 Tube Sizing from:
% https://titanium-stainless-steel.continentalsteel.com/viewitems/tegories-aerospace-met

A = pi.*(r_o.^2-r_i.^2); % Cross-sectional area of pole [m^2]
l = h./(sind(55)); % Pole length [m]
g = 9.81; % Gravitational acceleration [m/s^2]
m = 20; % Mass of the satellite dish [kg]
F1 = 8.*g.*m./8; % Vertical force (8g's accel over 8 supports) [N]
F2 = 3.*g.*m./8; % Horizontal force (3g's accel over 8 supports) [N]
Fx = F1.*cosd(35)+F2.*cosd(55); % Force in x-dir (in pole's axial direction) [N]
Fy = F1.*sind(35)-F2.*sind(55); % Force in y-dir (perpendicular to pole's central axis)
M = Fy.*l; % Moment at the base of the poles [N-m]
y = r_o; %[m]

Q = (2./3).*(r_o.^3-r_i.^3);
I = (pi./4).*(r_o.^4-r_i.^4);
t = 2.*(r_o-r_i);

sigma_xx = Fx./A + M.*y./I; % Pa
tau_xy = (Fy.*Q)./(I.*t); % Pa
sigma_yy = 0; % Pa

sigma_p1 = ((sigma_xx+sigma_yy)./2)+sqrt((((sigma_xx+sigma_yy)./2).^2+tau_xy.^2); % MPa
sigma_p2 = ((sigma_xx+sigma_yy)./2)-sqrt((((sigma_xx+sigma_yy)./2).^2+tau_xy.^2); % MPa
tau_max = sqrt((((sigma_xx+sigma_yy)./2).^2+tau_xy.^2); % MPa

index = linspace(1,length(r_o),length(r_o));
max_allowed = 276.*10^6.*ones(1,length(r_o));
max_shear = 207.*10^6.*ones(1,length(r_o));
```

```matlab
% Material Properties of 6061-T6 Aluminum from:
% https://asm.matweb.com/search/SpecificMaterial.asp?bassnum=ma6061t6

figure(1)
plot(index,sigma_p1)
hold on;
plot(index,sigma_p2)
hold on;
plot(index,tau_max)
hold on;
plot(index,max_allowed)
hold on;
plot(index,max_shear)
legend({'$\sigma_{p1}$','$\sigma_{p2}$','$\tau_{max}$','$Max \: Normal$','$Max \: Shear$

FS = max_allowed./sigma_p1;
FS_shear = max_shear./tau_max;
FS_goal = 1.5.*ones(1,length(r_o));

figure(2)
plot(index,FS)
hold on
plot(index,FS_shear)
hold on
plot(index,FS_goal)
legend({'$FS \: Normal$','$FS \: Shear$','$FS \: Goal$'},'Interpreter','Latex')
xlabel('$Index \: (Sizing \: Pair)$','Interpreter','Latex')
ylabel('$Factor \: of \: Safety$','Interpreter','Latex')
title('$CASE \: I$','Interpreter','Latex')

%% Horizontal load in other direction
% CASE II

h=0.25; % Parameter (vertical height from base to dish) [m]
r_o = .0005.*[4.7625 6.35 6.35 6.35 7.9375 7.9375 7.9375 9.525 9.525 9.525 11.1125 12.7
r_i = .0005.*[2.9972 4.572 3.8608 3.4036 6.1722 5.461 5.0038 7.0358 6.5786 6.223 7.8232

A = pi.*(r_o.^2-r_i.^2); % Cross-sectional area of pole [m^2]
l = h./(sind(55)); % Pole length [m]
g = 9.81; % Gravitational acceleration [m/s^2]
m = 20; % Mass of the satellite dish [kg]
F1 = 8.*g.*m./8; % Vertical force (8g's accel over 8 supports) [N]
F2 = 3.*g.*m./8; % Horizontal force (3g's accel over 8 supports) [N]
Fx = F1.*cosd(35)-F2.*cosd(55); % Force in x-dir (in pole's axial direction) [N]
```

```matlab
Fy = F1.*sind(35)+F2.*sind(55); % Force in y-dir (perpendicular to pole's central axis)
M = Fy.*l; % Moment at the base of the poles [N-m]
y = r_o; %[m]

Q = (2./3).*(r_o.^3-r_i.^3);
I = (pi./4).*(r_o.^4-r_i.^4);
t = 2.*(r_o-r_i);

sigma_xx = Fx./A + M.*y./I; % Pa
tau_xy = (Fy.*Q)./(I.*t); % Pa
sigma_yy = 0; % Pa

sigma_p1 = ((sigma_xx+sigma_yy)./2)+sqrt(((sigma_xx+sigma_yy)./2).^2+tau_xy.^2); % MPa
sigma_p2 = ((sigma_xx+sigma_yy)./2)-sqrt(((sigma_xx+sigma_yy)./2).^2+tau_xy.^2); % MPa
tau_max = sqrt(((sigma_xx+sigma_yy)./2).^2+tau_xy.^2); % MPa

index = linspace(1,length(r_o),length(r_o));
max_allowed = 276.*10^6.*ones(1,length(r_o));
max_shear = 207.*10^6.*ones(1,length(r_o));

figure(3)
plot(index,sigma_p1)
hold on;
plot(index,sigma_p2)
hold on;
plot(index,tau_max)
hold on;
plot(index,max_allowed)
hold on;
plot(index,max_shear)
legend({'$\sigma_{p1}$','$\sigma_{p2}$','$\tau_{max}$','$Max \: Normal$','$Max \: Shear$

FS = max_allowed./sigma_p1;
FS_shear = max_shear./tau_max;
FS_goal = 1.5.*ones(1,length(r_o));

figure(4)
plot(index,FS)
hold on
plot(index,FS_shear)
hold on
plot(index,FS_goal)
legend({'$FS \: Normal$','$FS \: Shear$','$FS \: Goal$'},'Interpreter','Latex')
xlabel('$Index \: (Sizing \: Pair)$','Interpreter','Latex')
ylabel('$Factor \: of \: Safety$','Interpreter','Latex')
```

```matlab
title('$CASE \: II$','Interpreter','Latex')

%% Horizontal Load in Z
% CASE III

h=0.25; % Parameter (vertical height from base to dish) [m]
r_o = .0005.*[4.7625 6.35 6.35 6.35 7.9375 7.9375 7.9375 9.525 9.525 9.525 11.1125 12.7
r_i = .0005.*[2.9972 4.572 3.8608 3.4036 6.1722 5.461 5.0038 7.0358 6.5786 6.223 7.8232

A = pi.*(r_o.^2-r_i.^2); % Cross-sectional area of pole [m^2]
l = h./(sind(55)); % Pole length [m]
g = 9.81; % Gravitational acceleration [m/s^2]
m = 20; % Mass of the satellite dish [kg]
F1 = 8.*g.*m./8; % Vertical force (8g's accel over 8 supports) [N]
F2 = 3.*g.*m./8; % Horizontal force (3g's accel over 8 supports) [N]
Fx = F1.*cosd(35); % Force in x-dir (in pole's axial direction left to right) [N]
Fy = F1.*sind(35); % Force in y-dir (perpendicular to pole's central axis up) [N]
Fz = F2; % Force in z-dir (perpendicular to pole's central axis into page) [N]
Mz = Fy.*l; % Moment at the base of the poles [N-m]
My = Fz.*l; % Moment at the base of the poles [N-m]
y = r_o; %[m]


Q = (2./3).*(r_o.^3-r_i.^3);
I = (pi./4).*(r_o.^4-r_i.^4);
t = 2.*(r_o-r_i);

sigma_xx = Fx./A + Mz.*y./I; % Pa     +[My.*y./I]
tau_xy = (Fy.*Q)./(I.*t); % Pa
sigma_yy = 0; % Pa
tau_yz = (Fz.*Q)./(I.*t); % Pa
sigma_zz = 0; % Pa
tau_xz = 0; % Pa

% First Circle
sigma_p1 = ((sigma_xx+sigma_yy)./2)+sqrt(((sigma_xx+sigma_yy)./2).^2+tau_xy.^2); % Pa
sigma_p2 = ((sigma_xx+sigma_yy)./2)-sqrt(((sigma_xx+sigma_yy)./2).^2+tau_xy.^2); % Pa
tau_max = sqrt(((sigma_xx+sigma_yy)./2).^2+tau_xy.^2); % Pa

% Second Circle
sigma_p3 = ((sigma_zz+sigma_yy)./2)+sqrt(((sigma_zz+sigma_yy)./2).^2+tau_yz.^2); % Pa
sigma_p4 = ((sigma_zz+sigma_yy)./2)-sqrt(((sigma_zz+sigma_yy)./2).^2+tau_yz.^2); % Pa
tau_max2 = sqrt(((sigma_zz+sigma_yy)./2).^2+tau_yz.^2); % Pa

% Third Circle
sigma_p5 = ((sigma_xx+sigma_zz)./2)+sqrt(((sigma_xx+sigma_zz)./2).^2+tau_xz.^2); % MPa
```

```
sigma_p6 = ((sigma_xx+sigma_zz)./2)-sqrt((((sigma_xx+sigma_zz)./2).^2+tau_xz.^2); % MPa
tau_max3 = sqrt((((sigma_xx+sigma_zz)./2).^2+tau_xz.^2); % MPa

index = linspace(1,length(r_o),length(r_o));
max_allowed = 276.*10^6.*ones(1,length(r_o));
max_shear = 207.*10^6.*ones(1,length(r_o));

figure(5)
plot(index,sigma_p1)
hold on;
plot(index,sigma_p2)
hold on;
plot(index,tau_max)
hold on;
plot(index,sigma_p3)
hold on;
plot(index,sigma_p4)
hold on;
plot(index,tau_max2)
hold on;
plot(index,sigma_p5)
hold on;
plot(index,sigma_p6)
hold on;
plot(index,tau_max3)
hold on;
plot(index,max_allowed)
hold on;
plot(index,max_shear)
legend({'$\sigma_{p1}$','$\sigma_{p2}$','$\tau_{max}$','$\sigma_{p3}$','$\sigma_{p4}$','

FS = max_allowed./sigma_p1;
FS_shear = max_shear./tau_max;
FS_goal = 1.5.*ones(1,length(r_o));

figure(6)
plot(index,FS)
hold on
plot(index,FS_shear)
hold on
plot(index,FS_goal)
legend({'$FS \: Normal$','$FS \: Shear$','$FS \: Goal$'},'Interpreter','Latex')
xlabel('$Index \: (Sizing \: Pair)$','Interpreter','Latex')
ylabel('$Factor \: of \: Safety$','Interpreter','Latex')
title('$CASE \: III$','Interpreter','Latex')
```

```matlab
%% Chase's Structural
% CASE I
r_o = 0.001.*[31.75 38.1 44.45 50.8 57.15 63.5 69.85 76.2 82.55 88.9 95.25 101.6 107.95
r_i = 0.001.*[30.861 37.211 43.561 49.911 56.261 62.611 68.961 75.311 81.661 88.011 94.3

% Titanium Tube Sizing from:
% https://titanium-stainless-steel.continentalsteel.com/viewitems/titanium/titanium-seam

A = pi.*(r_o.^2-r_i.^2); % Cross-sectional area of pole [m^2]
l = 0.1; % Pole length [m]
l_RTG = 0.6; % Half of RTG length [m]
g = 9.81; % Gravitational acceleration [m/s^2]
m = 250; % Mass of the satellite dish [kg]
F1 = 8.*g.*m; % Vertical force (8g's accel over 8 supports) [N]
F2 = 3.*g.*m; % Horizontal force (3g's accel over 8 supports) [N]
Fx = F2; % Force in x-dir (in pole's axial direction) [N]
Fy = F1; % Force in y-dir (perpendicular to pole's central axis) [N]
M = Fy.*l; % Moment at the base of the poles [N-m]
y = r_o; %[m]

Q = (2./3).*(r_o.^3-r_i.^3);
I = (pi./4).*(r_o.^4-r_i.^4);
t = 2.*(r_o-r_i);

sigma_xx = Fx./A + M.*y./I + (Fy.*l_RTG).*y./I; % Pa
tau_xy = (Fy.*Q)./(I.*t); % Pa
sigma_yy = 0; % Pa

sigma_p1 = ((sigma_xx+sigma_yy)./2)+sqrt(((sigma_xx+sigma_yy)./2).^2+tau_xy.^2); % MPa
sigma_p2 = ((sigma_xx+sigma_yy)./2)-sqrt(((sigma_xx+sigma_yy)./2).^2+tau_xy.^2); % MPa
tau_max = sqrt(((sigma_xx+sigma_yy)./2).^2+tau_xy.^2); % MPa

sigma_vm = sqrt(sigma_p1.^2-sigma_p1.*sigma_p2+sigma_p2.^2+3.*tau_max.^2);

index = linspace(1,length(r_o),length(r_o));
max_allowed = 880.*10^6.*ones(1,length(r_o));
max_shear = 550.*10^6.*ones(1,length(r_o));

% Material Properties of Titanium Ti-6Al-4V (Grade 5), Annealed from:
% https://asm.matweb.com/search/SpecificMaterial.asp?bassnum=mtp641

figure(7)
plot(index,sigma_vm)
hold on;
```

```matlab
plot(index,max_allowed)
legend({'$\sigma_{vm}$','$Max \: Normal$'},'Interpreter','Latex')

FS = max_allowed./sigma_vm;
FS_shear = max_shear./tau_max;
FS_goal = 1.5.*ones(1,length(r_o));

figure(8)
plot(index,FS)
hold on
plot(index,FS_goal)
legend({'$FS$','$FS \: Goal$'},'Interpreter','Latex')
xlabel('$Index \: (Sizing \: Pair)$','Interpreter','Latex')
ylabel('$Factor \: of \: Safety$','Interpreter','Latex')
title('$SRG \: CASE \: I$','Interpreter','Latex')

%% Chase's Structural
% CASE II
r_o = 0.001.*[31.75 38.1 44.45 50.8 57.15 63.5 69.85 76.2 82.55 88.9 95.25 101.6 107.95
r_i = 0.001.*[30.861 37.211 43.561 49.911 56.261 62.611 68.961 75.311 81.661 88.011 94.3

A = pi.*(r_o.^2-r_i.^2); % Cross-sectional area of pole [m^2]
l = 0.1; % Pole length [m]
l_RTG = 0.6; % Half of RTG length [m]
g = 9.81; % Gravitational acceleration [m/s^2]
m = 250; % Mass of the satellite dish [kg]
F1 = 8.*g.*m; % Vertical force (8g's accel over 8 supports) [N]
F2 = 3.*g.*m; % Horizontal force (3g's accel over 8 supports) [N]
Fz = F2; % Force in x-dir (in pole's axial direction) [N]
Fy = F1; % Force in z-dir (perpendicular to pole's central axis) [N]
M = Fy.*l; % Moment at the base of the poles [N-m]
y = r_o; %[m]

Q = (2./3).*(r_o.^3-r_i.^3);
I = (pi./4).*(r_o.^4-r_i.^4);
t = 2.*(r_o-r_i);

sigma_xx = M.*y./I + ((Fy.*l_RTG).*y)./I; % Pa
tau_xy = (Fy.*Q)./(I.*t); % Pa
sigma_yy = 0; % Pa

sigma_p1 = ((sigma_xx+sigma_yy)./2)+sqrt(((sigma_xx+sigma_yy)./2).^2+tau_xy.^2); % MPa
sigma_p2 = ((sigma_xx+sigma_yy)./2)-sqrt(((sigma_xx+sigma_yy)./2).^2+tau_xy.^2); % MPa
tau_max = sqrt(((sigma_xx+sigma_yy)./2).^2+tau_xy.^2); % MPa
```

```
sigma_vm = sqrt(sigma_p1.^2-sigma_p1.*sigma_p2+sigma_p2.^2+3.*tau_max.^2);

index = linspace(1,length(r_o),length(r_o));
max_allowed = 880.*10^6.*ones(1,length(r_o));
max_shear = 550.*10^6.*ones(1,length(r_o));

figure(9)
plot(index,sigma_vm)
hold on;
plot(index,max_allowed)
legend({'$\sigma_{vm}$','$Max \: Normal$'},'Interpreter','Latex')

FS = max_allowed./sigma_vm;
FS_goal = 1.5.*ones(1,length(r_o));

figure(10)
plot(index,FS)
hold on
plot(index,FS_goal)
legend({'$FS$','$FS \: Goal$'},'Interpreter','Latex')
xlabel('$Index \: (Sizing \: Pair)$','Interpreter','Latex')
ylabel('$Factor \: of \: Safety$','Interpreter','Latex')
title('$SRG \: CASE \: II$','Interpreter','Latex')

%% EDITED DISH SUPPORT ANALYSIS JUST GRAVITY

% Dish support structural analysis
% EDITED VERSION

h=0.25; % Parameter (vertical height from base to dish) [m]
r_o = 0.0095; % Parameter (outer radius of pole) [m]
r_i = 0.0083; % Parameter (inner radius of pole) [m]

% Aluminum 6061-T6 Tube Sizing from:
% https://titanium-stainless-steel.continentalsteel.com/viewitems/tegories-aerospace-met

theta = 55; % degrees
A = pi.*(r_o.^2-r_i.^2); % Cross-sectional area of pole [m^2]
l = h./(sind(theta)); % Pole length [m]
g = 9.81; % Gravitational acceleration [m/s^2]
rho = 2710; % Density of aluminum [kg/m^3]
m = rho.*A.*l; % Mass of a bar
F = m.*g; % Vertical force [N]
P = -F.*sind(theta)-F./sind(theta); % Force in y'-dir (in pole's axial direction) [N]
V = F.*cosd(theta); % Force in y-dir (perpendicular to pole's central axis) [N]
```

```
M = V.*l/2; % Moment at the base of the poles [N-m]
y = r_o; %[m]


Q = (2./3).*(r_o.^3-r_i.^3);
I = (pi./4).*(r_o.^4-r_i.^4);
t = 2.*(r_o-r_i);


sigma_xx = P./A - M.*y./I; % Pa
tau_xy = (V.*Q)./(I.*t); % Pa
sigma_yy = 0; % Pa


sigma_p1 = ((sigma_xx+sigma_yy)./2)+sqrt(((sigma_xx+sigma_yy)./2).^2+tau_xy.^2); % MPa
sigma_p2 = ((sigma_xx+sigma_yy)./2)-sqrt(((sigma_xx+sigma_yy)./2).^2+tau_xy.^2); % MPa
tau_max = sqrt(((sigma_xx+sigma_yy)./2).^2+tau_xy.^2); % MPa


sigma_vm = sqrt(sigma_p1.^2-sigma_p1.*sigma_p2+sigma_p2.^2+3.*tau_max.^2);


index = linspace(1,length(r_o),length(r_o));
max_allowed = 276.*10^6.*ones(1,length(r_o));
max_shear = 207.*10^6.*ones(1,length(r_o));


% Material Properties of 6061-T6 Aluminum from:
% https://asm.matweb.com/search/SpecificMaterial.asp?bassnum=ma6061t6


FS = max_allowed./sigma_vm;
FS_goal = 1.5.*ones(1,length(r_o));
disp(sigma_vm);
disp(FS)


%% EDITED DISH SUPPORT ANALYSIS


% Dish support structural analysis
% EDITED VERSION


h=0.25; % Parameter (vertical height from base to dish) [m]
r_o = 0.0095; % Parameter (outer radius of pole) [m]
r_i = 0.0083; % Parameter (inner radius of pole) [m]


% Aluminum 6061-T6 Tube Sizing from:
% https://titanium-stainless-steel.continentalsteel.com/viewitems/tegories-aerospace-met


theta = 55; % degrees
alpha = 90-theta; % degrees
A = pi.*(r_o.^2-r_i.^2); % Cross-sectional area of pole [m^2]
l = h./(sind(theta)); % Pole length [m]
```

```matlab
g = 9.81; % Gravitational acceleration [m/s^2]
rho = 2710; % Density of aluminum [kg/m^3]
m = 20/4; % Mass of satellite dish [kg]
F1 = 8.*m.*g; % Vertical force [N]
F2 = 3.*m.*g; % Horizontal force [N]
P = -(F2.*tand(theta)+F1)./(2.*sind(theta)); % Normal Force on support BC (in pole's axi
V = F2.*sind(theta)-F1.*cosd(theta); % Shear Force on support BC (perpendicular to pole'
M = V.*l/2; % Moment at the base of the poles [N-m]
y = r_o; %[m]

Q = (2./3).*(r_o.^3-r_i.^3);
I = (pi./4).*(r_o.^4-r_i.^4);
t = 2.*(r_o-r_i);

sigma_xx = P./A - M.*y./I; % Pa
tau_xy = (V.*Q)./(I.*t); % Pa
sigma_yy = 0; % Pa

sigma_p1 = ((sigma_xx+sigma_yy)./2)+sqrt(((sigma_xx+sigma_yy)./2).^2+tau_xy.^2); % MPa
sigma_p2 = ((sigma_xx+sigma_yy)./2)-sqrt(((sigma_xx+sigma_yy)./2).^2+tau_xy.^2); % MPa
tau_max = sqrt(((sigma_xx+sigma_yy)./2).^2+tau_xy.^2); % MPa

sigma_vm = sqrt(sigma_p1.^2-sigma_p1.*sigma_p2+sigma_p2.^2+3.*tau_max.^2);

index = linspace(1,length(r_o),length(r_o));
max_allowed = 276.*10^6.*ones(1,length(r_o));
max_shear = 207.*10^6.*ones(1,length(r_o));

% Material Properties of 6061-T6 Aluminum from:
% https://asm.matweb.com/search/SpecificMaterial.asp?bassnum=ma6061t6

FS = max_allowed./sigma_vm;
FS_goal = 1.5.*ones(1,length(r_o));
disp(sigma_vm);
disp(max_allowed)
fprintf('Factor of Safety = %s with a Von Mises Stress of %d \n',FS,sigma_vm);
```

11.6 Appendix VI: Heat Transfer with all variables

```
clear all

% Define parameters
cp = 897; % Specific heat capacity (J/kg*K)
R = 6873; %(km) radius of Earth
h = 400; %(km) altitude of satellite
betacr = asind(R/(R+h));
tau = 28512; %(s) avg orbital period
t = linspace(0, tau, 50); % Generate time values
sa = 2*pi*(1.5)^2*5+4*(2*pi*((1.4/2)/2)^2*1.2); %(m2) based on cylinder of r=1.5, h=5
d = sqrt(sa/pi); %diameter of sphere with the same surface area
A = pi*(d/2)^2;
sa2 = (2*pi*((1.4/2)/2)^2*1.2);
sbc = 5.67e-8;

cp = 897;
m = 3000; %(kg)

% Initialize arrays

beta_values = linspace(0, 90, length(t)); % Generate beta values from -90 to 90
T = zeros(length(t), length(beta_values));
st = zeros(length(t), length(beta_values));
fE = zeros(1, length(beta_values));
lb = zeros(1, length(beta_values));
ub = zeros(1, length(beta_values));
a = zeros(1, length(beta_values));
qIR = zeros(1, length(t));
% Loop to calculate T for each beta and t
for j = 1:length(beta_values)
    beta(j) = beta_values(j);
    if beta(j) < betacr
        fE(j) = (1./180).*acosd(sqrt(h.^2+2.*h.*R)./((R+h).*cosd(beta(j))));
    else
        fE(j) = 0;
    end
        lb(j) = (tau./2).*(1-fE(j));
        ub(j) = (tau./2).*(1+fE(j));
    if beta(j) < 30
        a(j) = 0.14;
        qIR(j) = 228;
    else
```

```matlab
        a(j) = 0.19;
        qIR(j) = 218;
    end

    for i = 1:length(t)

        % Turn off solar radiation during eclipse
        if lb(j) < t(i) && t(i) < ub(j)
            st(j,i) = 0;
        else
            st(j,i) = 1;
        end
        Tideal = 300; %(K)
        alpha = 0.15;
        emis = 0.85;
        AIR = A;
        qsol = 1414; %W/m2
        Asol = A;
        Qgen = 18500*4*0; %W

        % Calculate temperature using the given equation
        if i == 1
            T(j,i) = 293.15; % Initial temperature (K)
        else
            Q(j,i) = qIR(j).*AIR+(1+a(j))*qsol*Asol*st(j,i)*alpha+Qgen-A.*sbc.*emis.*T(j
            T(j,i) = T(j,i-1) + (t(i)-t(i-1))./(cp.*m).*Q(j,i);
        end
    end
end

% Create 3D plot
figure;
surf(t, beta_values, T);
xlabel('Time (s)');
ylabel('\beta (\circ)');
zlabel('Temperature (K)');
title('Temperature Vs Time and Beta Angle');
```

11.7 Appendix VII: Heat Transfer Boom

```
L=2
q = 4083
k = 237
h = 0.05
e = 0.85
T_surr = 0
M = 200
P = 47.0339
q2 = P / (M)
dx = (L) / (M-1)
Duplicate i =1,M
x[i] = (i-1)*dx
End
"Left"
0 =q + k*h^2*(T[2]-T[1])/dx + sigma#*e*(4*dx*h)*(T_surr^4-T[1]^4) + q2
"Right"
0 = k*h^2*(T[M-1]-T[M])/dx + sigma#*e*4*dx*h*(T_surr^4-T[M]^4) + q2
"Middle"
Duplicate i = 2, M-1
0 = k*h^2*(T[i-1]-T[i])/dx + sigma#*e*4*dx*h*(T_surr^4-T[i]^4) + k*h^2*(T[i+1]-T[i])/dx
End
```

References

[1] "Space exploration - Rockets, Technology, History | Britannica." Accessed: Feb. 06, 2024. [Online]. Available: https://www.britannica.com/science/space-exploration/Early-rocket-development

[2] "Voyager | Definition, Discoveries, & Facts | Britannica." Accessed: Feb. 06, 2024. [Online]. Available: https://www.britannica.com/technology/Voyager-space-probes

[3] "History | Mission," NASA's Europa Clipper. Accessed: Feb. 06, 2024. [Online]. Available: https://europa.nasa.gov/mission/history

[4] "New Study of Uranus' Large Moons Shows 4 May Hold Water - NASA." Accessed: Jan. 26, 2024. [Online]. Available: https://www.nasa.gov/centers-and-facilities/jpl/new-study-of-uranus-large-moons-shows-4-may-hold-water/

[5] R. J. Cartwright et al., "Evidence for Ammonia-bearing Species on the Uranian Satellite Ariel Supports Recent Geologic Activity," ApJL, vol. 898, no. 1, p. L22, Jul. 2020, doi: 10.3847/2041-8213/aba27f.

[6] "Ariel - NASA Science." Accessed: Feb. 09, 2024. [Online]. Available: https://science.nasa.gov/uranus/moons/ariel/

[7] "NASA Technical Standards | Standards," NASA Technical Standards System. https://standards.nasa.gov/nasa-technical-standards (accessed Feb. 03, 2024).

[8] "Ion Propulsion - NASA Science." Accessed: Feb. 06, 2024. [Online]. Available: https://science.nasa.gov/mission/dawn/technology/ion-propulsion/

[9] "Falcon User's Guide" (PDF). SpaceX, 2009. https://www.spaceflightnow.com/falcon9/001/f9guide.pdf (accessed Feb. 03, 2024).

[10] "SPACEMATDB - Space Materials Database. Material selection." Accessed: Feb. 06, 2024. [Online]. Available: https://www.spacematdb.com/spacemat/

[11] SpaceX, "Falcon 9," SpaceX, 2023. https://www.spacex.com/vehicles/falcon-9/

[12] B. Jorns, "Physics of electric propulsion: Journal of Applied Physics: Vol 132, No 11." https://aip.scitation.org/doi/10.1063/5.0118076

[13] P. Hill and C. Peterson, "Mechanics and thermodynamics of propulsion", 2nd ed., Addison Wesley, 1992. ISBN-13: 978-0201146592

[14] D. Lev, "The technological and commercial expansion of electric propulsion - ScienceDirect."

[15] K. Holste, "Ion thrusters for electric propulsion: Scientific issues developing a niche technology into a game changer: Review of Scientific Instruments: Vol 91, No 6." https://aip.scitation.org/doi/10.1063/5.0010134

[16] E. Dale, B. Jorns, and A. Gallimore, "Future Directions for Electric Propulsion

Research," Aerospace, vol. 7, no. 9, Art. no. 9, Sep. 2020, doi: 10.3390/aerospace7090120.

[17] S. Caldwell, "4.0 In-Space Propulsion," NASA, Oct. 10, 2021. https://www.nasa.gov/smallsat-institute/sst-soa/in-space-propulsion.

[18] NASA, "Uranus: Facts - NASA Science," science.nasa.gov, 2023. https://science.nasa.gov/uranus/facts/.

[19] "Radioisotope Thermoelectric Generators (RTGs) - NASA Science," science.nasa.gov. https://science.nasa.gov/mission/cassini/radioisotope-thermoelectric-generator/

[20] "Advanced Stirling Radioisotope Generator (ASRG)," NASA RPS.gov. https://rps.nasa.gov/system/downloadable_items/36_APP_ASRG_Fact_Sheet_v3_9-3-13.pdf.

[21] Wikipedia Contributors, "Cassini–Huygens," Wikipedia, May 13, 2019. https://en.wikipedia.org/wiki/Cassini%E2%80%93Huygens

[22] S. Surampudi, "Overview of the Space Power Conversion and Energy Storage Technologies," 2011. Available: https://www.lpi.usra.edu/sbag/meetings/jan2011/presentations/day1/d1_1200_Surampudi.pdf

[23] P. Davis, "Mission Timeline | Toolkit," NASA Solar System Exploration. https://solarsystem.nasa.gov/missions/dawn/mission/toolkit/mission-timeline.

[24] "Deep Space 1 - NASA Science." Accessed: Feb. 06, 2024. [Online]. Available: https://science.nasa.gov/mission/deep-space-1/

[25] "Voyager 2 - NASA Science." Accessed: Feb. 07, 2024. [Online]. Available: https://science.nasa.gov/mission/voyager/voyager-2/

[26] "Voyager Backgrounder" (PDF). NASA, Oct. 1980. Accessed: Feb. 06, 2024. [Online]. Available: https://ntrs.nasa.gov/api/citations/19810001583/downloads/19810001583.pdf

[27] "Gravity Assists - NASA Science," science.nasa.gov. https://science.nasa.gov/mission/cassini/gravity-assists/

[28] "NASA - NSSDCA - Spacecraft - Details," nssdc.gsfc.nasa.gov. https://nssdc.gsfc.nasa.gov/nmc/spacecraft/display.action?id=1997-061A

[29] J. W. Dankanich and T. Polsgrovet, "Mission Benefits of Gridded Ion and Hall Thruster Hybrid Propulsion Systems," in Proc. Joint Propulsion Conf., AIAA-2006-5 162, Sacramento, CA, July 9-12, 2006, NASA Marshall Space Flight Center, Huntsville, AL. Available: https://ntrs.nasa.gov/api/citations/20060047631/downloads/20060047631.pdf.

[30] "EIS | Instruments," NASA's Europa Clipper. Accessed: Feb. 26, 2024. [Online]. Available: https://europa.nasa.gov/spacecraft/instruments/eis

[31] "Effect of downsampling and then tiling a Narrow-Angle Camera (NAC)...," ResearchGate. Accessed: Apr. 11, 2024. [Online]. Available: https://www.researchgate.net/figure/Effect-of-downsampling-and-then-tiling-a-Narrow-Angle-Camera-NAC-image-for-impact_fig5_360822683

[32] "Imaging Science Subsystem (ISS) - NASA Science." Accessed: Feb. 26, 2024. [Online]. Available: https://science.nasa.gov/mission/cassini/spacecraft/cassini-orbiter/imaging-science-subsystem/

[33] "Composite Infrared Spectrometer (CIRS) - NASA Science." Accessed: Feb. 26, 2024. [Online]. Available: https://science.nasa.gov/mission/cassini/spacecraft/cassini-orbiter/composite-infrared-spectrometer/

[34] "Europa-UVS | Instruments," NASA's Europa Clipper. Accessed: Feb. 26, 2024. [Online]. Available: https://europa.nasa.gov/spacecraft/instruments/europa-uvs

[35] "Visible and Infrared Mapping Spectrometer (VIMS) - NASA Science." Accessed: Feb. 26, 2024. [Online]. Available: https://science.nasa.gov/mission/cassini/spacecraft/cassini-orbiter/visible-and-infrared-mapping-spectrometer/

[36] "RADAR - NASA Science." Accessed: Feb. 26, 2024. [Online]. Available: https://science.nasa.gov/mission/cassini/spacecraft/cassini-orbiter/radio-detection-and-ranging/

[37] J. Taylor et al., "Cassini Orbiter/Huygens Probe Telecommunications," NASA Jet Propulsion Laboratory, Jan 2002. [Online]. Available: https://descanso.jpl.nasa.gov/DPSummary/Descanso3–Cassini2.pdf

[38] "Basics of Space Flight Section II. Flight Projects." Accessed: Feb. 19, 2024. [Online]. Available: `https://www3.jpl.nasa.gov/basics/cassini/hga.html`

[39] "Radio Frequencies for Space Communication." Accessed: Feb. 19, 2024. [Online]. Available: https://www.spaceacademy.net.au/spacelink/radiospace.htm

[40] "Harris' High Compaction Ratio (HCR) Unfurlable Space Reflector Antenna," Harris Corporation, 2018. [Online]. Accessed: February 19, 2024. Available: `https://satcatalog.s3.amazonaws.com/components/713/SatCatalog_-_L3Harris_Technologies_-_3m_Ka-Band_High_Compaction_Ratio_Reflector_Antenna_-_Datasheet.pdf?lastmod=20210714070621.`

[41] "Basics of Space Flight Section II. Flight Projects." Accessed: Feb. 19, 2024. [Online]. Available: https://www2.jpl.nasa.gov/basics//cassini/lga.html.

[42] "Small Deep Space Transponder - General Dynamics Mission Systems." Accessed: Feb. 19, 2024. [Online]. Available: https://gdmissionsystems.com/products/communications/spaceborne-communications/tracking-telemetry-and-control/small-deep-space-transponder

[43] "CT-2020 - Star Tracker | SatCatalog." Accessed: Feb. 19, 2024. [Online]. Available: https://www.satcatalog.com/component/ct-2020/

[44] "5.0 Guidance, Navigation, and Control - NASA." Accessed: Feb. 19, 2024. [Online].
Available: https://www.nasa.gov/smallsat-institute/sst-soa/guidance-navigation-and-control/#5.2.5

[45] "Dawn Spacecraft & Mission Overview – Spacecraft & Satellites." Accessed: Feb. 19,
2024. [Online]. Available:
https://spaceflight101.com/spacecraft/dawn-spacecraft-mission-overview/

[46] "How sun sensors work," SOLAR MEMS Technologies. Accessed: Feb. 19, 2024.
[Online]. Available: https://solar-mems.com/newspace/how-sun-sensors-work/

[47] "Coarse Sun Sensor | satsearch." Accessed: Feb. 19, 2024. [Online]. Available:
https://satsearch.co/products/bradford-coarse-sun-sensor

[48] "REACTION WHEEL UNIT." Bradford Space. Dec 2019. Accessed Feb. 19, 2024.
[Online]. Available:
`https://satcatalog.s3.amazonaws.com/components/186/SatCatalog_-_`
`Bradford_Space_-_W45E_-_Datasheet.pdf?lastmod=20210716013730`.

[49] "Monopropellant Hydrazine Thrusters." Accessed: Feb. 19, 2024. [Online]. Available:
https://www.space-propulsion.com/spacecraft-propulsion/hydrazine-thrusters/index.html

[50] F. Zhu, "A GUIDE TO CUBESAT MISSION AND BUS DESIGN," Section 8.8
Control, Accessed: Feb. 19, 2024. [Online]. Available:
https://pressbooks-dev.oer.hawaii.edu/epet302/chapter/7-7/

[51] "Honeywell 1750A-5V: MIL-STD-1750A Lives On | The CPU Shack Museum," The
CPU Shack Museum | CPU History Museum for Intel CPUs, AMD Processor, Cyrix
Microprocessors, Microcontrollers and more. Accessed: Feb. 19, 2024. [Online].
Available:
https://www.cpushack.com/2013/10/25/honeywell-1750a-5v-mil-std-1750a-lives-on/

[52] D. Isbell et al., "Cassini Launch," NASA ADMINISTRATION, October 1997.
[Online]. Accessed: February 19, 2024. Available:
https://www.jpl.nasa.gov/news/press_kits/cassini.pdf.

[53] J. M. Millard and T. W. Luan, "Operational Thermal Control of Cassini Titan
Flybys," SAE Transactions, vol. 112, pp. 243–254, 2003.

[54] "Thermal Blankets - NASA Science." Accessed: Feb. 19, 2024. [Online]. Available:
https://science.nasa.gov/mission/cassini/thermal-blankets/

[55] V. Mireles and J. W. Stultz, "RTG Waste Heat System for the Cassini Propulsion
Module," NASA Jet Propulsion Laboratory. Available:
https://dataverse.jpl.nasa.gov/api/access/datafile/36401?gbrecs=true

[56] "Light-Weight Radioisotope Heater Unit | Thermal Systems," NASA RPS:
Radioisotope Power Systems. Accessed: Feb. 21, 2024. [Online]. Available:
https://rps.nasa.gov/power-and-thermal-systems/thermal-systems/light-weight-radioisotope-heater-unit

[57] "Gridded Ion Thrusters (NEXT-C)," Glenn Research Center | NASA. Accessed: Feb. 25, 2024. [Online]. Available:
https://www1.grc.nasa.gov/space/sep/gridded-ion-thrusters-next-c/

[58] "177 L Hydrazine Tank - OST 31-1 - Tank | SatCatalog." Accessed: Feb. 25, 2024. [Online]. Available:
https://www.satcatalog.com/component/177-l-hydrazine-tank-ost-31-1/

[59] H. Curtis, Orbital Mechanics for Engineering Students, 3rd ed. Waltham, MA, USA: Butterworth-Heinemann, 2014. ISBN: 978-0080977478.

[60] C. J. Hamilton, "Uranus," 1997. [Online]. Available:
http://www.iki.rssi.ru/solar/eng/uranus.htm. Accessed: Feb. 26, 2024.

[61] C. J. Hamilton, "Ariel," 1997. [Online]. Available:
http://www.iki.rssi.ru/solar/eng/ariel.htm. Accessed: Feb. 26, 2024.

[62] OpenStax, "9.7 Rocket Propulsion," Aug. 2016, Accessed: Feb. 26, 2024. [Online]. Available:
https://pressbooks.online.ucf.edu/osuniversityphysics/chapter/9-7-rocket-propulsion/

[63] N. Bailey, "Uplink: Innovation — Accion Systems: The near future of in-space propulsion..." SatMagazine. Accessed: Feb. 26, 2024. [Online]. Available:
http://www.satmagazine.com/story.php?number=825519252.

[64] H. S. Tsien, "Take-Off from Satellite Orbit," Daniel and Florence Guggenheim Jet Propulsion Center, California Institute of Technology, Pasadena, Calif., Publication No. 44.

[65] B. Weber, "Example: Nonimpulsive Maneuvers — Orbital Mechanics & Astrodynamics." Accessed: Feb. 21, 2024. [Online]. Available: https://orbital-mechanics.space/orbital-maneuvers/nonimpulsive-maneuver-example.html

[66] "ASM Material Data Sheet," asm.matweb.com.
https://asm.matweb.com/search/SpecificMaterial.asp?bassnum=mtp641

[67] "EPDM - bladder tank BT 01/0," ArianeGroup, https://www.space-propulsion.com/brochures/propellant-tanks/58lt-n2h4-bladder-tank-bt01-0.pdf (accessed Apr. 12, 2024).

[68] "31.10. change in diameter and volume of a thin spherical ...," SNS College of Technology, Coimbatore, https://snscourseware.org/snsctnew/files/1670304346.pdf (accessed Apr. 12, 2024).

[69] "XS-XTA-7L - MT Aerospace," SatCatalog,
https://www.satcatalog.com/component/xs-xta-7l/ (accessed Apr. 12, 2024).

[70] J. J. Watkins, B. T. Doyle, M. A. McHugh, and V. J. Krukonis, "High-pressure Naphthalene-Xenon Phase Behavior ," Department of Chemical Engineering, The Johns Hopkins University and Phasex Corporation,

https://web.archive.org/web/20190222041629id_/http://pdfs.semanticscholar.org/3390/d7e90c7bc7b
(accessed Apr. 12, 2024).

[71] "Carbon Fiber - an overview | ScienceDirect Topics," *www.sciencedirect.com*.
https://www.sciencedirect.com/topics/chemistry/carbon-
fiber#:~:text=Carbon%20fibers%20are%20also%20categorized

[72] "L-XTA – Large Xenon Tank Assembly," *Esa.int*, 2021.
https://connectivity.esa.int/projects/lxta-%E2%80%93-large-xenon-tank-assembly
(accessed Apr. 30, 2024).

[73] "ASM Material Data Sheet," asm.matweb.com.
https://asm.matweb.com/search/SpecificMaterial.asp?bassnum=MA6061T6

[74] Raymond Jefferson Roark, Warren Clarence Young, and Richard Gordon Budynas,
Roark's Formulas for Stress and Strain. McGraw Hill Professional, 2002.

[75] "Aluminum Drawn Tubing," Continental Steel & Tube Co.
https://titanium-stainless-steel.continentalsteel.com/viewitems/tegories-aerospace-
metals-aluminum-aluminum-tubing/aluminum-drawn-tubing (accessed Apr. 12, 2024).

[76] "Titanium Tubes & Tubing - Seamless and Welded," Continental Steel & Tube Co.
https://titanium-stainless-steel.continentalsteel.com/viewitems/titanium/titanium-
seamless-and-welded-tubing?&bc=100

[77] ANSYS, Inc. (2023). ANSYS Parametric Design Language (APDL) (Version 20.2)
[Software]. ANSYS, Inc. Available:
https://www.ansys.com/products/platform/ansys-parametric-design-language-apdl

[78] G. L. Bennett et al., "Mission of Daring: The General-Purpose Heat Source
Radioisotope Thermoelectric Generator," International Energy Conversion Engineering
Conference and Exhibit, https://nuke.fas.org/space/gphs.pdf (accessed Apr. 13, 2024).

[79] G. Birur, G. Siebes, and T. Swanson, "Spacecraft thermal control," NASA, Mar. 2001.
Available: `https://s3vi.ndc.nasa.gov/ssri-kb/static/resources/Preliminary_`
`Thermal_Analysis_of_Small_Satellites.pdfâĂŒ`

[80] G. Nellis and S. A. Klein, Introduction to Engineering Heat Transfer. Cambridge,
United Kingdom: Cambridge University Press, 2021.

[81] A. Zhang and Y. Li, "Thermal Conductivity of Aluminum Alloys-A Review," Materials
(Basel, Switzerland) - U.S. National Library of Medicine,
https://www.ncbi.nlm.nih.gov/pmc/articles/PMC10144406/#: :text=Aluminum%20has%20a%20the
(accessed Apr. 12, 2024).

[82] EBAD. "NEA⃝R Hold down Release Mechanisms (HDRM)." Ensign-Bickford
Aerospace Defense, 26 Sept. 2019, www.ebad.com/nea-hold-down-release-mechanisms-
hdrm/#1562325851331-b2e4385b-5dd4b4fc-1b51. Accessed 27 Apr. 2024.

[83] [1] "EBAD," NEA Model 9100 Hold Down Release Mechanism (HDRM),
https://www.ebad.com/wp-

content/uploads/2021/03/NEA_Hold_Down_Release_Mechanism__HDRM__-_Model_9100_released_1-27-22.pdf (accessed Apr. 27, 2024).

[84] "Plutonium," World Nuclear Association, https://world-nuclear.org/information-library/nuclear-fuel-cycle/fuel-recycling/plutonium.aspx#: :text=Plutonium%2D238%20is%20made%20by,at%20Savannah%20River (accessed Apr. 12, 2024).

[85] "Radiation Characteristics of Plutonium-238," Los Alamos Scientific Laboratory of the University, https://sgp.fas.org/othergov/doe/lanl/docs1/00314834.pdf (accessed Apr. 12, 2024).

[86] Lawrence Berkeley National Laboratory, "Alpha Decay," Alpha decay, https://www2.lbl.gov/abc/wallchart/chapters/03/1.html (accessed Apr. 12, 2024).

[87] [Office of Radiation Protection, "What is Ionizing Radiation?," Washington State Depart-
ment of Health – Office of Radiation Protection - What is Ionizing Radiation Fact Sheet, https://wsdot.wa.gov/publications/fulltext/localprograms/nucleargauge/story_content/external_file

[88] "Alpha Beta and Gamma Radiation," StudySmarter UK, https://www.studysmarter.co.uk/explanations/physics/nuclear-physics/alpha-beta-and-gamma-radiation/#: :text=Beta

[89] United States Nuclear Regulatory Commission, "Beta particle," NRC Web, https://www.nrc.gov/reading-rm/basic-ref/glossary/beta-particle.html (accessed Apr. 12, 2024).

[90] G. E. Chabot, Shielding of gamma radiation, $http://hps.org/documents/shielding_of_gamma_radiation.pdf$ (accessed Apr. 12, 2024).

[91] "Space Radiation Effects on Electronic Components in Low-Earth Orbit," NASA, https://llis.nasa.gov/lesson/824 (accessed Apr. 12, 2024).

[92] United States Nuclear Regulatory Commission, "0477 - H117 - Introductory Health Physics - 05 - external dose rate calculations.," Chapter 5 External Dose Calculations, https://www.nrc.gov/docs/ML1121/ML11210B521.pdf (accessed Apr. 12, 2024).

[93] J. J. M. de Goeij and M. L. Bonardi, "Specific Activity," Wikipedia, https://en.wikipedia.org/wiki/Specific_activity#cite_ref-de_GoeijBonardi2005_3-0 (accessed Apr. 12, 2024).

[94] D. H. Stoddard and E. L. Albenesius, "Radiation Properties of 238Pu Produced For Isotopic Power Generators," RADIATION PROPERTIES OF 238Pu PRODUCED FOR ISOTOPIC POWER GENERATORS (Technical Report) | OSTI.GOV, https://www.osti.gov/servlets/purl/4616364/ (accessed Apr. 12, 2024).

[95] X-Ray Mass Attenuation Coefficients - Titanium, https://physics.nist.gov/PhysRefData/XrayMassCoef/ElemTab/z22.html (accessed Apr. 12, 2024).

[96] S. Ryan, M. Bjorkman, and E. L. Christiansen, "Whipple shield performance in the shatter regime," International Journal of Impact Engineering, vol. 38, no. 6, pp. 504–510, Jun. 2011, doi: https://doi.org/10.1016/j.ijimpeng.2010.10.022.

[97] "National Aeronautics and Space Administration SUBJECT: Whipple Shield Sizing Equations," 1991. [Online]. Available: https://ntrs.nasa.gov/api/citations/19920010826/downloads/19920010826.pdf

[98] E. L. Christiansen, J. L. Crews, J. E. Williamsen, J. H. Robinson, and A. M. Nolen, "Enhanced meteoroid and orbital debris shielding," International Journal of Impact Engineering, vol. 17, no. 1, pp. 217–228, Jan. 1995, doi: https://doi.org/10.1016/0734-743X(95)99848-L.

[99] "1 N Monopropellant Hydrazine Thruster." Accessed: Apr. 29, 2024. [Online]. Available: https://www.space-propulsion.com/spacecraft-propulsion/hydrazine-thrusters/1n-hydrazine-thruster.html

[100] Rafael, "Rafael Space Propulsion Catalogue," Rafael, 2021. Available: https://www.rafael.co.il/wp-content/uploads/2021/07/RAFAEL-SPACE-PROPULSION-2021-CATALOGUE-2.pdf. Accessed on: April 28, 2024.

[101] PlumbingSupply.com®, "Some Friction Loss Tables," PlumbingSupply.com® - The Premier Online Plumbing Supplier Since 1995. Accessed: Apr. 29, 2024. [Online]. Available: https://www.plumbingsupply.com/ed-frictionlosses.html

[102] "NASA's Evolutionary Xenon Thruster (NEXT) Ion Propulsion System Information Summary," Jun. 2009. https://newfrontiers.larc.nasa.gov/NF3/PDF_FILES/43NEXT_NF3refdocument_May09.pdf

[103] "Next-C - aerojet rocketdyne," NEXT-C Data Sheet, https://www.rocket.com/sites/default/files/documents/NEXT-C_Data_sheet_01_2022_FINAL_DIGITAL.pdf (accessed Apr. 27, 2024).

[104] O. Räisänen, Electrostatic Ion Thruster Diagram. 2021. Accessed: Apr. 27, 2024. [Inkscape]. Available: https://commons.wikimedia.org/w/index.php?curid=20308289

[105] D. M. Goebel and I. Katz, "Fundamentals of electric propulsion: Ion and hall thrusters," Fundamentals of Electric Propulsion: Ion and Hall Thrusters (NASA.gov), https://descanso.jpl.nasa.gov/SciTechBook/series1/Goebel__cmprsd_opt.pdf (accessed Apr. 27, 2024). 4.3 DC Discharge Ion Thruster (pg. 100-102)

[106] D. M. Goebel and I. Katz, "Fundamentals of electric propulsion: Ion and hall thrusters," Fundamentals of Electric Propulsion: Ion and Hall Thrusters (NASA.gov), https://descanso.jpl.nasa.gov/SciTechBook/series1/Goebel__cmprsd_opt.pdf (accessed Apr. 27, 2024). Appendix D: Ionization and Excitation Cross Sections for Xenon

[107] "Hollow Cathodes," in Fundamentals of Electric Propulsion: Ion and Hall Thrusters , Jet Propulsion Laboratory California Institute of Technology: JPL SPACE SCIENCE AND TECHNOLOGY SERIES, 2008, pp. 243–323. Accessed: Apr. 27, 2024. [Online].

Available:
https://descanso.jpl.nasa.gov/SciTechBook/series1/Goebel_06_Chap6_cathodes.pdf

[108] Sovey, J.S., L.M. Carney, and S.C. Knowles. "Electromagnetic Emission Experiences Using Electric Propulsion Systems,: AIAA J. Propulsion and Power 5 (1989): 534-547.